Structural and Geomechanical Analysis of Naturally Fractured Hydrocarbon Provinces of the Bowen and Amadeus Basins: Onshore Australia

Daniel J Gillam B.Sc (Hons.)

Australian School of Petroleum

The University of Adelaide

This thesis is submitted in fulfillment of the requirements for the degree of Doctor of Philosophy in the Faculty of Science, The University of Adelaide

October 2004

THE UNIVERSITY OF ADELAIDE AUSTRALIA

SUB CRUCE LUMEN

ASP Australian School of Petroleum

Contents

Structural and Geomechanical Analysis of Naturally Fractured Hydrocarbon Provinces of the Bowen and Amadeus Basins: Onshore Australia

Abstract

Significant hydrocarbon resources onshore Australia occur within reservoirs with low matrix permeability. Such low permeability reservoirs include those of the mature Palm Valley and Mereenie Fields of the Amadeus Basin, the emergent coal seam methane (CSM) play in eastern Australia and stranded tight gas within existing fields of the Bowen and Cooper Basins. This thesis investigates structural and geomechanical aspects of the Bowen and Amadeus Basins, with particular reference to the role of natural fractures in enhancing hydrocarbon recovery in the low permeability reservoirs of onshore Australia.

This thesis first investigates natural fracture development and in-situ stress in the Scotia coal seam methane (CSM) field of the eastern Bowen Basin (Chapter 2). The key factors responsible for good well performance in the field are identified as: 1) relatively low stress to facilitate hydraulic fracture treatments; and, 2) a high degree of natural fracturing. However, the Scotia study is restricted by data limitations typical of most hydrocarbon development projects including: limited core and image log data, an absence of nearby outcrop similar to the reservoir, and ambiguous stress data.

Chapters 3–6 present an analogue study from the Goonyella Riverside coal mine of the northern Bowen Basin aimed at thorough characterisation of natural fracture development and in-situ stress within a coal measure succession similar to that of the Scotia Field. The study uses 3D seismic data, image log data and outcrop observations to identify the key controls on natural fracture development: namely the mechanical stratigraphy and proximity to seismically resolvable faults. Different fracture sets at Goonyella Riverside are linked to the tectonic evolution of the area: 1) coal cleats and compaction-related normal faults are interpreted to have formed during Late Permian burial and diagenesis; 2) thrust faults and subsidiary low-angle shear fractures are most likely to have formed during the Early to Mid Triassic Hunter Bowen Orogeny; and, 3) tensile joints are interpreted to have formed during Cretaceous uplift and unloading. The influence of natural fracture permeability in the tight coal measure sequence is highlighted by groundwater observations that show a single thrust fault and associated damage zone account for half the water entering the underground mine adit.

The Goonyella Riverside study also uses in-situ stress measurements taken during the course of the underground mine development to illustrate the partitioning of stress within a background reverse stress regime. The sandstone intervals are characterised by a reverse-stress regime with maximum horizontal stress (S_{Hmax}) approximately twice the magnitude of the vertical stress (S_v) while the coal seams are characterised by a normal-stress regime with S_{Hmax} approximately half the magnitude of S_v. Drilling strategies and predictive pre-drill techniques have been developed from the Scotia and Goonyella Riverside studies for similar CSM fields in eastern

Australia. Fracture swarms that cluster around seismic-scale intraformational faults may be targeted for high-rate wells and cleat orientations may be predicted pre-drill by the orientation of seismic scale structures. The study also highlights potential problems with conventional hydraulic fracture stimulation in formations with highly anisotropic rock properties such as coal measure sequences where there is high background stress typical of onshore Australia.

Chapters 7–10 investigate the structural evolution and natural fracture development in the Palm Valley and Mereenie Fields of the northern Amadeus Basin. Regional balanced cross-sections demonstrate the interaction of a basement-cored wedge with the sedimentary cover and a weak basal detachment in an intracratonic setting. Shortening across the northern margin of the Amadeus Basin during the Alice Springs Orogeny (ASO) is ~ 30 km, significantly less than the ~110 km implied by previous thin-skinned models. Deformation within the foreland is relatively mild compared to other fold and thrust belts. The Mereenie and Palm Valley anticlines developed as thin-skinned, salt-cored detachment folds above the basal detachment. Isostatic modelling shows that the effective elastic thickness of the lithosphere was significantly less than its contemporary thickness of ~88 km during the ASO. The modelled effective elastic thickness of 10 km is similar to contemporary intracratonic extensional provinces such as east Africa and the Basin and Range Province, implying significant heat flow prior to the ASO.

Natural fractures are vital for gas production in the Palm Valley Field and naturally fractured sweet spots could also provide high-rate wells in the Mereenie Field. The study builds on previous work and identifies two generations of natural fracturing that influence reservoir performance in the fields: 1) bed-bound fold-related fractures that provide access to the low permeability matrix; and, 2) pervasive, orogen-related regional fractures that plumb the entire reservoir by connecting the fold-related fractures and different reservoir intervals. The fold-related fractures may be predicted by modelling the fold geometry with Gaussian curvature. A strong correlation exists between areas of high fracturing, good well performance and areas of high Gaussian curvature in the Palm Valley Field. The study shows that curvature analysis is field-specific and needs to be calibrated with fracture or production data from within the field and cannot necessarily be calibrated to data from other fields. Regional fracture spacing varies systematically across the basin and can be correlated to background orogenic intensity defined by the balanced 2D sections. The most productive wells in both fields are expected to occur in locations where the pervasive regional fractures intersect zones of dense fold-related fractures or where there are large reservoir-effective crestal fractures (as currently targeted).

The Amadeus Basin study also uses the structural modelling to assess the untested Mereenie sub-thrust play as the structural evolution is critical to trap integrity. A balanced reservoir-scale 2D section constrained by seismic data shows the anticline developed as a salt-cored detachment fold. Faulting was late in the structural development, but prior to maximum burial and final hydrocarbon charge. Footwall closure and fault seal are identified as the critical risks to

the sub-thrust play. Much of the Mereenie seismic data does not extend over the footwall of the fault but the structural modelling indicates footwall closure is likely. Fault seal risk is assessed as moderate based on juxtaposition relationships, likely fault rock properties and reactivation potential. The study identifies the Mereenie sub-thrust play as a medium to high-risk near-field exploration opportunity due mainly to poor seismic imaging of the footwall.

Statement

This thesis contains no material that has been accepted for the award of any other degree or diploma in any university or other tertiary institution. To the best of my knowledge and belief it contains no material previously published or written by another person except where due reference has been made in the text.

I give consent for this copy of my thesis to be available for loan and photocopying when deposited in the University Library.

Acknowledgements

First and foremost, thank you to Thomas Flottmann of Santos Ltd for initiating this project and being an exceptional technical mentor over the last three years. I have learnt many of the arts of structural geology through his guidance and have enjoyed the many beers and rugby-related discussions over the last few years.

The efforts and guidance of my academic supervisor, Richard Hillis are greatly appreciated. His pragmatic approach to supervision has enhanced my PhD experience. Thank you for introducing me to petroleum geomechanics and for providing such a dynamic work environment through the stress group.

This work has been funded and supported by Santos Ltd and could not have occurred without their most generous contribution. The many discussions with Santos Ltd staff including Irwan Djamaludin, Dennis Cooke, Nick Hall, Mark Webster and Ray Johnson have greatly improved the quality of this thesis.

A big thank you to Doug Dunn, Jared Armstrong, Rob Swann and Peter Brisbane of BHP Billiton Mitsubishi Alliance (BMA) for providing mine access and logistic support for the Goonyella Riverside study. Thanks also to Dave Dewhurst at CSIRO Petroleum for helping out with rock testing.

Thank you to all those at the ASP and the Discipline of Geology and Geophysics at the University of Adelaide for assistance over the last three years. Martin Hand, Peter Tingate and Simon Lang are greatly appreciated for providing countless discussions and ideas on the beasts that are the Bowen and Amadeus Basins. Joan Esterle, Renate Sliwa, Philip Soole and others at CSIRO Exploration and Mining are thanked for access to the CSIRO Supermodel database and discussions on Bowen Basin geology. Thanks also to Noel Perkins of Soil Surveys Engineering for introducing me to rock mechanics.

To all those in the stress group during my time, including; Emma Nelson, Aaron Cummings, Scott Reynolds, Mark Tingay, Paul Lyon and Juergen Streit, my studies would have been far less insightful and enjoyable without you guys. Thanks also to Mark Reilly and the JRS lads, Scott Mildren and Jerry Meyer, for technical support and some fantastic Friday lunches.

Thank you to my family and friends, in and out of the University for putting up with my absentia and eccentric behavior over the last three years. Last but certainly not least, I would like to thank Helen for sticking by me. Her patience and support have helped more than words can say.

List of Symbols and Abbreviations

a	Probability of membrane seal	P_c	Fracture closure pressure
ASO	Alice Springs Orogeny	P_i	Fracture initiation pressure
b	Probability of juxtaposition seal	**PO**	Petermann Orogeny
BCF	Billion cubic feet	P_P	Pore pressure
c	Probability of fault reactivation	**PPL**	Petroleum production license
C_o	Cohesive strength	P_r	Fracture reopening pressure
C_m	Coal matrix compressibility coefficient	P_s	Fracture shut-in pressure
CSM	Coal seam methane	P_W	Wellbore fluid pressure
D	Flexural rigidity of the lithosphere	**RSZ**	Redbank Shear Zone
Dx	Deflection of the lithosphere	R_{vmax}	Vitrinite reflectance
E	Young's elastic modulus	**S'**	Effective stress
FS	Probability of fault seal integrity	S_1	Maximum principal stress
g	Acceleration due to gravity	S_1'	Effective maximum principal stress
GAB	Great Artesian Basin	S_2	Intermediate principal stress
$GR_{(max)}$	Average maximum gamma ray value corresponding to 100% shale	S_2'	Effective intermediate principal stress
$GR_{(min)}$	Average minimum gamma ray value corresponding to 0% shale	S_3	Minimum principal stress
h	Depth	S_3'	Effective minimum principal stress
K	Bulk modulus	S_{hmin}	Minimum horizontal stress magnitude
MMCFD	Million cubic feet of gas per day	S_{hmin}'	Effective minimum horizontal stress magnitude
MMSTB	Million stock tank barrels	S_{Hmax}	Maximum horizontal stress magnitude
n	Total number of parameters	S_{Hmax}'	Effective maximum horizontal stress magnitude
nw	Uncertainty associated with each aspect of fault seal	S_i'	Initial effective confining stress
S_n	Normal stress		
ΔS_{Pp}'	Change in effective stress due to pore pressure		

S_s	Shear stress
$\Delta S_s'$	Change in effective stress due to matrix shrinkage
S_v	Vertical stress magnitude
S_v'	Effective vertical stress magnitude
T	Tensile strength
Te	Effective elastic thickness of the lithosphere
T_h	Fault throw
U	Uncertainty
V_m	Coal matrix volume
V_{SH}	Shale content of a sample
Δz	Bed thickness
$30° \rightarrow 070°$	Dip and dip direction
α	Flexural parameter
λ	Wavelength
μ	Coefficient of friction
ν	Poisson's ratio
θ	The angle of a failure plane relative to S_1
ρ	Density
ρ_m	Density of material below the lithosphere

1 Introduction

1.1 Background

Significant hydrocarbon resources onshore Australia occur within reservoirs with low matrix permeability (commonly 0.01–10 mD). These low permeability reservoirs include: the mature Palm Valley and Mereenie fields of the Amadeus Basin; the emergent coal seam methane (CSM) play in eastern Australia, and; stranded tight gas within existing fields of the Bowen and Cooper basins (Do Rozario, 1991; Havord, 1991; Johnson et al., 2002). Natural fractures have been shown to have significant impact on similar tight reservoirs worldwide including, those of the San Juan, Appalachian, Piceance and Greater Green River basins onshore USA (Laubach, 2003a; Teufel, 2003). Hydrocarbon recovery has been significantly improved locally within these basins by exploiting natural fracture networks through targeted well placements (Krystinik et al., 1999; Teufel and Herrin, 2003). A prime example is the Rock Island 4H research well drilled by Union Pacific Resources Group Inc. in a structurally mild area of the Greater Green River Basin (GGRB). The well targeted sandstone reservoirs within the Frontier Formation with ~10% porosity and ~0.025 mD matrix permeability that are typically uneconomic in the absence of natural fractures. Rock Island 4H was drilled to a TVD of nearly 15 000 ft with a horizontal lateral of more than 1600 ft specifically designed to intersect fault-related natural fractures. The well intersected numerous fault-related fractures, tested at a rate of 12 MMCFD and maintained flow at 10 MMCFD due to the natural fractures (Krystinik et al., 1999; Krystinik et al., 2000).

To date, the majority of research on fractured, tight gas reservoirs has been undertaken in North America due to the present fiscal regime of high gas price and demand (Schubarth et al., 2003). Many of the technologies and practices developed in North America cannot be transferred directly to Australia due to both geological and fiscal reasons. Pattern drilling down to 10 acre spacings is possible in tight gas fields such as the Jonah Field of the Greater Green River Basin due to the high gas price and low drilling and completion costs (DuBois, 2004). In addition, many of the tight gas reservoirs of North America are characterised by relatively low background in-situ stress and hydraulic fracture stimulation is both an effective and affordable technology (Eberhard and Mullen, 2003; Finch et al., 1996; Zoback, 1992). In comparison, pattern drilling on close spacings is not an option in Australia as drilling and completion costs are much higher and the gas price considerably lower. In addition, much of onshore Australia is characterised by high background in-situ stress, and hydraulic fracture stimulation techniques are often less effective than in North America (Hillis et al., 1998; Johnson et al., 2002).

An improved understanding of natural fractures and in-situ stress has the potential to significantly improve exploitation of tight reservoirs onshore Australia. Detailed aims and the organisation of the thesis are discussed in section 1.2. A brief review of stress, natural fracture formation and naturally fractured reservoirs is presented in sections 1.3 and 1.4 as background for this thesis.

1.2 Thesis Aims and Overview

The aim of this thesis is to improve our understanding of natural fracturing and relevant structural geological concepts in two onshore Australian hydrocarbon provinces. A wide variety of data and techniques are used in this thesis to study the controls on natural fracture development in the Bowen and Amadeus basins. Several issues closely related to natural fracture development are also explored in this thesis, including the integrity of the sub-thrust play in the Mereenie Field and the partitioning of stress and effects of pore pressure within a coal measure succession.

This thesis comprises three studies. The first addresses natural fracture development in the Scotia coal seam methane (CSM) field of the Bowen Basin, southeast Queensland. The study was completed by Santos Ltd, with a significant contribution by the author immediately prior to PhD candidature. A short summary of the Scotia study is included as Chapter 2 of this thesis because it provided the impetus for the second study that focuses on the Goonyella Riverside mine. The Scotia study successfully identified that the key factors associated with good well performance in the Scotia Field are relatively low in-situ stress (strike-slip regime) to facilitate hydraulic fracture treatments, and a high degree of natural fracturing. However, the findings of the Scotia study are limited because the natural fracture systems at reservoir level do not outcrop and so could not be thoroughly characterised. In addition, the stress regime at Scotia is complex due to high horizontal stress and dramatic changes in rock properties between coal and inter-seam rock. Stress and pressure data for the Scotia Field are limited and the effects of rheological variations and pore pressure on in-situ stress could not be thoroughly investigated. A more thorough understanding of the natural fracture distribution may help target natural permeability sweet spots and a more thorough understanding of stress at reservoir level may significantly improve hydraulic fracture completions in Scotia and similar fields.

The second study presented in this thesis (Chapters 3–6) was designed to address the limitations of the Scotia study but also has implications for other CSM and tight gas projects in coal measure sequences. The study is a coalmine-based analogue study, integrating outcrop observations with 3D seismic data, in-situ stress data and extensive image log data from the Goonyella Riverside coal mine in the northern Bowen Basin. Chapter 3 introduces the geology of the Goonyella Riverside area and Chapter 4 presents outcrop observations from the mine. Chapter 5 presents seismic and image log interpretation and subsequent fracture characterisation over the Goonyella Riverside underground area. Chapter 6 investigates the distribution of stress and the effects of pore pressure on stress within the coal measure succession. The aim of the Scotia and Goonyella Riverside studies is to provide the geological information necessary to improve deliverability, reservoir management and well completions in CSM and tight gas projects in coal measure sequences. Increased flow rates via exploitation of natural fracture networks and successful well completions have the potential to improve the economics of CSM projects in eastern Australia.

The third study presented in this thesis (Chapters 7–10) investigates the structural and natural fracture development of the Mereenie and Palm Valley fields of the Amadeus Basin and is aimed at increasing the reserves and extending the life of these fields. The study addresses regional-scale to prospect-scale issues. Chapter 7 introduces the geology of the northern Amadeus Basin. Chapter 8 presents regional-scale and prospect-scale cross-sections that have been constructed to characterise the structural style and fracture development in both fields. Chapter 9 compares natural fracturing in the Mereenie and Palm Valley fields and uses the structural modelling from Chapter 8 to identify the key controls on natural fracturing in the Amadeus Basin. Chapter 10 presents an assessment of the Mereenie sub-thrust play incorporating the structural analysis of Chapter 8 and a fault seal analysis.

1.3 Subsurface Stress and Natural Fractures

Fracturing within a rock mass is a function of the rock properties, applied stress tensor and pore pressure. These issues must be understood in order to analyse natural fracturing in the subsurface.

1.3.1 Stress in the subsurface

Stress is defined as the force per unit area acting on a body and can be divided into two components: 1) shear stress that acts parallel to a plane, and: 2) normal stress that acts perpendicular to a plane. The stress acting on any plane may be completely described by the normal stress (S_n) and two orthogonal components of shear stress (S_{Sx} and S_{Sy}) or by the normal stress, the maximum shear (S_{Smax}) stress and the orientation of S_{Smax}, θ (Fig. 1.1). The three-dimensional stress field can be described in terms of the normal stress and two components of shear stress acting on three orthogonal planes (Fig. 1.2) and can be expressed mathematically by the stress tensor (Equation 1.1).

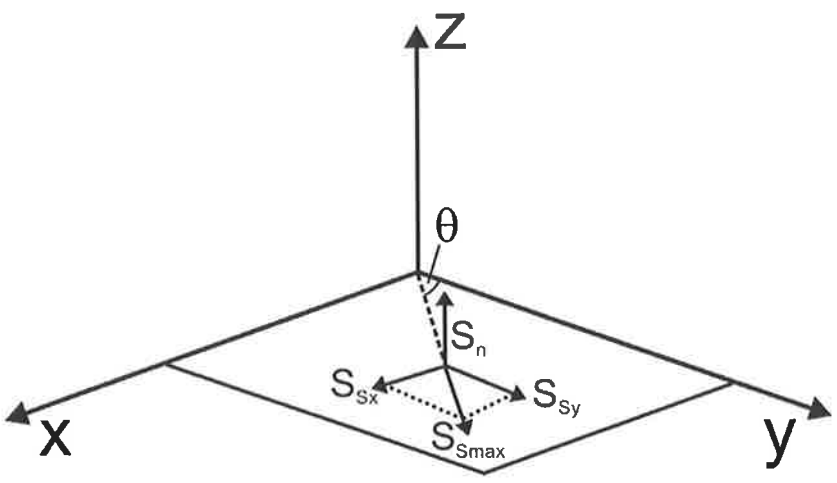

Fig 1.1. The components of stress acting on a plane (Meyer, 2002).

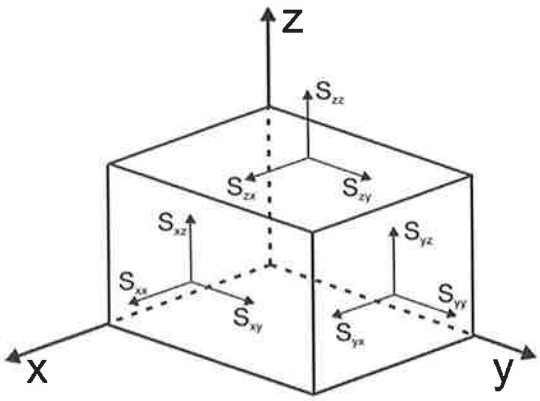

Fig 1.2. Components of stress acting on the three orthogonal faces of a cube. These nine values define the complete 3D stress tensor (Meyer, 2002).

$$S = \begin{pmatrix} S_{xx} & S_{xy} & S_{xz} \\ S_{yz} & S_{yy} & S_{yz} \\ S_{zx} & S_{zy} & S_{zz} \end{pmatrix}$$ Equation 1.1

The stress tensor can be simplified by defining the planes on which shear stress is zero. The normal stresses perpendicular to these planes are referred to as principal stresses, where S_1 is the maximum principal stress, S_2 is the intermediate principal stress and S_3 is the minimum principal stress (Equation 1.2; Jaeger and Cook 1969). A 2D Mohr diagram provides a representation of the stress acting on a plane by plotting Sn versus S_S. The magnitude of normal and shear stress on a plane of any orientation are represented on a Mohr diagram by a circle of radius $(S_1-S_2)/2$ with a centre $(S_1+S_2)/2$ located at S_S = zero (Fig. 1.3). The normal and shear stress acting on a plane in two dimensions can be described in terms of principal stresses as shown in Equations 1.3 and 1.4 (Jaeger and Cook, 1969).

$$S = \begin{pmatrix} S_1 & 0 & 0 \\ 0 & S_2 & 0 \\ 0 & 0 & S_3 \end{pmatrix}$$ Equation 1.2

$$Sn = \tfrac{1}{2}(S_1 + S_2) + \tfrac{1}{2}(S_1-S_2)\cos 2\theta$$ Equation 1.3

$$Ss = \tfrac{1}{2}(S_2-S_1)\sin 2\theta$$ Equation 1.4

The earth's surface can generally be considered a principal plane of stress because it is incapable of sustaining shear stress (Anderson, 1951). Where the earth's surface is near horizontal, the vertical stress (S_v) must be a principal stress, thereby confining the other two principal stress directions to the horizontal plane (S_{Hmax}, S_{hmin}). The stress tensor within most of the earth may then be completely described in terms of these principal stresses, Equation 1.5 (Jaeger and Cook, 1969).

$$S = \begin{pmatrix} S_{Hmax} & 0 & 0 \\ 0 & S_{hmin} & 0 \\ 0 & 0 & S_v \end{pmatrix} \qquad S = \begin{pmatrix} S_{Hmax} & 0 & 0 \\ 0 & S_v & 0 \\ 0 & 0 & S_{hmin} \end{pmatrix} \qquad S = \begin{pmatrix} S_v & 0 & 0 \\ 0 & S_{Hmax} & 0 \\ 0 & 0 & S_{hmin} \end{pmatrix}$$

Equation 1.5

Reverse stress regime | Strike-slip stress regime | Normal stress regime

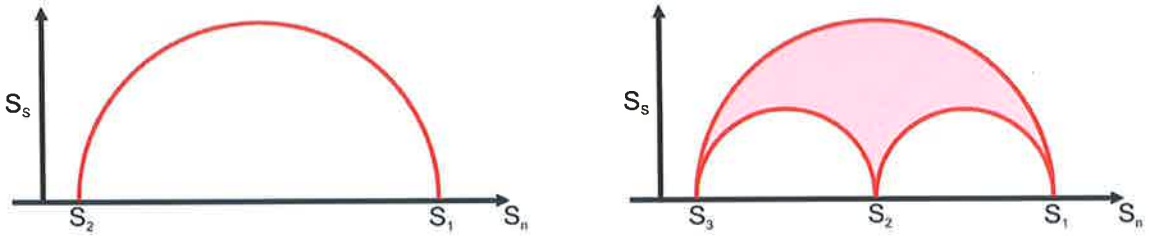

Figure 1.3. 2D (left) and 3D (right) Mohr diagrams

Vertical stress within the subsurface is a function of depth and density of the overburden as expressed in Equation 1.4 (Amadei and Stephansson, 1997). The controls on horizontal stress are typically more complex. A component of horizontal stress is imparted due to the overburden and Poisson's effect as described in Equation 1.6 (Amadei and Stephansson, 1997). However, in tectonically stressed settings, a component of the horizontal stress is applied by far-field tectonic forces that typically act close to horizontally (Coblentz et al., 1995; Zoback, 1992). The magnitude of the horizontal stress component transmitted by far-field tectonic strain (e) is proportional to the elastic modulus (E) of the material as described by Hooke's Law, Equation 1.8 (Amadei and Stephansson, 1997; Plumb, 1994).

$$S_v = \rho g h \qquad \text{Equation 1.6}$$

$$S_{hmin} = \frac{\upsilon}{1-\upsilon} S_v \qquad \text{Equation 1.7}$$

$$S = E\, e \qquad \text{Equation 1.8}$$

In tectonically relaxed settings, weak rocks with high Poisson's ratio are typically characterised by higher horizontal stress than interlayered strong layers (Amadei and Stephansson, 1997). In tectonically stressed settings, relatively strong rocks with higher elastic modulus are typically characterised by higher horizontal stress than interlayered weak rocks (Amadei and Stephansson, 1997).

1.3.2 Effect of pore pressure

Reservoir rocks, typically characterised by interconnected pore networks, behave as poro-elastic solids and failure is controlled by the effective stress (Fig. 1.4). The effective stress is defined as the applied stress minus the pore fluid pressure multiplied by Biot's constant (Jaeger and Cook, 1969). However, this is often simplified in practice by assuming linear elasticity as described by a Biot's constant equal to 1.

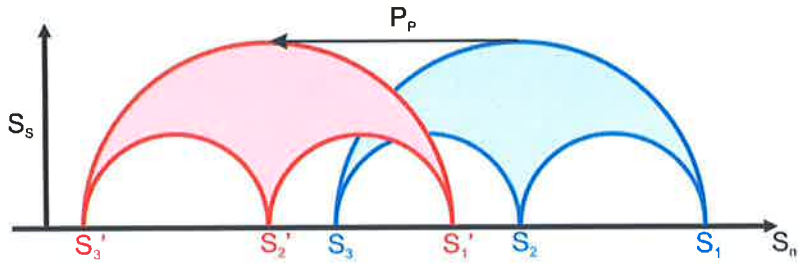

Figure 1.4. 3D Mohr diagram showing the effect of pore pressure.

1.3.3 Rock failure

A failure criterion describes the stress and pore pressure conditions that cause rock mass failure/fracturing. A wide variety of failure criteria are used in rock mechanics including the Hoek and Brown, Griffith, Mohr-Coulomb, Mogi, and Wiebols and Cook criteria (Hoek and Brown, 1980; Mogi, 1967; Wiebols and Cook, 1968). The Mohr-Coulomb criterion is the most simple of these as it is linear and ignores the effects of intermediate principal stress. The Mohr-Coulomb criterion has been shown to be a fair approximation in the absence of detailed polyaxial rock testing data (Colmenares and Zoback, 2002). Mohr-Coulomb theory states that failure across a plane is related to the normal stress and shear stress acting on the plane.

The shear stress necessary to cause brittle failure across a plane is resisted by cohesion (C) of the material and by frictional co-efficient (μ) multiplied by the normal stress across that plane, Equation 1.9 (Byerlee, 1978). The Mohr-Coulomb criterion describes a straight line on a Mohr diagram, its Ss intercept being C and slope = μ (Fig. 1.5). According to Mohr-Coulomb theory, failure occurs where the Mohr circle intersects the failure envelope.

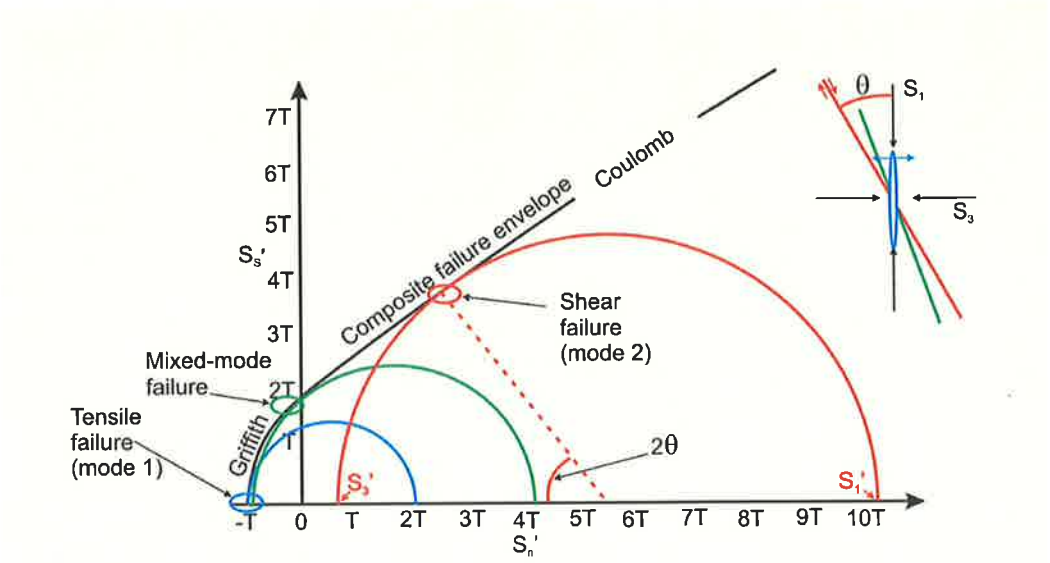

Figure 1.5. Mohr diagram showing the stress conditions required for the different modes of fracturing: mode1, mode 2 and mixed mode (Sibson, 1996). Mode 1 fractures typically form parallel to S_1 and mode 2 fractures form at an angle of θ to S_1 depending on μ, θ is typically in the range of 30–45° (Hobbs et al., 1976; Jaeger and Cook, 1969)

$$| Ss | = C + \mu S_n \qquad \text{Equation 1.9}$$

The Mohr-Coulomb criterion is only valid for rocks subjected to compressive stress (positive values of S_n'). Rocks are typically much weaker in tension due to micro-Griffith cracks and weaknesses along grain boundary contacts (Jaeger and Cook, 1969). The Griffith failure criterion describes failure for rocks in tension (Equation 1.10). A composite Griffith-Coulomb criterion is commonly used to describe rock failure for both compression and tension (Fig. 1.5).

$$Ss = (4T^2 + 4TS_n)^{1/2} \qquad \text{Equation 1.10}$$

Natural fractures can be classified by two end members. Tensile (mode 1) fractures, commonly referred to as joints, are characterised by movement normal to the fracture surface. Tensile fractures are defined on a Mohr diagram where the Mohr circle intersects the envelope on the S_n axis (i.e. zero shear stress). Shear (mode 2) fractures, commonly referred to as faults are characterised by movement parallel to the fracture surface. Shear fractures are defined on a Mohr diagram where the Mohr circle intersects the envelope on the positive side of the S_n axis. Mixed mode fractures are a hybrid of the two end members and are defined on a Mohr diagram where the Mohr circle intersects the failure envelope between the S_n and S_S intercepts (Jaeger and Cook, 1969; Sibson, 1996).

The Griffith and Mohr-Coulomb criteria show that tensile fractures can only form in the presence of differential stress (S_1-S_3) less than 4T and that shear fractures can only form where differential stress is greater than 4T (Fig. 1.5). Sibson (1996) argues that differential stress greater than 6T is required for mode 2 fractures to develop and that mixed mode fractures form under differential stress conditions between 4T and 6T.

1.3.4 Fracture permeability

The hydrodynamic properties of natural fractures in the subsurface are highly variable (Barton et al., 1997; Laubach et al., 2004). Fractured zones can be either beneficial or deleterious to reservoir performance depending on the reservoir and fracture conditions. Zones of enhanced fracturing may hinder hydrocarbon development in several ways. Elevated permeability associated with natural fracturing can cause early water breakthrough, significantly hampering hydrocarbon recovery. Alternatively, fractures may be mineralised and act as flow baffles/barriers that reduce permeability and/or compartmentalise a reservoir (Knipe et al., 1998; Lie Hui and Yi Yong, 1998; Ottesen Ellevset et al., 1998). Zones of elevated fracturing can also help reservoir performance, particularly in reservoirs with low matrix permeability by providing high permeability conduits that access the low permeability matrix (Aguilera, 1995; Berry et al., 1996; Nelson, 2001). One of the key aims of this thesis is to study the occurrence and nature of naturally fractured zones to help develop tight gas resources onshore Australia.

The hydrodynamic properties of natural fractures are often complex and difficult to predict. Some authors assert that fracture aperture and their hydrodynamic behaviour is a function of the in-situ stress tensor (Barton et al., 1997; Chanchani et al., 2003; Mildren et al., 2002b). The fracture susceptibility technique investigates potential hydraulic conductivity of a pre-existing fracture as a function of the in-situ stress field (Mildren et al., 2002b). The technique assumes that fractures subject to stresses conducive to reactivation (termed critically stressed fractures) are the most likely to be hydraulically conductive (Barton et al., 1995; Lisle and Srivastava, 2004; Mildren et al., 2002b). The fracture susceptibility technique may be represented graphically on a 3D Mohr diagram (Fig. 1.6). Fractures, represented by poles to planes, that plot closest to the failure envelope are closest to being critically stressed and are most likely to be open and hydraulically conductive (Fig. 1.6). The fracture susceptibility concept has been applied with varying degrees of success to issues of fault seal and naturally fractured reservoirs (Chanchani et al., 2003; Mildren et al., 2002b). The strength of the host rock is also an important control on fracture permeability. Fractures in strong rock such as quartzite tend to be less stress-sensitive than those in weak rocks such as chalk (Hillis, 1998).

However, there does not always appear to be a relationship between fracture orientation, the in-situ stress field and hydraulic conductivity. There are many instances where non-optimally oriented fractures are open and hydraulically conductive and optimally oriented fractures are

closed and non-conductive (Laubach, 2003a; Laubach et al., 2004; Parks and Gale, 1992). Diagenetic mineral bridges may prop open fractures imparting hydraulic conductivity to fractures poorly oriented with the in-situ stress field to be open and hydraulically conductive (Fig. 1.7). Mineralisation can also have a detrimental effect on fracture conductivity by rendering the most optimally oriented fractures nonconductive if the fracture is completely mineralised (Laubach, 2003b; Laubach et al., 2004).

The hydrodynamic behaviour of natural fractures is clearly a complex issue. Each situation is unique and there is no single solution or method to predict the hydrodynamic properties of natural fractures. Accordingly, all of the above mentioned factors should be considered.

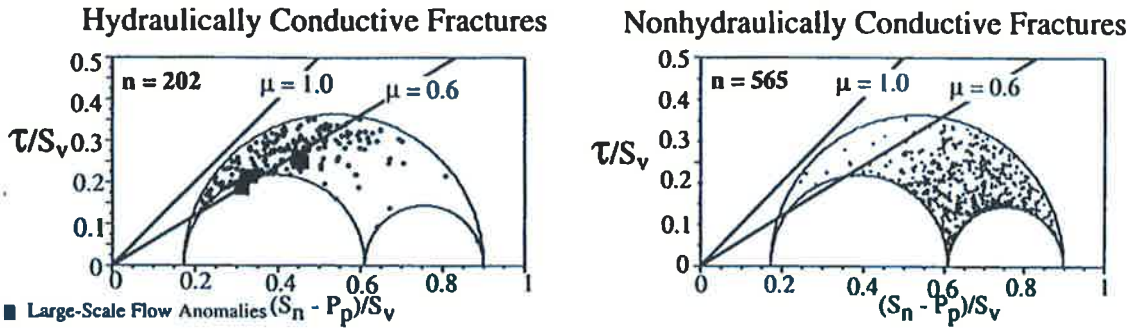

Figure 1.6. 3D Mohr diagrams illustrating the relationship between fracture orientation relative to the stress tensor and permeability. The Mohr diagram to the left shows hydraulically conductive fractures from a sample and the Mohr diagram to the right shows nonconductive fractures from the same sample. The hydraulically conductive fractures typically plot closer to the failure envelope (Barton et al., 1997).

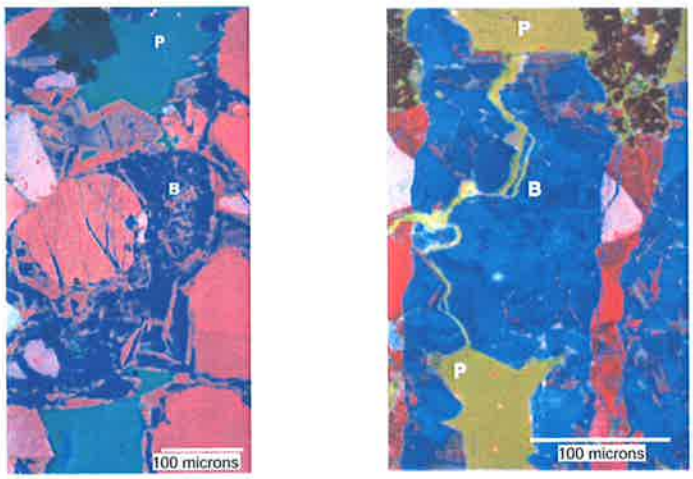

Figure 1.7. Cathodoluminescence images of partly mineral-bridged, open fractures. The figure on the left is of a Cretaceous sandstone from the East Texas Basin where fractures are hydraulically conductive despite being at high angles to S_{Hmax}. The figure on the right is of a Jurassic sandstone, northeastern Mexico. In both figures B indicates quartz mineral bridges and P indicates open fracture pore space (Laubach et al., 2004).

1.4 Fractured Reservoirs

The effect of open natural fractures on hydrocarbon reservoirs is variable and is dependent upon the properties of both the host rock and the natural fractures. The relative effects of the fracture network and primary porosity must be understood in order to effectively characterise and manage a fractured reservoir. Nelson (2001) classified fractured reservoirs according to the effect of the fracture system on overall reservoir performance:

- Type 1 fractured reservoirs are those where natural fractures provide essential reservoir porosity and permeability.
- Type 2 fractured reservoirs are those where natural fractures provide essential reservoir permeability and there is inherent matrix porosity.
- Type 3 fractured reservoirs are those where natural fractures assist permeability in an already producible reservoir.
- Type 4 fractured reservoirs are those where natural fractures provide no additional porosity or permeability but create significant anisotropy.

The Palm Valley and Scotia fields have been documented as type 2 fractured reservoirs (Aguilera 1995). It is suspected that natural fractures may assist reservoir performance in the Mereenie Field and others within the Cooper and Bowen basins defining them as type 3 fractured reservoirs (Hillis et al. 1999; Flottmann et al. 2002). Effective reservoir management within any type of fractured reservoir relies on a thorough understanding of the development, distribution and hydrodynamic properties of the fractures within the reservoir. Several geological parameters have been identified as important controls on fracture development within a sedimentary sequence including: composition; grain size; porosity; bed thickness, and; structural position/strain (Nelson, 2001). The aim of much of this thesis is to study the occurrence and controls of natural fractures in the Bowen and Amadeus basins using structural geological techniques.

1.4.1 Mechanical stratigraphy

The brittle fracture theory presented in Section 1.3 shows that the potential for natural fracturing increases where there is a decrease in rock strength (C, T or μ) or where there is an increase in either applied stress or fluid pressure. Section 1.3 only discusses brittle failure and does not consider ductile deformation under geological strain rates via mechanisms such as grain boundary sliding. In outcrop and in the subsurface, strong rocks are often more intensely fractured than adjacent weaker rocks (Hugman and Friedman, 1979; Narr, 1991; Nelson, 2001). This observation may be explained in terms of brittleness under geological strain rates. Strong rocks are typically more brittle and can sustain significantly less strain before failing via fracturing. Weak rocks are often more ductile and can dissipate strain more effectively via

methods such as grain boundary sliding and thus are less prone to fracturing under (Nelson, 2001). Fracturing may also be more intense within stronger intervals due to elevated stress within the stronger layers caused by a phenomenon referred to as stress partitioning (Amadei and Stephansson, 1997; Nelson et al., 2004).

The mechanical properties of a sedimentary sequence are a function of primary mineralogical composition, burial depth, diagenesis and retained porosity (Nelson 2001). There may be an entire suite of mechanical units with different mechanical properties defining the mechanical stratigraphy within a layered sedimentary sequence (Becker and Gross, 1996; Narr, 1991; Underwood et al., 2003). A mechanical unit is an interval of rock that has similar mechanical properties, within which, deformation is relatively consistent (Underwood et al., 2003). Mechanical units are dynamic and may become thinner with progressive deformation (Couples et al., 1998). There may be considerable differences in mechanical properties between adjacent mechanical units that may correspond to diagenetic or lithological variations (Fig. 1.8). Variations may be as subtle as variations in clay content within a massive sandstone sequence or as major as gross lithology changes between clastic, carbonate and coal intervals. A mechanical unit may be extensively fractured while units directly above and below may remain unfractured (Narr, 1991; Underwood et al., 2003).

Figure 1.8. The effects of mechanical stratigraphy in a sandstone and shale sequence (~0.5 m thick). Fractures are well developed in the sandstone layers and poorly developed in the shale layers. Fractures within the sandstone layers are spaced proportional to bed thickness and terminate at bedding boundaries separating mechanical units (Golder, 2001).

1.4.2 Fracture assemblages

Fractures may occur as predictable networks in association with larger structural features such as folds and faults. Fractures may also occur in less predictable networks as regional sets in relatively flat-lying beds with no clear relationship to major structural features.

Fold-related fractures

Fold-related fractures have been exploited in many reservoirs and can be successfully modelled using a variety of techniques due to their predictable nature (Berry et al., 1996; Hennings et al., 2000; Lisle, 1994; Masaferro et al., 2003; Stearns and Friedman, 1972). Idealised fold-related fracture assemblages that include tensile fractures and left and right lateral shear fractures have been described relative to the bending axis (Fig. 1.9). A type 1 fracture assemblage develops where bending is about an axis parallel to bed dip and a type 2 assemblage develops where bending is about an axis parallel to bed strike (Stearns and Friedman, 1972). It is important to note that these assemblages are idealised only, and that in nature there is usually significant departure from the idealised orientations due to heterogeneities and stress perturbations.

As a fold grows, whether by flexural slip or flexural flow mechanisms, bending strains develop in portions of the fold where flexure is high (Cooke et al., 2000; Couples et al., 1998; Lisle, 1994). Surface curvature is defined as the rate of change of dip around a fold and has been used with varying degrees of success to model fold-related fractures (Hennings et al., 2000; Lisle, 1994; Masaferro et al., 2003). Newly developed techniques of curvature analysis can assess 3D curvature, referred to as Gaussian curvature, which is defined as the product of the two greatest curvatures (k_1 and k_2) measured along two orthogonal curves through point k. Gaussian curvature provides a better proxy for strain than normal curvature and has been shown to be a superior indicator for fold-related fractures (Lisle, 1994; Masaferro et al., 2003; Wynn and Stewart, 2003). The cumulative strain within a folded volume can also be calculated using recently developed kinematic algorithms such as angular shear in extensional settings or flexural slip in compressional settings. Strain calculated via these techniques has been used with varying degrees of success to predict natural fracture occurrence (Griffiths et al., 2002; Hennings et al., 2000).

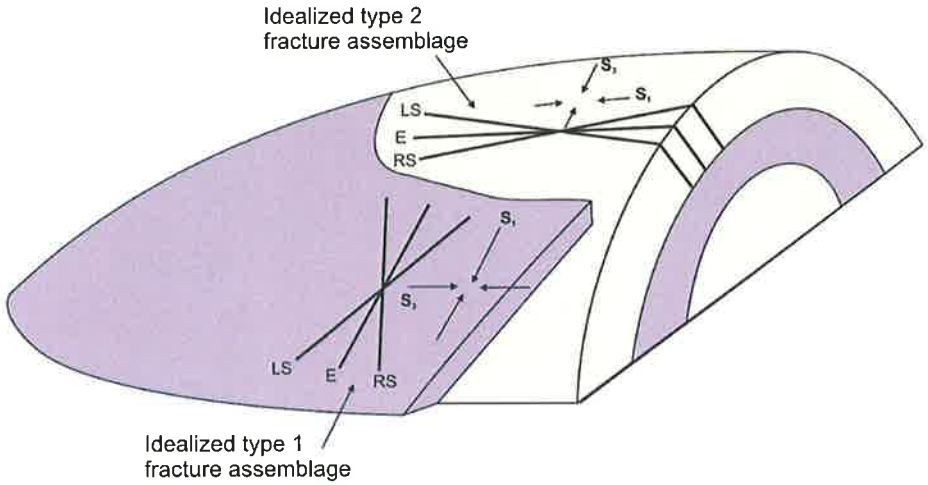

Figure 1.9. Idealised fold-related fracture assemblages. E = extensional fracture; LS = left lateral shear fracture, and; RS = right lateral shear fracture. A type 1 fracture assemblage develops where bending is about an axis parallel to bed dip and a type 2 assemblage develops where bending is about an axis parallel to bed strike (Stearns and Friedman, 1972).

Fault-related fractures

Fault-related fractures can occur in structurally mild areas and are exploited in a number of tight sandstone reservoirs including those of the Frontier Formation of the Greater Green River Basin (Krystinik et al., 2000). Fault cores may be less permeable than the host rock due to shale smear or porosity collapse via cataclasis and act as baffles to fluid flow, whereas fractures within the damage zone beyond the fault core can significantly enhance permeability (Caine et al., 1996; Knipe et al., 1998; Laubach, 2003a). Fractures may occur in association with faults either as part of the faulting process or due to subsequent stress perturbations and folding as shown in Figure 1.10 (Caine et al., 1996; Cowie, 1996; Shipton and Cowie, 2001). Fault-related fractures may be concentrated in fault damage zones, step overs or tips, however, fault zone architecture is highly variable and is a function of the host rock and pressure and stress history (Fig. 1.10). Shear fractures may form antithetic or synthetic sets that strike parallel to the main fault and generally decrease in intensity away from the main fault (Petit et al., 2000; Shipton and Cowie, 2001). It is unclear whether fault-related fractures continue to develop once a discrete slip surface has developed along the main fault. Some authors argue that fracturing ceases in the damage zone once a discrete fault surface has developed (Roberts, 1994), while others have shown that fracturing may occur during faulting and that there is a relationship between fault throw and damage zone width. Fracturing in the damage zone may depend on whether strain-hardening or strain-softening occurs (Hull, 1988; Knott et al., 1996; Shipton and Cowie, 2001). In some cases, fault populations have been shown to obey a power law relationship and the presence of sub-seismic scale shear fractures may be predicted from the extent of seismic scale faults. However, there may not always be a continuous population of fractures from wellbore-scale to seismic-scale (Fossen and Hesthammer, 2000; Yielding et al., 1996). In addition, faults

that demonstrate a protracted history of reactivation may have more fracturing associated with them than those that have experienced a single deformation phase.

Shipton et al (2001) evaluated damage zones associated with steeply dipping normal faults (70–80°) with up to 30 m of throw in high porosity Navajo Sandstone from Utah. The faults are interpreted to have formed at approximately 1.5–3.0 km depth with maximum temperature ~ 100°C and pressure ~ 80 MPa. They found that the majority of deformation bands and slip surfaces strike parallel to the fault with approximately equal proportions of synthetic and antithetic structures (Fig. 1.11). They observed no difference in the orientation of structures between the footwall and hangingwall sides of the fault. The width of the damaged zone and the density of structures in the damaged zone were found to correlate with fault throw. The damage zone width and fault throws were plotted against each other and correlate with a slope of 2.5 and an intercept of 7 m (i.e. a fault with 2m of throw would have a damage zone width of 2*2.5+7=12m ± 10-20%) (Shipton and Cowie, 2001).

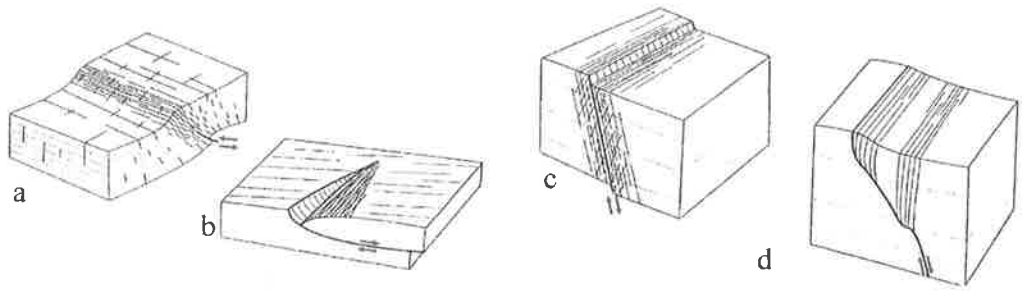

Figure 1.10. Idealised fault-related fracture patterns. a) relationship with folding and fault tip induced by underlying fault; b) fan-shaped fractures linked to a rollover caused by a listric normal fault; c) synthetic and antithetic shear fractures formed in the damage zone; d) swarms of fractures localised at a fault bend and tip (Petit et al., 2000).

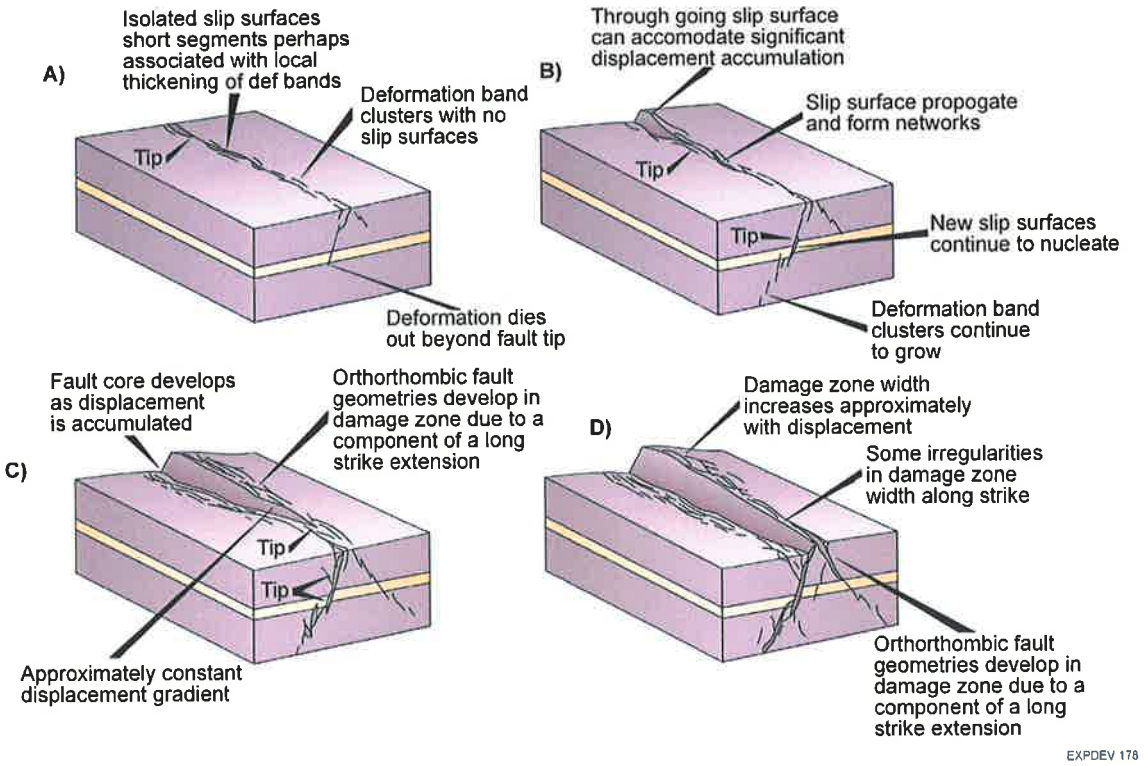

Figure 1.11. Model of fault growth in porous sandstone illustrating the evolution of a fault in the same rock mass through time. a) deformation ahead of the fault tip; b) principal slip surfaces coalesce to form a through going surface at the fault tip; c) further displacement mostly along the through going surface, slip surfaces continue to nucleate in the damage zone; d) damage zone increases in width (Shipton and Cowie, 2001).

Regional fractures

Natural fractures also occur as regional, near-vertical, bedding-normal sets that extend over laterally extensive areas with no clear relationship to major structural features and form in response to the background stress field (Fig. 1.12). Most pervasive, regional, high-angle fracture sets are interpreted to be a result of uplift. Unloading fractures typically only occur in the upper few hundred metres of the crust and are of little value to hydrocarbon exploitation, except in the shallowest reservoirs (Engelder, 1985; Voight and St. Pierre, 1974). However, regional fracture sets have also been shown to occur at significant depths within the crust and may be due to orogenic shortening rather than unloading. Regional fractures have been described in association with foreland basins of North and South America (Bell and Babcock, 1986; Scheidegger, 1983; Winslow, 1983) and Europe (Becker, 1989; Dunne and North, 1990). The regional fractures described by these authors form parallel to the regional maximum horizontal stress associated with orogenic activity and appear to be directly related to orogenic intensity. Lateral gradients in fracture intensity have been demonstrated between flat-lying and adjacent folded strata containing the same fracture set normal to the fold axes in front of the Appalachian and Andes mountains (Dean et al., 1979; Winslow, 1983). The fractures are interpreted to have formed in the flat-lying strata parallel to shortening direction and ahead of the orogenic front, prior

to incorporation into the fold and thrust belts (Dean et al., 1979; Lorenz et al., 1991; Winslow, 1983).

Lorenz et al. (1991) present a model for the formation of high-angle regional fractures at depth in the Cretaceous Mesaverde Group of the Piceance Basin, Colorado in front of a Laramide uplift. Their analysis shows that a set of regional fractures oriented parallel to regional shortening formed at maximum burial during a pulse of regional Laramide compression (Lorenz and Finley, 1991). The proposed mechanism requires significant differential horizontal stress and pore pressure that approaches, but does not and cannot exceed, the least principal stress. As the anisotropy and magnitude of the stresses increases, local tensile stresses form around flaws and micro-cracks in the rock that are oriented parallel to the far-field maximum compressive stress. Tensile fractures then form and propagate in the plane of the maximum and intermediate principal stresses and can occur up to hundreds of kilometres beyond an orogenic front in the absence of any folding or flexure (Lorenz and Finley, 1991; Lorenz et al., 1991). These regional fractures are responsible for high rate gas wells within the Piceance and San Juan basins, however, they are difficult to predict in the subsurface as they occur independently of any seismically resolvable structures (Lorenz and Finley, 1991; Teufel and Herrin, 2003).

Figure 1.12. Regional fracture sets within a flat-lying sandstone formation. Such fracture sets may extend over vast areas in the absence of any other structure (Golder, 2001).

1.4.3 Fracture detection and modelling

The presence of fractures at reservoir level can be detected directly at the wellbore via static methods such as core or by down-hole tools resistivity or acoustic image log tools. However, there are many sampling issues associated with static methods. For example, zones of intense fracturing can be damaged by the coring process and may not be preserved in the cored sample.

Also image logs typically under-sample fractures especially in the presence of adverse conditions such as high temperature, borehole rugosity or formation damage (Nelson, 2001; Rider, 2000). In addition, flow within a fractured reservoir is often dominated by only a few of the fractures and static methods are generally incapable of directly determining which fractures contribute to flow into the wellbore (Nelson, 2001).

Fractures can also be detected indirectly at the wellbore via dynamic methods such as pressure build-up tests, however, dynamic methods are generally not definitive and should be matched to geological observations (Aguilera, 1995; Houze et al., 1988; Mavor and Cinco, 1979). Well test results of most unfractured reservoirs can be matched to a radial flow model that assumes a porous medium of infinite radial extent. Fractured reservoirs do not conform to the radial flow model due to dual porosity behaviour and models typically assume well influx comes from the fracture system and that matrix-reservoir cross flow only occurs locally (Mavor and Cinco, 1979). Derivative curves of pressure build-up display a distinct hump (Fig. 1.13) due to the dual-porosity behaviour of a fractured reservoir (Aguilera, 1995; Chipperfield, 2004; Houze et al., 1988). Mini-fracture tests and hydraulic fracture treatment data may also indicate the presence of natural fractures due to near wellbore pressure losses or from after-closure analysis (Chipperfield, 2004; Roberts and Chipperfield, 2000).

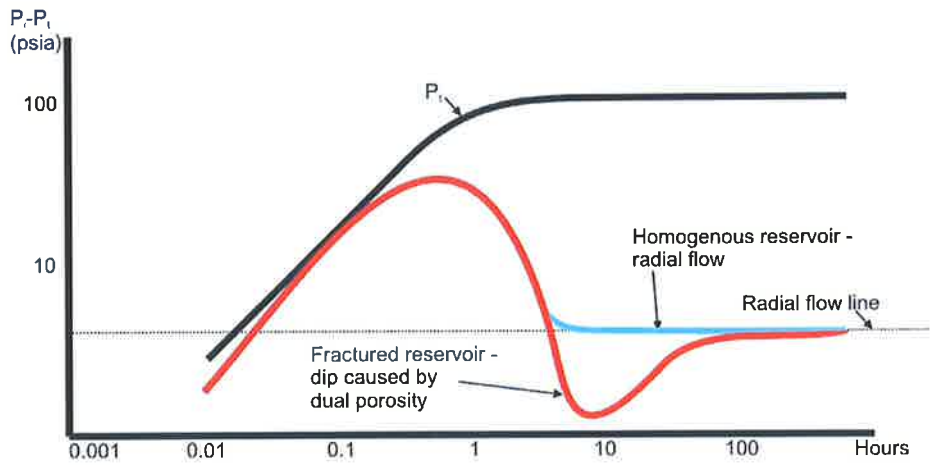

Figure 1.13. Derivative curves typical of a fractured reservoir with dual porosity and non-radial flow (red) and a homogenous reservoir with radial flow (blue). Note the characteristic hump describing dual porosity behaviour (Aguilera, 1995; Mavor and Cinco, 1979).

In any fractured reservoir, it is also critical to understand fracture development away from the wellbore and pressure transient for the purposes of reservoir management and the positioning of development wells. The fracture network may be modelled between wellbores in a number of ways depending on the available data and type of fracture system. Stochastic methods can be used to model fracture networks where there is a large amount of geological and well test data, particularly at the mature stage of field development. Software packages such as Golder Associates' Fracman and Veritas' ResFrac apply stochastic and deterministic methods to

represent the fracture network by a discrete fracture network (DFN). Monte Carlo simulations are carried out resulting in multiple model realisations and the models represent discontinuities as polygonal planar structures, either deterministically (i.e. given a definite location, size, transmissivity) or stochastically by specifying probability distributions for some or all of the fracture properties (Jones et al., 1999; Ouenes and Hartley, 2000).

In many instances there is insufficient well data from which to produce reasonably constrained DFNs thus other techniques are required. Several geophysical methods have been developed to detect and characterise fractures away from the wellbore. Amplitude versus offset (AVO) techniques have been successfully used to detect zones of intense fracturing that impart low-amplitude signatures to far offset traces (Lawrence, 1998; Ramos and Davis, 1997). Amplitude versus azimuth (AVAZ) techniques have also been successfully used to detect fracture-related variations in signal amplitude with source-receiver azimuth (Perez et al., 1999; Whale, 2004). However, there are many problems associated with these methods. AVO/ AVAZ theory is based on the unrealistic assumption of parallel, near-vertical fractures (except in the instance of regional fractures), and AVO or AVAZ signals may be destroyed where two fracture sets intersect each other at high angles (Parney et al., 2004). AVO/AVAZ signatures of fractures are small and the methods are only applicable where high quality, purpose-designed 3D seismic surveys are available. Where there is a good correlation with the seismic signature and either static or dynamic data, AVO or AVAZ signatures may be used to help populate DFN models away from the wellbore.

In most cases, purpose-designed 3D seismic data is not available and other techniques are required to understand fracture development away from the wellbore. Field-based analogue studies may be used to understand the controls on fracture development and constrain reservoir concepts and models. Problems may be encountered with analogue studies in distinguishing which of the fracture sets exposed in outcrop occur at reservoir level and which are due to uplift and unloading. Morphological and kinematic attributes of a folded surface may be used as proxies for fold-related fracturing as described in section 1.4.2 where there is good control on the reservoir geometry via closely spaced 2D or 3D seismic data. Fault-related fractures are also predictable by considering the fault geometry and deformation history with the palaeo-stress tensor. Geomechanical modelling using techniques such as boundary element modelling (BEM) or finite element modelling (FEM) can be used to model fault-related stress perturbations and identify zones of elevated stress that may correspond to fault-related fracturing (Kattenhorn et al., 2000; Maerten et al., 2002).

The best fracture models integrate geological, geophysical and dynamic data with analogue studies and appropriate modelling techniques. However, such comprehensive analysis is not always possible and the most appropriate method(s) must be selected based on the available data. This thesis applies structural geological techniques to identify the controls on natural

fracture development within hydrocarbon systems of the Bowen and Amadeus basins in order to assist fracture prediction in these areas.

2 Scotia Field Study

2.1 Background

The Santos-operated Scotia field is on the eastern margin of the Bowen Basin approximately 450 km northwest of Brisbane, Queensland. Scotia is a coal seam methane (CSM) field with gas production from the Permian Baralaba Coal Measures. The field is located in the northern part of the Burunga Anticline within the hangingwall of the west-dipping Scotia fault system (Fig. 2.1). Development of the Scotia CSM reservoir relies on three components (Flottmann et al., 2002; Johnson et al., 2002):

- an interconnected network of coal cleats and other natural fractures;
- phyteral porosity within the dull coal;
- hydraulic fracture stimulation to connect the wellbore to the natural fracture network.

A study was conducted by Santos Ltd, with a significant contribution by the author, to investigate these key components (Flottmann et al., 2002). The Scotia study was conducted prior to commencement of the author's PhD candidature; however, a summary of the Scotia study is presented in this chapter as the study is directly related to this thesis and provided the impetus for the Goonyella Riverside study presented in Chapters 3–6.

The objectives of the Scotia study were to:

- predict naturally fractured permeability sweet spots for improved well performance;
- improve well completions and hydraulic fracture stimulations;
- improve reservoir management and flow modelling.

The Scotia study involved:

- seismic mapping of the coal measures and faults with depth conversion for subsequent strain modelling;
- fracture characterisation using image log interpretation and outcrop studies;
- predictive, grid-based stress modelling using the seismic interpretation, rock property data and regional stress data;
- strain-based fracture modelling of the depth-converted seismic interpretation using curvature and 3D strain models in 3D Move software;
- fracture susceptibility modelling using fracture and in-situ stress data with SWIFT software.

Of these tasks, the author was responsible for outcrop mapping of natural fractures over the Scotia field, determination of the S_{Hmax} orientation using borehole breakout interpretation, and a

portion of the 3D structure/strain modelling. The author also contributed to the ideas behind natural fracture development in the Scotia Field.

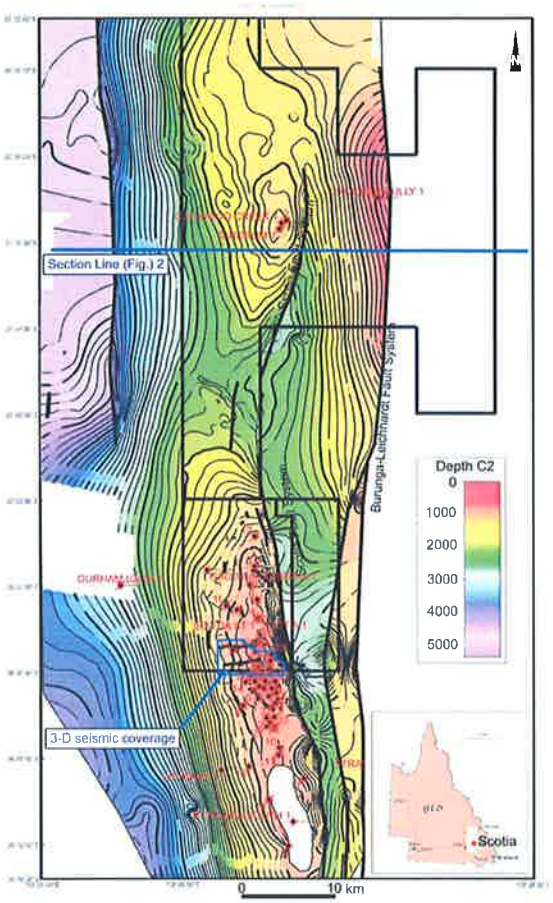

Figure 2.1. Location of the Scotia CSM Field and depth-to-structure map of the C2 coal seam of the Baralaba Coal Measures. The Burunga-Leichardt fault system dips towards east and the Scotia fault system dips towards west.

2.2 Geological Setting

Gas production in the Scotia Field is from the Late Permian Baralaba Coal Measures at depths of 700–1000 m. The field is in the northern Burunga Anticline within the hangingwall of the west-dipping Scotia fault system (Figs 2.1, 2.2). The Scotia fault system is part of the regional east-dipping Burunga-Leichhardt fault system. The Scotia fault system initiated after deposition of the Baralaba Coal Measures and continued during deposition of the Triassic Rewan Formation. The Permian-Triassic sequence is truncated by a significant erosional unconformity marking the base of the Jurassic-Cretaceous Surat Basin. The Bowen Basin is significantly folded and faulted and is overlain by the relatively undeformed Surat Basin. The Scotia fault system was reactivated during the Tertiary resulting in minor northeast shortening (Flottmann et al., 2002).

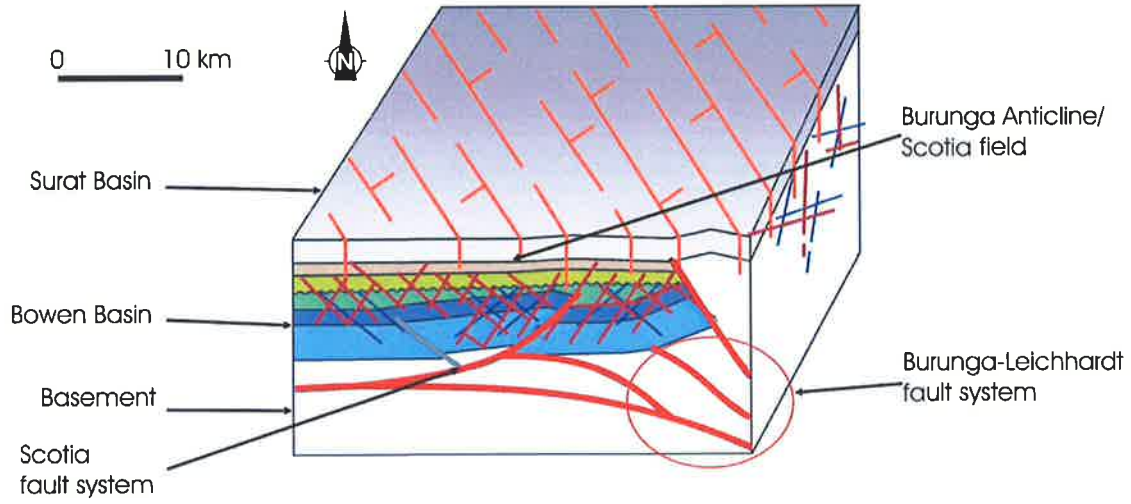

Figure 2.2. Diagram showing the Scotia CSM over the are of 3D seismic data relative to the east-dipping Burunga-Leichardt fault system and the west-dipping Scotia fault system (Fig. 2.1). The Scotia Field is within the Burunga Anticline in the hangingwall of the Scotia fault system (scale is approximate only).

2.3 Image Log and Core Fracture Interpretation

The reservoir-level natural fracture system was analysed by others using acoustic image logs from 14 wells (Scotia 3-16). Diagenetic coal cleats are below image log resolution and could not be assessed using the image logs. In the coal seams and interseam intervals of the Baralaba Coal Measures 185 fractures were encountered at an average density of 0.09/m (unweighted for dip). The fractures generally dip 30°– 60° and occur in three distinct sets that strike north-south, northeast and northwest (Figs 2.3, 2.4). The fractures occur more frequently in the interseams than in the coal seams. The coal seams are generally dull with thin vitrinite-rich bands (~20 mm). The dull coal intervals generally have poor diagenetic cleat development in core samples (Fig. 2.5) and structurally related fractures are the dominant fracture type. Many of the fractures sampled in the Scotia 4 core have slickensides and therefore formed as shear fractures or have been reactivated as shear fractures.

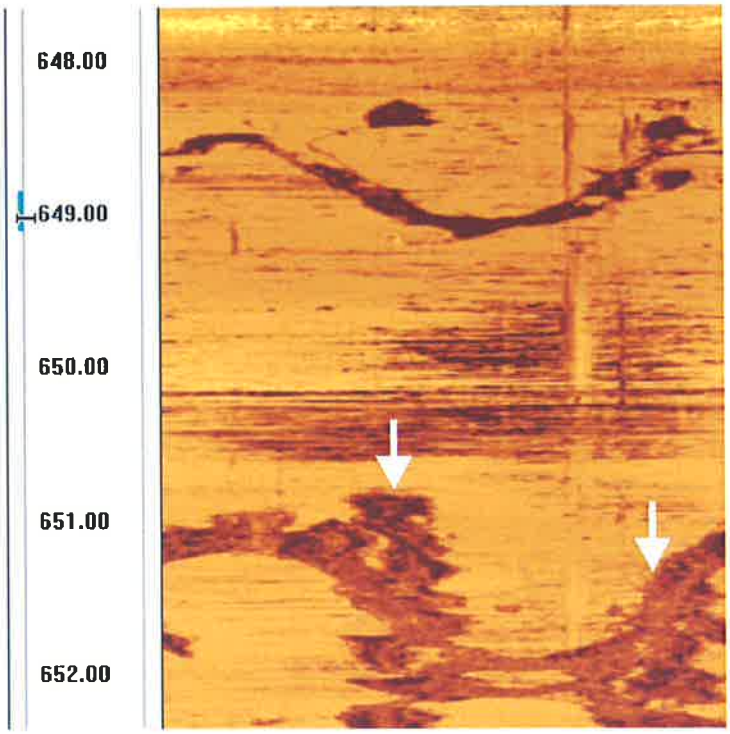

Figure 2.3. Low-angle fractures and borehole breakout (white arrows) interpreted from acoustic image logs, Scotia 15. The scale to the left is in metres.

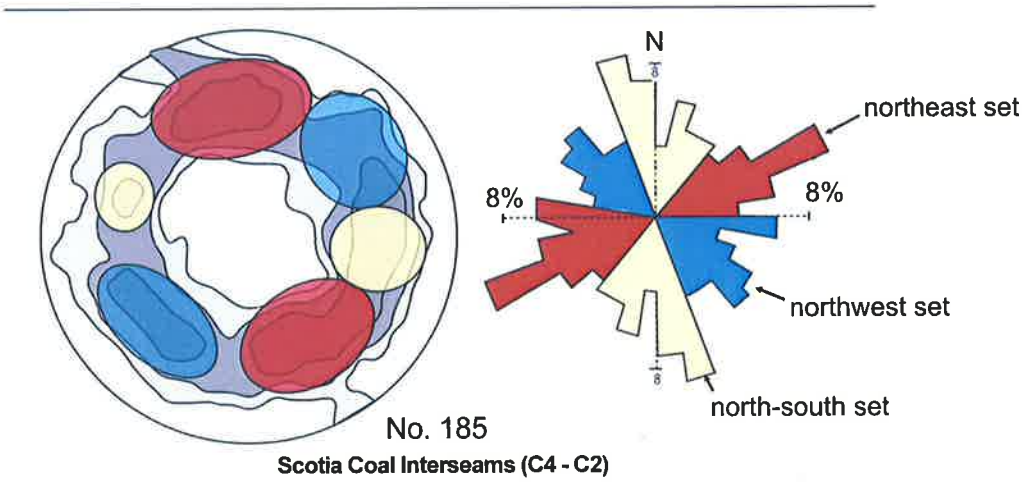

Figure 2.4. Stereonet and rose diagram showing the orientation of natural fractures within the Baralaba Coal Measures from image log interpretation (excluding cleats). The stereonet diagram plots the poles of fractures and is shaded according to fracture density (dark = high density) and the coloured zones show the distinct sets (185 fractures).

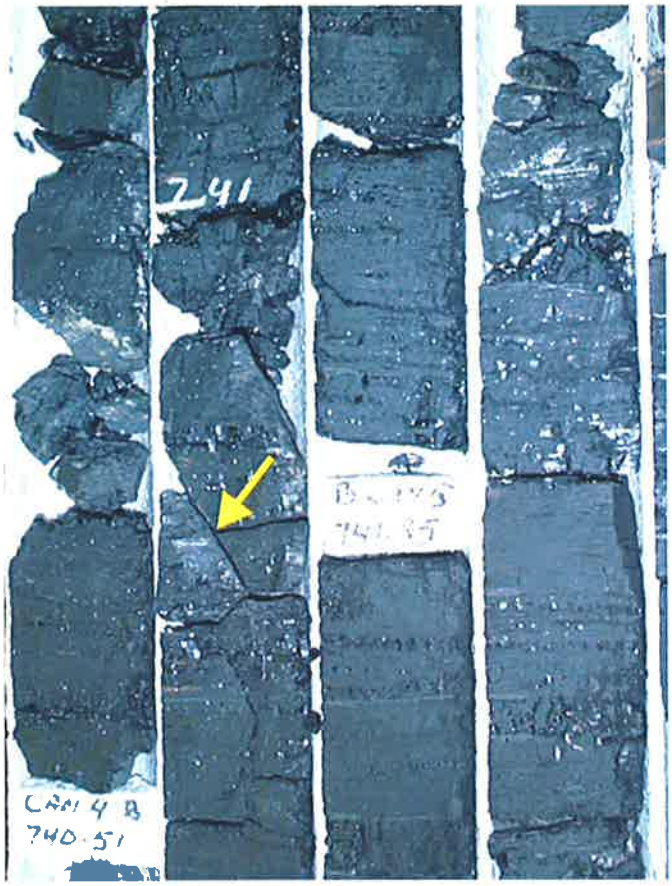

Figure 2.5. Structurally-controlled fractures in the C2 coal seam of the Baralaba Coal Measures, Scotia 4 (50 mm core). Note that cleat development is poor in the dull coal (majority of core sample).

Figure 2.6. Shear fracture with slickensides, Scotia 4 (50 mm core).

2.4 Outcrop Fracture Mapping

A field study was conducted by the author to determine the relationship between fractures in the outcropping Surat Basin and the fractures at reservoir depth. The aim of the field study was to provide information on fracturing between well locations and to develop an understanding of fracture timing and genesis in order to improve predictive fracture modelling.

The outcropping formations over the Scotia Field are the Jurassic Hutton Sandstone and Precipice Formation of the Surat Basin. Outcrop over the field is typically poor and is generally confined to road cuttings and creek beds. Outcrop mapping in the Surat Basin resulted in the measurement of 943 steep-dipping (80°– 90°) fractures from 149 locations. The fractures can be grouped into two sets, a NE–SW-striking set and a NW–SE-striking set (Fig. 2.7). The NW–SE-striking set is generally the dominant set and the northeast-southwest set typically abut the northwest-southeast set. The fractures are typically spaced proportionally to bed thickness and often display plume structures typical of tensile fractures (Price and Cosgrove, 1990). Mineralisation was not observed in any of the outcropping fractures.

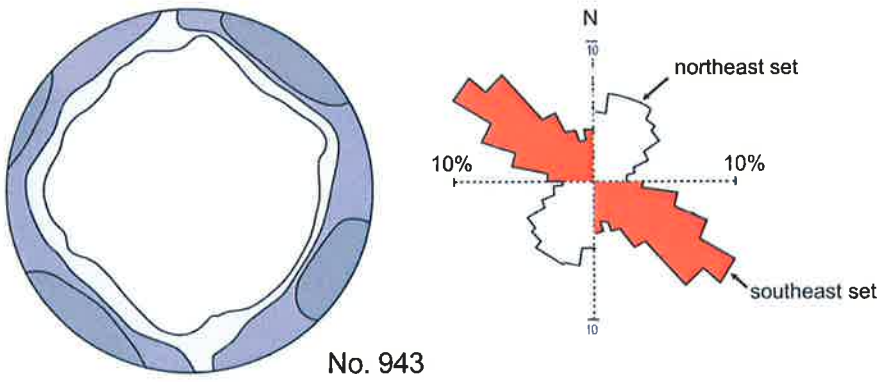

Figure 2.7. Stereonet and rose diagram showing the orientation of natural fractures from outcrop mapping within the Surat Basin (943 fractures). The stereonet diagram plots the poles of fractures and is shaded according to fracture density (dark = high density).

2.5 Fracture Interpretation

The fractures observed in outcrop have different strikes, dips and surface ornamentation to those at reservoir level (Figs 2.4, 2.7). The outcropping fractures are therefore interpreted to be of different age and generation than those at reservoir level. The image log interpretation and outcrop mapping document five major fracture sets, three at reservoir level (not including cleats) and two at outcrop level.

2.5.1 Reservoir level fractures

The majority of fractures at reservoir level formed during shortening along the Scotia fault system during the Triassic Hunter Bowen Orogeny (Holcombe et al., 1997a) and are therefore not present in the younger, outcropping Jurassic-Cretaceous units of the Surat Basin. The north–south- striking fractures at reservoir level are parallel to the major fold axis of the Burunga Anticline. They are interpreted as fold-related fractures due to outer arc extension during formation of the Burunga Anticline (phase 1 of Fig. 2.8). The NW–SE-striking fractures occur as conjugate sets and are interpreted as shear fractures formed during northeast compression associated with formation of the Burunga Anticline (also phase 1 of Fig. 2.8). The fractures are probably associated with sub-seismic, reservoir-scale thrust faults. The origin of the NE-SW-striking set is more enigmatic. The fractures may be related to sediment compaction during a period of vertical maximum principal stress (phase 2 of Fig. 2.8).

2.5.2 Outcropping fractures

The fractures observed in outcrop are typical of tensile joint sets formed via uplift and unloading (Price and Cosgrove, 1990). The joints probably formed during post-Cretaceous uplift and unloading (phase 3 of Fig. 2.8), although it is difficult to constrain their age due to the absence of mineralisation (Esterle and Sliwa, 2002). Unloading joints are typically restricted to a few hundred metres from the surface (Price and Cosgrove, 1990). Therefore, the uplift-related fractures observed in the Surat Basin sequence in outcrop probably do not penetrate to reservoir level. The outcrop and reservoir level fracture systems are unrelated, hence, the outcrop fracture observations cannot be used to help model the fracture distribution at reservoir level.

2.6 Fracture Modelling

The density of fold-related fractures interpreted from the image logs appears to be directly correlated with structural position over the Burunga Anticline with most fracturing along the crest and forelimb of the fold. The Burunga Anticline and the fractures were modelled using Midland Valley's 3D Move software using depth-converted seismic interpretation of the C2 coal seam reflector and the Scotia fault (seismic interpretation and depth conversion by others). The C2 surface was restored to its pre-deformational geometry (i.e. flat) and was then forward modelled to the present day geometry using 3D Move's flexural slip algorithm via an iterative process (Griffiths et al., 2002). The strain associated with the folding was recorded and used to create a best-fit natural fracture model using the fracture generator module of 3D Move (MVE, 2004) conditioned to the image log data (Fig. 2.9). The model predicts high fold-related fracture intensity in areas of high strain and Gaussian curvature along the crest and steeply dipping forelimb of the anticline (Lisle, 1994) and can be used to quantify fracture distribution between existing wells. The 3D Move parameters used to produce the model that best-fits the image log fracture data are presented in Table 2.1 (Flottmann et al., 2002). The flexural slip and fracture

generation methods are not described in detail here as this is background work setting the context for the studies presented in the following chapters. For details of the 3D Move flexural slip algorithm and fracture generation workflow see Griffiths et al. (2002) and the Midland Valley website (MVE, 2004).

Restoration parameters	
Shortening direction	050°
Restoration angle	240°
Fault throw	600 m
Fracture attributes	
Seed density	500
Tip-propagation/step	300
Probability attribute	Gaussian curvature

Table 2.1. Input parameters used in 3D Move to produce the best-fit fracture model (Flottmann et al., 2002).

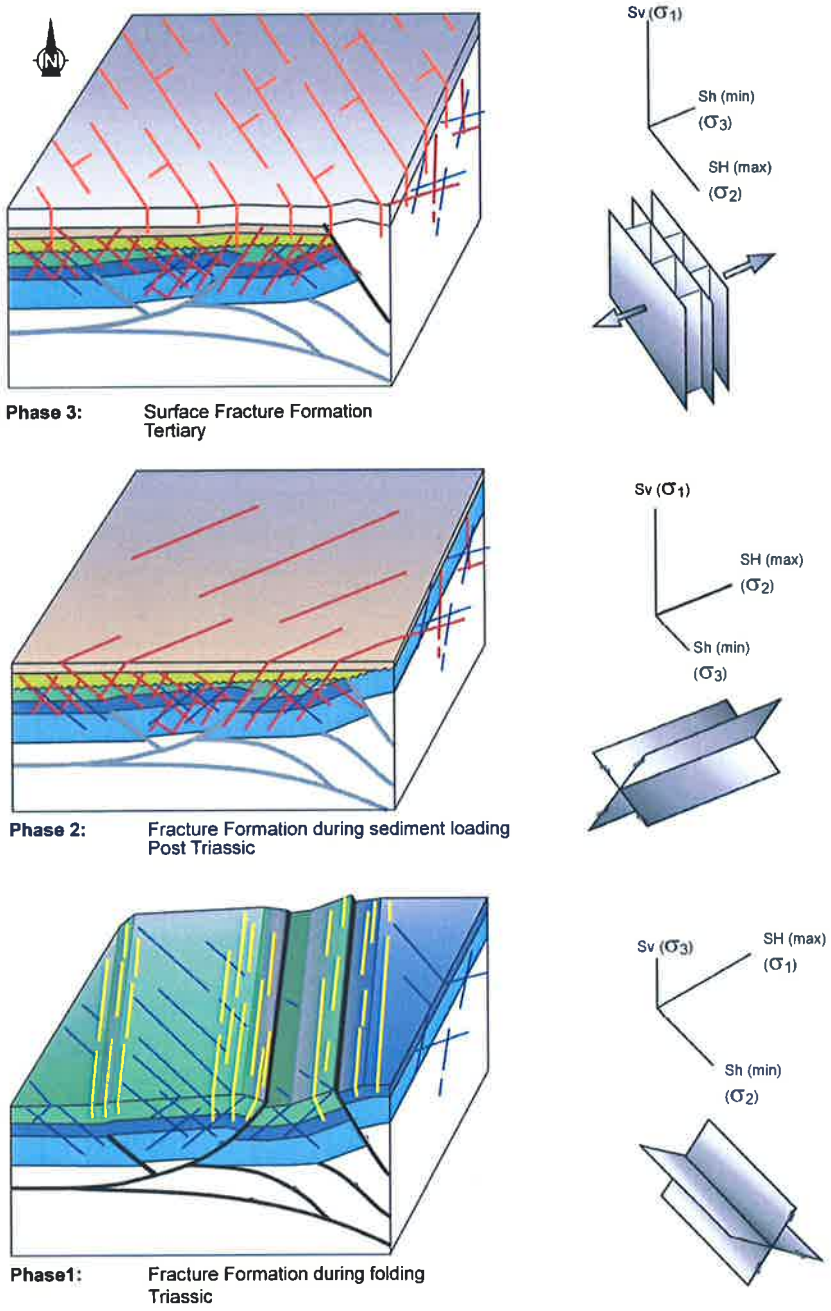

Figure 2.8. Diagram showing the three main phases of fracture development. Phase 1: fractures formed during faulting and folding of the Triassic Hunter-Bowen Orogeny (north-south, yellow and northwest-striking, blue sets). Phase 2: minor fracturing during post-Triassic sediment loading (northeast-striking, red set). Phase 3: surface fracturing formed during uplift and unloading (orange set), only extending a few hundred metres below the surface (Flottmann et al., 2002).

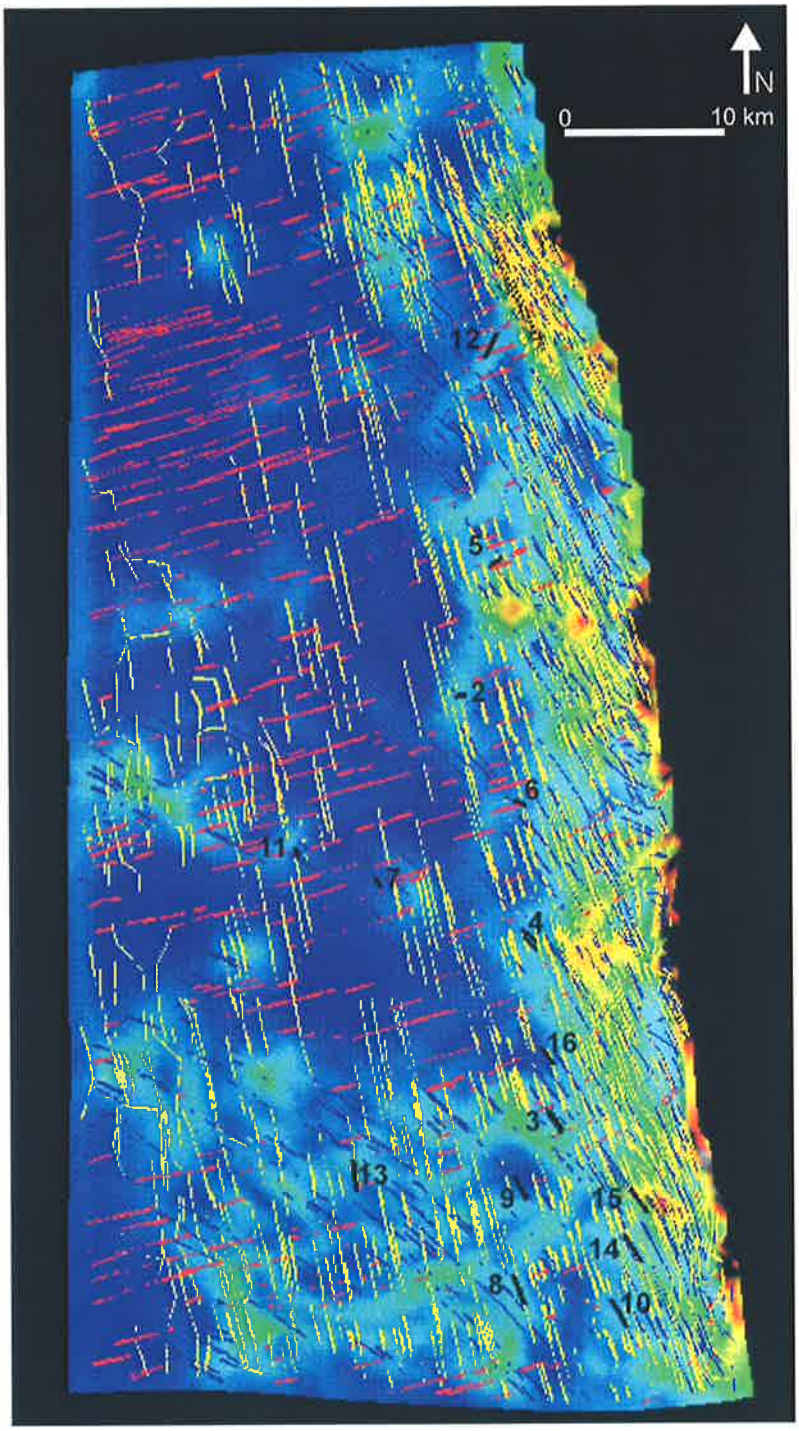

Figure 2.9. Natural fracture model of the fold-related fractures over the northern Burunga Anticline produced using the fracture generator module of 3D Move. Colour coding is Gaussian (3D) curvature, blue areas correspond to areas of low Gaussian curvature and red areas correspond to areas of highest Gaussian curvature (Flottmann et al., 2002). The model has been conditioned/matched to the wells with image log data as shown by the numbers 1–15 through an iterative process. The fracture sets are coloured the same as those shown in Figure 2.8.

2.7 In-Situ Stress and Implications

Only a brief summary of results of the Scotia study are presented here. The data types and methodologies are discussed in more detail in the case studies presented in subsequent chapters of this thesis. The in-situ stress field can significantly influence the hydraulic conductivity of a fracture set (Barton et al., 1995; Hillis, 1998). Density log data, hydraulic fracture closure pressures, rock strength data and image log interpretation were used to constrain the in-situ stress field:

- S_{Hmax} ~ 36 MPa/km oriented at 030°;
- S_v ~ 21 MPa/km;
- S_{hmin} 18–24 MPa/km across the field.

The orientation and magnitude of the in-situ stress field at Scotia is generally consistent with that documented by the Australian Stress Map (Hillis et al., 1999a; Hillis et al., 1998). The in-situ stress tensor is characterised by high S_{Hmax} and varies between strike-slip and reverse-stress regimes across the field. FAST (Mildren et al., 1994; Mildren et al., 2002a) analysis shows that fractures striking between 000°– 060° regardless of dip and those dipping less than about 50° striking between 60°–180° are most suitably oriented to be hydraulically conductive within the in situ stress field. High-angle fractures striking northwest–southeast are the least likely to be open and hydraulically conductive within the in-situ stress field defined by the blue regions in Figure 2.10.

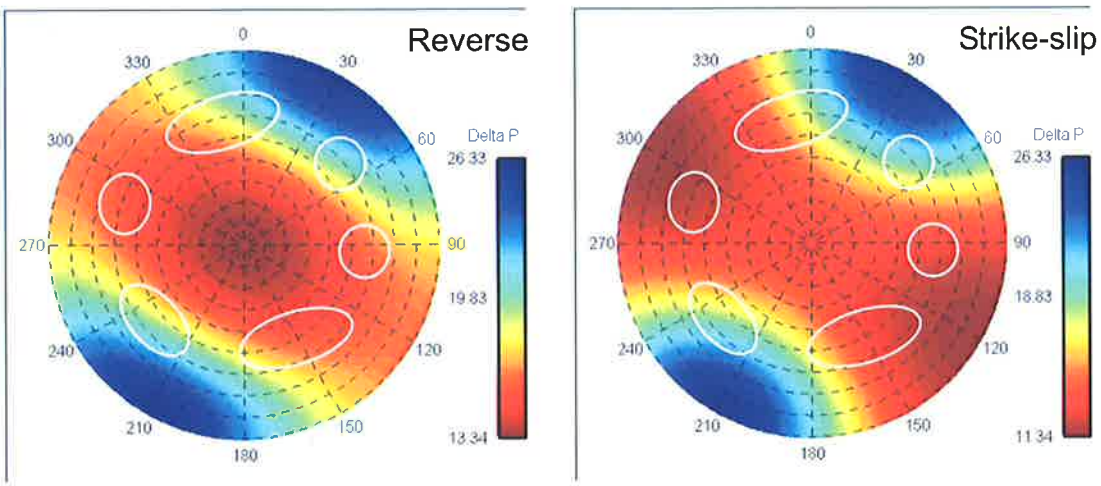

Figure 2.10. Structural permeability diagram showing fracture susceptibility of fractures in Baralaba Coal Measures at 870 m. The two diagrams have been constructed for reverse and strike-slip in-situ stress regimes defined by S_{hmin} gradients of 24 and 18 MPa/km respectively. Fractures with poles in the red areas are most likely to be open and hydraulically conductive (Flottmann et al., 2002). The major reservoir-level fracture sets observed are outlined by the white ellipses.

Hydraulic fracture completions are not effective in areas of the Scotia Field characterised by high mean stress particularly where there is a reverse-stress regime (Flottmann et al., 2002; Johnson et al., 2002). Scotia 15 is an area of high mean stress and a hydraulic fracture treatment was relatively unsuccessful with the well currently flowing only ~0.3 MMCFD despite it intersecting one of the most naturally fractured areas of the reservoir (Fig. 2.9). Conversely, successful hydraulic fracture treatments were achieved in Scotia 10 and 14, which are in areas of relatively low mean stress, typically a strike-slip regime, and the wells currently produce at relatively high rates (2.5 MMCFD).

Well completion difficulties are encountered in the Scotia Field due to slip along bedding surfaces at reservoir level resulting in sheared drill collars (Fig. 2.11) and decreased flow rates due to wellbore damage (Flottmann et al., 2002; Johnson et al., 2002).

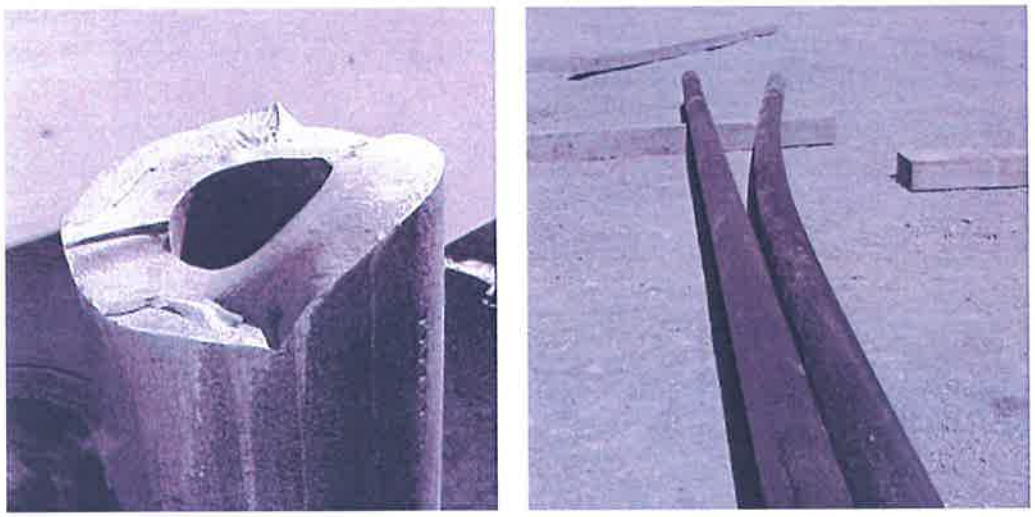

Figure 2.11. Sheared drill collar from the Scotia Field caused by bedding plane slip (Johnson et al., 2002).

2.8 Further Work

The Scotia study was extremely successful at identifying the two key factors responsible for well performance in the field: low mean stress (typically a strike-slip regime) to facilitate hydraulic fracture treatments; and, 2) a high degree of natural fracturing. However, the findings of the study are limited for the following reasons.

- The natural fracture systems at reservoir level do not occur in outcrop over the Scotia Field. Consequently, the effects of mechanical stratigraphy and sub-seismic structures could not be assessed.

- The stress regime is complex due to high horizontal stress and dramatic changes in rock properties between coal and inter-seam rock. The amount of stress data is limited and the effects of rheological variations could not be thoroughly investigated.

- The effects of pore pressure on in-situ stress and fracture susceptibility cannot be quantified as there is no post-dewatering/post-production stress data.

An advanced understanding of these issues has the potential to improve reservoir management, development drilling and completion techniques in the Scotia Field and similar reservoirs.

Chapters 3–6 of this thesis present an analogue study conducted by the author at the Goonyella Riverside open cut/underground mine in the northern Bowen Basin. The Goonyella study aims to improve the current understanding of the issues outlined above in two ways. The first involves integrating 3D seismic data with image log data and outcrop data in order to:

- characterise natural fracture development in a coal measure sequence similar to the Scotia Field;
- observe the effects of mechanical stratigraphy;
- observe the effects of sub-seismic structures on fracture development;
- investigate whether limited well data can provide thorough information about fracture styles and density.

Secondly, the Goonyella study uses stress data acquired from the underground exploration adit before and after dewatering in order to assess the distribution and partitioning of stress in a coal measure succession within a region of high background stress and also to observe the effects of pore pressure reduction on stress within coal and clastic intervals.

3 Goonyella Riverside – Background

3.1 Goonyella Riverside Mine

A coalmine was sought for an analogue study into natural fracture development and in-situ stress in a coal measure succession. CSIRO Exploration and Mining recommended BMA (BHP Billiton Mitsubishi Alliance) operated Goonyella Riverside over other mines based on:

- good exposure of structures in the mine workings;
- a recently acquired 3D seismic survey over the under ground development;
- closely spaced image log data over the under ground area;
- industry-leading stress data.

The Goonyella Riverside mine is located 30 km north of Moranbah township and 190 km southwest of Mackay (Figs 3.1, 3.2). Goonyella Riverside is operated as an open cut coal mine with an underground development in progress. The Goonyella Lower and Middle coal seams dip 3°– 6° towards east and are mined from west to east in a series of open cut pits up to 150 m deep that extend some 15–20 km from north to south (Fig. 3.1). The underground development will mine the Goonyella Middle Seam using the longwall method over an area approximately 2.5 X 3 km to depths in the order of 300 m.

3.2 Goonyella Riverside Study Outline

This chapter describes the tectonic history and the structural setting of the Goonyella Riverside mine. Chapters 4 and 5 describe the structures observed in outcrop, seismic and well data at Goonyella Riverside. The natural fracture systems are linked to the tectonic evolution of the basin and significant reservoir-scale observations are presented. Chapter 6 addresses the in-situ stress tensor and the related issues of fracture susceptibility, stress partitioning and the effects of pore pressure.

3.3 Constraints

The Goonyella study links reservoir-scale features with the tectonic development of the Bowen Basin and demonstrates the effect of stratigraphy on the development of natural fracture systems in a coal measure succession. The study provides insight into stress partitioning between coal and rock and the effects of pore pressure reduction on the in-situ stress tensor. It must be recognised that the setting of Goonyella Riverside is similar, but not the same, as the Scotia Field and other areas of the Bowen and Cooper Basin. Goonyella Riverside is located on the northwestern edge of the Bowen Basin while the Scotia Field is near the eastern margin. Deformation due to the Hunter-Bowen Orogeny is more intense along the eastern margin of the

Bowen Basin with increased basement involvement towards the south (Holcombe et al., 1997a). Consequently, caution must be exercised in drawing any direct analogies between Goonyella Riverside and Scotia.

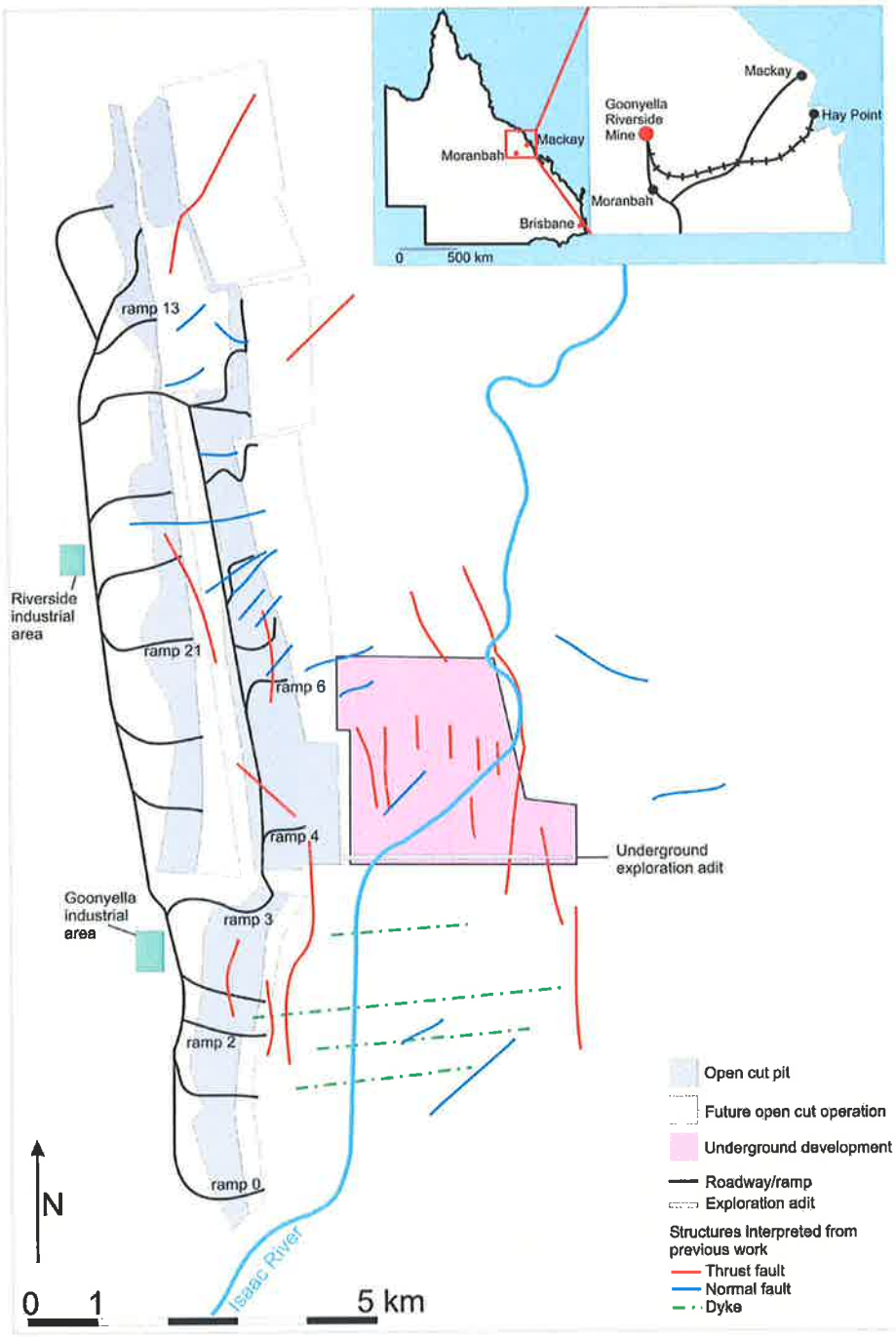

Figure 3.1. Location and layout of the BMA-operated Goonyella coal mine. The structures shown on the map have been interpreted by BMA and CSIRO geologists from open cut mapping and well data (Esterle and Sliwa, 2002).

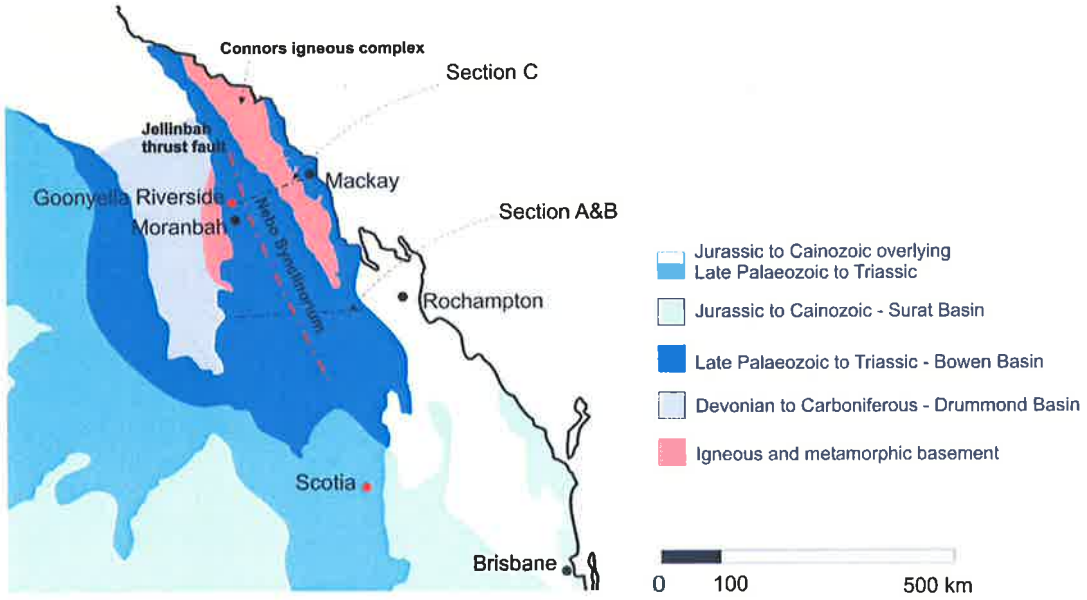

Figure 3.2. Map of the spatial distribution of the Permian-Triassic Bowen Basin and Jurassic Surat Basin. The Surat Basin unconformably overlies the southern Bowen Basin, limiting Permian outcrop in the most prospective areas.

3.4 Tectonic Evolution of Northeast Australia

The tectonic evolution of the host basin must be considered in order to effectively characterise a natural fracture system. Additionally, the contemporary tectonic setting dictates the in-situ stress tensor within the basin that in turn influences which fractures may be open and hydraulically conductive. This chapter discusses the tectonic evolution of the Bowen and overlying Surat basins and the more detailed setting of the Goonyella Riverside mine.

The structural architecture of the Bowen and overlying Surat basins is the result of a series of tectonic events as described below. Although there is some conjecture over the initiation and development of the Bowen Basin (Hammond and Mallett, 1987; Murray, 1990), it is generally accepted that it initiated as a backarc and developed into a foreland basin (Elliot, 1993; Fielding et al., 2001; Korsch and Totterdell, 1995b).

3.4.1 Basement: Devonian to Carboniferous

The Anakie Inlier, Drummond Basin and New England Fold Belt form the basement of the Bowen Basin (Figs 3.2, 3.3). From the Early Devonian to Late Carboniferous, eastern Australian was a convergent plate margin related to a west-dipping subduction system (Korsch et al., 1998). The associated backarc basin and accretionary complex are preserved as the Drummond Basin and New England Fold Belt respectively. The Drummond Basin initiated in the Late Devonian to Early Carboniferous (Henderson et al., 1998) as a backarc extensional system west of the

subducting plate margin. The basin displays significant syn-depositional growth normal faulting with up to 12 km of volcanic and volcaniclastic infill (Henderson et al., 1998). The New England Fold Belt initiated as the accretionary complex associated with the subduction zone and is characterised by deepwater sedimentary rocks and basement involved thrusting (Holcombe et al., 1997a; Holcombe et al., 1997b). Igneous activity associated with the subduction complex initiated in the Carboniferous and persisted in various stages up until the Late Triassic. Igneous bodies intruded parts of the New England Fold Belt and are preserved as the Connors and Auburn Arch (Dickins and Malone, 1973; Korsch et al., 1992) along the eastern margin of the northern and southern Bowen Basin respectively.

3.4.2 Early Permian

The transition from active accretion in the Mid Carboniferous to widespread extension during the Late Carboniferous and Early Permian is interpreted as the eastward retreat of the convergent slab and migration of the volcanic arc offshore (Holcombe et al., 1997b). The Bowen Basin initiated by Early Permian extension that formed half-graben in the western Bowen Basin (Denison Trough) identified in regional seismic surveys (Elliot, 1993; Korsch et al., 1992). The discrete half-grabens contain up to 4000 m of syn-rift non-marine sedimentary fill. Two fault sets create the half-graben and strike 0° and 120° (Elliot, 1993). The extensional fault systems influenced the deposition of the Early Permian section (Fielding et al., 1990) and subsequent reactivation of the faults has deformed the overlying Permian-Triassic section in some areas of the basin (Elliot, 1993). There is a distinct lack of large scale extensional structures in the eastern Bowen Basin compared to the western Bowen Basin. The mechanism responsible for the initiation of subsidence and basin formation in the eastern Bowen Basin remains speculative (Elliot, 1993; Murray, 1990).

3.4.3 Late Permian

An early Late Permian interval of passive thermal subsidence has been identified throughout the basin coincident with a marine transgression marking the greatest lateral extent of the basin (Fielding et al., 1995). During this period the Bowen Basin extended east of its present margin (at least until the end of the foreland closure in the Middle Triassic). The position of the original eastern margin remains speculative due to the intensity and nature of deformation associated with subsequent basin closure. The period was short lived and terminated by the onset of foreland thrust loading (Fielding et al., 1995). A basin-wide unconformity at approximately 260 Ma is synchronous with an uplift event recorded in the New England Fold Belt to the east (Holcombe et al., 1993).

3.4.4 Late Permian to Early Triassic

The thermal subsidence phase ceased in the Late Permian due to the onset of foreland loading caused by thrusting and crustal thickening along the eastern Australian margin during the Hunter-Bowen Orogeny (Korsch and Totterdell, 1995a). The Hunter-Bowen Orogeny was active for approximately 35 million years from the Late Permian to Middle Triassic ~265 Ma–230 Ma (Holcombe et al., 1997a). Foreland loading may have resulted from the landward migration of a continental magmatic arc during a period of crustal contraction (Holcombe et al., 1997a). The Hunter-Bowen Orogeny uplifted parts of the New England Fold Belt and imparted thin-skinned deformation to the succession. The New England Fold Belt forms the contemporary eastern margin of the Bowen Basin and is an amalgam of terrains bound by structures active during the Hunter-Bowen Orogeny (Holcombe et al., 1997a).

The foreland loading phase was characterised by rapid subsidence that was greatest along the eastern margin of the basin (Taroom Trough) and decreased westward. The sedimentary successions deposited during the foreland loading phase thin dramatically from east to west across the basin. The northeastern margin of the Bowen Basin was influenced by WSW-directed thrusting (Fielding et al., 1995).

3.4.5 Middle Triassic

The final pulse of thrusting during the Hunter-Bowen Orogeny resulted in uplift and propagation of thin-skinned thrust faults through the entire basin (Fergusson, 1991; Fielding et al., 1995). The subducting slab is interpreted to have undergone roll-back during the late Middle Triassic resulting in re-establishment of the volcanic arc some distance to the east of the present New England Fold Belt (Holcombe et al., 1997a). The uplift associated with thrust front propagation terminated sedimentation. Subsequent erosion during the Late Triassic produced an unconformity marking the top of the Permian-Triassic Bowen Basin (Fielding et al., 1995; Korsch et al., 1998).

3.4.6 Early Jurassic

Following the Late Triassic uplift and erosion, eastern Australia experienced a period of thermal sag. Subsidence was driven by thermal relaxation of the lithosphere (Korsch and Totterdell, 1995a) initiating the epicratonic Great Artesian Basin (GAB). The Surat Basin is the eastern portion of the GAB that developed as a relatively thin (approximately 2 km), yet laterally extensive basin over much of the Australian landmass (Elliot, 1993).

3.4.7 Cretaceous

The Early Cretaceous breakup of Gondwana resulted in a marine transgression in the Surat Basin. The Gondwana breakup resulted in the intrusion of various dykes, sills and plugs into the Bowen and Surat basins (Esterle and Sliwa, 2002). A brief period of compression followed, causing broad folds in the Surat Basin (Elliot, 1993), reactivation of shallow faults and movement along bedding planes (Esterle and Sliwa, 2002).

3.4.8 Late Cretaceous to Early Tertiary

Up to 1500 m of uplift occurred along the eastern margin of the Australian continent during the Late Cretaceous to Early Tertiary, resulting in the cessation of sedimentation and subsequent erosion. The incised land surface is preserved as the Tertiary unconformity overlain with continental sediments and basalts. Extensional conditions prevailed from the Late Cretaceous through to the Early Tertiary during the rifting and opening of the Coral Sea (Esterle and Sliwa, 2002).

3.4.9 Contemporary tectonic setting

The northern Indo-Australian Plate margin evolved from a passive margin to one characterised by sinistral oblique transpression due to collision with the Pacific Plate during the Miocene (Cullen and Pigott, 1989). The conditions persist today with the Indo-Australian Plate currently moving towards 035°N at a rate of 5.5 cm/yr (Fig. 3.4) (Chase 1978). The collision of the Indo-Australian Plate with the Pacific Plate has reactivated some of the older structures (Esterle and Sliwa, 2002) and influences the contemporary stress field in northeastern Australia (Coblentz et al., 1995; Coblentz et al., 1998; Hillis et al., 1999a). The Indo-Australian plate is characterised by unusually high in-situ stress, a result of the balance between ridge push forces along the southern plate margin with collision along the New Zealand, Papua New Guinea and Himalayan boundaries (Coblentz et al., 1995). The contemporary stress field in central Queensland is typically characterised by a reverse stress regime with maximum horizontal stress orientations of north-northeast (Hillis et al., 1999a). The contemporary orientation of S_{Hmax} is almost 90° to that inferred during the Late Triassic Hunter-Bowen Orogeny (east-west S_{Hmax} associated with west-verging thrusts).

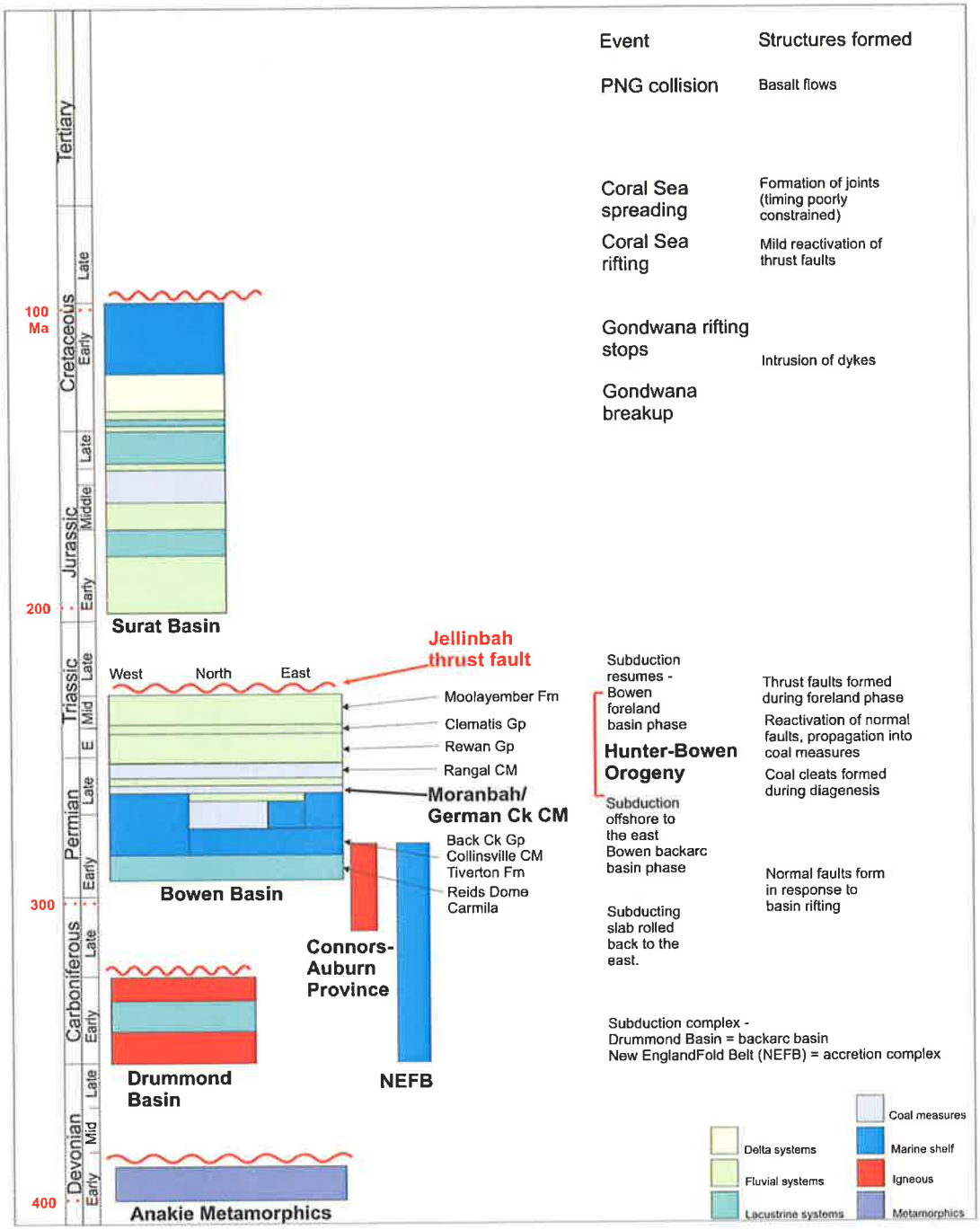

Figure 3.3. Time-space diagram and stratigraphy of the Drummond, Bowen and Surat basins, eastern Australia (Fielding et al., 2001). The Jurassic Surat Basin unconformably overlies the Permian-Triassic Bowen Basin. The coal seams mined at Goonyella Riverside are part of the Late Permian Moranbah-German Creek coal measures. The most severe deformation event was the Late Triassic Hunter-Bowen Orogeny (Jellinbah thrust fault).

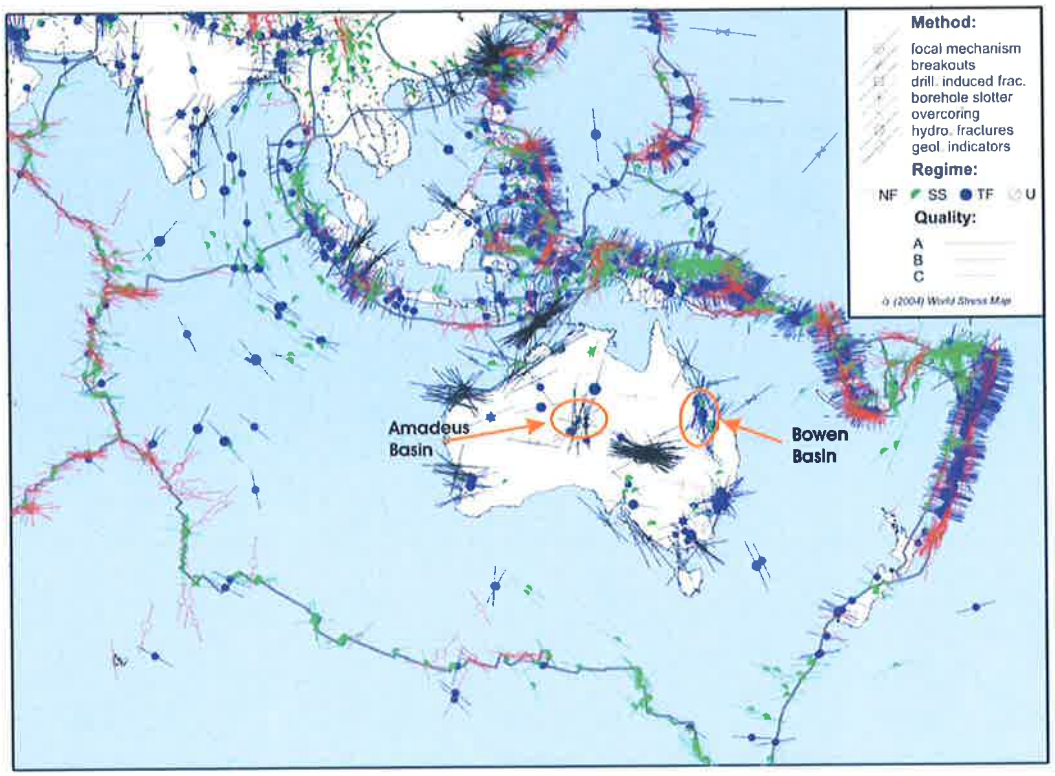

Figure 3.4. Contemporary tectonic setting of the Indo-Australian Plate showing the location of the Bowen and Amadeus basins. The lines indicate the direction of maximum horizontal stress and the colours represent the state of stress: red represents normal stress regimes; green represents strike slip stress regimes, and blue represents reverse stress regimes. The unusually high in-situ stress is a result of the balance between ridge push forces along the southern plate margin with collision along the New Zealand, Papua New Guinea and Himalayan boundaries (Coblentz et al., 1995).

3.5 Structural and Stratigraphic Setting of Goonyella Riverside

The structural and stratigraphic setting of Goonyella Riverside must be considered in order to understand the natural fracture system and the in-situ stress tensor. It is important to distinguish between tectonic history and contemporary tectonic setting. In the case of eastern Australia, natural fractures in the subsurface were created during various events in the tectonic history of the basin while the contemporary tectonic setting controls the in-situ stress tensor and the flow behaviour of older fractures. The mechanical stratigraphy determines the rheology and the manner in which the rocks responded to applied stresses during the tectonic history and how the rocks transmit stress within the contemporary tectonic setting.

3.5.1 Structural setting

Goonyella Riverside is set within the foreland (landward) end of the fold and thrust belt developed during the Triassic Hunter-Bowen Orogeny. Deformation in the area is typically mild and is characterised by open folds and minor thrusting (Holcombe et al., 1997a). Goonyella

Riverside is located on the east-dipping (approximately 10°) western limb of a regional syncline previously referred to as the Nebo Synclinorium (Dickins and Malone, 1973) some 30 km west of the Connors Arch Igneous complex. The most significant structure in the area is the regional, west-verging Jellinbah thrust fault formed at the end of the Hunter-Bowen Orogeny. The Jellinbah thrust fault is a north-south striking, regional structure with maximum throw in the order of 600–800 m some 15 km east of Goonyella Riverside (Esterle and Sliwa, 2002) (Fig. 3.2).

Figure 3.5 shows the extrapolated position of Goonyella Riverside on regional seismic line BMR89.B01. The seismic line is some 200 km south of Goonyella Riverside (Fig. 3.2) and some of the features in the section differ at the latitude of Goonyella Riverside. The Connors igneous complex is approximately 30 km to the east in the equivalent location of the Yarrabee and Dawson Fold zones at the latitude of Goonyella Riverside. The majority of structures preserved at Goonyella Riverside developed during the Hunter-Bowen Orogeny and subsequent events up to the Tertiary.

3.5.2 Stratigraphic setting

The coal seams mined at Goonyella Riverside are part of the Late Permian Moranbah-German Creek coal measures deposited in response to the onset of Late Permian foreland loading (Fielding et al., 1995). The coal measures are up to 700 m thick and immediately overlie the marine-influenced Middle Permian sag phase succession (Esterle and Sliwa, 2002). The lateral transition from the Moranbah Coal Measures in the north to the German Creek Coal Measures in the south records the southerly progradation from fluvial and upper delta plain sedimentation in the north to marginal marine sedimentation in the south (Esterle and Sliwa, 2002).

Three main coal seams are encountered at Goonyella Riverside: the Goonyella Lower Seam (GLS), the Goonyella Middle Seam (GMS) and the Goonyella Upper Seam (GUS) (Fig. 3.6). The seams are up to 8 m thick with various splits and rider seams. The coal seams are separated by a variety of clastic interburden sediments characterised by distributary channel sandstones (up to 60 m thick where amalgamated) intercalated with fine-grained and thinly bedded sandstones, siltstones and shale. The interburden is interpreted to have formed in environments varying from broad fluvial and upper delta-plain channel belts and adjacent floodplain deposits, lobate crevasse-splays and open lakes.

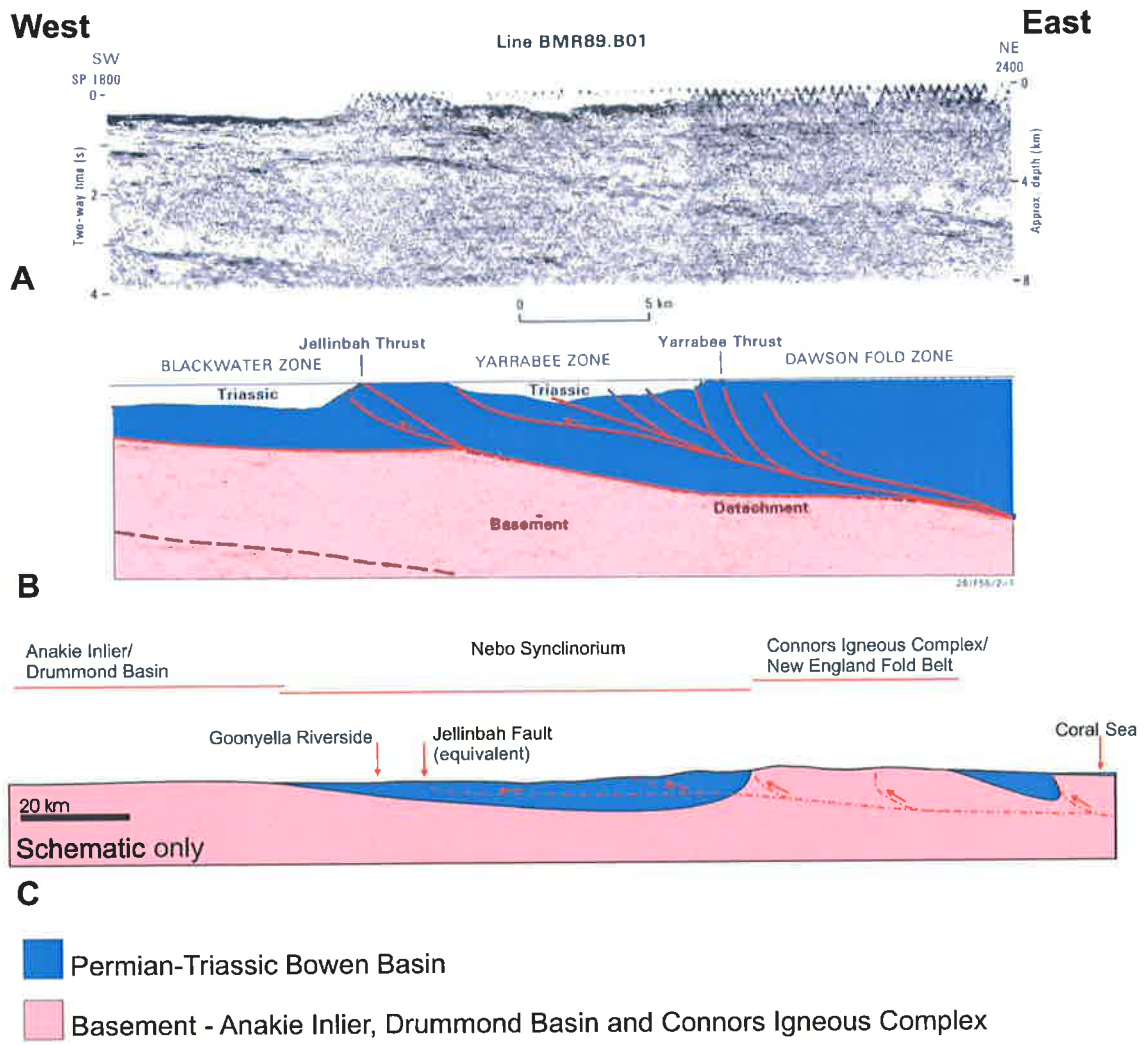

Figure 3.5. The location of cross-sections A, B and C are shown in Figure 3.2. A: Regional seismic line BMR89.B01 showing the general structural setting of the eastern Bowen Basin (Korsch et al., 1992). B: Interpretation of seismic section BMR89.B01 (Korsch et al., 1992). The regional Jellinbah thrust is a west-verging thrust with approximately 700 m of throw. C: Schematic cross-section through Goonyella Riverside. Goonyella Riverside is approximately 200 km north of section BMR89.B01 and 15 km to the foreland side (west) of the Jellinbah thrust equivalent.

Sediments comprise abundant volcanolithic and minor quartz grains (Baker et al., 1993; Esterle and Sliwa, 2002; Michaelson and Henderson, 2000). The interburden sediments at Goonyella Riverside are characterised by relatively low shale content.

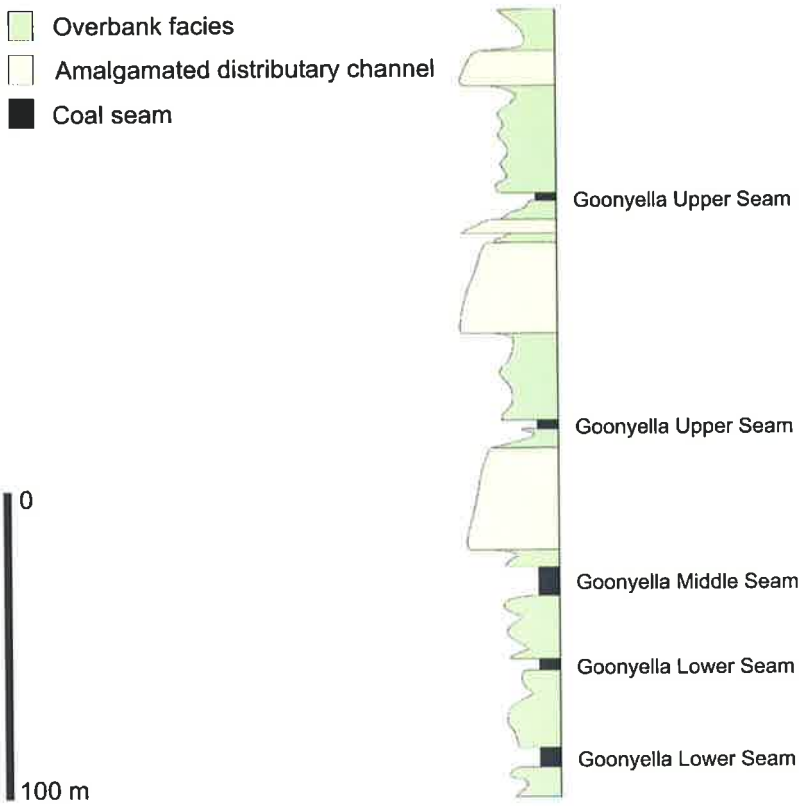

Figure 3.6. Typical stratigraphic section through Goonyella Riverside. The mine extracts coal from three coal seams in the Moranbah Coal Measures. The stratigraphic sequence comprises a series of coal seams up to 8 m thick with various splits and rider seams. The coal seams are separated by a variety of clastic sedimentary sequences grouped into amalgamated distributary channel sandstones and overbank facies comprising laminated siltstones and shales and isolated sandstone bodies.

This chapter has described the tectonic history and the structural setting of the Goonyella Riverside mine. The following chapter describes the geological mapping undertaken at Goonyella Riverside.

4 Structural Observations from the Goonyella Riverside Workings

4.1 Background

Various structures exposed in the mine workings reflect the tectonic evolution of the northern Bowen Basin, namely thrust faults, normal faults, dykes, joints and coal cleats. Unfortunately, the largest faults are smaller than those typically imaged by petroleum industry seismic reflection data. This is expected to be the case in most Australian coal mines as areas with significant faulting generally make for poor mining conditions and are thus avoided. Nonetheless, significant implications for hydrocarbon exploration and development may be drawn by observing the structures exposed in the mine workings. Observations made in the mine workings are used to calibrate the interpretation of the geophysical data in Chapter 5. It should be noted that the values presented here for cleat and fracture orientation are for a relatively small area. A regional overview of cleat and joint orientation in the central and northern Bowen Basin is addressed by various other authors (Esterle and Sliwa, 2002; Pattison et al., 1995).

Several problems were encountered that limited the scope of the mapping study:

- It is not possible to work within 10 m of a highwall due to health and safety requirements. Brief observations could be made at the face but not for any significant length of time. This restriction made it impossible to make detailed orientation measurements of exposures in the highwalls.
- Only a brief tour (1–2 hours) of the underground exploration adits was feasible due to mine scheduling. Detailed mapping of the structures exposed in the underground workings was not possible in this time frame.
- The most dominant structural features in the Goonyella Riverside area are north–south-striking thrust faults. The geometric arrangements of north–south-striking pits make it difficult to observe the thrust faults in the open cut workings. The best exposures of the thrust faults are in the east-west striking endwalls and in the underground adits (Fig. 4.1).

Several significant observations were made despite the limitations. These contribute to the understanding of deformation and natural fracture development in coal measure successions. In addition, the observations made in the mine workings enabled calibration of the geophysical data interpretation as described in proceeding chapters. This chapter describes the features observed in the Goonyella Riverside open cut and underground workings and discusses controls on their development and implications for hydrocarbon exploration and development. Figure 4.1 shows the location of all photos presented in this chapter.

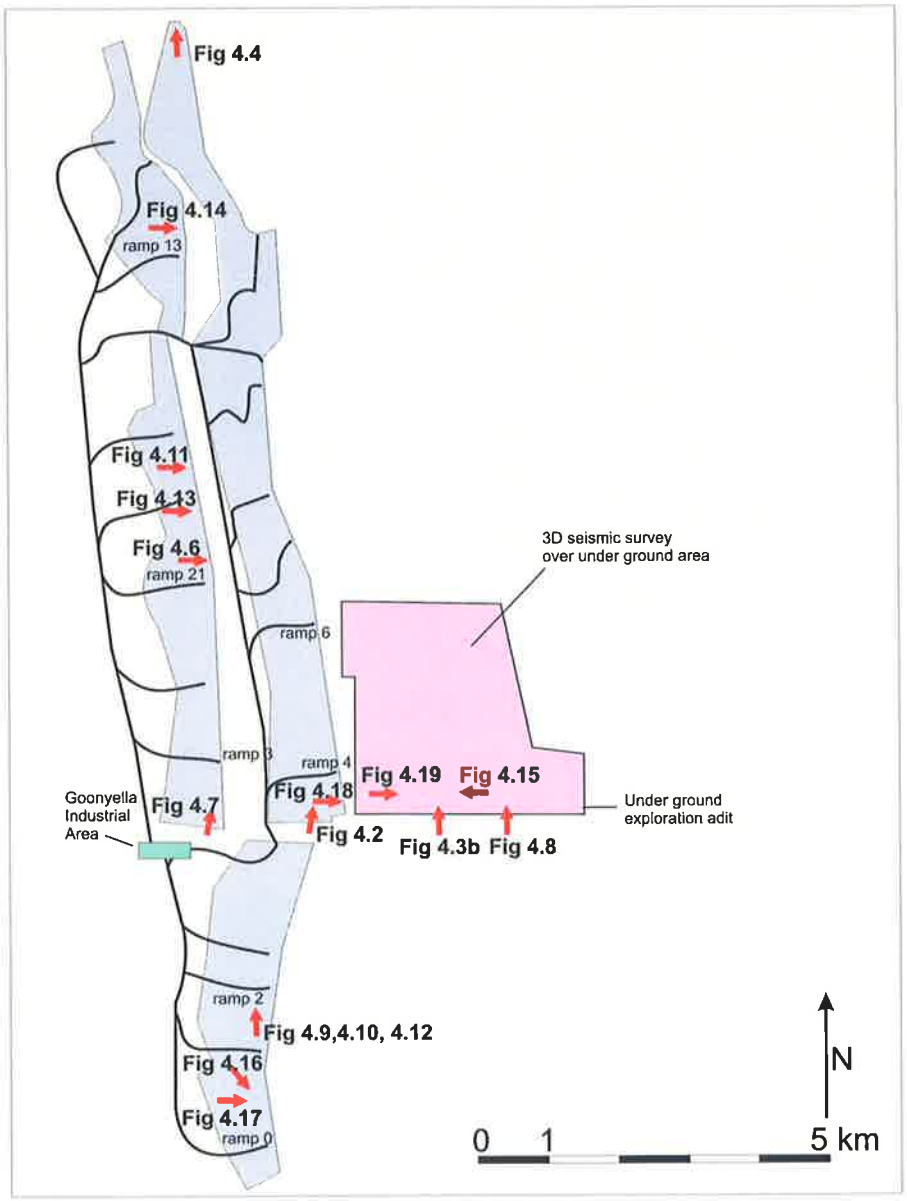

Figure 4.1. The location of photos throughout this chapter are labelled and marked with a red arrow. The direction of the arrow infers the direction the photo has been taken.

4.2 Mechanical Stratigraphy

A rock mass responds to applied stresses according to its mechanical properties. A rock mass with varied mechanical properties may develop different suites of structures. A mechanical unit is an interval of rock with relatively uniform mechanical properties and is typically characterised by consistent deformation. A series of mechanical units defines the mechanical stratigraphy of a rock package (Becker and Gross, 1996; Narr, 1991; Odling et al., 1999; Underwood et al., 2003; Wu and Pollard, 1995).

Mechanical units are a function of their composition and thus their sedimentology. Detailed laboratory work (Seedsman, 1998) has demonstrated that sandstone is the most competent lithology at Goonyella Riverside and that coal is the least competent (Table 4.1). There is a wide variety of palaeo-sedimentary environments including amalgamated distributary channels, crevasse splays, flood plains and peat mires (coal) within the coal measure succession at Goonyella Riverside (Esterle and Sliwa, 2002; LeBlanc Smith and Esterle, 1998). The rocks deposited in the different environments display varying mechanical properties defining mechanical units. It is emphasised here that not every bedding plane defines a mechanical unit (Underwood et al., 2003). A basic classification has been constructed from the mine mapping with three types of mechanical unit defined by their composition. They are:

1. **Coal unit**—comprises seams up to 10 m thick of banded coal with bright vitrinite and dull inertinite-rich layers and occasional thin stone bands in the order of 100 mm thick. A single coal seam may act as numerous individual mechanical units separated by bedding surfaces between the different coal types and thin stone bands.
2. **Overbank unit**—crudely groups all rocks deposited in the overbank environment except coal and consists of stacked, individual crevasse splays and floodplain siltstone, shale and organic-rich shale. A package of overbank material may act as numerous mechanical units as thin as 100 mm; for example, an individual crevasse splay or carbonaceous layer isolated in a massive siltstone may act as a separate mechanical unit.
3. **Distributary channel unit**—consists of sandstone deposited in amalgamated distributary channels. The amalgamated channel complexes range from 5–40 m thick and often behave as a single mechanical unit.

The mechanical stratigraphy has a significant effect on fault and joint development at Goonyella Riverside. Thrust fault flats/detachments typically occur along bedding planes between mechanical units, commonly at the top of coal seams. Joint spacing is commonly proportional to mechanical unit thickness as joints are bound at the top and bottom by bedding planes separating mechanical units. Figure 4.2 shows the ramp 4-6 highwall to the immediate west of the underground development. The photo has been coloured according to the three types of mechanical units: coal, overbank and distributary channel.

Property	Sandstone	Siltstone	Coal
Density (g/cm^3)	2.5 (0.1)	2.5 (0.1)	1.5 (0.2)
UCS (MPa)	45.9 (15.3)	36.0 (17)	9.3 (2.4)
Elastic Modulus (GPa)	11.5 (6.8)	8.2 (3.3)	3.4 (1.2)
Poisson's Ratio	0.34 (0.1)	0.30 (0.1)	0.36 (0.15)
Friction Angle	27.7° (3.1)	25.7° (6.3)	30° (4.3)

Table 4.1. Rock properties determined by geotechnical testing (Seedsman, 1998). Average values are given with standard deviation in brackets.

Figure 4.2. The ramp 4-6 highwall (striking north-south) in front of the development underground mine. The three major types of mechanical units are shown here. Coal seams, overbank and amalgamated distributary channels are coloured purple, green and red respectively. The overbank facies and coal may behave as numerous, thin mechanical units. The amalgamated distributary channels typically behave as single mechanical units. The highwall is approximately 70 m high and 3 km long, in this photo looking northeast.

4.3 Cleats

Cleat is a generic term used to describe natural fractures in coal, regardless of the fracture type (mode 1 or mode 2). Most commonly, cleats occur in two sets that are mutually perpendicular and perpendicular to bedding and often consistent over regionally extensive areas. Cleat sets displaying this geometry are interpreted to be mode 1 tensile fractures. One set is generally more pervasive and is termed the face cleat. The other set is typically less dominant and truncated by the face cleat and is termed the butt cleat. It is widely thought that face cleats form first due to their abutting relationship with the butt cleat set (Pashin, 1998).

Coal cleats were observed in all coal seams at Goonyella Riverside though the remainder of this discussion focuses on the Goonyella Middle Seam. Cleat development is variable and appears to be a function of the coal composition as described by previous authors for Bowen Basin and other coals (Laubach et al., 1998; Pashin, 1998; Pattison et al., 1995). Face cleat spacing in the bright vitrinite rich layers is typically in the order of 5 mm. Face cleat spacing in the dull inertinite rich layers is more variable ranging from 20–150 mm. The face cleats generally strike east-west ± 10° although no detailed analysis could be carried out due to the limited sampling. The butt cleats are arranged in an orthogonal pattern about the face cleats and strike near north-south.

The butt cleats are less developed and the spacing is more variable. The face and butt cleats are locally overprinted in damage zones around faults as discussed in following sections.

It is apparent that the largest influence on cleat development at Goonyella Riverside is coal composition. In order to understand the distribution of cleats, the composition of the coal seam must be considered. The Goonyella Middle Seam consists of a series of layers or 'plies'. The base of the seam is characterised by a bright vitrinite rich ply approximately 2 m thick that gives way to duller inertinite rich layers towards the top of the seam (Fig. 3). Cleats are most closely spaced in the vitrinite rich base of the seam. Cleat development has also been shown to be a function of coal rank in addition to coal composition (Laubach et al., 1998; Law, 1993). The effect of rank on cleat development could not be assessed as the coal rank is relatively consistent (1–11% Rvmax) across the Goonyella Riverside area (Esterle and Sliwa, 2002).

The coal cleats are the oldest structures exposed in the mine workings and developed in the latest Permian to Early Triassic (Pattison et al., 1995). The coal cleats form as tensile fractures during coal diagenesis and reflect the in-situ stress field at the time of their formation (Laubach et al., 1998; Pattison et al., 1995). Face cleats are thought to develop parallel to S_{Hmax} and may be used as a palaeo-stress indicator implying an east-west S_{Hmax} at the time of their formation during the Hunter-Bowen Orogeny. This is consistent with the tectonic model of basin development. A detailed review of the genesis and distribution of coal cleats in the Bowen Basin is provided by Pattison et al. (1995).

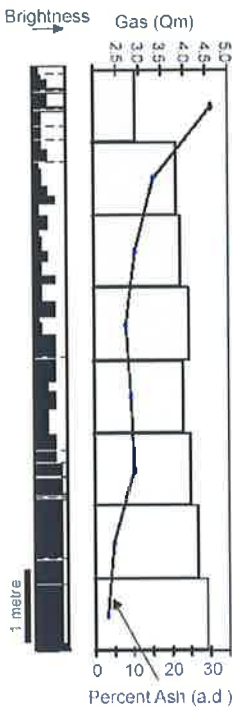

Figure 4.3a. (left) Typical profile of the Goonyella Middle Seam. The seam has a high vitrinite content at the base and becomes less bright and more ash-prone towards the top of the seam corresponding to a decreased gas content (Esterle and Sliwa, 2002). The cleats are most closely spaced at the vitrinite rich base of the seam. **Figure 4.3b.** (right) Base of Goonyella Middle Seam in underground exploration adit. A bright vitrinite rich layer is shown in the bottom of the photo approximately 300 mm thick with cleat spacing in the order of 5 mm. Cleat spacing in the overlying dull band is in the order of 20–30 mm. The white material in the photo is lime, applied as part of the underground mining process (pen for scale bottom left).

4.4 Thrust Faults

Thrust faults are the largest-scale structural features at Goonyella Riverside. The thrust faults strike approximately north-south ± 20° and are interpreted as subsidiary structures of the regional Jellinbah thrust fault some 15 km to the east. The faults are Middle to Late Triassic coinciding with the final stages of the Hunter-Bowen Orogeny (Esterle and Sliwa, 2002).

The geometric arrangement of north–south-striking highwalls with north–south-striking faults makes it difficult to determine the true fault geometry by observing the highwalls alone. The underground exploration adit and open cut endwalls (striking east–west) provide a dip-section.

4.4.1 Thrust fault geometry

A photo provided by Tony Knight of BMA shown in Figure 4.4 provides an excellent view of the true thrust fault geometry. The photo was taken in the endwall at the northern end of Goonyella Riverside. The fault has some features similar to the classical ramp-flat geometry (Suppe, 1983)

and other features that can only be explained by trishear theory (Allmendinger, 1998; Erslev, 1991; Hardy and Ford, 1997). The hangingwall has been displaced from east to west (right to left in Fig. 4.4) along a detachment at the top of the coal seam and a ramp dipping 30°. The top of the coal seam acts as a detachment surface that separates relatively competent sandstone and siltstone above from relatively incompetent coal below. A fault bend syncline-anticline pair has developed in the hangingwall as it translated over the footwall ramp.

Displacement at the fault tip is accommodated by folding rather than slip on a discrete surface resulting in a fault-tip/fault-propagation fold. The fault tip fold is characteristically asymmetric with a steep west-dipping (slightly overturned in places) forelimb and shallow east-dipping backlimb indicative of the west vergence. The various mechanical units display different responses to the faulting. The less competent unit (labelled CS) has not maintained constant thickness, thinning against the fault in the hangingwall and thickening against the fault in the footwall. The more competent unit (labelled Si) has maintained constant bed thickness in both the footwall and hangingwall.

Faults are not planar structures. In 2D, a thrust fault is made up of ramps and flats as demonstrated in Figure 4.5. In 3D, a thrust is made up of 1) flats; 2) frontal ramps that dip the opposite direction to transportation; 3) lateral ramps that strike parallel to transport direction; and, 4) oblique ramps as an intermediate between frontal and lateral ramps. The only parts of the thrust faults clearly visible in the open cut highwalls are the lateral thrust ramps (Figs 4.6, 4.7) due to the geometric arrangement of north–south-striking thrust faults and north–south-striking highwalls.

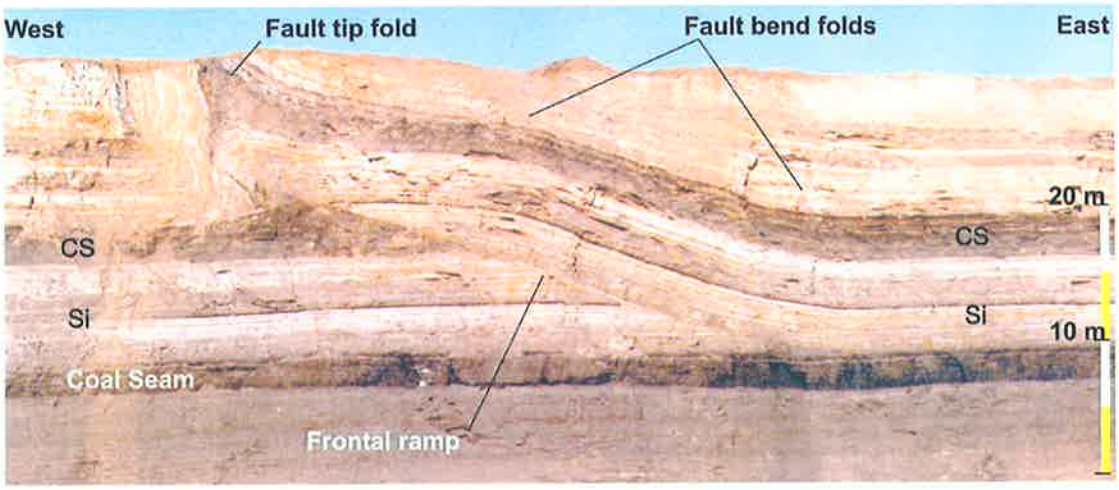

Figure 4.4. Thrust fault exposed in the northern endwall of Goonyella Riverside, scale is approximate only. The hangingwall is detached along the top of the coal seam with a cut off angle of approximately 30° above the detachment. A fault bend syncline-anticline pair has developed in the hangingwall as described by Suppe (1983), however, constant bed thickness has not been preserved within the less competent carbonaceous shale layers (CS). Photo courtesy of Tony Knight of BMA.

The lateral thrust ramps exposed in the highwalls strike east-west and dip 30°-60° towards north or south. The top of the Goonyella Middle Seam has acted as the thrust detachment (thrust flat) and is not offset in each of the lateral ramps observed in the highwalls. The frontal ramps (Fig. 4.4) combined with the lateral ramps (Fig. 4.6) provide a 3D visualisation of the processes that occur during thrust faulting in a coal measure succession.

Several lateral thrust ramps were observed in the highwalls near ramps 3 and 21. The lateral ramps observed near ramp 21 are part of the same thrust complex that has approximately 2 m of throw. The spacing of the larger lateral ramps is in the order of 100–500 m along strike. The lateral ramps dip 30°– 60° and have been misinterpreted by some previous workers as reactivated normal faults based on their steep angle. However, if these structures are considered in their 3D context they are clearly east–west-striking lateral thrust ramps associated with west-directed thrusting.

The geometry of bed thinning in the hangingwall and thickening in the footwall of the relatively ductile carbonaceous shale is best described by trishear theory (Allmendinger, 1998; Erslev, 1991; Hardy and Ford, 1997). Trishear theory describes a discrete triangular zone of deformation in the sedimentary section ahead of a propagating fault tip and provides a more comprehensive description of heterogeneous strain distribution at the tips of propagating faults than earlier fault-fold models (Suppe, 1983; Suppe and Medwedeff, 1990). Trishear theory accounts for footwall synclines, downward-steepening dips as well as thickening and thinning of forelimb strata (Allmendinger, 2003; Erslev, 1991). The observations made here demonstrate that the assumption of constant bed thickness applied to cross-section balancing is not always applicable, especially at reservoir-scale within layered media of varying properties such as a coal measure succession.

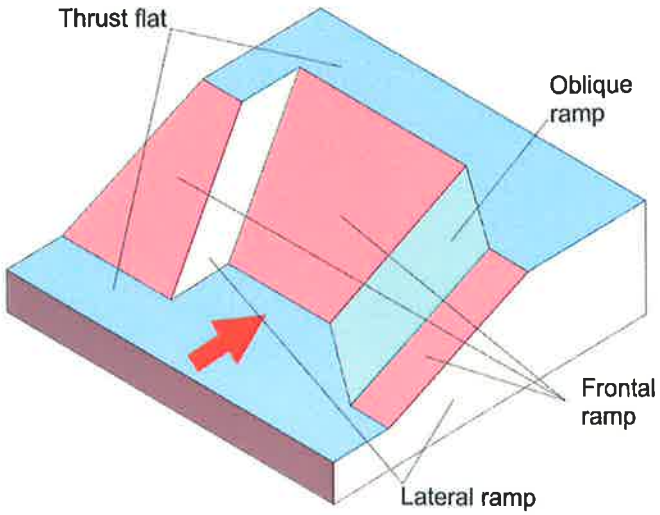

Figure 4.5. Schematic 3D cut-away diagram of thrust fault footwall geometry (Price and Cosgrove, 1990). Frontal ramps (red) strike perpendicular to transport direction (Fig. 4.4). Lateral ramps (yellow) strike approximately parallel to transport direction (Figs 4.6, 4.7) and oblique ramps (green) strike in all other directions. The dip of lateral ramps may vary from near horizontal up to 90°. Near vertical lateral ramps have strike slip sense of movement and may be termed tear faults. Steep lateral ramps may be mistaken for strike slip faults if viewed in isolation.

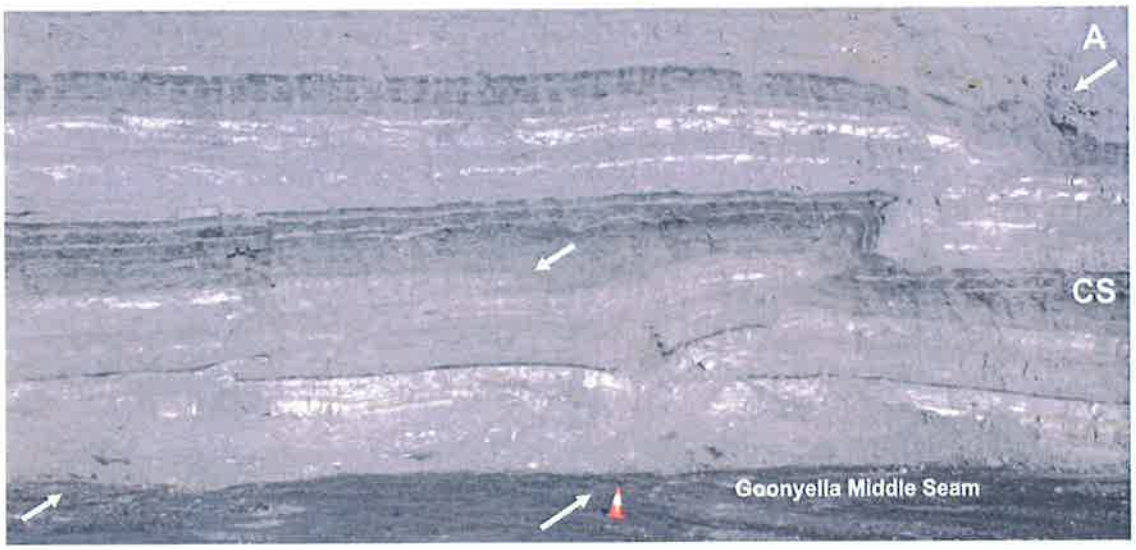

Figure 4.6. Lateral thrust ramps (marked by arrows) exposed in the highwall near mine access ramp 21. The position of ramp 'A' is shown in Figure 4.7. The lateral ramps dip 30°– 60° and strike in the direction of fault movement (east-west). The Goonyella Middle Seam is the thrust detachment (thrust flat) and is not offset; yet the immediately overlying beds are offset by approximately 2 m. Constant thickness is not preserved in the less competent carbonaceous shale (labelled CS). Witches hat for scale (60 cm high).

Figure 4.7. View of ramp 21 highwall looking towards NNE. The highwall is approximately 50 m high. Lateral ramps are exposed in the highwall at A, B and C. The location of Figure 4.6 (A) is shown. Throw on the fault is approximately 2 m, lateral ramp spacing is in the order of 100–500 m. The top of the Goonyella Middle Seam (base of pit) is the thrust fault detachment and is not offset.

4.4.2 Fault zones

The thrust faulting has resulted in a variety of fault rocks and subsidiary structures in the different lithologies. Coal demonstrates a distinctly different response to faulting than the other rock types. Figure 4.8 shows a small thrust fault with approximately 200 mm of throw in the Goonyella Middle Seam. The coal has been milled along the fault surface creating a thin core of cataclasite 5–20 mm wide. The cataclasite is very weak and crumbles under finger pressure. There is no apparent evidence for mineralisation along the fault surface. The coal is commonly weakened and the fabric overprinted within the damage zone of a few metres away from the fault core. Figure 4.9 shows a thrust fault with an unknown amount of displacement (fault throw is thought to be in the order of a few metres). The original coal fabric has been overprinted with a foliation parallel to the fault surface within the damage zone ~1 m wide. The foliation surfaces are spaced 50–200 mm and reduce the strength of the coal. The thrust faults do not appear to affect the coal outside the relatively discrete zone of overprinting.

Siltstone and sandstones respond differently to thrust faulting than coal. The more competent lithologies are characterised by relatively clean, discrete fault surfaces. The less competent lithologies are often characterised by a thin zone of milled rock along the fault core (Fig. 4.10).

Figure 4.10 shows a thin core of milled siltstone with foliation parallel to the fault surface. Clusters of low-angle fractures, often with discrete amounts of displacement parallel to the fracture plane occur within the damage zone near the main thrust faults. The low-angle fractures typically dip in the same or opposite direction as the main fault, forming conjugate sets. They are considered subsidiary structures of the main fault. It is not clear how far from a larger fault the subsidiary structures develop; the density of subsidiary structures appears to decrease away from the fault core.

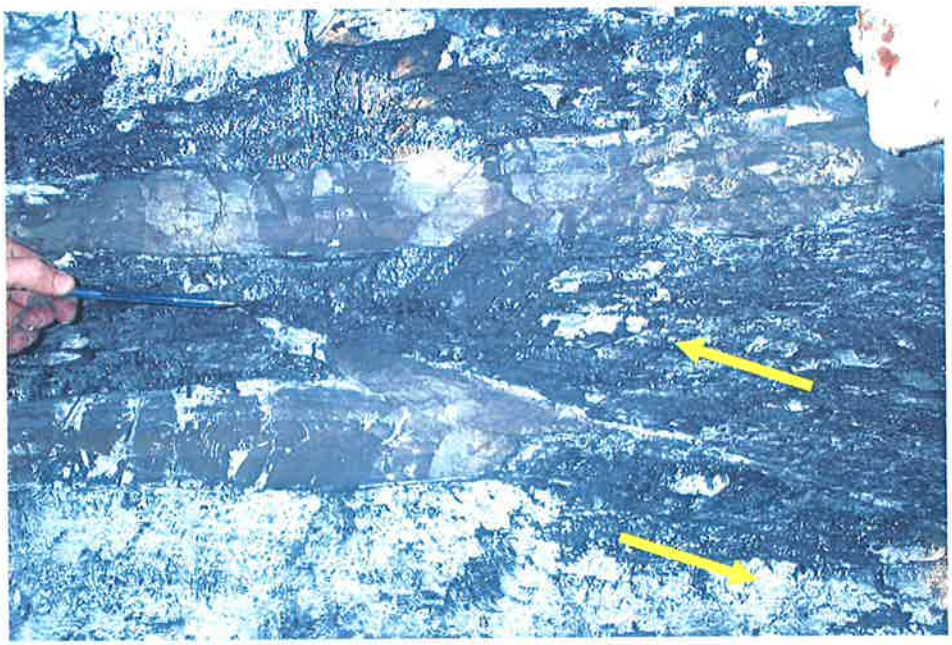

Figure 4.8. Thrust fault in the Goonyella Middle Seam taken in underground exploration adit. The largest fault in the underground area has a maximum throw in the order of 3–5 m. The fault shown here is a splay off the large fault and has a throw of around 200 mm. The coal has been milled in a zone approximately 5 mm thick along the fault plane and damaged in a zone up to 1 m either side of the fault. The stone bed has been offset along clean fracture surfaces.

Figure 4.9. Thrust fault in highwall near ramp 2 with coal in the hangingwall (top right) and siltstone in the footwall (bottom left). The fault throw is not certain but is thought to be in the order of 1–3 m. The coal fabric has been overprinted with a foliation parallel to the fault (30°→070°) in a damage zone approximately 1 m wide.

Figure 4.10. Same thrust fault as shown in Figure 4.9. The siltstone has been milled in a thin zone 5–10 mm wide along the fault core with foliation parallel to the fault surface (30°→070°).

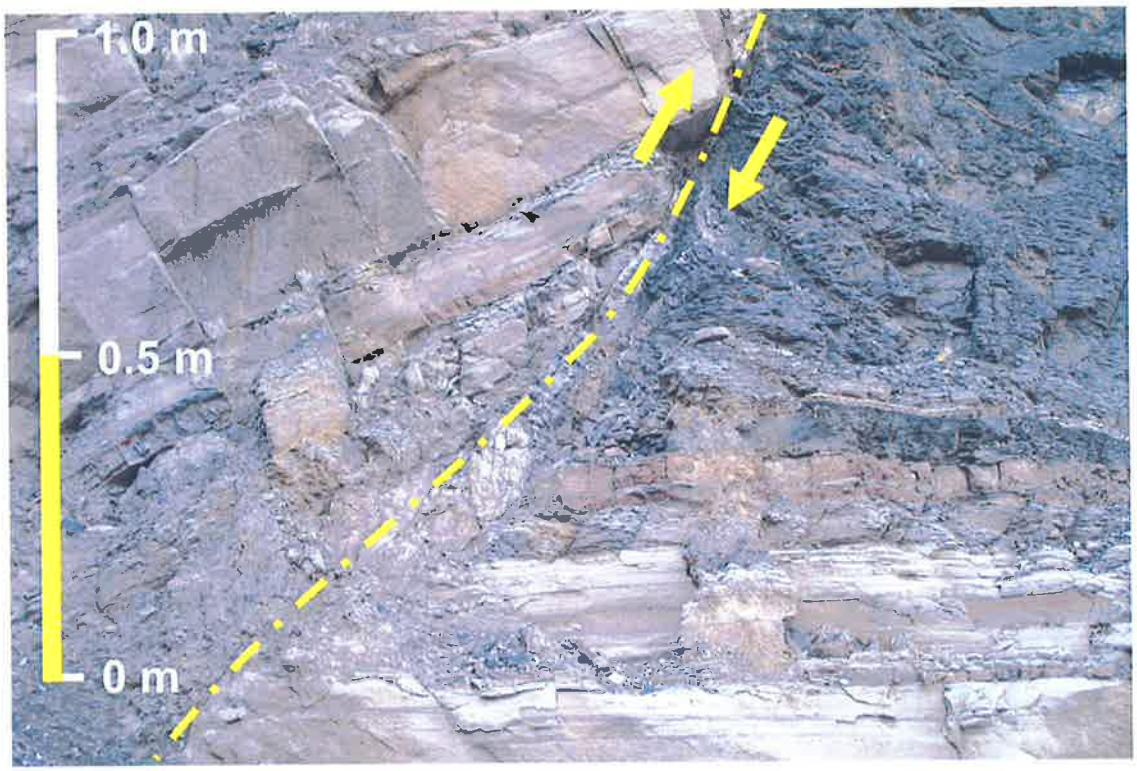

Figure 4.11. Close-up of thrust fault endwall in ramp 21 highwall (Fig. 4.7 C). The thicker relatively competent sandstone layers have deformed in a brittle fashion developing a discrete fault plane. The less competent shale and thin siltstone beds have deformed in a non-elastic fashion and have rotated into the fault plane developing a core a few centimetres thick.

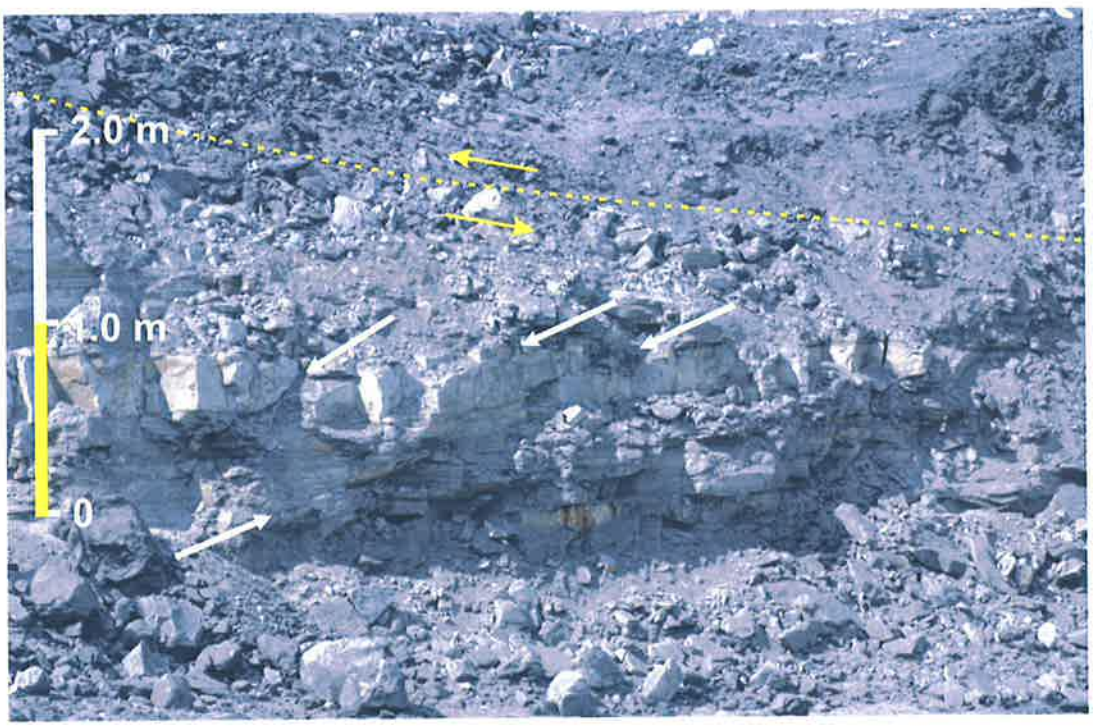

Figure 4.12. Same thrust fault as shown in Figures 4.9 and 4.10 (yellow dashed line). A cluster of low-angle fractures (white arrows) interpreted as subsidiary structures within the damage zone.

Figure 4.13. Low-angle fracture/small fault in highwall near ramp 21 (yellow arrow). The fracture has no discernable offset and terminates at the top of the underlying coal seam and at the base of the thin overlying carbonaceous shale. Low-angle fractures such as these develop within the damage zones of thrust faults.

4.5 Normal Faults

Several non-pervasive, moderately dipping normal faults were observed in the highwall near ramp 13 (Fig. 4.14) and in the underground workings (Fig. 4.15). The faults strike east-west ± 20° and dip 45°– 70°. The faults offset the top of the Goonyella Middle Seam and overlying units and appear to die out in the Goonyella Middle Seam. The normal faults have maximum throw in the order of 1 m. There appears only minor damage along the fault surface with some milling of the seam in a very thin zone (a few mm). Apart from the very thin zone of milled material, the faults have not overprinted the coal fabric. The exact origin and timing of the faults is uncertain. It is thought that they may have developed in zones of dilation within the hangingwall of larger thrust faults.

Larger normal faults have been observed in coal mines in the Bowen Basin including Goonyella Riverside by previous workers (Esterle and Sliwa, 2002). The faults have been traced over 12 km along strike with maximum throw in the order of 80 m and are interpreted as a response to movement along basement structures (Esterle and Sliwa, 2002). The large normal faults were not encountered during the mine mapping and are not discussed further.

4.6 Dykes

An ignous dyke approximately 1 m wide extends the full height of the highwall near ramp 2 (Fig. 4.16). The dyke strikes east-west ± 10° and dips 80°– 90°. The dyke appears to have had minimal effect on the host rock; no aureole or alteration was observed along the host rock-dyke contact. The coal-dyke contact was not exposed and the effect of the dyke on the coal could not be ascertained. The dyke is offset along bedding planes with ductile deformation about the slip planes. A joint swarm is centred about the dyke. The joints are spaced 100–500 mm and extend almost the full height of the highwall, terminating at the base of a carbonaceous shale layer (Fig.4.17). Similar dykes have been described by others in a regional context noting that they typically strike northeast throughout much of the northern and central Bowen Basin (Esterle and Sliwa, 2002) and have been dated as Early Cretaceous (Pattison, 1990).

In is interpreted that the joint swarm formed in response to intrusion of the dyke and may be classified as hydraulic joints (Engelder, 1985). The intrusion may have locally elevated fluid pressures by way of fluid displacement, heating or some other mechanism. The joint swarm is restricted to a stack of crevasse splay sands restricted vertically and laterally by a facies change to overbank shale. The joint swarm does not occur in the shale, possibly because low permeability prevented the elevation of pore pressure in the shale required to form the joint swarms. Ductile deformation of the dyke about the slip planes implies that movement along the bedding planes occurred before the dyke cooled. Movement along the bedding planes may have been induced by the elevation of pore pressure associated with the dyke intrusion.

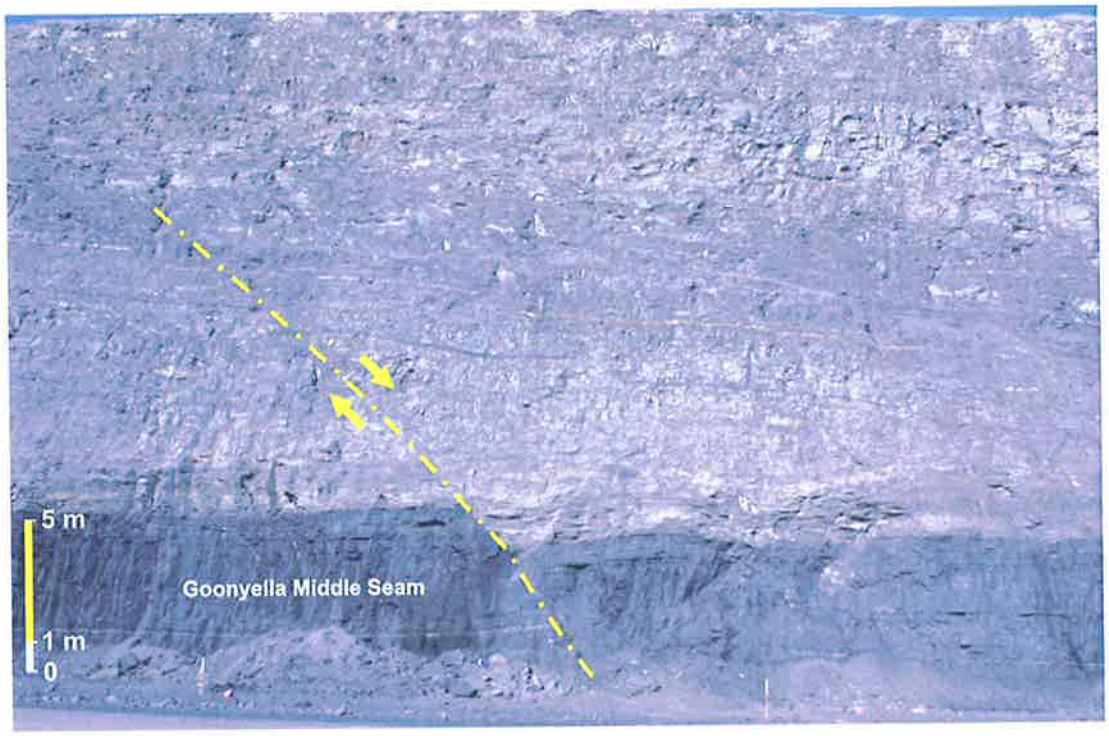

Figure 4.14. A normal fault exposed in the highwall near ramp 13. The fault is one of eight similar faults exposed in 500 m of highwall. The fault strikes east-west and offsets the top of the Goonyella Middle Seam and overlying beds by 1–1.5 m. The faults appear to die out in the coal seam. The faults may have developed as accommodation structures above a deeper thrust fault.

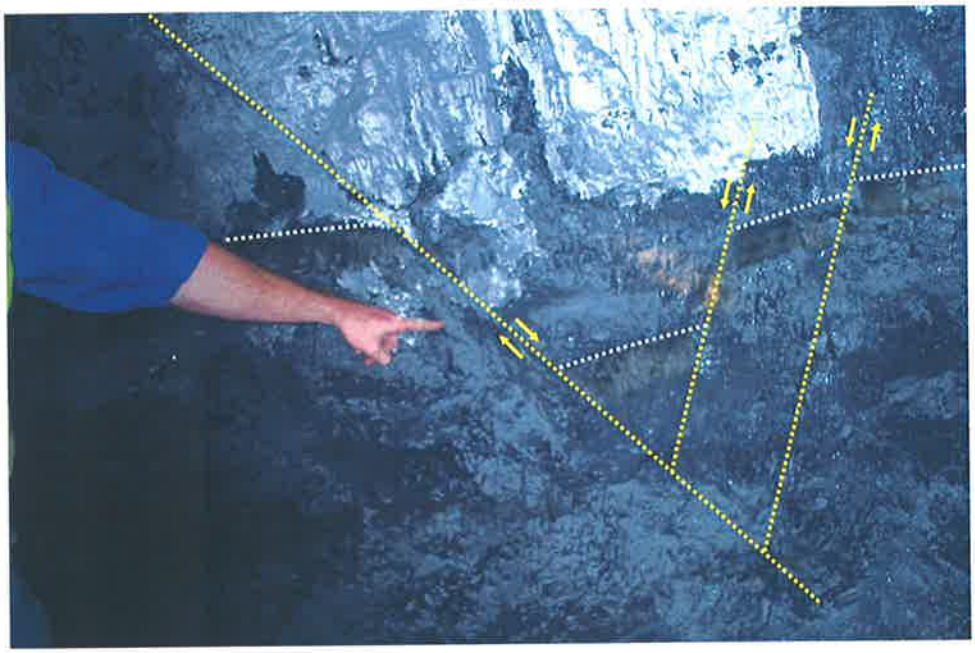

Figure 4.15. East–west-striking normal faults (yellow dashed lines) in the underground mine workings. The faults are within the Goonyella Middle Seam and offset a stone marker bed (white dashed lines) by up to 500 mm.

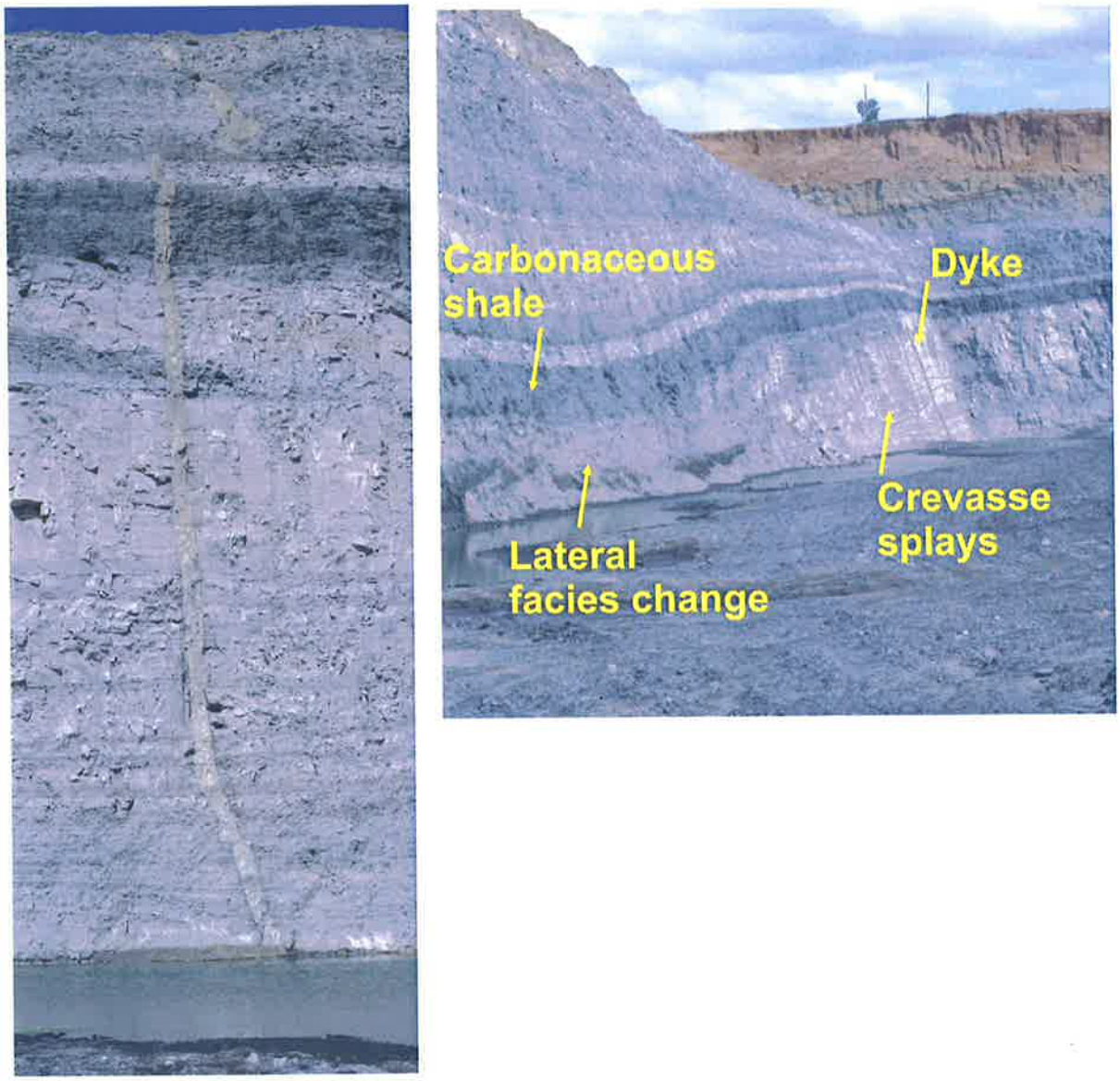

Figure 4.16 (left) and **Figure 4.17** (right). Early Cretaceous east–west-striking dyke in the highwall near ramp 2. The dyke is approximately 1m wide and is offset along bedding planes. Joint swarms have developed around the dyke, but only in the more permeable crevasse splay package. The vertical and lateral facies change to lower permeability shale may have restricted the elevation of pore pressure and resulting joint swarms to the crevasse splay package.

4.7 Joints

Joints are the youngest structural feature at Goonyella Riverside. The timing of joint development is poorly constrained but is thought to be between Early and Late Cretaceous (Esterle and Sliwa, 2002). The joints are near vertical and have hackle and plume structure surface ornamentation characteristic of tensile failure. No mineralisation was noted in any of the joints observed. The joints have various orientations; however, a detailed analysis could not be carried out due to the access restrictions. Three main orientations were noted, an east–west-striking set, a northwest-striking set and a southeast-striking set. The east–west-striking joint set appeared to be the most dominant set, however this observation may be influenced by the

geometric relationship with the highwall orientation (i.e. the east-west striking joints are perpendicular to the highwall and may appear more densely spaced than the other sets).

The mechanical stratigraphy controls joint occurrence, height and spacing at Goonyella Riverside. Joints are typically well developed in the sandstone units and in sandstone lenses within the overbank units and are either absent or poorly developed in siltstones and shales within the overbank units and coal seams due to differences in rock properties during the loading-unloading cycle (Engelder, 1985; Voight and St. Pierre, 1974). Joints within sandstone bodies typically terminate at bedding planes, defining the top and bottom of mechanical units. Figure 4.18 demonstrates a joint set developed in an 8 m thick sandstone layer that has behaved as a single mechanical unit. The joints terminate at the upper and lower contacts and are approximately 6–7 m apart (i.e. a spacing to height ratio of 0.75–0.875). Joint spacing generally appears proportional to joint height in most of the exposures in the open cut and underground workings with spacing to height ratios in the range 0.7–1 (Fig. 4.18). Exceptions to this are the joint swarm associated with the dyke near ramp 2 and the joint swarms observed in the coal in the underground workings (Fig. 4.17). The joint swarms in the coal strike east–west ± 10° with individual joints spaced 50–500 mm.

The joint sets with spacing to height ratios in the range 0.7–1 are similar to those described by various authors for layered sedimentary sequences throughout the world (Becker and Gross, 1996; Narr, 1991; Odling et al., 1999; Underwood et al., 2003; Wu and Pollard, 1995). Joint sets such as these have been frequently interpreted in the literature as a response to horizontal tensile stresses created by slight amounts of expansion during uplift and unloading (Davis and Reynolds, 1996; Engelder, 1985; Price and Cosgrove, 1990). Unloading is the most likely origin of the joints at Goonyella Riverside as there is no evidence to suggest any other origin and they may be termed unloading joints (Engelder, 1985).

The origin of the joint swarm about the dyke has already been discussed; however, the origin of the joint swarms observed in the underground workings remains uncertain. The joint swarms may have developed in association with the small normal faults in a zone of dilation in the hangingwall of a deeper thrust fault.

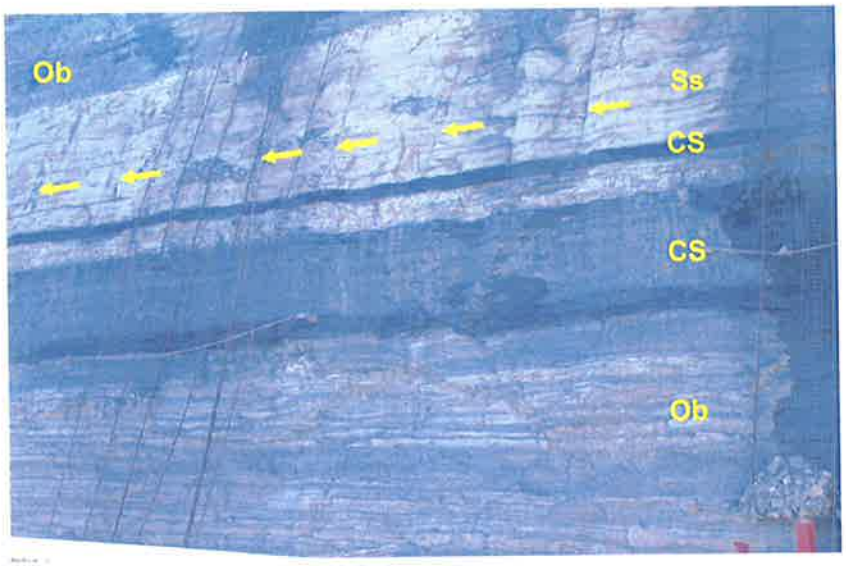

Figure 4.18. Jointing (yellow arrows) in 8 m thick distributary channel sandstone labelled Ss. The sandstone has deformed as a single mechanical unit. The joints terminate at mechanical interfaces that bound the top and bottom of the sandstone and are spaced 6–7 m (i.e. a spacing to height ratio of 0.75–0.875).

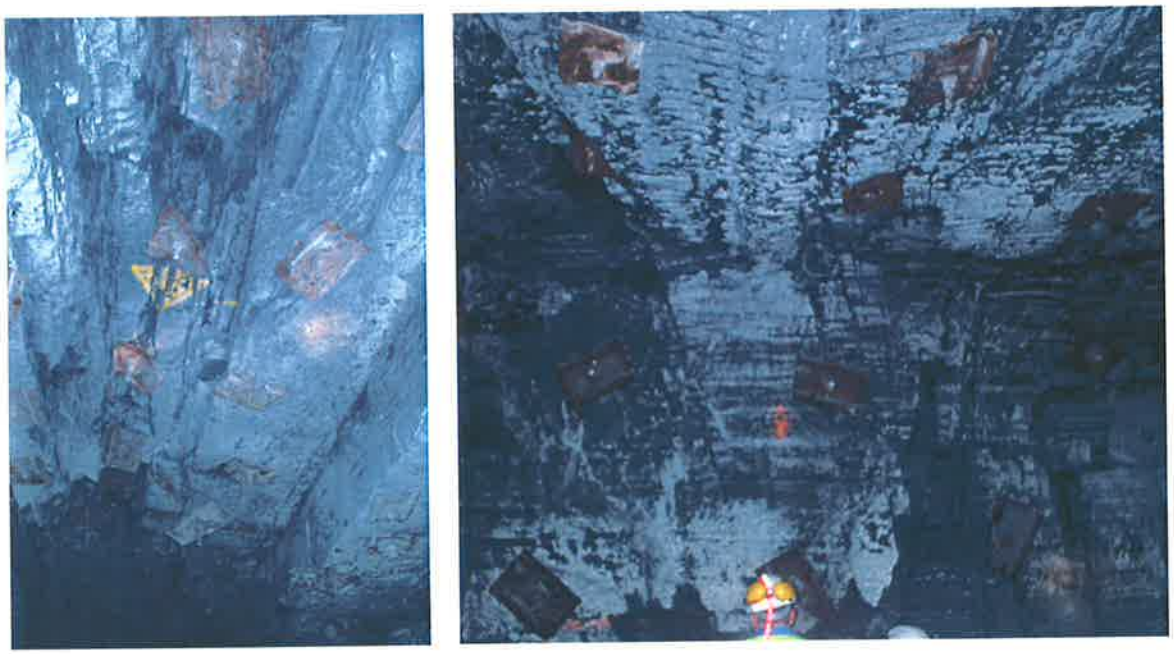

Figure 4.19. Joint swarms observed in the underground workings. The figure on the left is of the roof. The steel plates are about 300 mm long. The joint swarms extend the full height of the underground adit (4 m) and occur in zones 2–20 m wide. Joint spacing is in the range 50–500 mm and joints were only observed in the coal.

4.8 Synopsis

The structural features observed in the mine workings provide insight into the deformation mechanisms within a coal measure succession and demonstrate the variable behaviour of the different lithologies (mechanical units). The following summarises the key observations and implications for hydrocarbon exploration and development.

1. The distribution of cleats in the Goonyella Riverside coal seams is a function of coal composition. Low ash, vitrinite rich layers have closely spaced cleats in the order of 5 mm. High ash, inertinite rich layers have cleat spacings in the order of 20–150 mm (Fig. 4.3). An appreciation of the coal composition and distribution is critical to the understanding of primary cleat development. In petroleum/CBM exploration this issue may be approached by several methods including sequence stratigraphic analysis of the coal seam (Bocking pers. Comm., Bocking and Associates 2003).

2. The face cleat direction is relatively consistent in the Goonyella Riverside area (i.e. east-west ± 15°) and reflects the direction of maximum horizontal stress at the time of coal diagenesis.

3. Thrust fault detachments commonly occur along the top of coal seams. It is apparent that the contact between the coal seams and overlying strata is a mechanically weak layer along which, slip can readily occur. The contacts provide detachment surfaces for small reservoir-scale thrust faults (Fig. 4.4) and may provide detachment surfaces for regional scale thrust faults. Contacts such as these may provide complications during drilling and completion of hydrocarbon wells if slip occurs along the plane during the life of the well. Problems may include stuck pipe and damaged casing (Johnson et al., 2002).

4. Fault core development is variable between the different lithologies. Coal is typically milled into a fine powder a few tens of millimetres within fault cores. Fault cores within siltstones and shales are characterised by grain boundary sliding and clay smear within a zone a few tens of millimetres thick. Fault cores appear poorly developed within sandstones at Goonyella Riverside; however, they may be characterised by a thin band of cataclasite (no cataclasite was observed in outcrop). The damage zones also vary with lithology. Subsidiary low-angle fractures occur within the damage zones in sandstones and siltstones whereas damage zones within coal comprise only a small halo of cleat overprinting around the core. The fault core and damage zone associated with the thrust faults may have complex fluid flow properties. Porosity reduction in the fault core may reduce permeability perpendicular to the fault whereas fracturing within the damage zone may increase permeability parallel to the fault.

5. Lateral ramps of the thrust faults strike parallel to fault movement and dip approximately 45°– 60°. The lateral ramps of the thrust complex near ramp 21 (throw approximately 2 m) are

spaced in the order of 100–500 m (Fig. 4.7). Features such as these are below the resolution of typical petroleum industry seismic data, yet may act as flow baffles or barriers and compartmentalise hydrocarbon reservoirs where there has been porosity reduction in the fault core, particularly those reservoirs immediately above coal seams.

6. Constant bed thickness is not preserved in the less competent beds deformed by the thrust faults (Fig. 4.7). This demonstrates that the assumption of constant bed thickness applied to cross-section balancing is not always applicable, particularly within layered media with significant competency contrasts such as a coal measure succession. The deformation may be better described by trishear theory (Erslev, 1991).

7. The east–west-striking normal faults and joint swarms may have developed in zones of dilation in the hangingwalls of the north–south-striking thrust faults. Such zones may offer enhanced permeability if suitably oriented within the in-situ stress field.

8. Dykes similar to that exposed in the highwall near ramp 2 (Fig. 4.16) compartmentalise hydrocarbon reservoirs, yet the associated joint swarms may provide increased permeability depending on their orientation relative to the in-situ stress field.

9. Joint height and spacing is controlled by the thickness of the mechanical units. Joint spacing to height ratios are typically in the range 0.7–1 (Fig. 4.18).

10. The majority of high-angle fractures are interpreted as joints formed during uplift. If this is the case, they are not likely to exist at depths greater than a few hundred metres. The exceptions are the joint swarms associated with the dyke and zones of dilation.

Structural features such as those described above may either increase or decrease permeability in a hydrocarbon reservoir depending on their orientation within the in-situ stress field, their connectivity, mineralisation, and the relative effects of the fault core and damage zone (Caine et al., 1996; Knipe et al., 1998; Laubach, 2003a). All the features observed are below the resolution of typical petroleum industry seismic data, but may be detected by core and image log data. The exception to this is the coal cleats, which may be below image log resolution, at least in the vitrinite layers (Bocking pers. comm., Bocking and Associates 2003).

The various structural features observed in the mine workings are linked to specific events in the basins tectonic history (Esterle and Sliwa, 2002) and have distinctive orientations as listed in Table 4.2. These observations help calibrate the seismic and image log interpretation in the following chapter.

Feature	Age	Tectonic event	Dip	Dip direction
Coal cleat (face)	Late Permian	Diagenesis	80-90°	000/180°±15°
Thrust fault	Late Triassic	Hunter-Bowen Orogeny	0-30°	090°±20°
Normal fault	Late Triassic	Hunter-Bowen Orogeny	45-70°	000/180°±20°
Joint swarms	Late Triassic	Hunter-Bowen Orogeny	80-90°	000/180°±20°
Dyke	Early Cretaceous	Gondwana break up	80-90°	175/355°
Joint	Poorly constrained	Uplift	80-90°	000/180°±40°

Table 4.2. List of key structural features observed in the Goonyella Riverside mine. The features have distinctive orientations and can be linked to events in the tectonic history of the basin. The timing of the joint development is poorly constrained; however, they must have formed prior to development of the contemporary stress orientation.

5 Seismic and Well Data Analysis

5.1 Background

The previous chapter discussed the various structures exposed in the open cut and underground workings of Goonyella Riverside. The next two chapters present data and interpretation for the underground area (Fig. 5.1). Geophysical techniques including 3D seismic surveying and image logging have been adopted by BMA to delineate subsurface structures that may influence underground mining conditions. The geophysical techniques are common to both the petroleum and coal mining industry, but there are several important distinctions between data acquired for petroleum and coal mining purposes:

- 3D seismic data acquired for the coal mining industry are typically higher frequency and may have better resolution than standard petroleum industry data due to the shallower target depth.
- Coal exploration boreholes are much more closely spaced than petroleum wells and provide a more accurate representation of the subsurface. In the Goonyella Riverside underground area, 18 wells have acoustic scanner image logs.

The geophysical data acquired for underground mine planning provides the opportunity for a detailed 3D analysis of the natural fracture system. The geophysical interpretation is calibrated with the mine mapping discussed in the previous chapter.

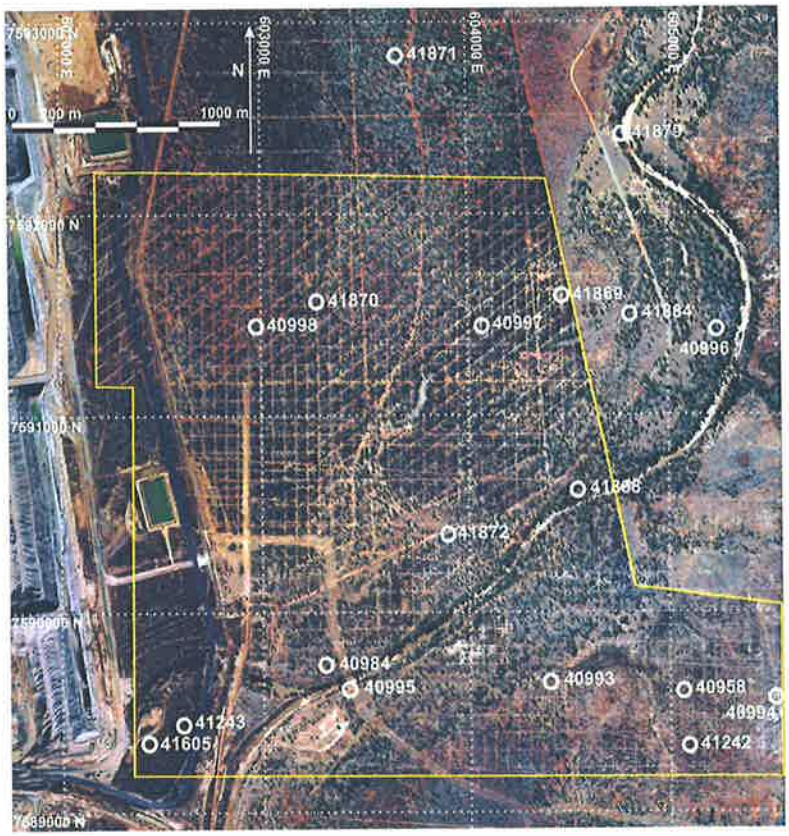

Figure 5.1. Location of 3D seismic survey (yellow outline) and boreholes with acoustic scanner image logs in the Goonyella Riverside underground area. The open cut mine is located to the immediate west.

5.2 3D Seismic Survey

A 3D seismic survey was acquired in three stages over the proposed Goonyella Riverside underground area to help predict underground mining conditions. The combined survey was one of the first 3D surveys to be acquired for the coal mining industry in the Bowen Basin.

5.2.1 Acquisition and processing

Velseis and Trace Energy Services acquired 8.25 km^2 of 3D seismic data in three overlapping stages. This data was combined by Velseis Processing to produce a single volume over the entire underground area (Velseis, 2002).

The field acquisition parameters were designed to have maximum offsets tuned to the depth of the main reflector, the Goonyella Middle Seam. Dynamite was the energy source used for each of the stages and a slanted shot line pattern was adopted to reduce the effect of acquisition footprint (i.e. the shot line azimuth is at an angle to both the in-line and cross-line orientation) (Velseis, 2002). Significant amplitude banding persists in the survey despite these efforts. The amplitude banding as seen in Figure 5.2 is parallel to bedding strike and is thought to be due to near surface geology effects. Highly weathered beds at the surface reduce the amount of energy that is transmitted to the target horizons and impart a zone of low amplitude compared to zones

below more resistant beds. The near surface effects are very difficult or impossible to remove from the Goonyella Riverside data due to the very shallow depth (150–350 m) of the target horizon (Driml pers.comm., Velseis Processing Pty Ltd. 2002).

Velseis Processing generated synthetic seismograms to link borehole data to the seismic reflectors. The most dominant reflector is the peak at the base of the Goonyella Middle Seam (Fig. 5.3). The significant events above and below the Goonyella Middle Seam are caused by the other coal seams.

A depth-converted volume was created by Velseis Processing using seam pick information at borehole locations. The geologic picks were combined with horizon picks to produce average velocity control points at the borehole locations. The average velocities were then gridded to produce an average velocity map to the base of the Goonyella Middle Seam. The depths are only considered accurate for the base of the Goonyella Middle Seam horizon due to the type of depth conversion adopted (Velseis, 2002).

The shallow target depth (150–300m) allows high-frequency data to be recorded providing excellent vertical resolution. The dominant frequency at the target depth is in the range 200–250 Hz providing vertical resolution in the order of 2 m (assuming vertical resolution ~ $\lambda/4$).

5.2.2 Interpretation

The base of the Goonyella Middle Seam is the strongest reflector and can be traced throughout the entire volume with high confidence (Fig. 5.3). The Goonyella Middle Seam dips 2°– 10 ° towards the east and is offset by several faults. The faults strike north-south to northeast-southwest and dip towards the east at approximately 30°. The faults are interpreted as thrust faults with maximum throws in the order of 5 m. The faults are of the same magnitude and style as the thrust faults observed in the mine workings and are considered subsidiary structures of the regional Jellinbah thrust fault. The faults can be traced as low-amplitude trends on an amplitude map of the base of the Goonyella Middle Seam (Fig. 5.2).

Figure 5.3 shows an east-west cross-line through borehole 40993 parallel to the dip direction. Borehole 40993 intersects the base of the Goonyella Middle Seam 8 m above the thrust fault shown in Figure 5.3. The fault has maximum throw in the order of 5 m and is intersected by the underground exploration adit. Unfortunately, the main fault could not be observed in the adit as it was covered in lime powder as part of the mining process.

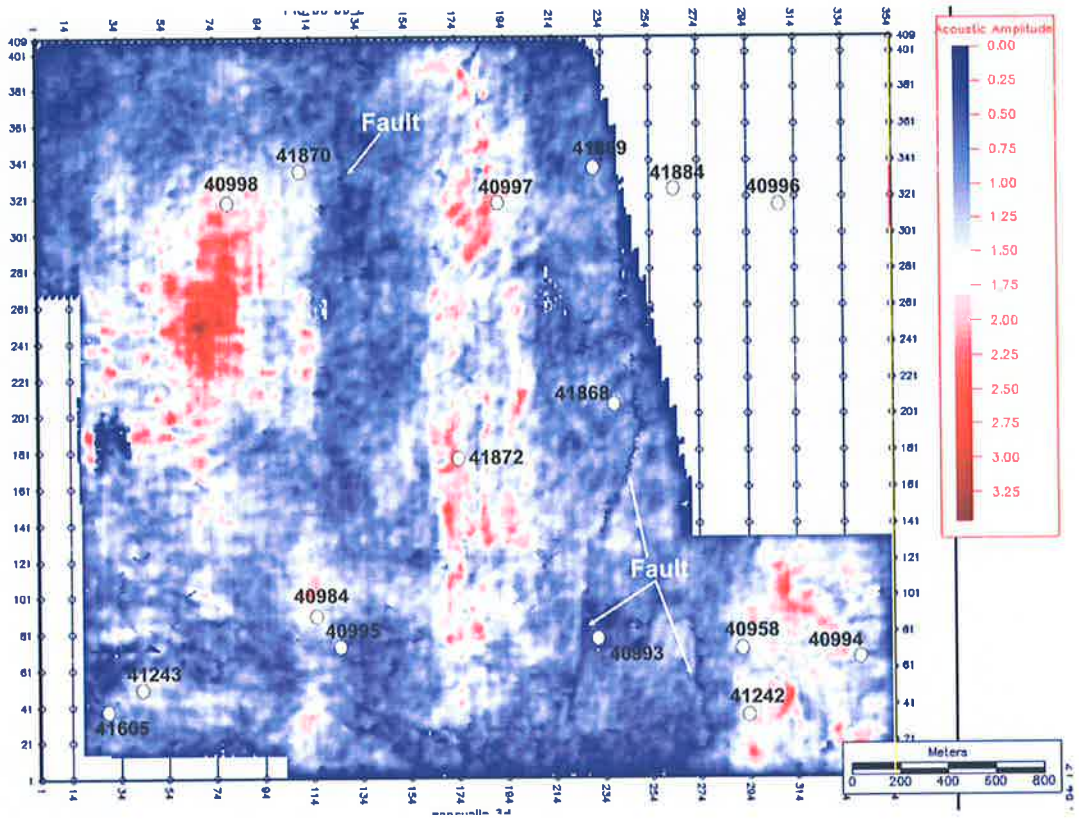

Figure 5.2. Amplitude map of the base of the Goonyella Middle Seam. Thrust faults with maximum throws in the order of 2–5 m appear as low-amplitude trends on the amplitude map. The thrust faults are the most significant structural feature within the 3D survey and are interpreted as subsidiary structures to the regional Jellinbah thrust fault.

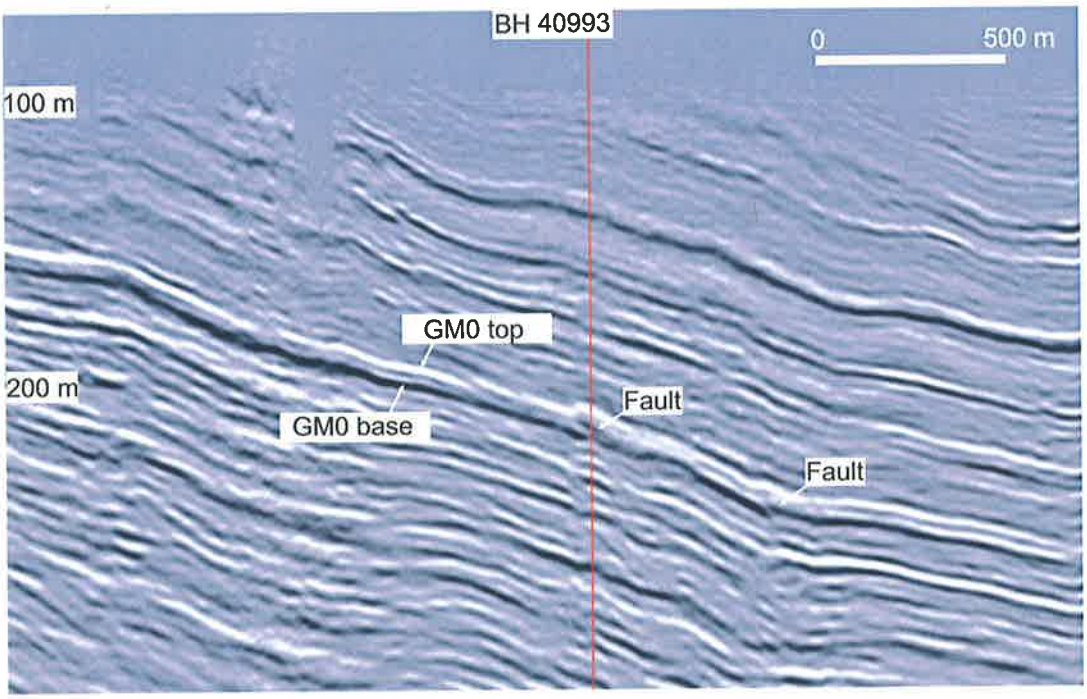

Figure 5.3. Cross-line through borehole 40993. The bedding dips 2°– 10° eastwards. The thrust faults as shown dip approximately 30° east and have maximum throws in the order of 5 m. Borehole 40993 intersects the base of the Goonyella Middle Seam 8 m above the thrust fault shown here.

5.2.3 Limitations

There are numerous reservoir-scale features that are sub-seismic despite the high frequency of the seismic data. The small normal faults, coal cleats and joint sets have little or no offset and cannot be detected by conventional seismic methods. In addition, faults with more significant throw but of limited lateral extent, or those that do not offset the coal seam, may not be detected (Velseis, 2002).

Several methods have been developed by the petroleum industry and have been applied to the coal seam methane industry to detect and characterise otherwise sub-seismic scale features. Amplitude versus offset (AVO) (Lawrence, 1998; Ramos and Davis, 1997) and amplitude versus azimuth (AVAZ) (Perez et al., 1999) techniques have been developed to detect variations in signal amplitude with source-receiver offset and source-receiver azimuth respectively. Zones of intense fracture density impart a low-amplitude signature to ray paths with large offsets and azimuths perpendicular to fracture strike. The signature imparted by zones of increased fracturing is small and is very sensitive to the quality of the seismic survey. The north–south-striking zones of amplitude variation would most likely overprint any small AVO or AVAZ response that may arise from zones of elevated fracturing (Djamaludin pers. comm., Santos 2002). Consequently, the application of AVO and AVAZ methods has not been considered further.

5.3 Image and Wireline Log Interpretation

Boreholes are regularly used in both open cut and underground coal mining to delineate the depth, thickness and quality of the coal seams and predict likely mining conditions. Core samples of the coal seams are routinely taken; however, the floor or roof rocks are not generally cored. The coal samples are usually sent for laboratory testing leaving little or no coal sample from most wells. Slimline acoustic scanner (SAS) image logs were acquired in 18 of the wells in the underground area by Reeves Wireline. The SAS logs are used to detect natural fractures and help constrain geotechnical issues that may influence the underground mining process. A suite of other wireline logs were acquired in the wells with SAS logs, namely sonic, density and gamma-ray logs.

5.3.1 Mechanical stratigraphy from wireline logs

The concept and importance of mechanical stratigraphy is discussed in Chapter 4. Rocks with different mechanical properties behave differently and develop different suites of structures. The gamma, sonic and density logs were used to infer the mechanical stratigraphy by identifying coal seams, amalgamated distributary channel sandstones and overbank units in the wells with SAS image logs.

Some stratigraphic picks provided by BMA were used to help identify and correlate some of the coal seams and major sandstone bodies. The three different mechanical stratigraphic units have distinctive signatures on the wireline logs as listed below (Fig. 5.4).

- **Coal seams**: The coal seams are readily identified by characteristically low sonic, gamma and density responses.
- **Amalgamated distributary channel unit**: A gamma log value of 90 API units was used as a sandstone cut-off (Esterle, 2002, pers. comm). An interval of five or more consecutive metres with gamma values below 90 API units is classified as an amalgamated distributary channel unit. Five metres was selected as an arbitrary cut off between amalgamated and isolated distributary channels based on published data of distributary channel geometry (Payenberg and Lang, 2003; Reading, 1996).
- **Overbank unit**: Intervals not classified as either a coal seam or amalgamated distributary channel unit have been grouped as overbank units. The individual crevasse splays and distributary channels <5 m thick are grouped as part of the overbank unit due to the impracticality of gaining meaningful fracture statistics over such short intervals.

It is emphasised that an interval classified according to the three types of mechanical units may act as numerous individual mechanical units within that interval. Figure 5.4 shows a wireline log suite from a section of borehole 40996 with acoustic scanner data. Coal seams over 1 m thick are shaded purple, amalgamated channels are shaded red and overbank units are shaded green. Within the logged interval there is a coal-prone interval below and including the Goonyella Middle Seam (GM0) and a sandstone-prone interval above and including the sandstone body labelled MP41. The following sections of this thesis demonstrate that overbank units in the sand-prone interval have a different structural style to overbank units in the coal-prone interval.

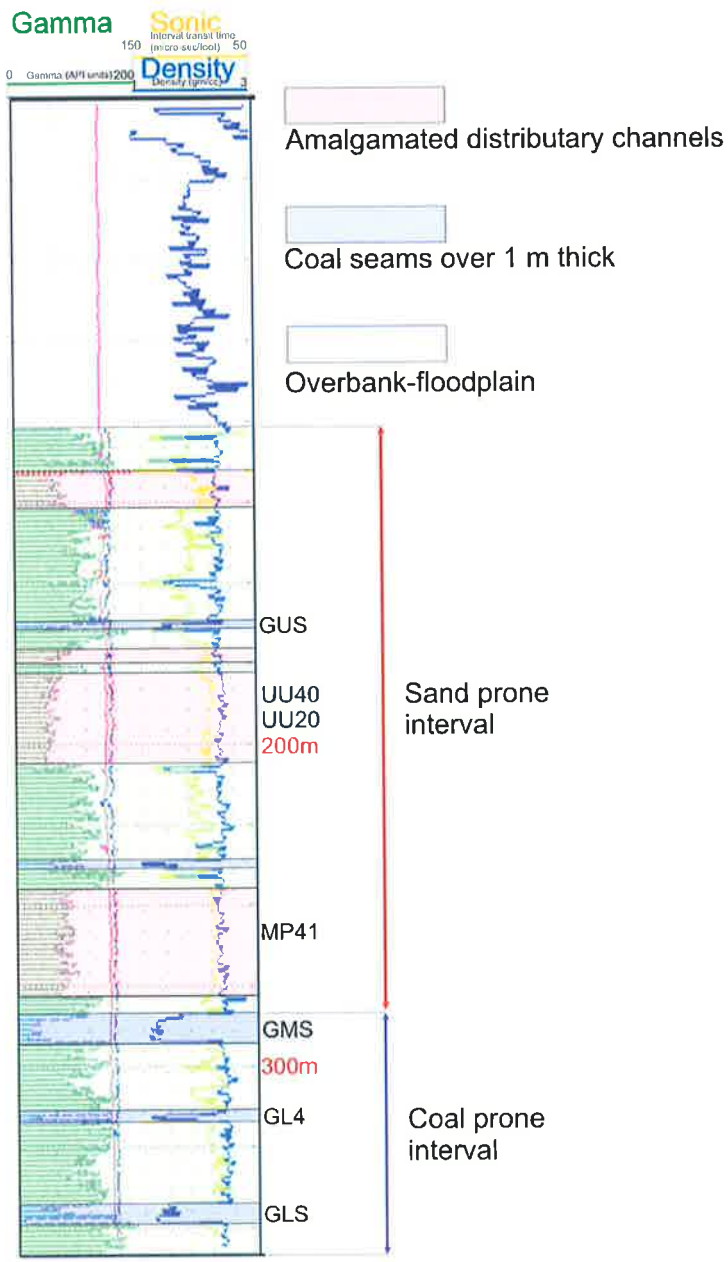

Figure 5.4. Mechanical stratigraphy identified on the wireline log suite from borehole 40996. The gamma ray log is in green from the left. The sonic and density logs are in yellow and blue respectively from the right hand side. A sandstone cut off of 90 API units has been adopted. Amalgamated distributary channel units are identified by >5 m less than 90 API units and are shaded red. Coal seams are readily identified by a low density and sonic response and are shaded purple. The remaining intervals not identified as amalgamated distributary channels or coal seams are grouped as overbank units and are shaded green in the log shown. The interval names on the right hand side of the log are those used by BMA.

5.3.2 Image log interpretation

Slim acoustic scanner logs (SAS) were acquired by Reeves Wireline in 18 wells over the underground area to help predict potential mining conditions. The SAS logs provide an oriented image of the borehole wall and detect fracture location and orientation. The intervals with SAS logs are listed in Table 5.1. The SAS tool measures both the arrival time and the peak amplitude of the reflected acoustic signal from the borehole wall (Rider, 2000). Travel time varies around a

non-circular hole. Enlarged zones caused by caving, borehole breakout etc. are characterised by a longer travel time. The travel time is used with the borehole fluid velocity to compute a 360° calliper image. The 360° calliper is plotted in grey-scale throughout this work.

The amplitude of the reflected wave is a function of the borehole wall properties. Where the wellbore wall is rugose, such as in coals, the reflection is low-amplitude compared to cemented sandstone which is typically characterised by high-amplitude reflections. Throughout this work the acoustic image is displayed using a standard palette of earth tones ranging from yellow (high amplitude) through brown to black (low amplitude).

Various features can be detected by the SAS logs including structural and sedimentary features, borehole breakouts and acquisition and processing artefacts. The intersection of an inclined plane with a vertical, circular borehole defines a sine wave on an unwrapped image (compensated amplitude or transit time). The amplitude of the sine wave defines the dip angle of the plane. The phase of the sine wave with respect to true north defines the dip direction. The SAS data from the 18 wells was interpreted using Reeves' PC Imagepro software.

Borehole	Top SAS interval (m below surface)	Base SAS interval (m below surface)	Total SAS interval (m)
40958	82.6	335.0	252.4
40984	34.9	207.1	172.2
40993	32.8	286.5	253.7
40994	150.0	368.0	218.0
40995	44.3	215.8	171.5
40996	102.9	354.0	251.1
40997	50.3	280.0	229.7
40998	37.2	210.0	172.8
41242	89.8	343.0	253.2
41243	24.1	167.9	143.8
41605	21.0	110.0	89.0
41868	34.2	301.5	267.3
41869	43.3	306.5	263.2
41870	42.4	232.3	189.9
41871	37.9	291.3	253.4
41872	32.3	252.0	219.7
41879	28.2	340.5	312.3
41884	173.0	321.8	148.8
		Total	**3862.0**

Table 5.1. Slim acoustic scanner logs (SAS) were acquired in 18 wells within the underground area (Fig. 5.1). The SAS logs were acquired in the intervals immediately above and below the Goonyella Middle Seam. A total of 3862 m of image log was recorded in the 18 wells.

5.3.3 Natural fractures

Natural fractures appear as either complete or partial sinusoids on an unwrapped image log. Fractures that appear as distinct, complete or partial sinusoids are termed high-confidence picks. Other fractures that are not readily picked have more error associated with the interpretation and are termed low-confidence picks. The confidence of the picks is a function of the image quality, which in turn is a function of the impedance contrast between fractures and the other material, fracture aperture and signal to noise ratios. It is considered that apart from coal cleats, all other structural features described in Chapter 4 are resolvable on the SAS logs (Bocking pers. comm., Bocking and Associates 2003). Examples of high-confidence picks of natural fractures in the different mechanical units are shown in Figures 5.5–5.7 (relative to true north). Most natural fractures appear as low-amplitude events (brown sinusoids) on the amplitude images. The response on the transit time image is variable; some fractures appear as longer transit time (white sinusoids) events and others are not detected. The remainder of this chapter discusses only high-confidence fractures.

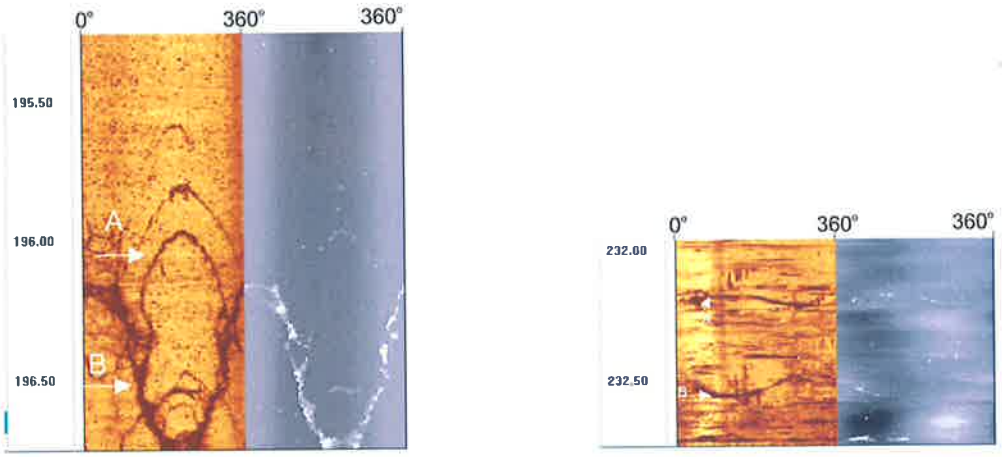

Figure 5.5. High-confidence high (left) and low (right) angle fractures in the distributary channel unit . The amplitude image is yellow-brown scale and the transit time image is grey scale. The figure on the left is from borehole 41871, A 80°→010°N; B 85°→185°N. The figure on the right is from borehole 41884, A 30°→280°N; B 30°→035°N.

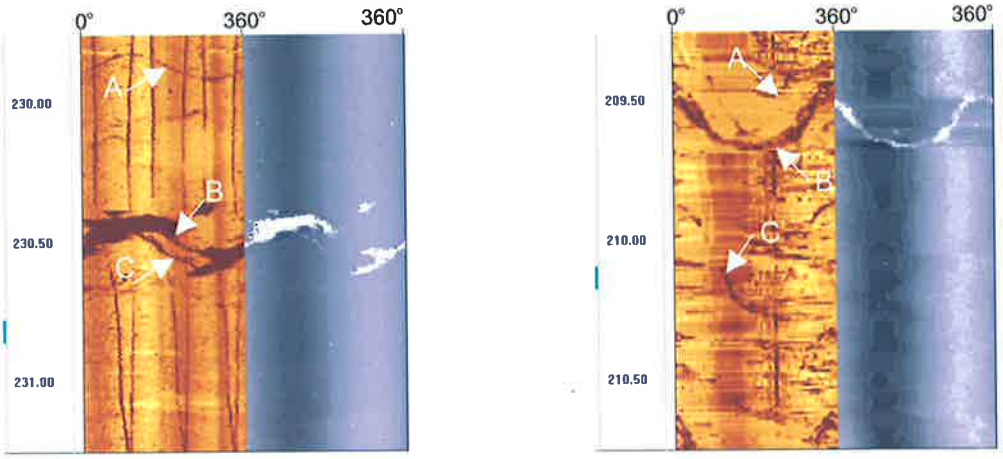

Figure 5.6. High-confidence fractures in the overbank unit. The amplitude image is yellow-brown scale and the transit time image is grey scale. The figure on the left is from borehole 41869 and shows low to moderately dipping fractures; A 39°→296°N; B 51°→280°N and C 50°→266°N. The figure on the right is from borehole 40996 and shows moderately to high dipping fractures; A 79°→179°N; B 63°→178°N and C 78°→189°N.

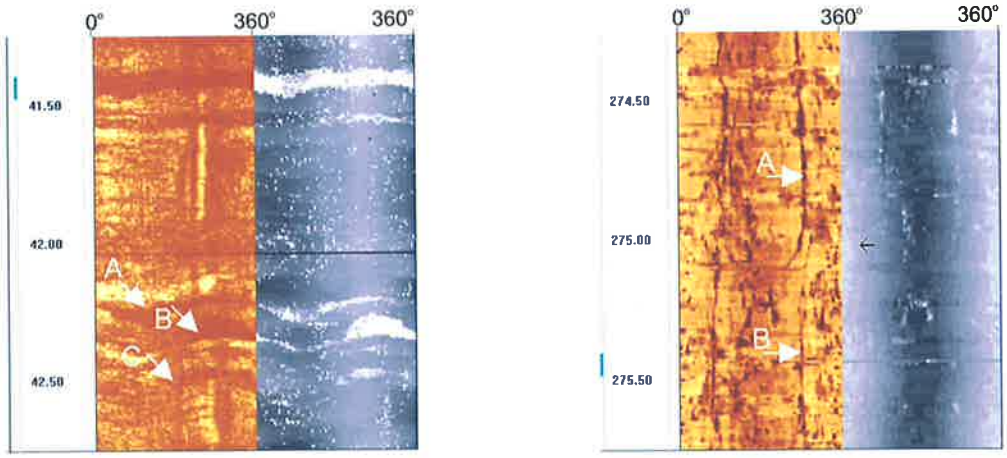

Figure 5.7. Natural fractures in coal seams, amplitude images (yellow-brown scale) are shown with transit time images (grey scale). The figure on the left is from borehole 41868 and shows low-angle fracturing in one of the Goonyella upper seams: A 29°→108°N; B 31°→095°N and C 35°→104°N. The figure on the right is from borehole 41242 and shows high-angle fractures in the Goonyella Middle Seam: A 89°→010°N and B 89°→189°N.

5.3.4 Open versus closed fractures

The ability of SAS logs to determine fracture aperture is ambiguous. Open and closed fractures may appear similar on an SAS image unlike resistivity images that can estimate fracture aperture based on relative resistivity/conductivity contrasts (Schlumberger, 1991). Some interpreters of SAS data consider that open and hydraulically conductive fractures are visible on both the amplitude and transit time images and that closed fractures are only visible on the amplitude image (Green, 2003 (pers comm)). Others argue that only fractures with considerable aperture

(in the order of mm) are distinguishable from closed fractures (Elkington, 2003, pers comm). No attempt has been made here to distinguish fracture aperture based solely on their image log appearance.

5.3.5 Artefacts

Acquisition and processing artefacts can cause ambiguity in the interpretation process (Fig. 5.8). Acquisition artefacts such as bit markings and off-centred SAS tool and processing errors impede interpretation over some sections of the logged intervals. Fractures are often picked with low confidence in intervals with significant artefacts. Severe artefacts will cause an apparent low density of high-confidence fractures.

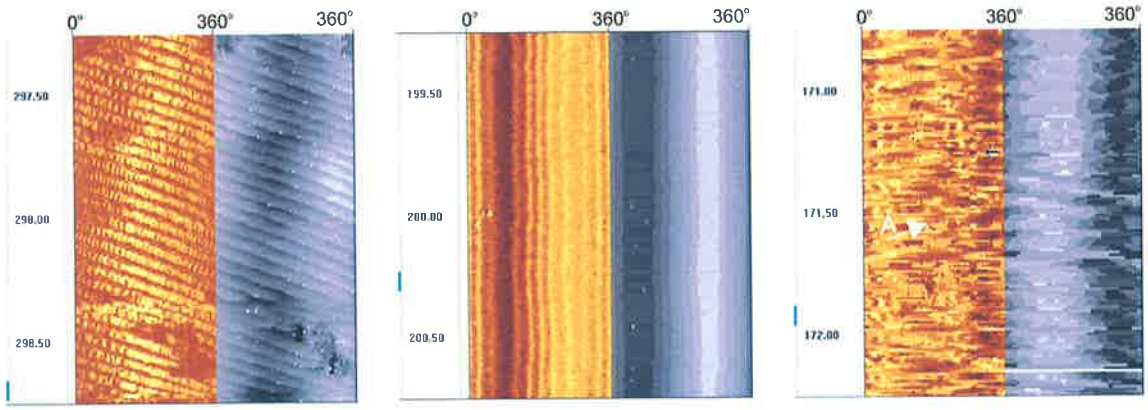

Figure 5.8. Acquisition and processing artefacts amplitude images (yellow-brown scale) are shown with transit time images (grey scale). The figure to the left from borehole 41869 is an example of bit markings formed during the drilling process that can mask structures intersected by the borehole. The figure in the centre from borehole 40993 is an example of an off-centred SAS. Off-centred tools can impede interpretation. The figure to the right from borehole 40984 is probably a processing artefact. Processing artefacts such as these are quite common and can impede image interpretation. The arrow marked A points to a fracture that is almost entirely masked by the processing artefact.

5.4 Fracture Classification and Interpretation

A total of 1723 high confidence fractures were interpreted on the SAS image logs from the 18 wells. Figure 5.9 presents stereo and rose plots of all high-confidence fractures. There are some fractures in almost every orientation but the rose plot shows two dominant fracture orientations. There is a dominant east–west-striking trend and a north–south-striking trend.

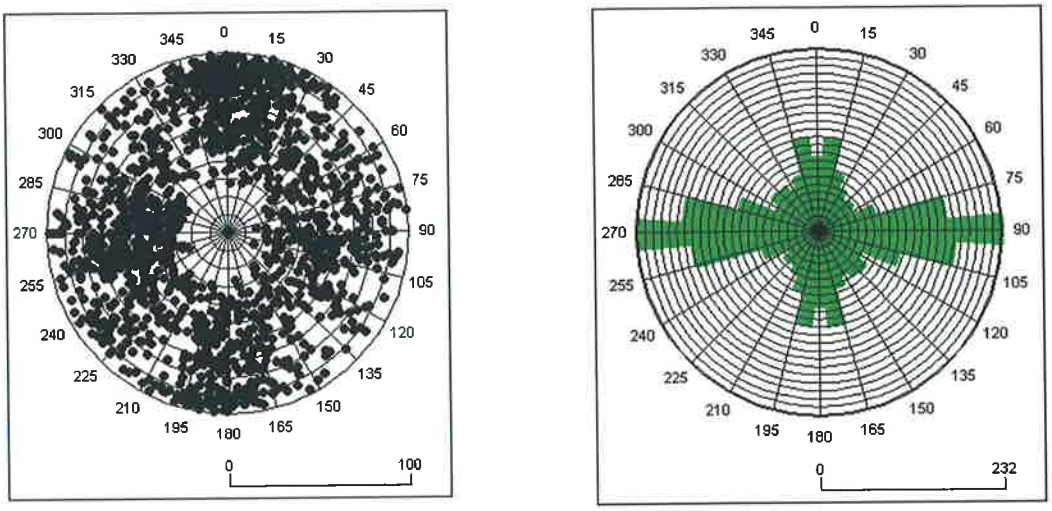

Figure 5.9. Stereo and rose plot of all high-confidence fractures, a total of 1723. Fractures appear in almost every orientation yet the rose plot shows that the fracture population is distinctly bimodal. There is a dominant north–south-striking trend and an east–west-striking trend.

In outcrop samples, a fracture may be interpreted as either tensile, shear or mixed mode based on surface ornamentation such as plume structures and slickenlines or by other relationships such as infilling or offset. Such indicators are not identifiable on the image logs acquired at Goonyella Riverside so the fractures must be classified in another fashion. Observations made during the mine mapping, discussed in Chapter 4, may be used to help classify the fracture sets according to their dip angle. Fracture orientations were not restored for regional dip, as the regional dip is very low (generally <6°):

- Low-angle fractures (<45°) generally appear to be subsidiary structures associated with larger thrust faults.
- The moderate-dipping fractures (45°-70°) are typically small normal faults.
- The high-angle fractures (70-90°) are considered tensile joints.

This classification is in accordance with basic Andersonian theory (Fig. 5.10) (Anderson, 1951). Low-angle fractures that dip less than 45° are most likely shear fractures (small faults) formed in a reverse-stress regime. High-angle fractures that dip more than 70° are most likely tensile fractures (joints) formed in either normal or strike-slip stress regimes. Alternatively, they may have developed as shear fractures in a strike-slip stress regime. Moderate-dipping fractures that dip 45°– 70° may be either shear fractures formed in a normal stress regime, anomalously high-angle shear fractures formed in a reverse regime or anomalously low-angle tensile fractures.

It should be noted that this simplistic classification considers only pure tensile and shear failure, and does not consider mixed mode failure (Price and Cosgrove, 1990). Mixed mode fractures

may develop in either normal, reverse- or strike-slip stress regimes. A mixed mode origin may explain many of the fractures that do not conform to classic Anderson theory (Anderson, 1951) and may account for many of the moderately dipping fractures.

Figure 5.11 shows combined rose and stereo plots for all fractures separated according to dip angle. The low-angle fractures have a dominant strike of north-south ± 15°, the high-angle fractures have a dominant strike of east-west ± 5°. The moderately dipping fractures have two dominant strike directions, north-south ± 15° and east-west ± 15°. Logs of natural fracture density classified according to fracture dip angle and mechanical stratigraphy are presented in Appendix A.

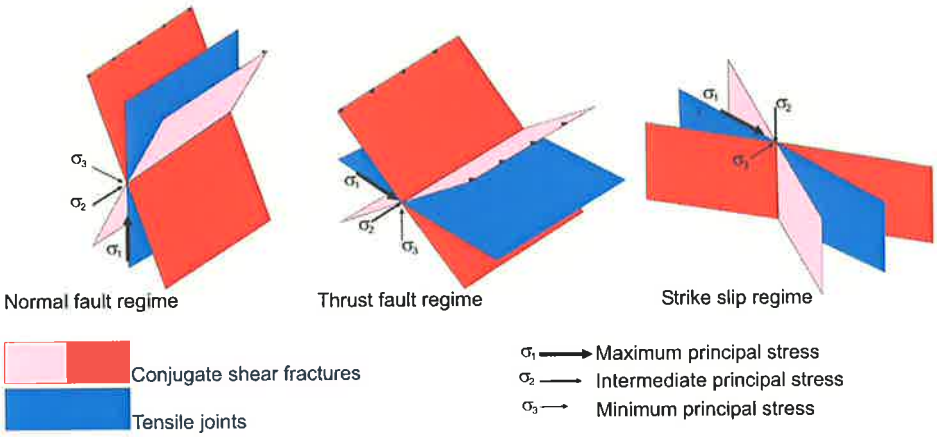

Figure 5.10. Classification of fractures in accordance with basic Anderson theory (Anderson, 1951). The figure demonstrates the expected orientation of shear and tensile fractures in normal, reverse- and strike-slip stress regimes. High-angle fractures (>70°) are most likely 1) tensile fractures formed in either a normal or strike-slip stress regime or 2) shear fractures formed in a strike-slip stress regime. Low-angle fractures (<45°) are most likely shear fractures formed in a reverse-stress regime. Intermediate-dipping fractures (45°-70°) are most likely shear fractures formed in normal stress regime; they may also be anomalously high-angle shear fractures formed in a reverse-stress regime or anomalously low-angle tensile fractures (Price and Cosgrove, 1990).

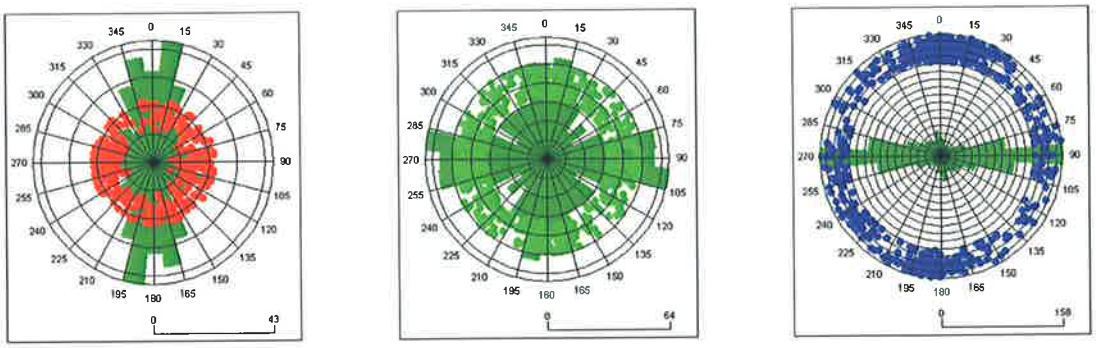

Figure 5.11. The plot on the left is of all 379 high-confidence, low-angle fractures. The low-angle fractures have a dominant strike of north-south. The plot in the centre is of all 672 high-confidence moderately dipping fractures. The moderately dipping fractures have dominant strike directions of north-south and east-west. The plot on the right is of all 673 high-confidence high-angle fractures. The high-angle fractures have a dominant strike direction of east-west.

The orientations of the low- and high-angle fractures presented in Figure 5.11 are consistent with the outcrop observations made in Chapter 4. The low-angle fractures are interpreted as low-angle shear fractures that developed as subsidiary structures to the larger thrust faults. The high-angle fractures are here on interpreted as high-angle tensile fractures/joints that developed either during uplift or in zones of dilation about thrust faults or in association with the dykes.

The orientation of the moderate-angle fractures is bimodal and their origin is less certain. The north–south-striking, moderate-angle fractures may be anomalously high-angle versions of the north–south-striking low-angle set. The east–west-striking, moderate-angle fractures may be anomalously low-angle versions of the east–west-striking high-angle set or they may be small normal faults as described in Chapter 4.

5.4.1 Faults and damage zones

Several thrust faults are intersected by wells with image logs. As observed in the outcrop examples, the different mechanical units demonstrate varying responses to faulting. Examples of faults intersecting overbank units and coal are shown in Figures 5.12 and 5.13 respectively.

- **Faults in overbank units**: The largest fault in the underground area is intersected by boreholes 40993 and 41868. The fault is an east-dipping thrust fault with maximum throw in the order of 5 m and is resolvable in the seismic volume (Fig. 5.3). Borehole 40993 intersects the fault 7 m below the Goonyella Middle Seam (GM0) (Fig. 5.3) and borehole 41868 intersects the fault 20 m above GM0. In both wells the fault occurs in the overbank unit and has a 0.5–1 m thick core comprising a series of closely spaced, subsidiary low-angle fractures. This supports the interpretation of low-angle fractures as reverse sense shear fractures. Low-angle fractures also occur in the overbank unit within the damage zone but they do not occur in the coal. It is considered significant that low-angle fractures do not occur within the coal seam in either borehole 40993 or 41868; yet in each well low-angle fractures occur in the intervals immediately above and below the coal seam.
- **Faults in coal**: Borehole 41868 intersects a low-angle fault and one of the Goonyella Upper seams at 44 m depth. The fault is almost parallel to bedding and has overprinted the coal fabric in a zone about the fault (Fig. 5.13). The throw of the fault is uncertain as it is above the top of the seismic volume.

These two examples and outcrop observations demonstrate that low-angle fracturing and overprinting in the coal seams is generally restricted to the fault core and there is no defined damage zone. The overbank and distributary channel units display different behaviour. Low-angle fractures may occur as both discrete concentrations in the fault cores and within damage zones as disseminated fractures scattered throughout the rock volume (Figs 5.12, 5.13).

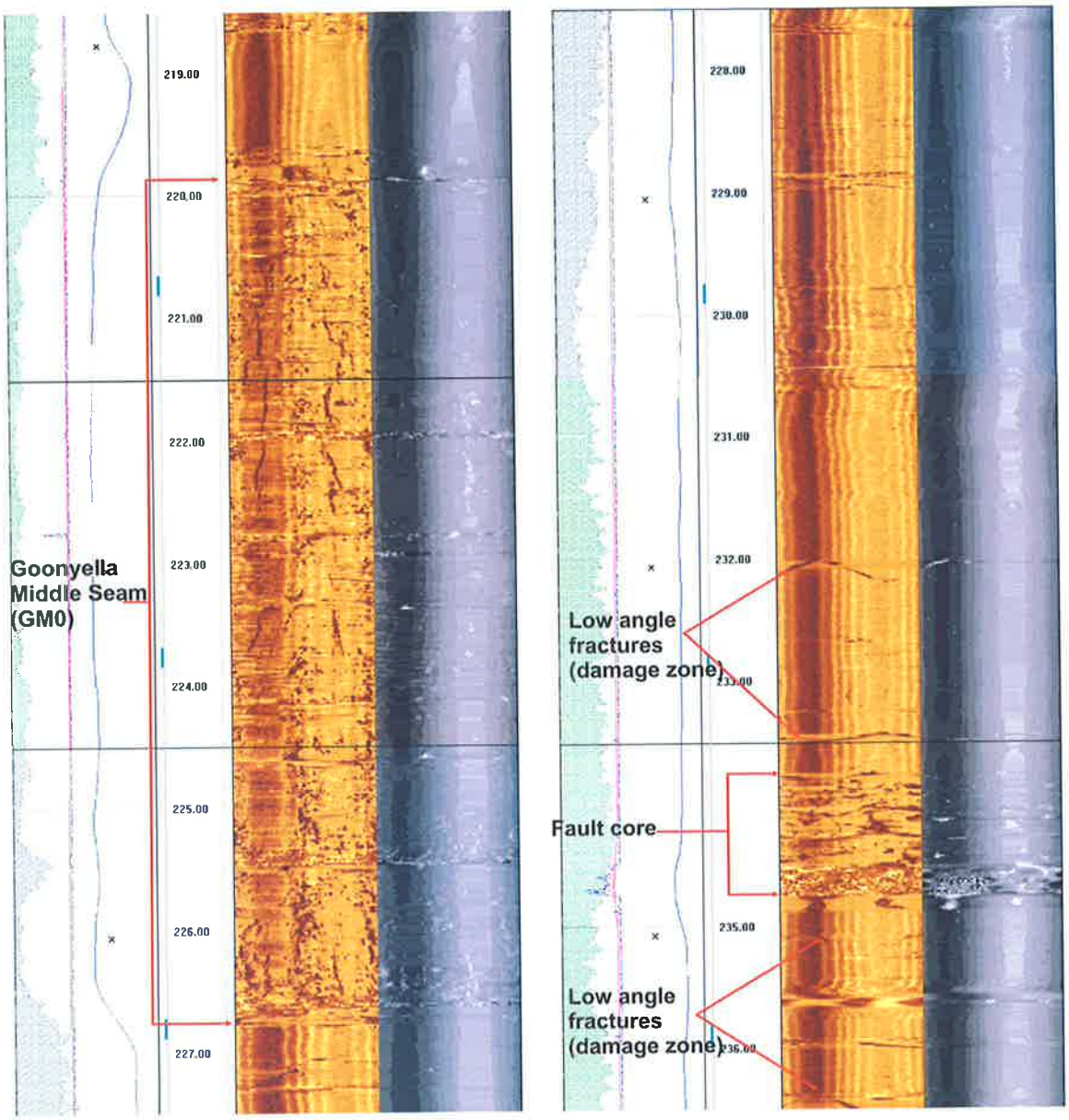

Figure 5.12. Borehole 40993 intersects the Goonyella Middle Seam (GM0) 7 m above a seismically resolvable fault. The fault is an east-dipping thrust fault with maximum throw in the order of 5 m and is resolvable in cross lines and amplitude maps as shown in Figures 5.2 and 5.3. The fault core is approximately 1m thick comprising a series of subsidiary low-angle fractures. Low-angle fractures also occur within the overbank facies above and below the fault core within the damage zone, however they do not occur in the Goonyella Middle Seam. Borehole 41868 intersects the same fault 20 m above GM0 and demonstrates similar relationships.

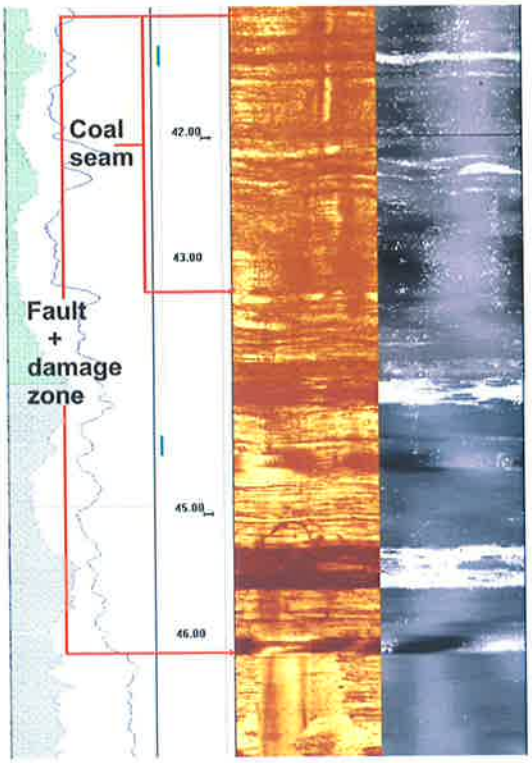

Figure 5.13. A Goonyella Upper Seam is intersected by a thrust fault at approximately 44 m in borehole 41868. The fault is not within the 3D seismic volume. The coal fabric is overprinted within the fault core similar to that in outcrop near the ramp 2 highwall (Fig. 4.9). The low-angle features are either shear fractures or overprinting of the primary coal cleats.

5.4.2 Coal seams

A total of 294 high-confidence fractures were interpreted in the coal seams over a cumulative interval of 343.8 m. Of these, 237 were high-angle, 42 were moderate-angle and only 15 were low-angle fractures. Figure 5.14 shows plots of high-confidence low-, moderate- and high-angle fractures interpreted in the coal seams. Most of the high-angle fractures strike 090° with a relatively small amount of scatter. The population of low-angle fractures is less well defined probably due to the small sample size, but the most common strike directions are 015° and 140°. The majority of the moderate-angle fractures strike 100°; there is also a smaller group that strikes 000°

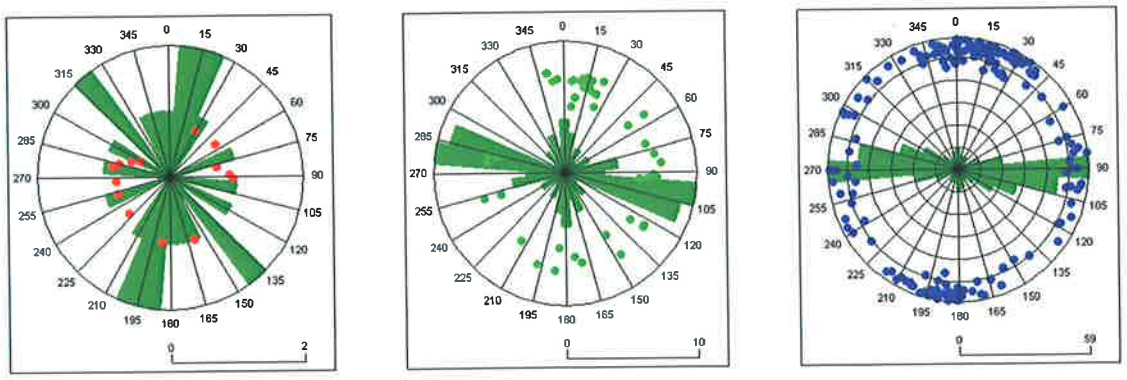

Figure 5.14. Plots of high-confidence low (red), moderate (green) and high-angle (blue) fractures in the coal seams interpreted on the SAS logs. There are 15 low-angle, 42 moderate-angle and 237 high-angle fractures in a cumulative interval of 343.8 m of coal seams.

5.4.3 Amalgamated distributary channel units

A total of 207 high-confidence fractures were interpreted in the amalgamated distributary channel units over a cumulative interval of 1086.2 m. Of these, 94 were high-angle, 76 were moderate-angle and 37 were low-angle fractures. Figure 5.15 shows plots of high-confidence low-, moderate- and high-angle fractures interpreted in the amalgamated distributary channel units. Most of the high-angle fractures strike 090° with a sub-set striking 310° and a relatively small amount of scatter. The low-angle fractures generally strike between 340° and 010°. The majority of the moderate-angle fractures strike 080° and 140° however there is considerable scatter.

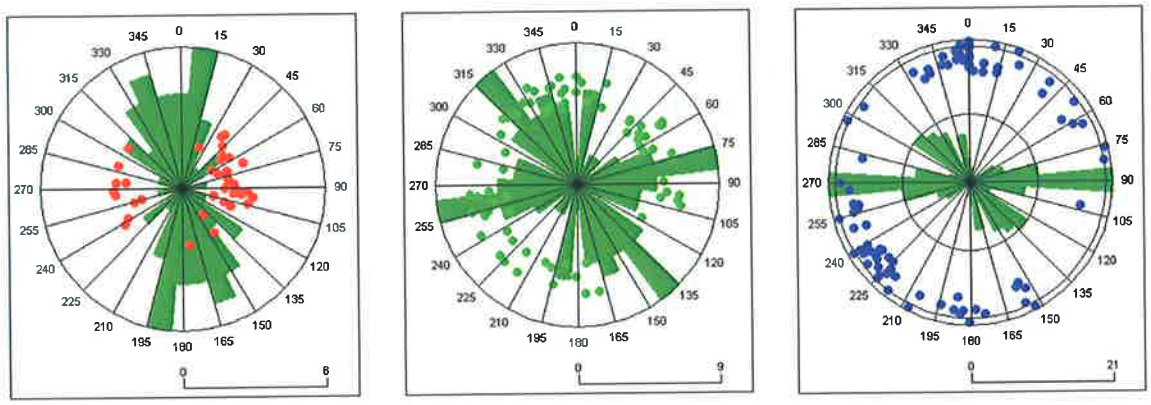

Figure 5.15. Plots of high-confidence low (red), moderate (green) and high (blue) angle fractures in the amalgamated distributary channel units interpreted on the SAS logs. There are 37 low-angle, 76 moderate-angle and 94 high-angle fractures in a cumulative interval of 1086.2m.

5.4.4 Overbank units

A total of 1223 high-confidence fractures were interpreted in the overbank units over a cumulative interval of 2424.8 m. Of these, 342 were high-angle fractures, 554 were moderate-angle fractures and 327 were low-angle fractures. Figure 5.16 shows plots of high-confidence low-, moderate- and high-angle fractures interpreted in the overbank units. Most of the high-angle fractures strike 090°. The low-angle fractures generally strike between 350° and 010°. The majority of moderate-angle fractures strike between 350°–020° and 075°–105°.

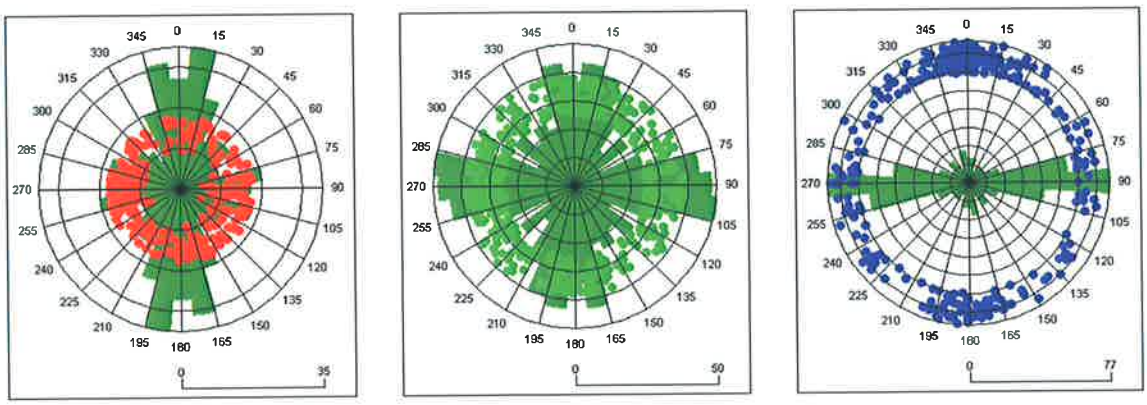

Figure 5.16. Plots of high-confidence low (red), moderate (green) and high (blue) angle fractures in the overbank units interpreted on the SAS logs. There are 327 low-angle, 554 moderate-angle and 342 high-angle fractures in a cumulative interval of 2 424.8 m.

5.5 Fracture Statistics

Two of the most important characteristics of a fracture population with respect to petroleum field development are fracture orientation and density. Many of the wells have too few fractures to provide statistically meaningful populations. To reduce scatter between wells, and provide a more coherent picture, the following section considers the fracture data from the 18 wells as a single population. The orientation and density of fractures is considered with respect to the previously established mechanical stratigraphy of the sequence.

5.5.1 Orientation

The plots of low-, moderate- and high-angle fractures display some very significant trends (Figs 5.14–5.16). Table 5.2 shows the dominant orientation of low-, moderate- and high-angle fractures grouped according to the mechanical units and as a combined total. Figures 5.17 and 5.18 demonstrate the variation in low- and high-angle fracture orientation between the wells. The figures demonstrate the variability in average fracture orientation between wells and how a single well may not accurately represent the fracture population away from the immediate area of the well.

Unit	Low angle (<45°)	Moderate angle (45°-70°)	High angle (>70°)
	Mean strike	Mean strike	Mean strike
Coal	15°	105°; 360°	95°
Overbank	360°	90°; 185°	90°
Channel	350°	145°; 85°	90°; 135°
Combined	360°	90°; 360°	90°

Table 5.2. The mean strike and range of the most significant groups of fractures. Fractures are grouped according to facies into low-, moderate- and high-angle fracture sets. It is important to note that the vast majority of low-angle fractures strike north-south ± 15° and that the vast majority of high-angle fractures strike east-west ± 15°. The moderate-angle population is bimodal, one group strikes north-south and the other strikes east-west.

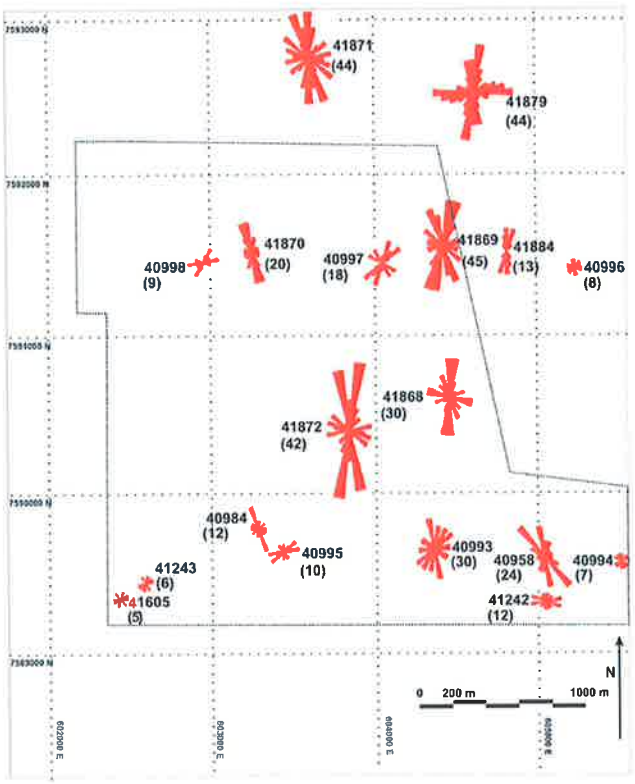

Figure 5.17. Low-angle fracture orientation in the different wells. The orientations presented are for all high-confidence low-angle fractures. The number of high-confidence fractures interpreted at each well is noted in brackets.

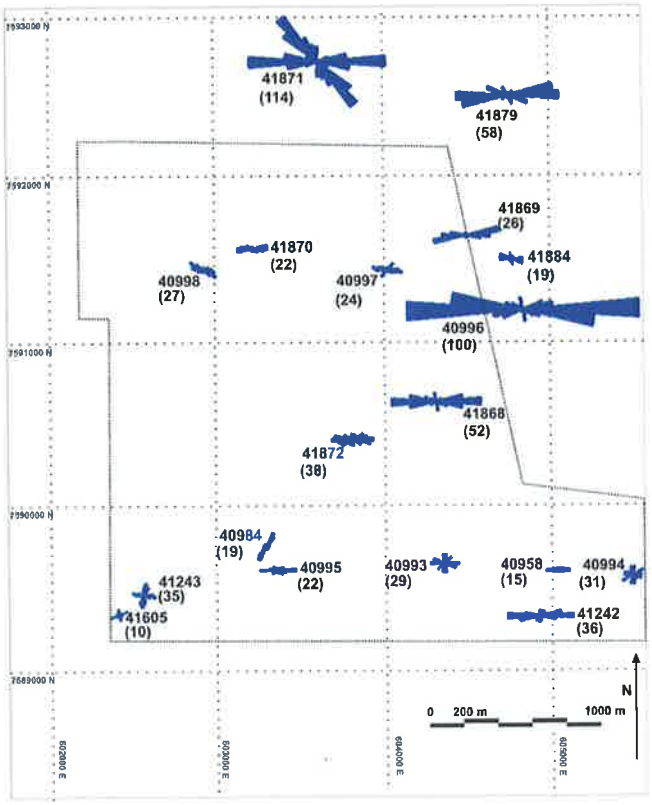

Figure 5.18. High-angle fracture orientation in the different wells. The orientations presented are for all high-confidence high-angle fractures. The number of high-confidence fractures interpreted at each well is noted in brackets.

5.5.2 Density

The density of low-, moderate- and high-angle fractures varies between the different mechanical units and between wells. Fracture densities were weighted to account for the relative angle between the fracture plane and the borehole trajectory by dividing the raw fracture count by $\sin\theta$, where θ = angle between borehole trajectory and dip of fracture plane (Narr, 1991). Table 5.3 lists the weighted and unweighted density of low-, moderate- and high-angle fractures in the different mechanical units. Low-angle fractures are significantly more frequent in the overbank facies than in either the coal or amalgamated channel units; high-angle fractures are most frequent in the coal seams and least frequent in the channel facies. The variation between the mechanical units is demonstrated in Figure 5.19.

Unit	Low angle		Medium angle		High angle	
	Unweighted	Weighted	Unweighted	Weighted	Unweighted	Weighted
Coal	0.04 /m	0.05 /m	0.12 /m	0.23 /m	0.69 /m	3.97 /m
Overbank	0.14 /m	0.16 /m	0.23 /m	0.43 /m	0.14 /m	0.81 /m
Channels	0.03 /m	0.04 /m	0.07 /m	0.13 /m	0.09 /m	0.50 /m
Combined	0.09 /m	0.10 /m	0.17 /m	0.32 /m	0.17 /m	0.98 /m

Table 5.3. Unweighted and weighted fracture densities for low-, moderate- and high-angle fractures in the different units. Low-angle fractures are significantly more frequent in the overbank facies than in either the coal or amalgamated channel units. High-angle fracture density is greatest in the coal and least in the channel facies.

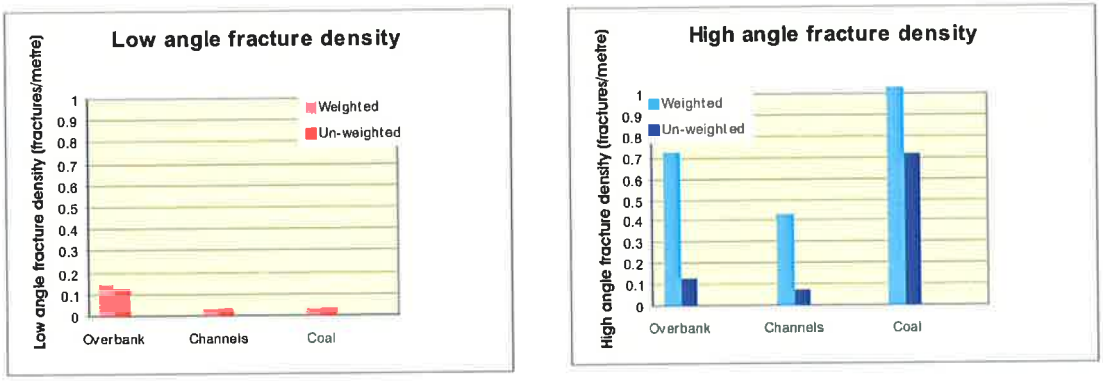

Figure 5.19. Comparison of low and high-angle fracture density in the different facies.

5.5.3 Variability between boreholes

There is always some range in fracture density within any fracture population. Variations may arise due to several reasons: due to sampling errors (Narr, 1991) or they may be real due to spatial variations of either mechanical properties (Becker and Gross, 1996; Narr, 1991; Odling et al., 1999; Underwood et al., 2003; Wu and Pollard, 1995) or applied strain (Cooke et al., 2000; Hennings et al., 2000; Mollema and Aydin, 1997). The fractures must be considered in the context of their origin in order to assess the spatial variation in fracture density.

It has been argued in previous sections that most of the high-angle fractures are uplift-related and the primary controls on their distribution are lithology and thickness of the individual mechanical units. Variation of uplift-related joint density from the image log interpretation can be accounted for by spatial variations in the mechanical units sampled by the image logs. Thick distributary channel units with well developed but widely spaced joints have low fracture density and may appear even lower due to sampling errors due to the low angle between joints and the boreholes (Narr, 1991). Overbank units with numerous thin sandstone bodies may have well

developed, more closely spaced joints within the sandstone bodies and have high joint density. Overbank units with high shale and siltstone and low sandstone contents typically have limited joint development and low density.

It has been argued in previous sections that the majority of low-angle fractures are related to larger thrust faults. Low-angle fractures have been shown in both outcrop and image log data to cluster around larger thrust faults (Figs 5.12, 5.13). The density of low-angle fractures is thus a function of the proximity to the larger thrust faults. Figure 5.20 is a contour map of low-angle fracture density from the image log data. The values are unweighted and are a combined total for the different units in the mechanical stratigraphy. The faults shown are at the level of the GM0 base near the bottom of the logged interval. The figure shows that the density of low-angle fractures increases with proximity to the seismically resolvable thrust faults. Low-angle fracture density is relatively consistent in the direction parallel to thrust fault strike and more variable perpendicular to thrust fault strike. Such a result might have been anticipated but its verification has major implications for reservoir exploitation in similar thrust faulted sequences. The low-angle fractures associated with the thrust faults may impart significant permeability anisotropy and influence reservoir behaviour.

Wells with SAS logs in the underground area are spaced significantly closer than typical petroleum wells and demonstrate how effectively/ineffectively a single borehole may represent both the orientation and density of a fracture population. Figures 5.17 and 5.18 describe the variation in orientation of high- and low-angle fractures. The histograms presented in Figures 5.21–5.22 provide a graphical description of fracture density variation between wells in the different mechanical units, as summarised below.

- The density of low-angle fractures in the coal and distributary channel units is ~ zero with a few high-density intervals within boreholes 41868 and 41884/41869 in discrete zones around fault cores.
- The low-angle fracture densities in the overbank unit cluster around 0.1/m, implying that the overbank units are more prone to develop low-angle fractures than either the coal or distributary channel units. The wells with higher low-angle fracture densities are close to seismically resolvable faults.
- The high-angle fracture density is anomalously high in borehole 41871, in both the overbank and distributary channel units. The well falls outside the 3D seismic survey and the structure near well 41871 is uncertain. The increased density may be due to a zone of dilation as described in Chapter 4 or it may be close to a dyke.

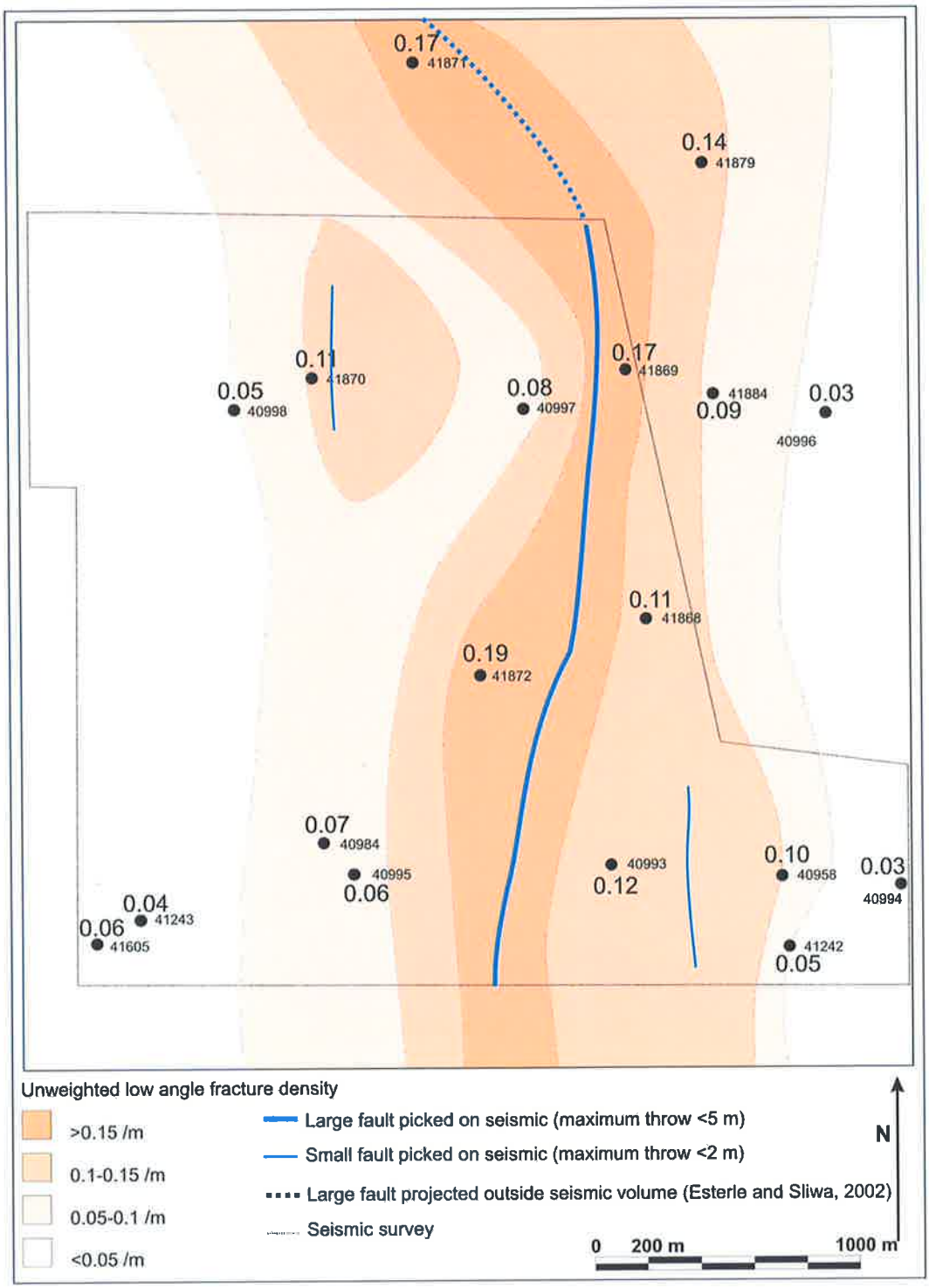

Figure 5.20. Contour map of unweighted low-angle fracture density with seismically resolvable faults projected to near the middle of the logged interval.

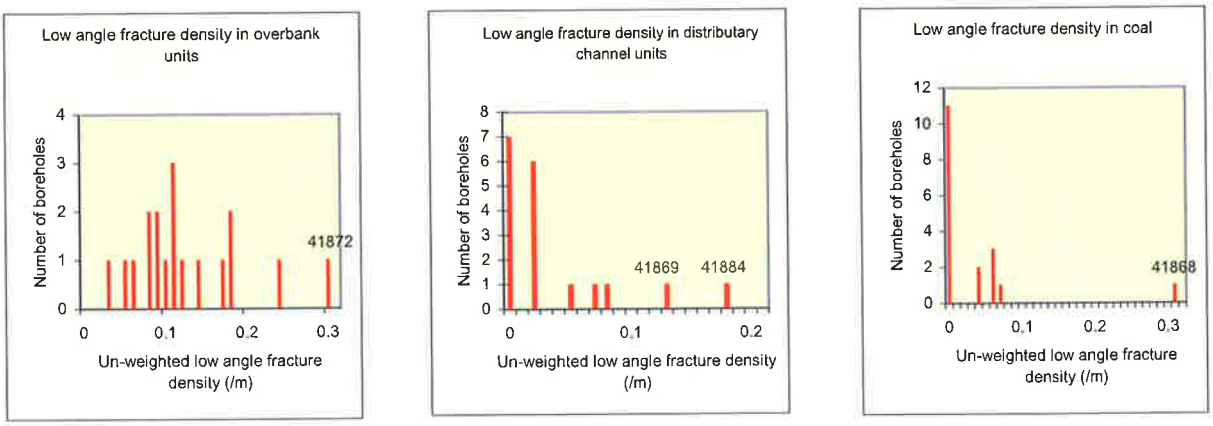

Figure 5.21. Histograms of unweighted low-angle fracture density in the different units. Boreholes with anomalously high fracture counts are close to seismically resolvable faults.

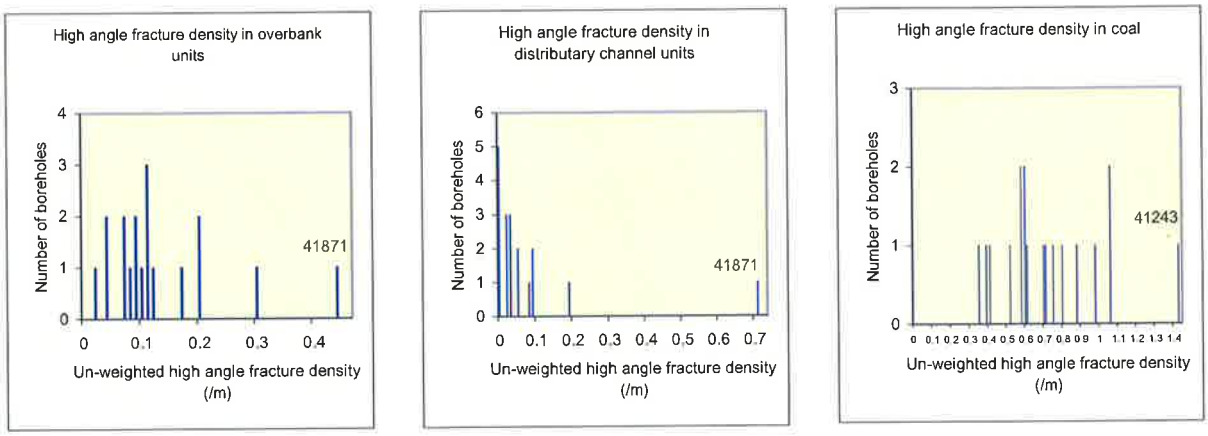

Figure 5.22. Histograms of unweighted high-angle fracture density in the different units.

5.5.4 Variations in overbank unit

Low-angle fracture density at Goonyella Riverside is also a function of the mechanical stratigraphy. The effect of the mechanical stratigraphy may be analysed by comparing low-angle fracture density within overbank units in the sand-prone and coal-prone intervals (Table 5.4). The low-angle fracture density in overbank units within the sand-prone interval (0.16/m) is approximately that in overbank units within the coal-prone interval (0.08/m). The difference between the two intervals can be explained in terms of mechanical stratigraphy, bedding plane slip and strain partitioning. The overbank units are the least competent units within the sand-prone interval and applied strain (during the Hunter Bowen Orogeny) is accommodated within the sand-prone interval via thrust faulting and associated fracturing in the overbank units. In comparison, the overbank units are the most competent within the coal-prone interval and a significant portion of applied strain is accommodated via bedding plane slip and plastic

deformation of the coal. Low-angle fractures are thus less dense in the overbank units within the coal-prone interval than overbank units within the sand-prone interval.

Interval	Cumulative thickness	Sum	Density
Sandstone-prone	1638.6 m	267	0.163/m
Coal-prone	786.2 m	61	0.078/m

Table 5.4. Density of thrust-related low-angle fractures (<45°) in the overbank units within the coal-prone and sand-prone intervals.

5.6 Synopsis

5.6.1 Observations

It has been demonstrated that mechanical stratigraphy and the tectonic history of the basin are the primary controls on fracture development at Goonyella Riverside. Several important observations have been made regarding the orientation and distribution of the fracture sets that may be applied to analogous hydrocarbon systems.

A cumulative total of 1723 high-confidence fractures were interpreted in 3862 m of image log data from 18 wells. The fracture orientations present a bimodal north-south and east-west striking distribution. Initial outcrop observations (Chapter 4) indicated that the majority of low-angle fractures have a different origin to the high-angle fractures and must therefore be considered as different sets. Accordingly, the 1723 fractures are grouped into low-, moderate- and high-angle fractures. The low-angle fractures generally strike north-south ± 15° and the high-angle fractures generally strike east-west ± 15°. The orientation of the moderate-angle fractures is bimodal, some striking north-south and others striking east-west.

The orientations of the high-, low- and moderate-angle fractures is consistent with observations made in the mine workings. The majority of low-angle fractures are associated with larger thrust faults. The majority of high-angle fractures are uplift-related tensile joints.

The spacing of the high-angle, uplift-related fractures is controlled by the mechanical stratigraphy. High-angle fracture spacing is proportional to thickness of the individual mechanical units. They are most closely spaced in the coal (not cleats) and most widely spaced in the distributary channel units.

The spacing of the low-angle thrust-related fractures is controlled by both the mechanical stratigraphy and the proximity to larger thrust faults. Figure 5.20 demonstrates the relationship

between low-angle fracture density and proximity to seismically resolvable thrust faults. Low-angle fracture density within the damage zone increases with proximity to the seismically resolvable thrust faults and is relatively consistent in the direction parallel to fault strike.

Low-angle fractures are denser within the overbank units (0.14/ m) than either the coal (0.04/ m) or distributary channel units (0.03/ m). Within the overbank units, they are most dense in the sandstone-prone interval (0.17/ m) and least dense in the coal-prone interval (0.08/ m). These variations can be explained by the variations in rheological properties between the different units and their interaction with each other. The top and base of the coal seams are effective zones of mechanical decoupling, along which slip can readily occur. Much of the strain applied during the thrusting event was focused at the coal-rock contacts and accommodated by bedding plane slip. Low-angle fractures (subsidiary structures to the thrust faults) did not frequently develop in the coal seams or in the coal-prone interval because bedding plane slip accommodated most of the thrust-induced strain. Mechanical decoupling could not occur as readily in the sandstone-prone interval because there are fewer extensive detachment surfaces, resulting in more strain distributed throughout the sandstone-prone interval. Low-angle fractures developed throughout the sandstone-prone interval in response to the elevated strain. Within the sandstone-prone interval, low-angle fractures preferentially developed in the overbank units because they are less resistant to fracturing than the more competent distributary channel units.

5.6.2 Implications for hydrocarbon development

The image log data used in this study comes from wells significantly more closely spaced than typical petroleum wells and demonstrate how ineffectively a single well with image log data may represent a fracture network away from the immediate well area. However, fracture networks can be accurately described from image log data if they are considered in the context of mechanical stratigraphy and local tectonic history.

Fracture systems at the surface may not reflect fracture systems at reservoir depth. Uplift-related joints are often the most prevalent features in outcrop yet they are unlikely to occur deeper than a few hundred metres and are probably absent from most hydrocarbon systems in on-shore Australia as demonstrated by the Scotia study (Chapter 2). Conversely, tectonically-induced fractures that occur at reservoir depths will not exist at outcrop levels if the fractures are older than the outcropping rocks, again demonstrated by the Scotia study. When modelling a fracture system it is critical to identify which groups of fractures may occur at reservoir level. Of the fractures identified at Goonyella Riverside, coal cleats, thrust faults and associated damage zones and normal faults are expected to occur at typical reservoir depths in similar settings.

Coal cleat development influences both reservoir permeability and well completions/stimulations and is a primary control on the economic viability of coal seam methane projects (Gray, 1987;

Johnson et al., 2002; Zuber and Boyer, 2002). Coal type appears to be the most significant influence on cleat development. Vitrinite-rich layers typically have more closely spaced cleats providing increased coal permeability and may improve the success of cavitation completions. However, it is difficult to model discrete coal cleats from image log data because diagenetic coal cleats are below image log resolution. An alternative method for coal cleat modelling may be the prediction of coal type using sequence stratigraphic approaches to predict vitrinite-rich intervals (Bocking, 2003, pers comm). The work presented in this chapter shows that cleat orientation may be predicted pre-drill by the orientation of seismically resolvable structures if they formed under the same stress orientations. In accordance with basic Andersonian theory, cleats should generally strike perpendicular to thrust faults and parallel to normal faults if the structures formed under the same stress orientations. It is therefore imperative to understand the structural relationships and timing between burial, diagenesis (cleat formation) and emplacement of seismically resolvable structures. In the instance of Goonyella Riverside, east-west cleats and seismically resolvable north–south-striking thrust faults formed during an extended period of east-west S_{Hmax} immediately prior to and during the Hunter Bowen Orogeny.

Fault-related fractures similar to those at Goonyella Riverside may provide high permeability sweet spots within otherwise tight reservoirs provided the fractures are un-mineralised and hydraulically conductive within the in-situ stress field. In fact, the thrust fault and damage zone intersected by borehole 40993 has accounted for almost half the ground water entering the underground exploration adit at Goonyella Riverside ~3 m high, 5 m wide and 2500 m long (Callow and Briese, 2002). Similar faults may have comparable effects that could go undetected with typical petroleum-standard seismic data in the absence of core or image logs, and well test data should be carefully analysed to detect any evidence for natural fracture contribution. Complex flow patterns may occur due to low permeability in the fault core and higher permeability in the damage zone (Caine et al., 1996; Knipe et al., 1998; Laubach, 2003a). Permeability may be enhanced in the direction parallel to the fault due to fracturing in the damage zone but may be significantly reduced in the direction perpendicular to the fault due to porosity reduction in the fault core (Fig. 5.23). Faults with a well-developed core and small damage zone may act as flow baffles or barriers, whereas faults with small cores and well-developed damage zones may act as more effective conduits (Caine et al., 1996; Knipe et al., 1998; Laubach, 2003a). The observations made in this chapter show that faults within coal-prone intervals have less developed damage zones and may contribute less to permeability sweet-spots than similar faults in coal-free intervals. The damage zones of similar faults are exploited in many fields with low matrix permeability including those of the San Juan, Greater Green River and Piceance Basins. A notable example is the horizontal Rock Island 4H well that flowed at 12 MMCFD from a fault-related fracture sweet-spot in a Frontier Formation sandstone reservoir with ~10% porosity and ~0.025 mD at 15, 000 ft (Krystinik et al., 1999). Fault-related fracture swarms similar to those observed at Goonyella Riverside and exploited by Rock Island 4H could be targeted for high-rate wells in existing Australian on-shore fields such as Scotia by

targeting seismically resolvable intra-formational fault zones. In addition, lateral ramps of similar faults may act as flow baffles and compartmentalise a reservoir by reducing permeability in discrete zones perpendicular to the main fault strike (Fig. 5.23). Any offset/infill wells should ideally avoid previously tapped fracture swarms to avoid drainage interference and should be based on appropriate elliptical drainage patterns (Bell and Babcock, 1986; Hart et al., 2002; Teufel and Herrin, 2003).

Even with significant fault-related fracture permeability, hydraulic fracture completions may be required to connect the fractured, isolated sand bodies for commercial production (Cumella et al., 2002). Difficulties may arise with hydraulic fracture completions near faults due to fault-related stress perturbations and the typically high-stress environment of onshore Australia as described in Chapter 2 (Bell, 1996b; Bell and Babcock, 1986; Hillis et al., 1998; Yale, 2003).

The observations made in Chapters 4 and 5 provide predictive tools for the characterisation of fracture systems in analogous hydrocarbon systems where fracture data may be sparse. Fundamental characteristics of the fracture population may be appreciated by considering relevant analogues in the context of available seismic data, sedimentology and tectonic evolution of the hydrocarbon system and the in-situ stress regime.

Fluid flow along fractures is a stress sensitive phenomena (Barton et al., 1995). Several factors determine if a fracture is open and hydraulically conductive or closed and a potential barrier to fluid flow. They include:

- condition of the fracture e.g. mineralised vs. non-mineralised (Fisher and Knipe, 1998; Knipe et al., 1998; Laubach et al., 2004);
- orientation of the fracture relative to the in-situ stress tensor (Barton et al., 1995);
- magnitude of the in-situ stress tensor (Meyer, 2002);
- stress sensitivity of the fractures (Hillis, 1998);
- pore pressure.

Stress data acquired in the Goonyella Riverside underground area is presented in the following chapter. The data provides insight into stress partitioning in a coal measure succession and the effects of pore pressure reduction. The findings may be used to improve well completions and reservoir management in analogous settings where stress data is sparse or absent.

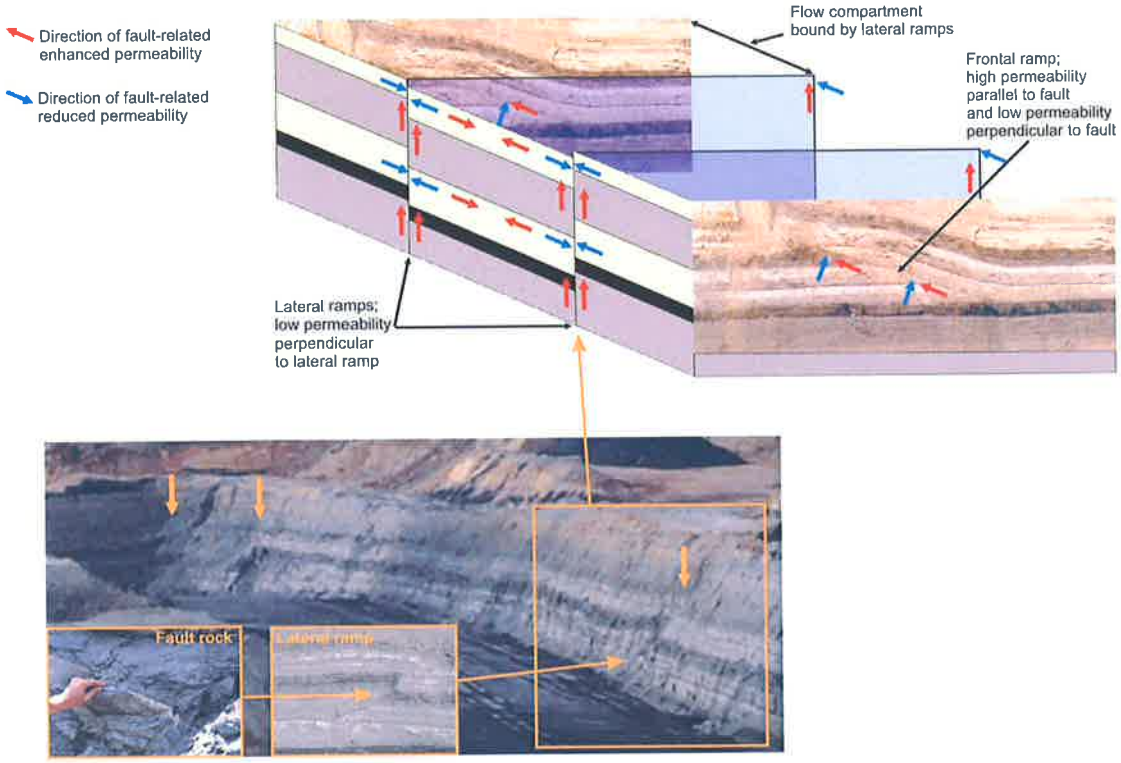

Figure 5.23. Conceptual diagram of fault-related permeability in a coal measure sequence dominated by thrust faults. Permeability may be reduced in the direction perpendicular to the faults and lateral ramps due to porosity reduction in the fault core creating flow baffles resulting in reservoir compartmentalisation. However, permeability may be enhanced in the direction parallel to the faults and lateral ramps due to fracturing within the damage zone creating high permeability conduits.

6 In-situ Stress and Structural Permeability

6.1 Background

Flow along natural fractures is believed to contribute significantly to groundwater inflow into the Goonyella Riverside underground exploration adit. Flow along the large seismically resolvable thrust fault (Figs 5.2, 5.3) has accounted for up to 50% of the ground water inflow into the exploration adit (Callow and Briese, 2002). Natural fractures may similarly contribute to flow in tight hydrocarbon reservoirs. Fluid flow along fractures is a stress-sensitive phenomena (Barton et al., 1995). Knowledge of the in-situ stress tensor and fracture population are critical in the assessment of a fractured reservoir in order to understand which fractures will be open and hydraulically conductive and which fractures may be closed and act as potential barriers to fluid flow (Barton et al., 1995; Meyer, 2002; Mildren et al., 2002b). Fractures subjected to an in-situ stress state promoting failure, termed critically stressed fractures, are those most likely to be hydraulically conductive (Barton et al., 1995). The likelihood of fractures being critically stressed, thus open and hydraulically conductive within the in-situ stress tensor is referred to as fracture susceptibility (Mildren et al., 2002b). In order to determine fracture susceptibility, the nature of the fracture systems must be understood in conjunction with the nature of the in-situ stress tensor. Stress data acquired in the Goonyella underground area provide an opportunity to assess fracture susceptibility and the effects of stress partitioning and pore pressure reduction in a coal measure succession.

6.2 In-situ Stress Determination

Various consultants have acquired stress data in the coal and roof rocks both before and after construction of the exploration adit. Three methods have been used to determine the in-situ stress tensor in the Goonyella underground area. Hydraulic fracturing (Edgoose, 2000) and step rate injection testing were used in surface boreholes prior to adit construction (Casey, 2000). Overcoring tests were conducted in the exploration adit (Mills, 2001; Nemcik, 2000). It is considered here that stress testing after the adit construction (i.e. the overcoring) represents reduced pore pressure conditions after development. Borehole breakouts interpreted on the image logs are also used to constrain the principal horizontal stress orientations. A brief description of the different methods and the results is presented below. All the in-situ stress data presented herein is summarised from consultants' reports except for the borehole breakouts on image logs that were interpreted by the author.

6.2.1 Hydraulic fracture tests

Hydraulic fracture tests were conducted in boreholes 41869 and 41871 prior to adit construction (Edgoose, 2000). Hydraulic fracture tests use an inflatable packer system (Fig. 6.1) to isolate a section of open wellbore (Enever, 1993). Fluid is then pumped into the wellbore, increasing the pressure until the rate of pressurisation decreases (i.e. fracture initiation pressure—Pi). Pi is defined on the pressure-time curve as the point at which the pressure buildup deviates from linearity (Fig. 6.2). Fracture initiation requires that the fluid pressure within the wellbore exceeds the minimum stress concentration at the wellbore wall and any tensile strength of the formation (Enever, 1993; Meyer, 2002). The initiation pressure (Pi) for a vertical fracture in an open, vertical wellbore is given by Equation 6.1 assuming an impermeable formation.

Pumping is stopped after fracture initiation and the system sealed. The pressure at which transient flow into the fracture ceases is the shut-in pressure (Ps). Once the shut-in phase is completed the pressure in the test interval is released to allow the fracture to close. The closure pressure (Pc) is the minimum pressure required to hold the fracture open against S_{hmin}. Pc is equal to the magnitude of S_{hmin} if the fracture is vertical and has propagated into the far field (Equation 6.2) (Gronseth, 1982; Gronseth and Kry, 1982). In a low-permeability formation the shut-in pressure and closure pressure may be virtually coincident (Fig. 6.2). The existing fracture (no tensile strength) is then reopened by another pressure increase. The pressure at which the fracture reopens is termed the reopening pressure (Pr) and is given by Equation 6.3 (Enever, 1993). The reopening cycle is repeated at least once to ensure that the fracture is propagated into the far field stress tensor so that reliable, repeatable values of Pr and Pc are obtained (Hillis et al., 1999a; Meyer, 2002). Pi, Pr and Pc and hence S_{hmin} may be read directly off a pressure time plot for a hydraulic fracture test (Fig. 6.2). S_{Hmax} may then be calculated using Equation 6.3. Given the assumptions in Equations 6.1–6.3 the calculated value of S_{Hmax} is less reliable than S_{hmin}/Pc which are directly measured from the test.

The orientation of the principal in-situ stresses may be determined by the orientation of the induced fracture which is parallel to S_{hmin} (Fig. 6.1). An impression packer with a rubber membrane is used to gain an impression of the wellbore wall. The impression packer is pressurised and a sinusoid is imparted by the induced fracture. A remote reading digital compass is used to confirm the orientation (Enever, 1993; Hillis et al., 1999a). The results of the hydraulic fracture tests in boreholes 41869 and 41871 are presented in Table 6.1.

$$Pi = 3S_{hmin} - S_{Hmax} - P_P + T \qquad \text{Equation 6.1}$$

$$Pc = S_{hmin} \qquad \text{Equation 6.2}$$

$$Pr = 3S_{hmin} - S_{Hmax} - P_P \qquad \text{Equation 6.3}$$

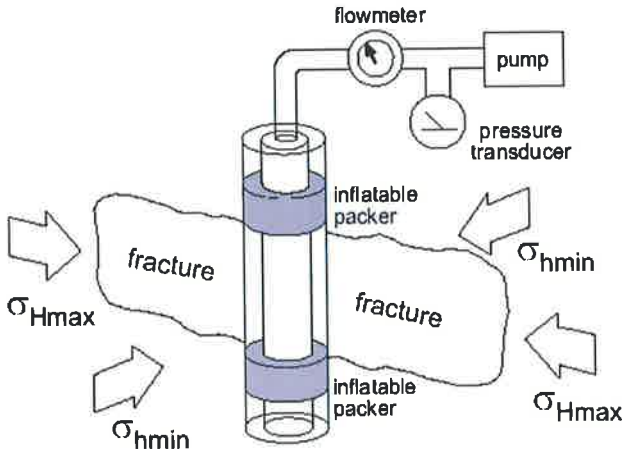

Figure 6.1. Schematic of a hydraulic fracture test showing the initiated fracture relative to the principal stress directions and the packer system (Bell, 1996a).

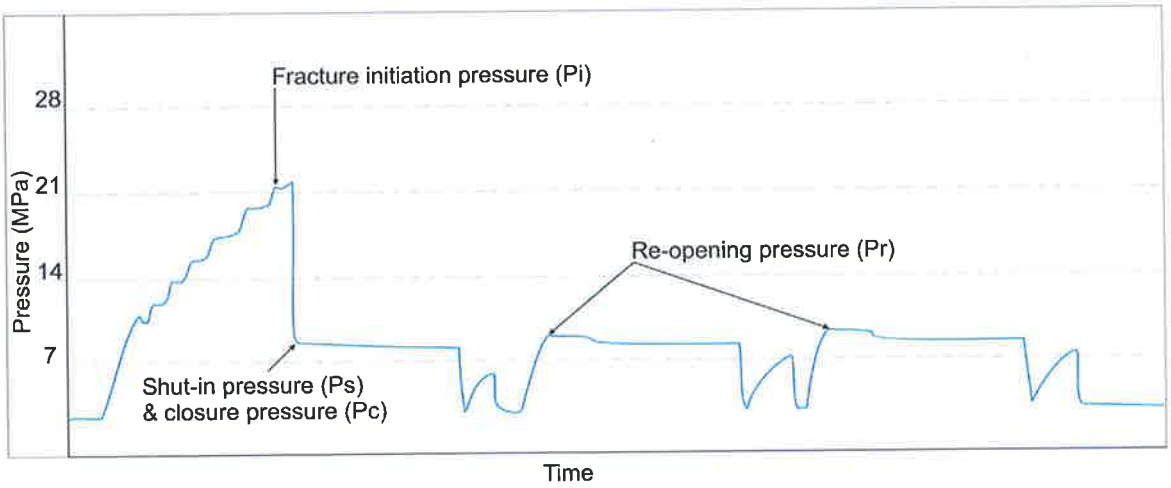

Figure 6.2. Sample hydraulic fracture test from the Goonyella underground area showing fracture initiation pressure (Pi), shut-in pressure (Ps), closure pressure (Pc) and re-opening pressure (Pr). Shut-in and closure pressures are coincident due to the relatively low permeability formation.

BH/Test Number	Depth (m)	σ_h (MPa)	σ_H (MPa)	σ_H orientation (°)
41869 #3	215.0-215.42	8.3	14.2	002
41869 #4	217.5-217.92	11.0	21.1	037
41869 #5	219.5-219.92	8.3	15.5	025
41869 #8	240.0-240.42	9.0	15.7	024
41871 #2	187.0-187.42	6.3	8.9	346
41871 #4	193.5-193.92	5.5	8.4	320
41871 #5	203.5-203.92	6.2	10.0	030
41871 #6	208.5-208.92	7.4	11.9	019
41871 #9	236.5-236.92	7.6	12.3	028

Table 6.1. Results of hydraulic fracture tests in rock from boreholes 41869 and 41871 (Edgoose, 2000).

6.2.2 Step rate injection tests

Step rate injection tests were conducted in boreholes 41870 and 41884 to determine the in-situ stresses within the coal seams prior to construction of the exploration adit (Casey, 2000). Step rate injection tests are similar to hydraulic fracture tests but are specifically designed for coal. The fluid injection rate is increased (approximately doubled) over a period of equal time increments. Step rate analysis plots pressure against a series of increasing injection rates. As fracture dilation/breakdown occurs the rate of pressure increase slows for successive rate increases. The intersection of the two lines (Fig. 6.3) is considered to represent an opening pressure interpreted to be coincident with the minimum stress in coal (Casey, 2000). The results of the step rate injection tests in boreholes 41870 and 41884 are presented in Table 6.2.

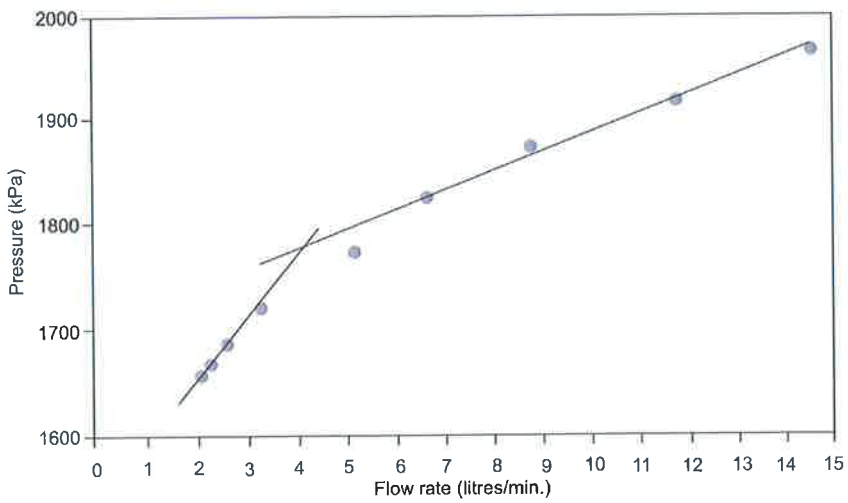

Figure 6.3. Sample step rate injection test from borehole 41870 in the Goonyella Middle Seam between 169.5–180.0 m (Casey, 2000). The rate of pressure increase slows for successive flow rate increases as fracture dilation/breakdown occurs. The intersection of the two lines is considered to represent an opening pressure interpreted to be coincident with the minimum stress in coal.

Borehole	Depth (m)	Opening Pressure (MPa)	Reservoir Pressure (MPa)	σ_h (MPa)
41870	169.5-180.0	1.780	1.169	1.78
41884	258.5-269.0	2.960	2.160	2.96

Table 6.2. Results of step rate injection tests in the Goonyella Middle Seam in boreholes 41870 and 41884 (Casey, 2000).

6.2.3 Overcoring

Overcoring is a stress relief method that isolates a rock sample from the surrounding rock. Stresses are inferred from strains or displacements created by the relief process. At Goonyella Riverside the overcoring method measured the amount of expansion occurring in a 58 mm pilot hole when a 90 mm rock annulus surrounding the pilot hole is relieved of stress by being detached from the surrounding rock mass. The CSIRO method of overcoring (Worotnicki, 1993) measures the rock expansion by gluing a thin-walled plastic cylinder (hollow inclusion cell) containing a number of strain gauges into the pilot hole. As the isolated sample is removed from the stress field of the surrounding rock, the strain gauges in the hollow inclusion cell record the strain associated with the relief process (Hillis et al., 1999a; Worotnicki, 1993). The recovered core (with the cells in place) is then loaded radially to measure the elastic properties. The elastic properties determined by biaxial tests conducted on the recovered samples are used in conjunction with the strain measurements to determine the in-situ stress.

A total of six overcoring tests were conducted in the exploration adit approximately 10 m behind the exposed face. Four tests were conducted in the Goonyella Middle Seam and two in the shale roof rock. The tests are considered to be indicative of pore pressure-depleted conditions because the adit had been drained. The overcoring tests provide principal stresses that may not act horizontally and vertically (Figs 6.4, 6.5; Table 6.3), but they may be resolved to provide values of vertical and maximum and minimum horizontal stress (Mills, 2001; Nemcik, 2000). Tests conducted in such environments may be significantly influenced by mining-induced, loading or transient fluid conditions. These effects may impart major variations from expected test results (each test was conducted 10 m behind the adit face to mitigate these effects). The test results are discussed briefly to account for some of the variation.

Tests GRV5 and GRV6 were conducted in shale roof strata approximately 10 m behind the exposed face. Significant differences exist between the two samples in both the horizontal and vertical stress gradients determined (Table 6.3). The discrepancies can be accounted for by the location of each test. Test GRV6 was conducted over a pillar at the start of a mine heading and is a zone of stress concentration, hence the elevated vertical and horizontal stresses. Test GRV5 is considered to be more representative of far-field conditions away from stress

concentrations around the adit. Tests GRV1 and GRV2 were conducted at the same location in different orientations in the Goonyella Middle Seam at 160 m. Tests GRV8 and GRV9 were conducted at the same location in different orientations in the Goonyella Middle Seam at 200 m. Tests GRV1, GRV8 and GRV9 gave consistent results and are interpreted to be representative of the stress conditions in the coal seam. Test GRV2 is not consistent with the other three tests and is not considered further.

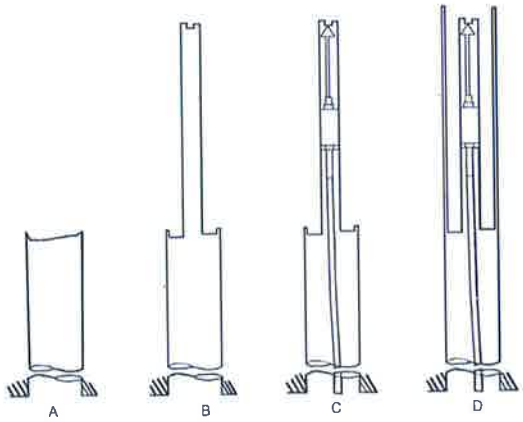

Figure 6.4. Schematic illustration of the overcoring technique. A: The initial borehole is drilled to the required depth of testing. B: A pilot hole is drilled large enough to accommodate the hollow inclusion cell (containing the strain gauges). C: The hollow inclusion cell is glued into the pilot hole. D: Stress is relieved from the hollow inclusion cell and the enclosing rock by removing the surrounding annulus of rock (Hillis et al., 1999a).

Lith	Test	Depth	E	S_1 (dip, dip direc)	S_2 (dip, dip direc)	S_3 (dip, dip direc)
Shale	GRV5	285 m	26 GPa	10 MPa (6°, 213°)	6.7 MPa (2°, 213°)	5.2 MPa (84°, 011°)
Shale	GRV6	225 m	14 GPa	13 MPa (5°, 008°)	8.2 MPa (77°, 257°)	6.9 MPa (12°, 099°)
Coal	GRV1	160 m	2.4 GPa	1.9 MPa (83°, 301°)	1.2 MPa (1°, 035°)	0.5 MPa (7°, 125°)
Coal	GRV2	160 m	2.2 GPa	2.8 MPa (86°, 281°)	1.8 MPa (1°, 180°)	0.9 MPa (3°, 090°)
Coal	GRV8	200 m	2.1 GPa	2.3 MPa (67°, 227°)	1.0 MPa (19°, 012°)	0.4 MPa (12°, 106°)

Table 6.3. Overcoring test results from Goonyella Riverside mine heading in coal and shale roof rock. The overcoring test provides principal stresses that do not act exactly horizontally and vertically. The values may be resolved to provide values of vertical stress and maximum and minimum horizontal stress (Mills, 2001; Nemcik, 2000).

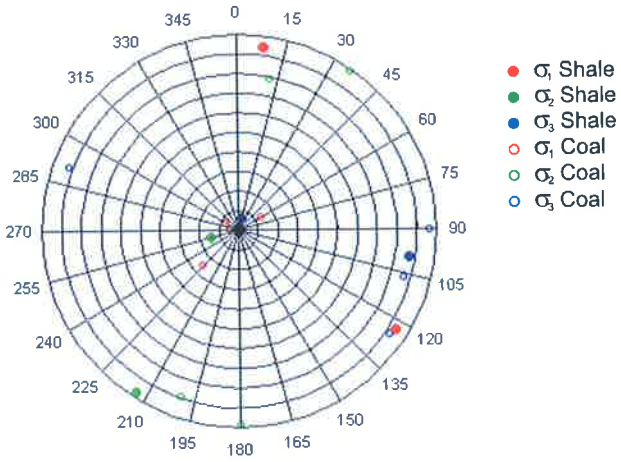

Figure 6.5. Summary of orientations obtained from overcoring tests. Tests in shale are presented as filled circles and tests in coal are presented as open circles. σ_1 is red, σ_2 green and σ_3 blue.

6.2.4 Borehole breakouts

Borehole breakouts form as a result of compressive failure at the azimuth of greatest compressive stress concentration about a borehole(Prensky, 1992; Zoback and Healy, 1984). Compressional failure occurs when there is a large difference between radial and circumferential stress and where the stress concentration exceeds the compressive rock strength. Breakouts develop as a result of cross-cutting micro-shear fractures. Rock flakes isolated by the intersecting shear fractures spall into the borehole resulting in borehole elongation (Fig. 6.6). Breakouts may be detected on image logs. Breakouts appear as intervals of extended travel time and low amplitude on SAS image logs.

Breakouts were interpreted in five of the wells with SAS image logs. The breakouts occur in thin intervals no greater than 300 mm thick and strike between 79°– 112° indicating σ_{Hmax} directions ranging from 349°– 022°. Figure 6.7 shows a rose plot of σ_{Hmax} determined from all breakouts, hydraulic fracture tests and overcoring; the average is ~ 020°N.

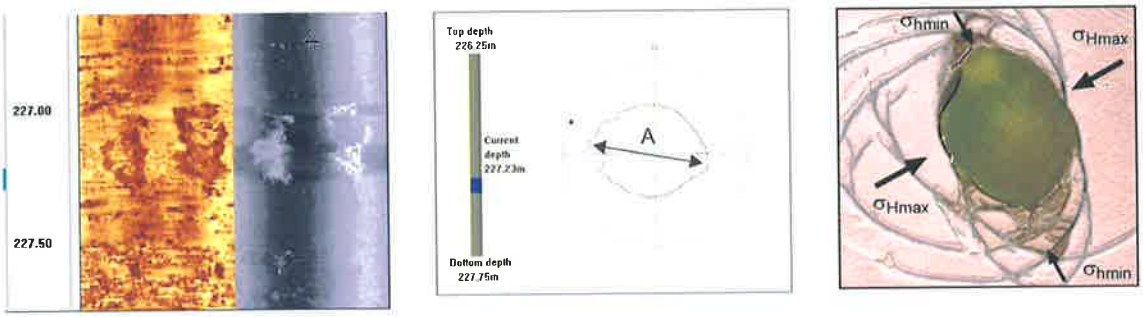

Figure 6.6. Left: Borehole breakout in borehole 40958, breakouts create elongated boreholes resulting in longer travel times in the direction of S_{hmin}. Centre: Transit time calliper plot from borehole 40958. Right: Experimental breakout formation demonstrating the effect of shear fractures and borehole elongation (Syarifuddin and Busono, 1999).

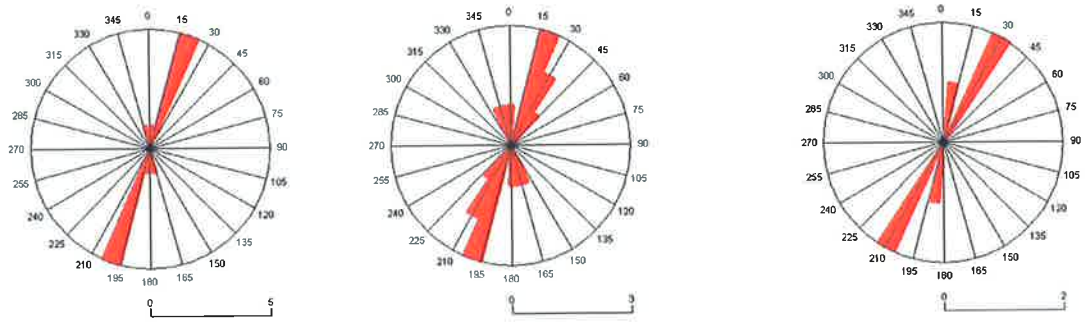

Figure 6.7. S_{Hmax} orientation determined by borehole breakouts (left), hydraulic fracture tests (middle) and overcoring (right). The average for all three methods is 020°N.

6.3 Stress Gradients

Vertical stress is not measured directly from either the hydraulic fracture or step rate injection tests. The vertical stress is considered to be due to the weight of the overburden and can be estimated using Equation 6.4 (Amadei and Stephansson, 1997). Detailed laboratory testing of the Goonyella Middle Seam and the floor and roof rocks has constrained the density of the sandstone and siltstone to 2.5 g/cm^3 and the coal to 1.5 g/cm^3 (Seedsman, 1998). These values are consistent with density values derived from the density logs below approximately 100 m (Fig. 5.4). In the upper 100 m the density of the sandstone and siltstone is in the order of 1.9 g/cm^3 probably due to near surface weathering. The vertical stress gradients are thus 25 MPa/km – 0.6 Mpa.

$$S_v = \rho g h \qquad \text{Equation 6.4}$$

6.3.1 Hydraulic fracture tests

The stress gradients in sandstone at Goonyella Riverside calculated from the hydraulic fracture tests and the weight of the overburden are:

- S_v ~ 25 MPa/km – 0.6 MPa - Equation 6.4
- S_{hmin} ~ 35 MPa/km - Directly from closure pressure
- S_{Hmax} ~ 59 MPa/km - Equation 6.3.

There is significant scatter in the stress magnitudes (Fig. 6.8) but the stress regime is clearly one where $S_{Hmax} > S_{hmin} > S$ (i.e. consistent with a reverse fault stress regime).

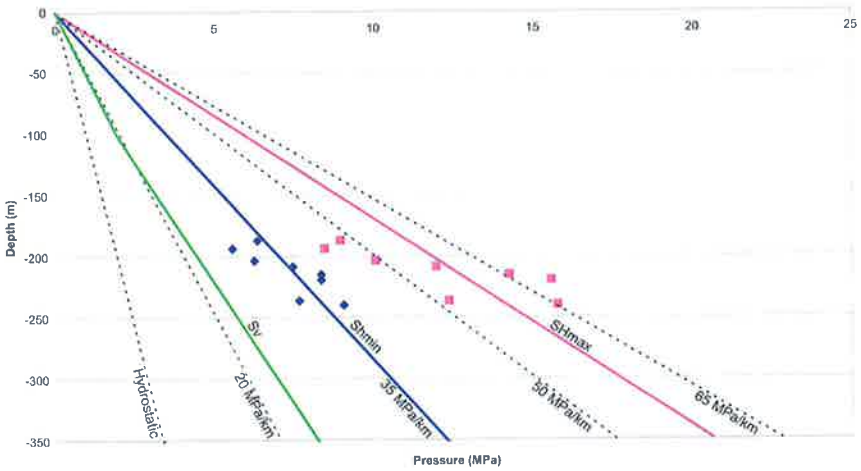

Figure 6.8. Stress gradients in sandstone calculated from hydraulic fracture tests (S_{Hmax} and S_{hmin}) and weight of overburden (S_v).

6.3.2 Step rate injection tests

The stress gradients in coal at Goonyella Riverside calculated from the step rate injection tests and the weight of the overburden are:

- S_v ~ 25 MPa/km – 0.6 MPa - Equation 6.4
- S_{hmin} ~ 10.7 MPa/km - Directly from opening pressure
- S_{Hmax} ~ 14.0 MPa/km - Equation 6.3.

The horizontal stress magnitudes from the step rate injection tests are considerably lower than those from the hydraulic fracture tests (Fig. 6.9). The stress regime in the coal is one where $S_v > S_{Hmax} > S_{hmin}$ (i.e. consistent with a normal fault stress regime).

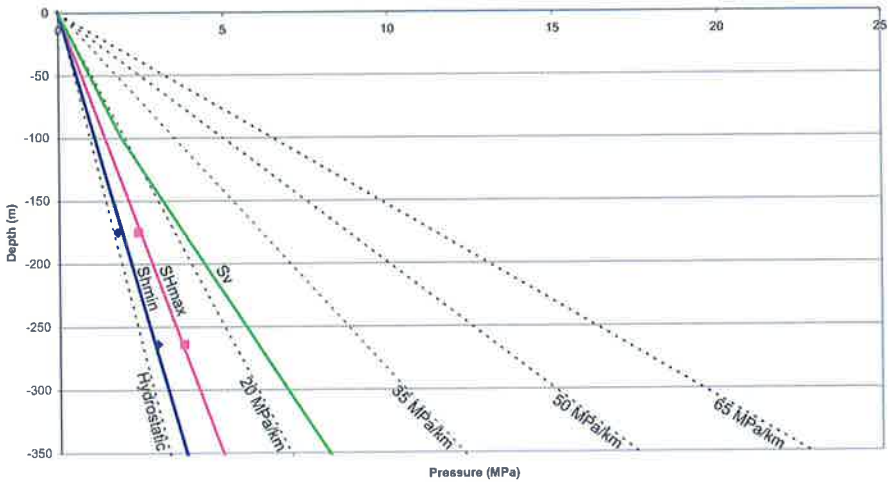

Figure 6.9. Stress gradients in Goonyella Middle Seam calculated from step rate injection tests (S_{Hmax} and S_{hmin}) and weight of overburden (S_v).

6.3.3 Overcoring

The stress gradients calculated in the siltstone roof rock from the overcoring tests at ~ 290 m depth are consistent with a reverse fault stress regime (Fig. 6.10):

- S_v ~ 19 MPa/km - Test GRV5
- S_{hmin} ~ 27 MPa/km - Test GRV5
- S_{Hmax} ~ 32 MPa/km - Test GRV5.

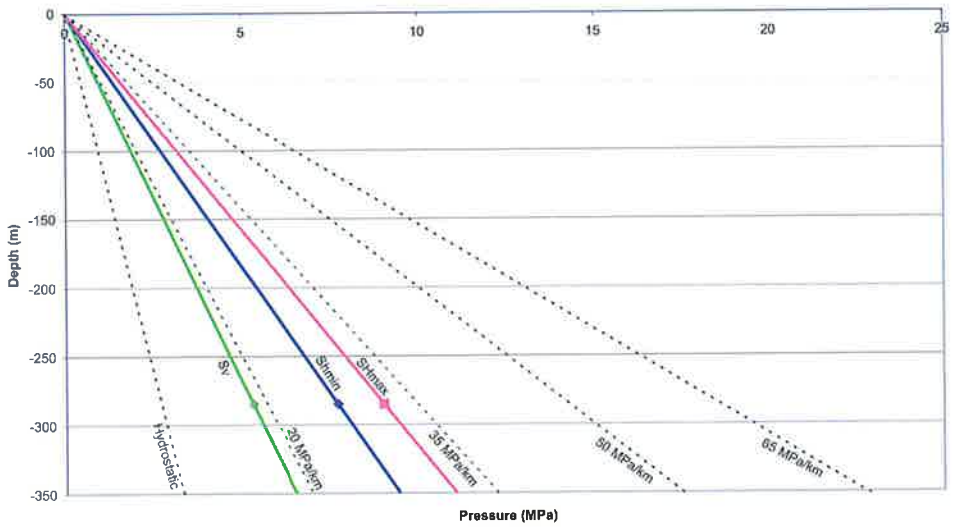

Figure 6.10. Stress gradients in siltstone calculated from overcoring tests in the exploration adit (S_{Hmax} and S_{hmin}) and weight of overburden (S_v).

The stress gradients calculated in the Goonyella Middle Seam from the overcoring tests are consistent with a normal fault stress regime (Fig. 6.11):

- S_v ~ 12 MPa/km - Tests GRV1, 8 and 9
- S_{hmin} ~ 3 MPa/km - Tests GRV1, 8 and 9
- S_{Hmax} ~ 6 MPa/km - Tests GRV1, 8 and 9.

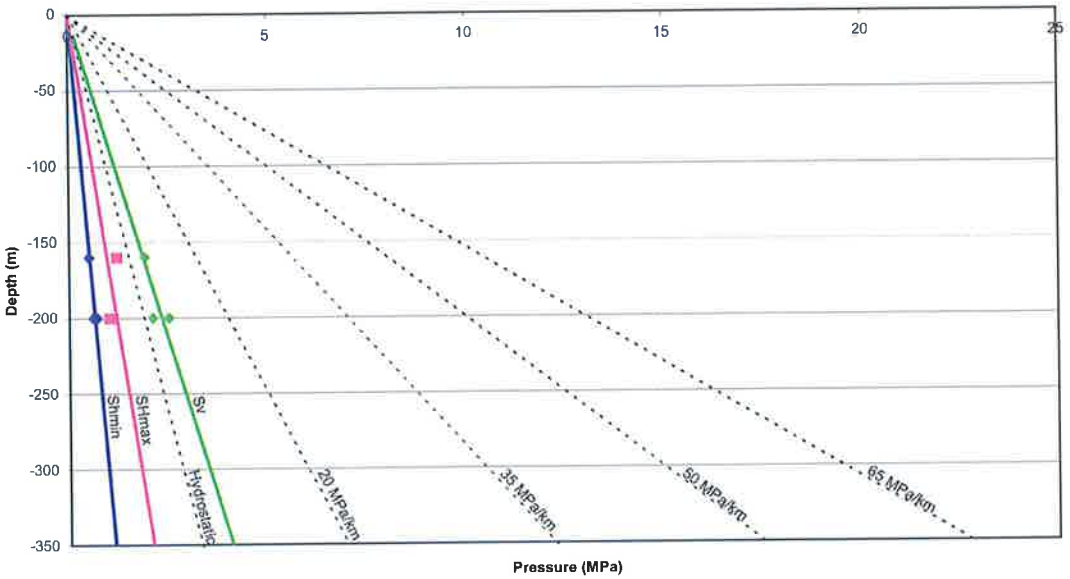

Figure 6.11. Stress gradients calculated in Goonyella Middle Seam from overcore tests.

6.3.4 Summary

The stress gradients derived for coal and rock by the different test methods are presented in Table 6.4.

Lithology	Method	S_v	S_{Hmax}	S_{hmin}	Stress regime
Coal	Step test	25 (MPa/km)- 0.6 MPa*	14 (MPa/km)	10.7(MPa/km)	Normal
Coal	Overcore	12 (MPa/km)**	6 (MPa/km)	3 (MPa/km)	Normal
Rock	H-fracture	25 (MPa/km)- 0.6 MPa*	59 (MPa/km)	35 (MPa/km)	Reverse
Rock	Overcore	19 (MPa/km)**	32 (MPa/km)	27 (MPa/km)	Reverse

Table 6.4. Stress gradients derived for coal and rock using overcoring, hydraulic fracture and step rate injection testing. The coal and rock are characterised by normal and reverse stress regimes respectively.
* The step tests and hydraulic fracture tests do not give a direct measurement of S_v, S_v is calculated from the density log data. At 100 m depth the S_v gradient would be ~19 MPa/km due to near surface weathering effects. Below 100 m S_v is ~ 25 MPa/km.
** The overcoring tests provide a direct measure of S_v and provide an apparently low gradient due to the effects of near surface weathering in ~ the top 100 m.

The different stress testing methods establish that the rock is characterised by a reverse stress regime ($S_{Hmax}>S_{hmin}>S_v$) and that the coal is characterised by a normal stress regime ($S_v>S_{Hmax}>S_{hmin}$) where:

Rock

Hydraulic fracture: $S_{hmin} \sim 1.4\ S_v$; $S_{Hmax} \sim 2.4\ S_v$

Overcore: $S_{hmin} \sim 1.4\ \sigma_v$; $S_{Hmax} \sim 1.6\ S_v$

Coal

Step rate injection: $S_{hmin} \sim 0.4\ S_v$; $S_{Hmax} \sim 0.6\ S_v$

Overcore: $S_{hmin} \sim 0.25\ S_v$; $S_{Hmax} \sim 0.5\ S_v$

The different stress testing methods also indicate that the stress tensor may be pore pressure-sensitive. The horizontal stress gradients measured in both coal and rock by overcoring methods (drained conditions) are lower than those measured by the hydraulic fracturing and step rate injection test methods.

Limitations

It is emphasised that the sample of stress data is not comprehensive due to 1) the small sample size; 2) the difference between the test methods before and after adit construction; 3) the difference between the test locations before and after adit construction; and, 4) the variation in the rock between the hydraulic fracture (sandstone) and overcoring (siltstone) tests. Nonetheless, it is considered that the trends displayed by the data are significant as discussed below.

6.4 Stress Partitioning

The concept of stress partitioning may be used to explain the difference in horizontal stress gradients between coal and rock at virgin conditions (Amadei and Stephansson, 1997; Evans et al., 1989). Abrupt changes in horizontal stress can take place across contacts between strata with different mechanical properties in both tectonically stressed and relaxed basin settings (Amadei and Stephansson, 1997; Plumb, 1994). In a tectonically relaxed basin the maximum principal stress acts vertically due to the weight of overburden. The horizontal stresses that arise are a result of Poisson's effect and are a function of the vertical stress and the Poisson's ratio of the material as expressed in Equation 6.5. Materials with higher Poisson's ratio exhibit higher horizontal stress magnitudes (Amadei and Stephansson, 1997; Plumb, 1994). Hence, coal (ν~0.36) is expected to have a higher horizontal stress gradient than either shale or sandstone (ν~0.30-0.34) in a relaxed basin setting.

$$S_{hmin} = \frac{\upsilon}{1-\upsilon} S_v$$ Equation 6.5

In a tectonically stressed setting such as most of eastern Australia (Enever, 1990; Enever and Jeffrey, 2000; Enever et al., 1994b; Hillis et al., 1999a) load is not only applied due to the weight of overburden but also by a far-field tectonic force that acts close to horizontal. A component of the horizontal stress is due to Poisson's effect but a much larger component is due to tectonic loading. The magnitude of the horizontal stress component transmitted by far-field tectonic forces is proportional to the elastic modulus of the material as described by Hooke's Law. Materials with higher elastic moduli have higher horizontal stress magnitudes (Amadei and Stephansson, 1997; Evans et al., 1989; Plumb, 1994). Coal (E~2-4 GPa) is expected to have a significantly lower horizontal stress gradient than either shale or sandstone (E~10-20 GPa) in a tectonically stressed setting. This model fits the calculated stress gradients for Goonyella Riverside and explains observations made by previous workers in coal measure successions along the east coast of Australia in the Sydney and Bowen basins (Enever, 1990; Enever et al., 1994a; Enever and Jeffrey, 2000; Enever et al., 1994b; Hillis et al., 1999a). Laboratory and field testing has shown that the effect of rock mass anisotropy decreases with increased confinement (Amadei and Stephansson, 1997) and so the effects of mechanical anisotropy are expected to decrease with increasing depth.

6.5 Effects of Pore Pressure

The stress data acquired at Goonyella Riverside provide an opportunity to analyse the relationship between pore pressure and the stress tensor. The hydraulic fracture and step rate injection testing represent stress gradients determined at virgin pore pressure conditions where the water table is approximately 40–50 m below the surface. It is uncertain what the exact pore pressure was at the time of overcoring as no direct measurements were taken. However, it was noted that the test holes were either dry or had only minor seepage at the time of testing (Mills, 2001; Nemcik, 2000). It is thus considered here that the overcoring tests in the exploration adit represent depleted pore pressure conditions below virgin pressure levels. The limitations of the data must be borne in mind; nonetheless it is considered that the displayed trends may be significant.

6.5.1 Rock

The concept of pore pressure stress coupling has typically been used to describe the phenomena of S_{hmin} reduction relative to S_v with pore pressure reduction in normal fault stress regimes (Hillis, 2001; Teufel et al., 1991). Much work has been done to identify coupling of S_{hmin} with pore pressure yet to the author's knowledge no one has thoroughly demonstrated the relationship of S_{Hmax} with P_P due to difficulties involved with accurate measurement of S_{Hmax} in

the field. Most previous work on pore pressure stress coupling has been in relaxed basin settings (normal stress regimes) such as the North Sea where it can influence stability of uncased wellbores, sand production, faulting and seismicity during reservoir depletion and flooding (Addis, 1997; Hillis, 2001; Santarelli et al., 1998; Teufel et al., 1991). In such settings, the differential stress (S_1'-S_3') defined by S_v'-S_{hmin}' becomes larger with reservoir depletion because S_v' increases at a higher rate than does S_{hmin}'. On a Mohr circle diagram this has the effect of increasing the diameter of the circle with decreasing pore pressure (Fig. 6.12). As a result, failure of intact rock or reactivation of existing fractures may occur due to pore pressure reduction.

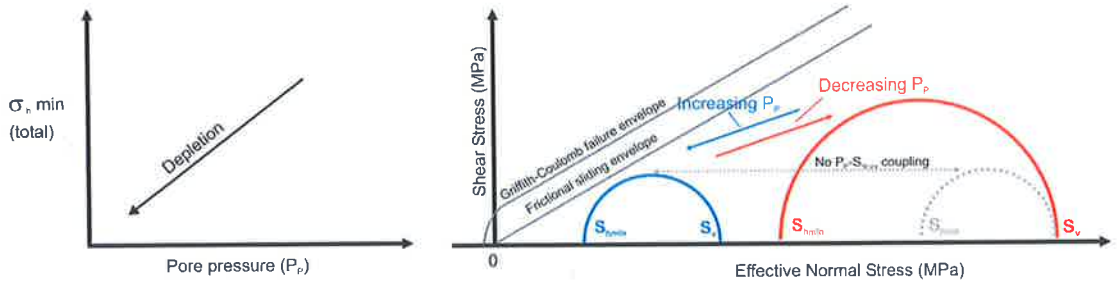

Figure 6.12. The effect of pore pressure stress coupling in a normal fault stress regime as documented by numerous authors using oil-field data. S_{hmin} decreases with decreasing pore pressure. On a Mohr circle diagram this has the effect of increasing the diameter of the circle with decreasing pore pressure with the potential to induce failure due to pore pressure reduction (Hillis, 2001; Teufel et al., 1991).

In the case of a tectonically stressed basin characterised by a reverse-stress regime, the differential stress and hence the diameter of a Mohr circle is defined by S_{Hmax}' - S_v'. If σ_{Hmax} is similarly coupled to P_P as S_{hmin}, the differential stress in a reverse fault stress regime becomes smaller with reservoir depletion. This has the effect of decreasing the diameter of the Mohr circle and taking it further from the failure envelope with decreasing pore pressure (Fig. 6.13).

Data from Goonyella Riverside indicate that a P_P - S_{Hmax} coupling relationship may exist in the inter-seam rock. The data from Goonyella Riverside show a reduction of the S_{Hmax} gradient from 59 MPa/km at virgin conditions (hydraulic fracture testing) to 32 MPa/km at depleted pressure conditions (overcoring data). The data demonstrate that a P_P - S_{Hmax} coupling relationship may exist; however, a P_P - S_{Hmax} ratio cannot be calculated because the pore pressure at the time of overcoring is not constrained.

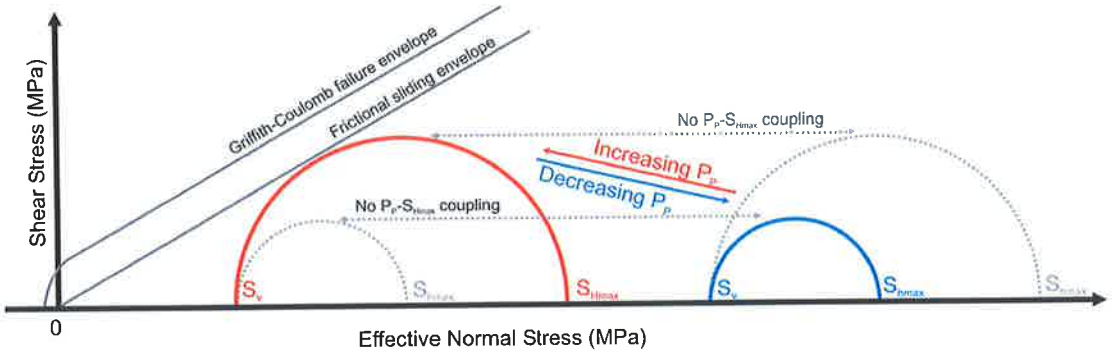

Figure 6.13. An idealised diagram demonstrating the possible effect of pore pressure-stress coupling in a reverse stress regime. With decreasing pore pressure the differential stress becomes smaller making the Mohr's circle smaller and taking it further from the failure envelope than if P_P-S_{Hmax} coupling does not occur.

6.5.2 Coal

The step rate injection and overcoring test results demonstrate that the coal is characterised by a normal fault stress regime (Table 6.4), yet the stress gradients derived from the overcoring tests are significantly less than the stress gradients derived from the step rate injection tests. The discrepancy in the stress gradients may reflect: 1) the effect of pore pressure reduction on the in-situ stress tensor; 2) differences and errors in the test methods; or, 3) stress perturbations around the adit. Unfortunately there is no pore pressure data at the time of overcoring and the number of tests is limited which precludes a thorough assessment of the difference in stress gradients. Previous workers have noted that pore pressure affects coal matrix volume (Harpalani and Chen, 1992; St George and Barakat, 2001) and it is postulated that the reduction in pore pressure, hence volume may in turn reduce stress in coal seams (Gray, 1987). It is proposed here that at least some of the discrepancy in the stress gradients calculated from step rate injection and overcoring tests is due to pore pressure reduction and resulting coal matrix shrinkage.

Matrix Shrinkage

It has been shown that coal matrix volume decreases as pore pressure is decreased and that a relationship exists between coal matrix strain and the quantity of gas released (Harpalani & Chen 1999; St George & Barakat 2001) (Fig. 6.14). The coal matrix compressibility/shrinkage coefficient (C_m) is defined as the rate of change of coal matrix volume (V_m) to the change in gas pressure (P_P) expressed in Equation 6.6 (Harpalani and Chen, 1999; St George and Barakat, 2001). Several factors have been invoked to control coal matrix shrinkage including rank, petrographic composition, ash content of the coal and the gas composition (Levine, 1996).

$$C_m = \frac{1}{V_m}\left(\frac{\Delta V_m}{\Delta P_P}\right) \qquad \text{Equation 6.6}$$

Assuming that the total coal rock volume remains constant due to lateral confinement, the decrease in the coal matrix volume due to shrinkage equates to a similar increase in cleat aperture (Harpalani and Chen, 1999). It has been proposed that an increase in cleat aperture may limit the transmission of stress and reduce the effective horizontal stress in a coal seam (Gray, 1987; St George and Barakat, 2001). The change in effective stress due to matrix shrinkage ($\Delta S'$) for a sample under pressure is given in Equation 6.7 where K = bulk modulus of the coal. The effective confining stress (S') is a function of the initial confining stress (S'_i), the change in effective stress due to the change in gas pore pressure (ΔS_{Pp}) and the change in effective stress due to matrix shrinkage ($\Delta S'_s$) as expressed in Equation 6.8 (St George and Barakat, 2001).

$$\Delta S' = KC_m \qquad \text{Equation 6.7}$$

$$S' = S'_i + \Delta S'_{Pp} - \Delta S'_s \qquad \text{Equation 6.8}$$

It is proposed that the orientation of the face cleat relative to the far-field S_{Hmax} influences the effect of S_{Hmax} reduction. The effect of S_{Hmax} reduction is expected to be greatest when the face cleats are perpendicular to the far-field S_{Hmax} direction. The least amount of reduction is expected when the face cleats are parallel to the far-field S_{Hmax} direction. The face cleats at Goonyella Riverside are ~70° to S_{Hmax} (i.e. almost perpendicular to S_{Hmax}). The vertical stress in the coal is also reduced as the rocks above the coal seam are capable of partially arching the coal for a finite period.

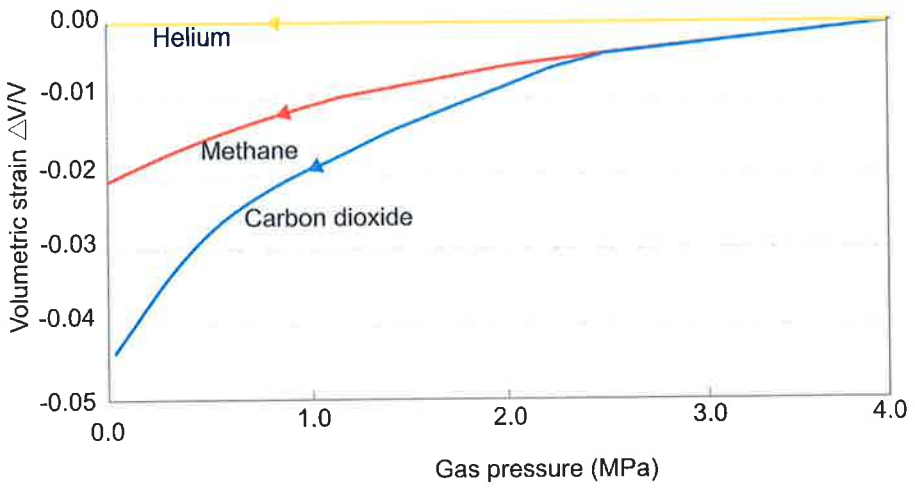

Figure 6.14. Volumetric strain of coal matrix with decreasing pore pressure and different gas types (St George and Barakat, 2001). The coal matrix volume is reduced by 2% by decreasing the pore pressure from 4 MPa to 0 if the gaseous phase is methane.

Matrix shrinkage and stress coupling

Figure 6.15 illustrates the effect of coal matrix shrinkage on the stress tensor in a tectonically stressed setting. Although the process of matrix shrinkage and stress change is a continuum, it may be thought of in three stages:

1. **Virgin conditions**: The vertical stress gradient in the rock is approximately the same as the coal. The horizontal stress gradient is significantly higher in the rock than the coal due to the higher elastic modulus of the rock relative to the coal.

2. **During and immediately after dewatering**: As pore pressure is removed more gas can desorb from the matrix, the coal matrix shrinks and becomes mechanically decoupled. The cleat aperture increases and the transmission of far-field stresses is inhibited resulting in a drop in S_{Hmax}. The vertical stress gradient in the coal is reduced as the overburden can arch the coal for a finite period.

3. **Following load readjustment**: After a finite amount of time the overburden may readjust as it may no longer arch the coal and the vertical stress may recover to near virgin conditions. The horizontal stress gradient in the coal does not recover to virgin conditions as the coal is not capable of transmitting far-field stresses.

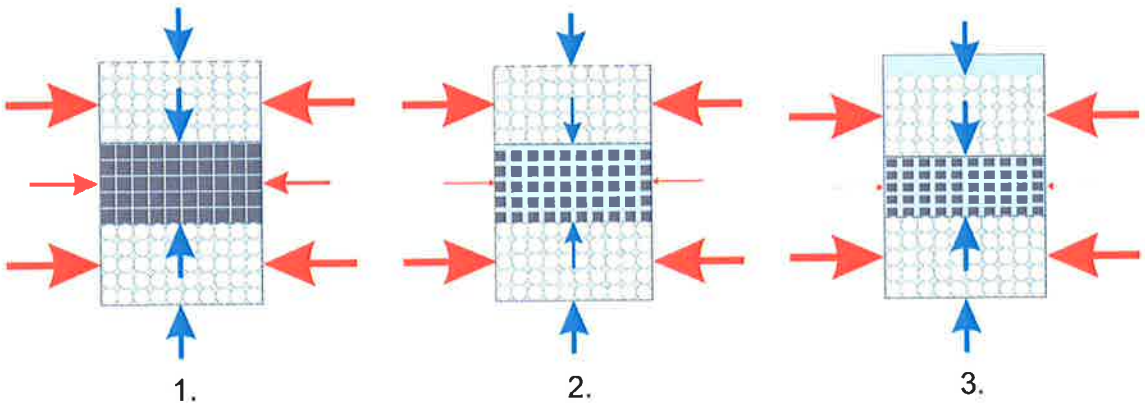

Figure 6.15. Schematic diagram of the effects of coal matrix shrinkage on stress in a tectonically stressed setting. 1) Virgin conditions: the vertical stress gradient in the clastic layers is approximately the same as the coal; the horizontal stress gradient is significantly higher in the rock due to a much higher modulus. 2) During and immediately after dewatering: as pore pressure is removed, more gas can desorb from the matrix and the coal matrix shrinks and becomes mechanically decoupled. 3) Following load readjustment: with time the overburden readjusts as it is not able to span the coal and the vertical stress may recover to near virgin conditions. The horizontal stress gradient in the coal does not recover to virgin levels.

6.6 Fracture Susceptibility

Fracture susceptibility is a technique used to investigate whether a pre-existing fracture is likely to be hydraulically conductive within the in-situ stress field (Mildren et al., 2002b). The technique assumes that fractures subject to stresses that would reactivate them are the most likely to be hydraulically conductive (Barton et al., 1995). The fracture susceptibility technique (Meyer, 2002; Mildren et al., 2002b) follows Sibson's (1996) approach to the generation of fracture-related permeability. Failure criteria may be expressed in terms of differential stress and fluid pressure required for tensile, shear and mixed mode failure. The propensity for each mode of failure to occur, hence for fractures to be hydraulically conductive, can be quantified by the contemporary stress field expressed on a 3D Mohr diagram and the Griffith-Coulomb failure envelope for intact rock or the frictional sliding envelope for cohesionless pre-existing fractures (Mildren et al., 2002b; Sibson, 1996).

All fractures plot as points in the region constrained by the three Mohr circles (shaded area in Fig. 6.16). The reactivation potential of a fracture is measured in terms of the change in pore pressure (ΔP_P) required to move it to failure. ΔP_P is the horizontal distance between where a pre-existing fracture plots on the Mohr diagram and the failure envelope (Barton et al., 1997; Hillis, 2001; Meyer, 2002; Mildren et al., 2002b). A small or negative ΔP_P implies a high reactivation potential and a large ΔP_P infers a low reactivation potential. The failure envelope used for fracture susceptibility assessment is based on the properties of the fracture fill. Zero cohesive strength (Co), a co-efficient of friction of 0.6 and a frictional sliding envelope (Byerlee, 1978) are commonly used for un-mineralised fractures in the absence of any other information. If the fractures are mineralised or the fracture fill has some finite strength, a non-zero value of cohesive strength should be used and a Griffith-Coulomb failure envelope adopted.

A value of ΔP_P can be assigned to all points in 3D space (shaded area of Fig. 6.16). The ΔP_P values can be plotted on a polar plot using a colour scale to produce a structural permeability diagram. Fractures can then be superimposed on the structural permeability diagram to assess the likelihood that they are hydraulically conductive (Meyer, 2002; Mildren et al., 2002b). Fracture susceptibility diagrams have been produced for the coal and rock using stress gradients derived by the different testing methods (Figs 6.17–6.20). All diagrams have been constructed for a depth of 250 m and the Mohr diagrams kept at the same scale for comparison purposes.

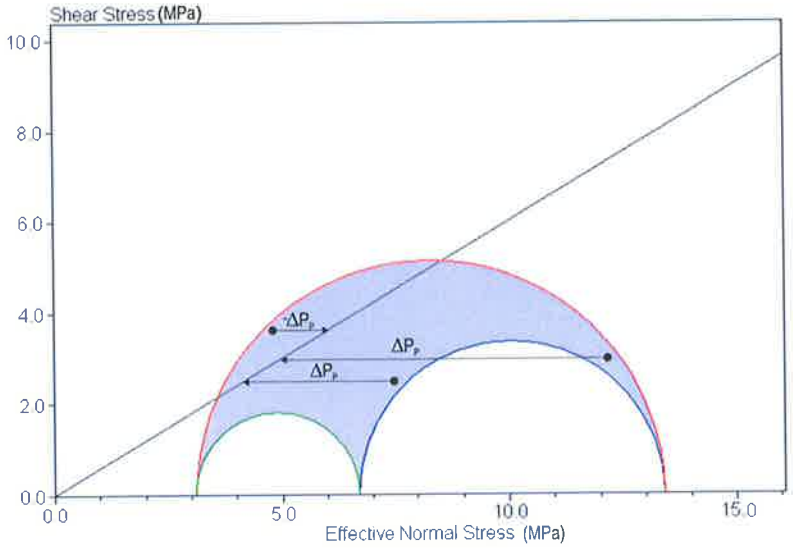

Figure 6.16. A 3D Mohr diagram showing the in-situ stress at 240 m in borehole 41869. S_{Hmax}=15.7 MPa, S_{hmin} = 9 MPa derived from hydraulic fracture testing, S_v = 5.4 MPa and P_P = 2.3 MPa are assumed due to the weight of the overburden and a water column 10 m below the surface respectively. The failure envelope used is the frictional sliding envelope, μ = 0.6 and T_0 = 0. All fractures plot in the shaded area of the diagram. The horizontal distance between any orientation and the failure envelope (ΔP_P) is used to assess the potential hydraulic conductivity.

6.6.1 Rock

Hydraulic fracturing: virgin conditions

The Mohr circle diagram and fracture susceptibility diagram constructed for rock at 250 m using stress gradients derived from hydraulic fracture testing are shown in Figure 6.17. A hydrostatic gradient is assumed with the water table 50 m below the surface. The frictional sliding envelope assumes zero tensile strength and a friction angle of 30°. The plotted fractures are all fractures interpreted from SAS image logs in the overbank and distributary channel units. The thrust faults exposed in the mine working are within the area shaded white. The low-angle fractures are the most suitably oriented to be reactivated and thus hydraulically conductive. The high-angle fractures are furthest from the failure envelope and are thus least suitably oriented to be hydraulically conductive.

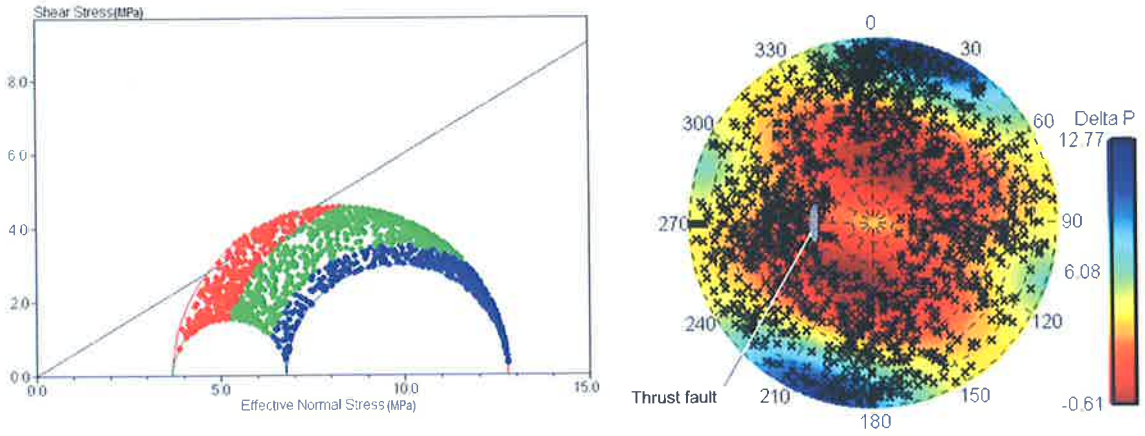

Figure 6.17. Mohr diagram (left) and fracture susceptibility diagram (right) for fractures interpreted in the overbank and distributary channel units from the SAS image logs and stresses at 250 m depth. The fractures are colour coded on the Mohr's circle diagram according to dip; low-angle fractures are red, moderat-angle fractures are green and high-angle fractures are blue.

Overcoring: depleted conditions

The Mohr circle and fracture susceptibility diagrams constructed for rock at 250 m using stress gradients derived from overcoring are shown in Figure 6.18. Pore pressure is assumed to be zero in the absence of any other information, although it may be anywhere between zero and hyrdrostatic. The low-angle fractures generally plot closer to the failure envelope than either the moderate- or high-angle fractures as for virgin conditions because the stress orientations have not changed. However, the differential stress is smaller for depleted conditions possibly due to P_P - S_{Hmax} coupling. As the Mohr circle is smaller, the ΔP_P value of the most optimally oriented low-angle fractures (3.21) is larger than for virgin conditions (-1.86). This implies less potential for hydraulic conductivity in the low-angle fractures under depleted conditions.

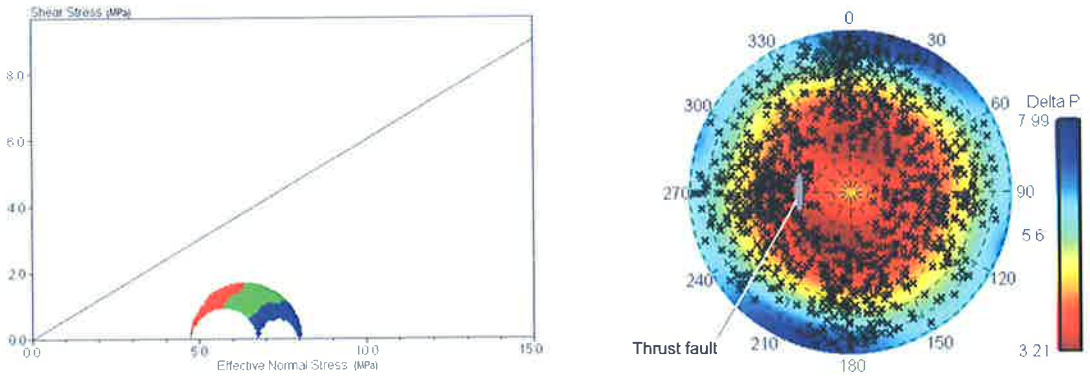

Figure 6.18. Mohr diagram (left) and fracture susceptibility diagram (right) for rock at 250 m assuming zero pore pressure. The ΔP_P value of the most optimally oriented fractures (3.21) is larger than for virgin conditions (1.86).

6.6.2 Coal

Step rate injection: virgin conditions

The Mohr circle and fracture susceptibility diagrams constructed for coal at 250 m using stress gradients derived from the step rate injection tests are shown in Figure 6.19. A hydrostatic gradient is assumed with the water table approximately 50 m below the surface. The frictional sliding envelope assumes zero tensile strength and a friction angle of 30°. The plotted fractures are all fractures interpreted from SAS image logs in the coal seams; coal cleat orientations observed in the mine workings are shown in the area shaded white. The moderate-angle fractures are closest to being critically stressed and are thus most suitably oriented to be hydraulically conductive. The coal face cleats (striking east-west) and flat-lying fractures are furthest from the failure envelope and are thus least suitably oriented to be hydraulically conductive. The orientation of fractures suitably oriented to be hydraulically conductive differs between the rock and coal because, despite the S_{Hmax} azimuth being the same, the stress regime changes from a reverse fault stress regime ($S_v > S_{Hmax} > S_{hmin}$) in the rock to a normal fault stress regime ($S_v > S_{Hmax} > S_{hmin}$) in the coal.

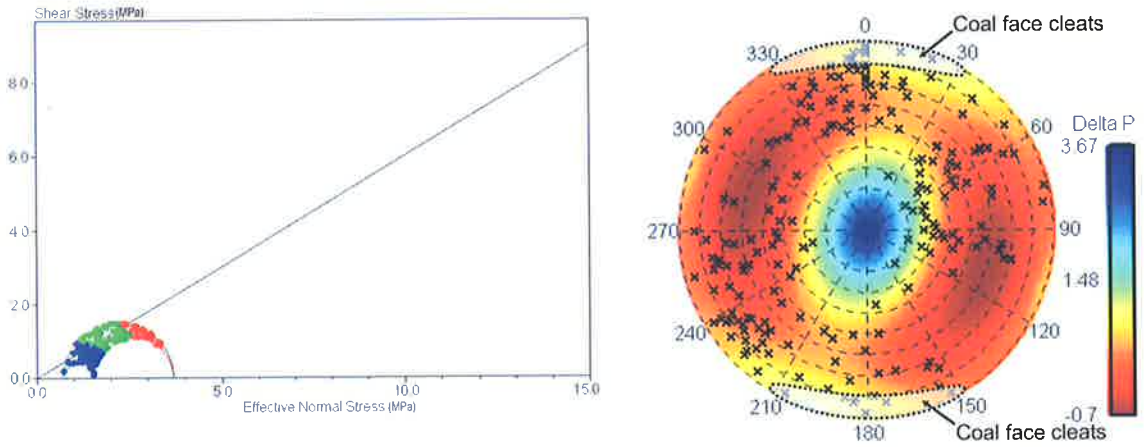

Figure 6.19. Mohr diagram (left) and fracture susceptibility diagram (right) for fractures interpreted in the coal from the SAS image logs and stresses at 250 m depth. The fractures are colour coded on the Mohr's circle diagram according to dip; low-angle fractures are red, moderate-angle fractures are green and high-angle fractures are blue.

Overcoring: depleted conditions

The Mohr circle and fracture susceptibility diagrams constructed for coal at 250 m using stress gradients derived from overcoring tests is shown in Figure 6.20. Pore pressure is assumed to be zero in the absence of any other information, although it may be anywhere between zero and hyrdrostatic. The differential stress and location of the Mohr circle is similar to that constructed using step rate injection data. The Mohr circle would shift further left towards the failure

envelope if pore pressure were greater than zero at the time of overcoring. The moderate-angle fractures are the most suitably oriented to be hydraulically conductive and the coal face cleats (striking east-west) and flat-lying fractures are least suitably oriented to be hydraulically conductive as for non-depleted conditions.

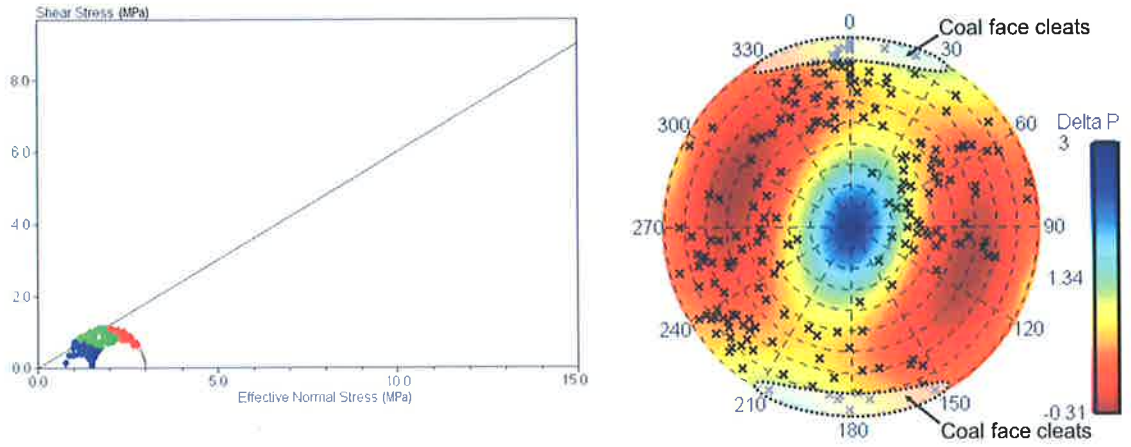

Figure 6.20. Mohr diagram (left) and fracture susceptibility diagram (right) for coal at 250 m assuming zero pore pressure. The Mohr's circle would plot further left towards the failure envelope if the pore pressure were greater than zero at the time of overcoring.

6.7 Synopsis

The stresses measured in the inter-seam rock at Goonyella Riverside are consistent with those presented for the northern Bowen Basin in the Australian stress map (Hillis et al., 1999a; Hillis et al., 1998). The inter-seam rock is characterised by a reverse-stress regime with S_{Hmax} oriented 020°. The Goonyella Middle Seam has significantly lower horizontal stress magnitudes than the inter-seam rock and is characterised by a normal-stress regime with S_{Hmax} also oriented 020°. The significant partitioning of stress between the coal and inter-seam is attributed to the regionally high horizontal stress and differences in mechanical properties between the coal and inter-seam, namely the elastic modulus. The stress distribution between coal and inter-seam at Goonyella Riverside is expected to be analogous to hydrocarbon projects in similar lithologic and high-stress environments.

The findings of this study may be used to assist hydraulic fracture stimulations in similar settings where there is limited or no stress data and the relationship between coal and the inter-seam is less well constrained. Conventional hydraulic fracture completions that treat large intervals of wellbore in these areas may be ineffective for a number of reasons. High background stress causes high initiation and propagation pressures that can prevent successful completion and/or damage the reservoir. Even if a hydraulic fracture is successfully propagated away from the wellbore, it is likely that it will propagate in the lowest stress intervals. This study has shown that

in the presence of high background stress, sandstone intervals within a coal measure sequence are the most stressed and hydraulic fracture treatments over large intervals of a wellbore may thus not treat the sandstone reservoir intervals. A more appropriate strategy may be the use of pinpoint fracture completion technology. Pinpoint fracture completions isolate individual reservoir intervals and constrain the propagation of the induced fracture to the desired interval (Schlumberger, 2004; Thompson et al., 2002).

The fracture susceptibility diagrams demonstrate the effect of stress partitioning between the inter-seam rock and coal. The inter-seam rock is characterised by higher horizontal stresses; accordingly the fractures in the inter-seam rock generally plot further from the failure envelope. The low-angle fractures and thrust faults are most suitably oriented to be hydraulically conductive in the inter-seam rock. This is supported by the field observation that the largest thrust fault intersected by the adit accounted for approximately 50% of all water entering the adit (Callow and Briese, 2002). The fracture susceptibility diagrams show that the face cleats in the coal seams are not suitably oriented to be hydraulically conductive within the in-situ stress field. This situation is not expected to be isolated to Goonyella Riverside. Regional studies show that the dominant face cleat orientation in the Bowen Basin is east-west ± 30° (Pattison et al., 1996) and that the S_{Hmax} azimuth is approximately 030°N (Hillis et al., 1999a) hence limiting hydraulic conductivity along face cleats. The most prospective areas with regard to cleat permeability in the basin will occur where cleats are most suitably oriented for reactivation (i.e. cleats ~060° and S_{Hmax} ~030°).

The effect of pore pressure in the coal and inter-seam is unclear due to limited testing and differences in the test methods at virgin and dewatered conditions. The acquired data implies the stress tensor is coupled with pore pressure in both the coal and inter-seam. P_P-S'_{Hmax} coupling in the inter-seam rock would result in a decrease of differential stress with a decrease in pore pressure (Fig. 6.13). $P_P - S'_{hmin}$ coupling in the coal seams via matrix shrinkage (Fig. 6.15) would cause a differential stress increase with pore pressure reduction. If P_P-S'_{Hmax} coupling occurs in reverse fault stress regimes there are significant implications:

- If P_P-S'_{Hmax} coupling is reversible, differential stress would become larger with increasing pore pressure and a smaller rise in pore pressure would be required to induce failure than a model that does not incorporate P_P-S'_{Hmax} coupling.
- Fractured reservoir evaluation may be significantly affected. Optimally oriented fractures may move further from the failure envelope for a given reduction in pore pressure than if P_P-S'_{Hmax} coupling did not occur (Figs 6.17, 6.18). As the optimally oriented fractures move further from the failure envelope (ΔP becomes larger), their potential for hydraulic conductivity decreases. Consequently, for a given drop in pore pressure the decline in hydraulic conductivity along an optimally oriented fracture may be greater than if P_P-S'_{Hmax} coupling did not occur.

- P_P-S'_{hmin} coupling in normal stress regimes will have the opposite effect, causing fractures to move closer to the failure envelope and be more hydraulically conductive with reservoir development/pore pressure reduction (Figs 6.19, 6.20). Fractured reservoirs in a reverse fault stress regime may demonstrate faster production decline for a given drop in pore pressure than fractured reservoirs in a normal fault stress regime (Fig. 6.21). This may have significant implications for reserve estimates and production strategy.

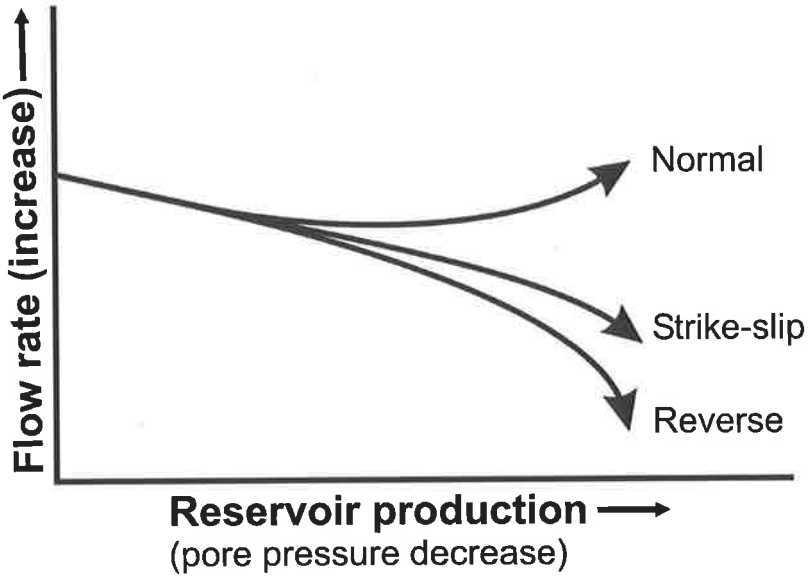

Figure 6.21. Predicted depletion paths for fractured reservoirs in normal, strike-slip and reverse fault stress regimes in the presence of pore pressure stress coupling. For a given reduction in pore pressure, the flow rate in a reverse stress regime will decrease at a faster rate than in a normal stress regime. Flow rates may increase in a normal stress regime if the fractures move closer to the failure envelope due to pore pressure stress coupling.

The bedding planes between coal and inter-seam have acted as mechanical discontinuities over geologic time (Fig. 4.4) and they may also activate during reservoir development with deleterious effects to CSM developments. Pore pressure increase has been shown to cause movement on optimally oriented surfaces however a reduction in pore pressure may also cause bedding plane slip to occur along a coal-clastic interface. It is clear that the coal seams respond quite differently to pore pressure changes due to dewatering than the inter-seam. Because the coal is more compressible than the inter-seam it becomes mechanically decoupled with pore pressure reduction and becomes at least partially isolated from the far-field stress tensor. As the layers respond differently to pore pressure reduction the layers will readjust resulting in minor bedding plane slip. Bedding plane slip during reservoir development has the potential to create significant wellbore deformation and reduction in productivity in CSM projects as described in Johnson et al. (2002) and Chapter 2 (Fig. 2.10) for the Scotia field.

The practice of elevating pore pressure during hydraulic fracture completions followed by pore pressure reduction due to dewatering may create further complexity and exacerbate the problem. If a well is hydraulically fractured at the same time an adjacent well is dewatered, significant effective stress gradients may be created between the wells, further contributing to the problem. Cavitation completions that avoid significant pore pressure elevation could be considered where the strength and elastic properties of the coal and reservoir characteristics are suitable (Sinka, 1998). Cavitation completions that do not require casing at or near the inter-seam/coal contact would eliminate the issue of damaged casing/collars. Ideally, coal seam dewatering should be avoided to minimise coal compaction. If dewatering is necessary, the way in which the reservoir is dewatered will also impact on the propensity for bedding plane slip to occur. An equal and simultaneous amount of dewatering across a field could be considered to reduce the risk of bedding plane slip.

7 Amadeus Basin Study – Background

7.1 Introduction

The mature Mereenie and Palm Valley fields of the northern Amadeus Basin are both, to a varying degree, fractured reservoirs that are in production decline. This part of the thesis uses a variety of techniques in structural geology from regional cross-section construction to curvature analysis to optimise development of the Palm Valley and Mereenie reservoirs and to help assess the potential for additional reserves. The Palm Valley gas field is approximately 120 km southwest of Alice Springs and has been in operation since 1983 (Fig. 7.1). The original gas in place in the Palm Valley fracture network and matrix was estimated at 10.79 BCF and 834.01 BCF respectively (Aguilera, 1995). The Palm Valley Field is a type 2 fractured reservoir (Berry et al., 1996; Nelson, 1985) with an interconnected network of fractures accessing the low permeability matrix (~0.1 mD) of the Ordovician Stairway Sandstone and Pacoota Sandstone (Berry et al., 1996). Wells that do not intersect the fracture network record only minor gas shows, whereas wells that intersect major fractures have recorded flows as high as 137 MMCFD (Do Rozario, 1991).

The Mereenie oil and gas field is approximately 250 km west-southwest of Alice Springs and has been in operation since 1984. Initial recoverable reserves were estimated at 19 MMSTB of oil and 590 BCF of gas (Havord, 1991). Mereenie is a type 3 fractured reservoir where fractures assist matrix flow in the relatively high permeability (up to 10 mD) and porosity (8%) intervals of the Ordovician Pacoota Sandstone. It is thought that naturally fractured sweet-spots within the Mereenie field could contribute substantially to reservoir performance (Campagna and Flottmann, 2002; Hillis et al., 1999b).

The reservoirs at Mereenie are considerably less fractured than at Palm Valley although they both occur in similar structural settings. This study considers both structures in the context of basin evolution and compares their structural development to elucidate the mechanism(s) behind natural fracture development. An improved understanding of fracture development will assist future development drilling and may increase reserves and extend field life. The as yet untested Mereenie sub-thrust play also has the potential to increase field reserves. The sub-thrust play is explicitly dependent on the structural evolution of the Mereenie Anticline and is assessed as part of this study.

This chapter describes the necessary background for the study, including a brief description of current tectonic models and of the stratigraphy of the Amadeus Basin. Chapter 8 presents a series of regional cross-sections constructed through the Mereenie and Palm Valley anticlines that are used to assess the Mereenie sub-thrust play, to understand fracturing within the basin, and to improve the current understanding of basin evolution. Chapter 9 presents a comparison

between the Mereenie and Palm Valley fields to elucidate the mechanisms of, and controls on, natural fracture development in the northern Amadeus Basin. Chapter 10 assesses structural issues relating to the Mereenie sub-thrust play and potential additional reserves.

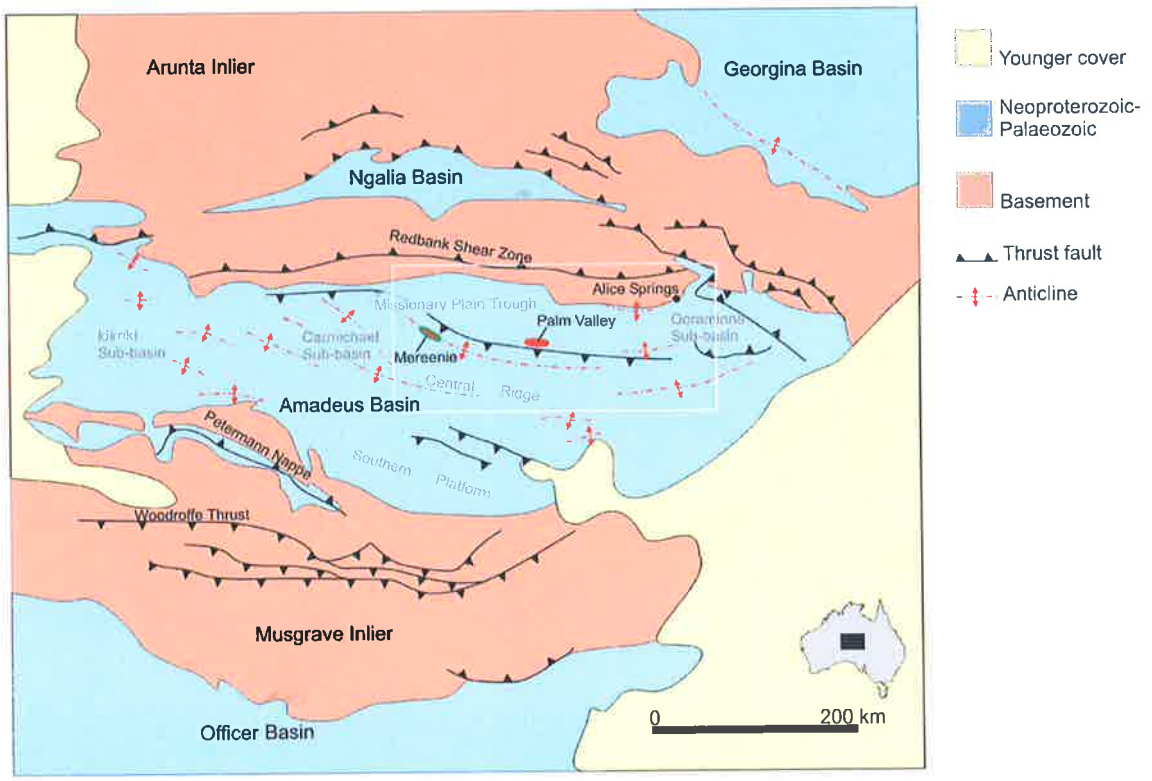

Figure 7.1. Regional map of central Australia showing basement provinces with Neoproterozoic-Palaeozoic and younger cover. The location of Figure 7.3 is outlined by the white rectangle (Flottmann and Hand, 1999; Kennard and Lindsay, 1991).

7.2 Tectonic Evolution of the Amadeus Basin

The initial phases of the Amadeus Basin remain enigmatic because good quality outcrop below the Heavitree Quartzite is scant and seismic imaging below the salt-bearing Bitter Springs Formation is poor. Korsch and Lindsay (1989) constructed basin subsidence curves to help constrain the basin evolution. They identify three major tectonic cycles based on the subsidence curves (Fig 7.2):

- Stage 1 (900–590 Ma): initiation as an intra-cratonic extensional basin;
- Stage 2 (580–450 Ma): compression in the southern Amadeus Basin during the Petermann Orogeny (PO) and contemporaneous extension in the northern Amadeus Basin;
- Stage 3 (450–300 Ma): compression during the Alice Springs Orogeny (ASO).

Stage 3 is of particular interest to this study as the Mereenie and Palm Valley structures formed during the ASO. The following brief descriptions of Stages 1, 2 and 3 of basin development provide necessary background for the following chapters and are based principally on Korsch and Lindsay (1989).

7.2.1 Stage 1 (900-590 Ma): extension

Several lines of evidence, including subsidence curves and geological associations, suggest that the Amadeus Basin and other interior basins of similar age initiated as extensional basins approximately 900 Ma (Korsch and Lindsay, 1989; Lee et al., 2002). However, no significant normal faults have been identified in the Amadeus Basin. This is often accounted for by the poor seismic imaging of the proposed rift sequence below the thick salt-bearing Bitter Springs Formation. A number of geological associations, similar to modern rift settings, have been cited as further evidence for an initial phase of extension around 900 Ma. Firstly, fluvial sediments and basalts occur together in the Dixon Range Beds and Mount Harris Basalt in the southwest of the basin. Secondly, the Heavitree Quartzite unconformably overlies an unnamed section of basalt and felsic volcanics in the northwest of the basin, and thirdly the mafic Stuart Dyke Swarm intrudes metamorphic rocks of the Arunta Block and has Rb-Sr isotopic ages of 897 Ma correlated with the Mount Harris Basalt (Korsch and Lindsay, 1989; Shaw et al., 1991a). A long period of thermal subsidence followed the rifting phase resulting in widespread Neoproterozoic sedimentation. Isopach maps constructed by Wells et al. (1970) show that the Neoproterozoic succession is asymmetric with greatest thickness along the southwest margin adjacent to the inferred rift that became the locus of the subsequent Petermann Orogeny.

7.2.2 Stage 2 (580-450 Ma): mixed extension and compression

The Amadeus Basin was dominated by synchronous compression in the south and extension in the north of the basin during the Cambrian.

Southern Amadeus

Major thrusting and nappe formation referred to as the Petermann Orogeny occurred along the southwest margin of the Amadeus Basin between 570–530 Ma (Camacho et al., 1997; Maboko et al., 1992; Walter et al., 1995). The focus of the Petermann Orogeny is the site of inferred rifting during Stage 1, implying inversion of major rift faults during the Petermann Orogeny (Hand and Sandiford, 1999). Deformation was focused along the northern portion of the Musgrave Block in the vicinity of the Woodroffe fault system (Fig. 7.1). The Woodroffe Thrust is a mylonite zone up to 3 km thick that dips ~30° towards south and offsets the Moho by ~20 km (Hand and Sandiford, 1999). Total crustal shortening due to the Petermann Orogeny is estimated at 60–100 km, uplifting the Musgrave basement block and effectively isolating the Amadeus Basin from the Officer Basin to the south (Close et al., 1998; Hand and Sandiford, 1999; Scrimgeour and Close,

1999). A limited foreland basin and peripheral bulge developed during the Petermann Ranges Orogeny, termed the Mount Currie Sub-basin and Central Ridge respectively (Lindsay, 1987; McNaughton and Huckaba, 1978). A thick molasse wedge, the Mount Currie Conglomerate, was deposited in the Mount Currie Sub-basin in front of the Petermann Ranges in the area of the southern platform (Fig 7.1).

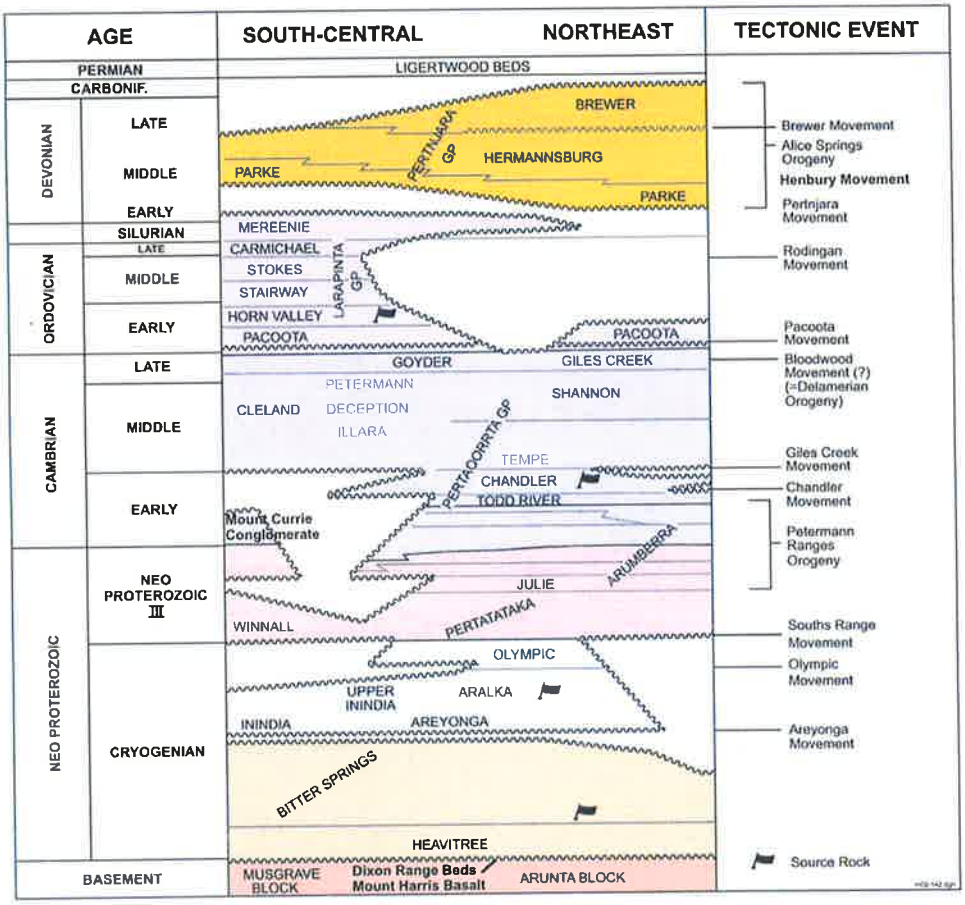

Figure 7.2. Time-space plot of the Amadeus Basin showing the relationships between stratigraphic groups and tectonic events (Gibson et al., 2004).

Northern Amadeus

The subsidence curves for the northern Amadeus Basin indicate that the Carmichael, Idirriki and Ooraminna sub-basins and Missionary Plain Trough subsided due to thermal recovery following a short period of extension approximately contemporaneously with the Petermann Orogeny. The exact nature of the extensional event is unclear because seismic imaging below the Bitter Springs Formation is poor. The zone of extension and marine sedimentation in the north was partitioned from the zone of compression and terrestrial sedimentation in the south by a flexural high or peripheral bulge termed the Central Ridge (Lindsay, 1987; McNaughton and Huckaba, 1978). The Arumbera Sandstone is an approximate time equivalent of the Mount Currie Conglomerate, sourced from the Petermann Ranges Nappe and recycled Mount Currie Conglomerate. The stratigraphic interval from the Arumbera Sandstone through to the Silurian

Mereenie Sandstone was deposited during Stage 2. Sediments were typically sourced from the west, bypassing the Central Ridge, and were directed into the northern sub-basins and Missionary Plain Trough from the south and west. Maximum sediment thickness above the central ridge is in the order of 2000 m compared to 14 000 m in the Carmichael Sub-basin (Kennard and Lindsay, 1991; Lindsay and Korsch, 1991).

7.2.3 Stage 3 (400-300 Ma): Alice Springs Orogeny

A third, compressional stage of basin development referred to as the Alice Springs Orogeny (ASO) occurred between 400–300 Ma (Shaw and Black, 1991; Shaw et al., 1984). The ASO is of particular significance to this study because the Mereenie and Palm Valley structures were formed and charged during this period. The ASO uplifted the Arunta Inlier, effectively isolating the Amadeus Basin from the Ngalia Basin to the north. Deformation was focused along the north-dipping Redbank Shear Zone along the contemporary northern basin margin. The ASO created the MacDonnell Homocline and emplaced several basement-cored nappes along the northern margin of the Amadeus Basin (Fig. 7.3). The MacDonnell Homocline has a strike length of over 200 km and is characterised by steep southerly dips that are locally overturned. The homocline is fronted by an asymmetric synclinal zone that merges with sub-horizontal sections of the Amadeus Basin in the Missionary Plain (Fig. 7.3).

The presence of basement-cored nappes within the Bitter Springs Formation along the northern margin of the Amadeus Basin led early workers to propose thin-skinned models for the ASO. Early models of the ASO and the Redbank Shear Zone were of a thin-skinned Alpine type with up to 70 km of shortening over a distance of approximately 110 km (Teyssier, 1985). Several lines of evidence have since emerged inconsistent with Alpine type models. Regional seismic data shows that the Redbank Shear Zone dips at 35°– 45° and vertically offsets the Moho by ~20 km thereby limiting maximum crustal shortening to ~30 km (Goleby et al., 1994; Goleby et al., 1989; Wright et al., 1991). Thick-skinned models and shortening of ~30 km are also corroborated by ^{40}Ar-^{39}Ar data that show the basement was only uplifted ≤12 km during the Alice Springs Orogeny (Flottmann and Hand, 1999; Shaw et al., 1992). A suite of thin-skinned features developed in front of the basement culmination during the ASO (Flottmann and Hand, 1999; Wells et al., 1970) and these are the subject of subsequent chapters.

Sedimentological and geochemical evidence suggests the ASO had a protracted history with several distinct phases of orogenic activity (Bradshaw and Evans, 1988; Forman et al., 1967; Wells et al., 1970). The proposed stages are recorded by stratigraphic relationships in the Pertnjara Group of the Amadeus Basin and in the Ngalia Basin and include the following.

1. The Rodingan Movement was the initial stage of the ASO resulting in up to 3000 m of erosion in the east of the basin creating the unconformity between the Larapinta Group and Mereenie Sandstone (Bradshaw and Evans, 1988; Wells et al., 1970).

2. The Pertnjara Movement created the unconformity between the Mereenie Sandstone and the base of the Pertnjara Group (Bradshaw and Evans, 1988; Forman et al., 1967).

3. The Henbury Movement occurred prior to and during deposition of the Hermannsburg Sandstone (Bradshaw and Evans, 1988; Wells et al., 1970).

4. The Brewer Movement resulted in substantial uplift and erosion of the northeast of the basin removing up to 1200 m of Hermannsburg Sandstone prior to deposition of the Brewer Conglomerate (Bradshaw and Evans, 1988). Approximately 2.5 km of section has since been removed to form the current topography implying that the Brewer Conglomerate was 5–6 km thick in front of the homocline (Tingate et al., 1986).

5. The Mount Eclipse Movement refers to the Early Carboniferous stage of deformation that affected the Ngalia Basin to the north of the Amadeus Basin (Bradshaw and Evans, 1988; Wells and Moss, 1983). It appears that deformation along the MacDonnell Homocline may have ceased by this time and the locus of deformation had shifted north to the Ngalia Basin.

The preceding discussion implies an intimate association between basin dynamics and sediment deformation. A clear relationship exists between the location of rift basins and subsequent orogenic activity suggesting major inversion (Hand and Sandiford, 1999). The locus of Stage 1 extension is the present southwest margin of the basin and was the site of the subsequent Petermann Ranges Orogeny. Stage 2 extension occurred along the northern basin margin and became the site of the subsequent Alice Springs Orogeny.

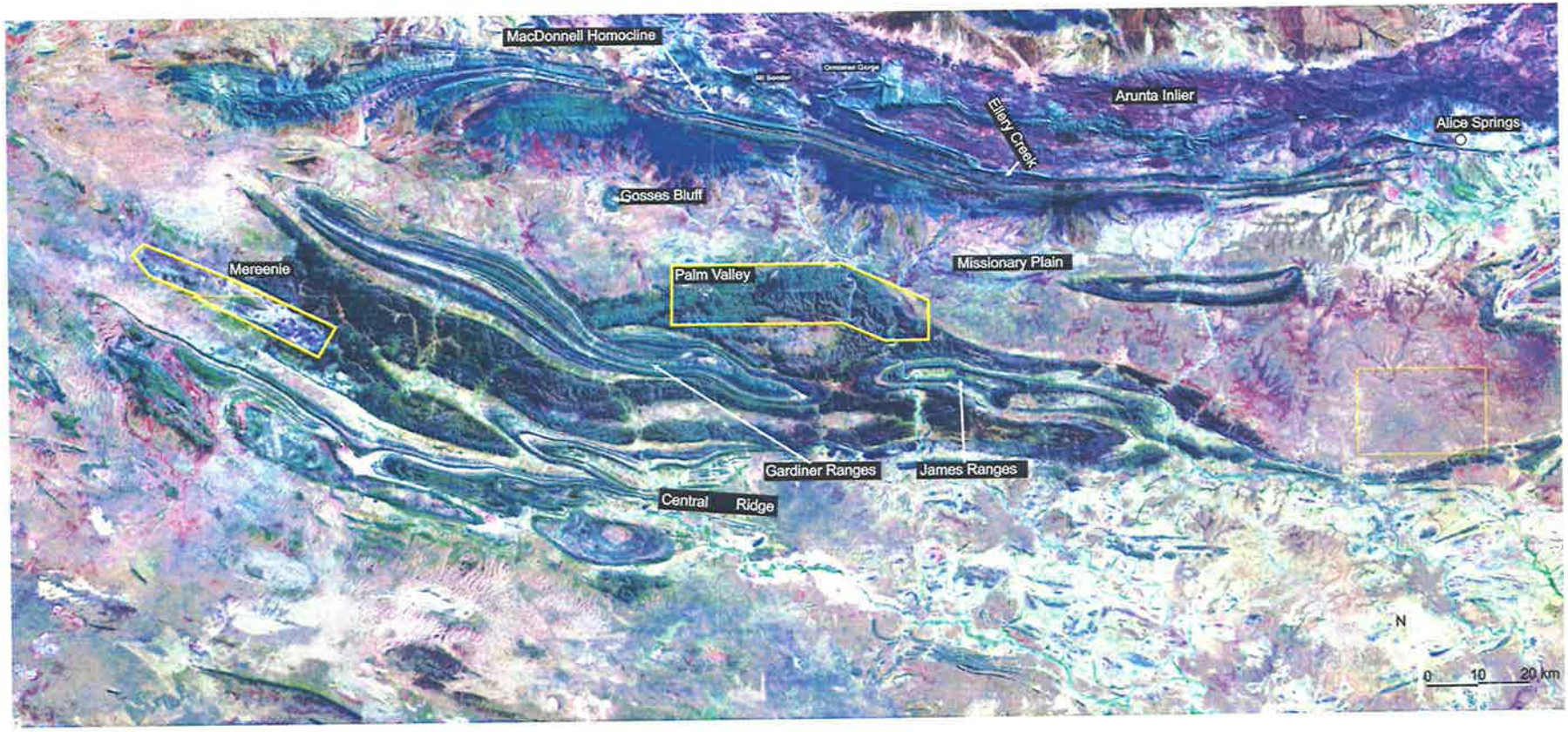

Figure 7.3. Landsat image of the central Amadeus Basin showing the MacDonnell Homocline and thin-skinned structures including the Mereenie, Palm Valley, Gardiner and James Range anticlines. The location of the landsat image is shown in Figure 7.1 (NASA, 2004).

7.3 Stratigraphy of the Northern Amadeus Basin

The stratigraphy of the Amadeus Basin provides a first order control on deformation style within the basin and a brief introduction is included here as background to the following chapters. The Amadeus Basin is a remnant of a much more extensive basin termed the Centralian Basin (Walter et al., 1995). There is significant variation in stratigraphy across the Amadeus Basin. Maximum sediment thickness above the central ridge is in the order of 2000 m compared to 14 000 m in the Carmichael Sub-basin. Many of the formations are poorly understood and, in parts, inconsistently named. The following description focuses on the stratigraphy of the northern Amadeus Basin. The stratigraphic sequence in the northern Amadeus Basin can be grouped into five major intervals: 1) the Proterozoic; 2) the Cambrian Pertaoorrta Group; 3) the Ordovician Larapinta Group; 4) the Silurian; and, 5) the Devonian Pertnjara Group (Fig. 7.2).

7.3.1 Proterozoic

The Heavitree Quartzite was deposited in a post-rift, thermal phase and lies unconformably over an inferred rift sequence comprising the Bloods Range Beds and Dixon Range Beds and the Musgrave and Arunta basement inliers (Lindsay and Korsch, 1991). The Heavitree Quartzite is a sandy, fluvial and tidal sequence up to 700 m thick (Clarke, 1979). The sandstones are preserved as quartzite and are the most lithified and competent rocks within the Amadeus Basin sequence.

The Bitter Springs Formation conformably overlies the Heavitree Quartzite and comprises the Gillen and Loves Creek Members. The Gillen Member comprises significant evaporites and carbonates deposited in a shallow marine, low-stand systems tract. The average thickness of the evaporite sequence across the basin is estimated to be ~ 800 m (Lindsay and Korsch, 1991). The overlying Loves Creek Member is a mixed siliciclastic and carbonate sequence deposited in lacustrine conditions during transgressive and high-stand systems tracts (Southgate, 1991).

The Areyonga Formation is a fluvial and glaciogene sequence unconformably overlying the Bitter Springs Formation (Lindsay and Korsch, 1991). The Pertataka and Julie formations overlie the Areyonga Formation. The Pertataka and Julie formations are a shallowing-upward depositional sequence comprising deep-water pelagic and turbidite units (Pertataka Formation) grading to oolitic platform carbonates at the top of the Julie Formation in the eastern portion of the basin (Lindsay and Korsch, 1991). The entire Proterozoic succession from the Heavitree Quartzite to the Julie Formation is typically ~2000 m thick, but is up to 4000 m in the south and 3000 m in the northeast of the basin (Lindsay and Korsch, 1991).

7.3.2 Cambrian: Pertaoorrta Group

The Cambrian Pertaoorrta Group comprises the Arumbera Sandstone through to the Goyder Formation. The sequence ranges from 2000–3000 m thick in the northern sub-basins and thins over the central ridge (Lindsay and Korsch, 1991). Sediment supply was predominantly from the southwest and typically bypassed the southern platform area in response to the Petermann Ranges Orogeny. The Arumbera Sandstone is the earliest Cambrian formation and is a thick deltaic-marine clastic sequence. The Arumbera Sandstone has been identified in all the northern sub-basins and onlaps the Missionary Plain Trough and the Central Ridge (Kennard and Lindsay, 1991; Lindsay and Korsch, 1991). The Chandler and Tempe formations overlie the Arumbera Sandstone. The Chandler Formation comprises shale, thin carbonate layers and, east of Palm Valley, halite deposits (Bradshaw, 1991). The Tempe Formation unconformably overlies the Chandler Formation and comprises shoreface sandstones, siltstones, shales and skeletal limestones (Kennard and Lindsay, 1991). The Illara Sandstone, Deception Formation and Petermann Sandstone overlie the Tempe Formation in the Carmichael Sub-basin. The Illara Sandstone is an eastward-prograding, low-stand fluvial wedge. The Deception Formation overlies the Illara Sandstone and comprises a mix of fluvial and marine siltstones and sandstones. The Petermann Sandstone and Cleland Sandstone (Idirriki Sub-basin) are time equivalents and overlie the Deception Formation, comprising braided stream, fluvial and overbank units (Kennard and Lindsay, 1991).

The Goyder Formation is the youngest formation in the Cambrian Pertaoorrta Group and is of particular importance to this study as it provides a potential juxtaposition seal to the Mereenie sub-thrust play. The lower member is interpreted as a late high-stand deposit of west-sourced fluvio-deltaic siliciclastics in the western part of the basin (Carmichael Sub-basin) grading to marine carbonates in the eastern part of the basin. The upper Goyder Formation is predominantly silty, fine-grained sandstone interpreted as a late highstand, nearshore to outer shelf sequence. The sandstones are typically calcareous, kaolinitic and/or manganiferous with some thin glauconitic intervals (Kennard and Lindsay, 1991; Lindsay and Korsch, 1991).

7.3.3 Ordovician: Larapinta Group

The late Cambrian to Ordovician Larapinta Group hosts all the known commercial hydrocarbon accumulations in the Amadeus Basin. The Larapinta Group comprises the Pacoota Sandstone, Horn Valley Siltstone, Stairway Sandstone and the Stokes Siltstone. The Larapinta Group is in the order of 1500 m thick in the Carmichael Sub-basin and 1000 m thick in the Missionary Plain Trough (Lindsay and Korsch, 1991).

The Pacoota Sandstone is dominantly a marine shoreface succession with some braided stream intervals (Deckelman, 1991). The Pacoota Sandstone can be divided into four units, the P4, P3, P2 and P1 (Williams et al., 1965). The P4 unit is a sequence of quartz arenite and orthoquartzite

at the base of the Pacoota Sandstone. The P3 unit is a sequence of interbedded sandstone and shale that extends from the top of the P4 to the base of the lowest glauconitic layer within the P2. The P2 unit is a sequence of interbedded, locally glauconitic sandstone, argillaceous sandstone, shale and limestone. The P1 unit is an interbedded sequence of non-glauconitic sandstone and shale that extends from the top P2 to the base of the Horn Valley Siltstone (Deckelman, 1991).

The Horn Valley Siltstone is a sequence of bioturbated shale and siltstone with interbedded bioclastic limestone and dolomite. The sequence was deposited in shallow marine-shelf conditions during a transgressive-regressive cycle and was buried rapidly, preventing oxidation and facilitating preservation of organic matter, and is the source rock of the Mereenie and Palm Valley fields (Do Rozario, 1991; Elphinstone and Gorter, 1991; Lindsay and Korsch, 1991). The Stairway Sandstone has a gradational contact with the Horn Valley Siltstone which comprises an intertidal marine sequence of sandstone, siltstone and shale (Do Rozario, 1991). The shallow marine Stokes Formation overlies the Stairway Sandstone and comprises a series of interbedded sandstone, siltstone and shale.

7.3.4 Silurian: Mereenie Sandstone

The Mereenie Sandstone unconformably overlies the Larapinta Group and comprises shallow marine, fluvial and aeolian sequences. The Mereenie Sandstone is approximately 500 m thick in the Mereenie area.

7.3.5 Devonian-Carboniferous: Pertnjara Group

The ASO resulted in significant uplift of the Arunta Inlier, effectively isolating the Amadeus Basin from the Ngalia Basin to the north (Fig. 7.1). Syntectonic erosion and sedimentation sourced from the north deposited the Pertnjara Group between the MacDonnell Homocline and the Central Ridge. The Pertnjara Group comprises the Parke Siltstone, Hermannsburg Sandstone and Brewer Conglomerate. The Brewer Conglomerate is a synorogenic molasse sequence deposited as a series of coalescing alluvial fans. It is a polymict conglomerate containing clasts up to 1 m reflecting progressive stripping of the source area. The Pertnjara Group is in the order of 4000 m thick in the Carmichael Sub-basin and thins towards the south and east to approximately 2600 m in the Missionary Plain Trough and does not occur over the Central Ridge. Up to 2500 m of section has been removed from the Pertnjara Group along the northern basin margin due to subsequent uplift and erosion (Tingate, 1991).

This chapter has provided an introduction to the Amadeus Basin study and briefly describes the tectonic evolution and stratigraphy of the basin. The following chapter presents detailed structural modelling and section construction through the Mereenie and Palm Valley fields. The

structural modelling is used subsequently in Chapters 9 and 10 to help constrain natural fracture development in the basin and assess the Mereenie sub-thrust play.

8 Structural Modelling and Construction of Cross-sections

8.1 Background

This chapter presents structural modelling and regional cross-sections constructed through the Mereenie and Palm Valley fields. Subsequent chapters of this thesis use the structural modelling to help understand fracture development in the Mereenie and Palm Valley fields and reduce risk associated with the Mereenie sub-thrust play.

8.2 Mechanical Stratigraphy

The stratigraphy of the Amadeus Basin exerts a first-order control on deformation style within the basin. Significant rheological variations within the sequence have created a basin-wide mechanical stratigraphy that may be divided into three pre-ASO intervals and one syn-ASO interval.

1. The basal sequence, comprising the Mesoproterozoic igneous and metamorphic basement and the overlying Neoproterozoic Heavitree Quartzite. Deep burial and extensive diagenesis of the Heavitree Quartzite have imparted rheological properties similar to those of the basement (Flottmann and Hand, 1999).

2. The Bitter Springs Formation, namely the Gillen Member is an evaporite- and carbonate-bearing sequence and constitutes a mechanically weak layer. The Bitter Springs Formation acts as a regional detachment surface and effectively decouples overlying units from the basal sequence (Flottmann and Hand, 1999; Forman et al., 1967).

3. The upper sequence, comprising the late Neoproterozoic through to the Silurian Mereenie Sandstone. The sequence is a siliciclastic succession with minor carbonate intervals and has deformed in a relatively elastic manner. Minor detachment surfaces occur along various shale intervals throughout the sequence but do not play a significant role in the basin-scale deformation kinematics.

4. The Pertnjara Group is a syn-ASO molasse wedge in front of the basement culmination and has had a significant impact on the dynamics and evolution of the MacDonnell Homocline and the location of foreland folds.

8.3 Basement-Cover Interaction

Recently developed thick-skinned models have superseded previous thin-skinned models of the northern Amadeus Basin tectonic evolution. The presence of basement-cored downward-facing synformal anticlines embedded within the Bitter Springs Formation along the northern basin margin had previously been explained via an Alpine-style thin-skinned model (Teyssier, 1985). However, subsequent evidence including deep seismic profiling and geochemical work show that the major basement fault zones (i.e. Redbank Shear Zone) dip at 35°– 45° and that a thick-skinned model is more appropriate (Goleby et al., 1989; Shaw and Black, 1991). Flottmann and Hand (1999) have explained the interaction between basement and the sedimentary cover during the Alice Springs Orogeny and account for the basement-cored folds within a thick-skinned model. Figure 8.1 shows a simplified, sequentially restored section along a section through the MacDonnell Homocline and Mount Sonder (Flottmann and Hand, 1999). The geometry of the basement culmination is similar to the core of trishear fault propagation folds described for the intra-continental Laramide uplift in Wyoming, USA (Allmendinger, 1998; Erslev, 1991).

Flottmann and Hand (1999) explain the basement-cored synformal anticlines as tilted basement-cored wedges created via significant displacement partitioning between the basement and cover. The basement and the Heavitree Quartzite form the wedge proper that propagated towards the foreland along a detachment within the Bitter Springs Formation. The upper sequence accommodates the same amount of displacement by back-thrusting along a detachment within the Bitter Springs Formation (Fig. 8.1). Although the Redbank Shear Zone vertically offsets the Moho by ~ 20 km (Goleby et al., 1989), it only displays ~3 km of vertical offset at existing outcrop level (Flottmann et al., 2004; Shaw et al., 1992). Flottmann et al (2004) argue this discrepancy can be accounted for because most of the upper crustal displacement was accommodated by shortcut thrusts in the footwall of the Redbank Shear Zone. The footwall shortcut thrusts influenced homocline formation and rotated the basement wedges through 90° emplacing the downward-facing, synformal basement-cored anticlines (Fig. 8.1).

8.4 Detachment Folds

Shortening of the Bitter Springs Formation and upper sequence during the ASO was accommodated by folding and minor faulting within the foreland in front of the MacDonnell Homocline. The vergence of the folds is bi-directional (i.e. hinterland-ward and foreland-ward), typical of fold and thrust belts with weak, sub-horizontal detachments (Davis and Engelder, 1985). Some of the folds are breached by faults (e.g. the Gardiner Range Anticline) and others are not (e.g. the Palm Valley and James Range anticlines). The variation in fold orientation from northwest–southeast in the Mereenie to east–west, east of Palm Valley (Fig. 7.2) has received significant previous study. Bradshaw and Evans (1988) interpret the variation to be due to

different phases of deformation with different shortening vectors. The author believes a more compelling hypothesis is presented by Stearns et al (1995) who interpret the variation in fold strike is due to an arcuate junction between underlying basement blocks and a single folding phase.

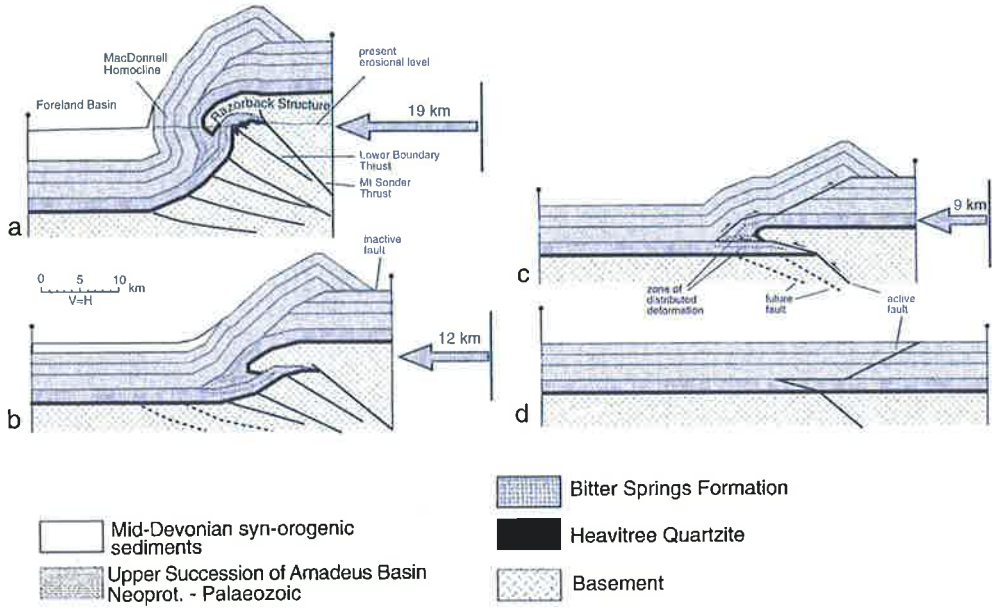

Figure 8.1. Sequentially restored cross-section showing the final deformational geometry along a section through Mount Sonder. The Razorback structure is an intercutaneous basement wedge confined to the Bitter Springs Formation. Footwall shortcut thrusts caused rotation of the wedge and emplacement of basement-cored folds. Arrows on right indicate orogenic shortening in kilometres (Flottmann and Hand, 1999).

The folds of the Amadeus Basin foreland are similar to those described by various authors in other forelands with weak basal layers (Currie et al., 1962; Gil and Jurado, 1998; Mitra, 2003; Poblet and McClay, 1996) and are interpreted herein as detachment folds. The geometry and evolution of detachment folds is strongly dependent on the mechanical stratigraphy and is sensitive to stratigraphic thickness and ductility contrasts (Currie et al., 1962; Davis and Engelder, 1985). Detachment folds form in stratigraphic packages with high competency contrasts between a mechanically weak basal layer, such as an evaporite sequence or an overpressured shale, and relatively competent overlying units. Detachment folds are characterised by parallel fold geometry in the competent units (i.e. the upper section). Projection of the parallel fold form within the competent units to an anticlinal core results in a space problem that is accommodated by disharmonic folding of the mechanically weak basal layer in the fold core (Fig. 8.2). The disharmonic folding eventually terminates in a basal detachment within the mechanically weak basal layer (Dahlstrom, 1969; Mitra, 2003), in this instance within the Bitter Springs Formation (Fig. 8.2).

Detachment folds first form by symmetric or asymmetric folding, with the fold wavelength controlled by the thickness of the mechanically competent units. The ductile basal unit flows from the synclines to the anticlines in the early stages of folding via non-elastic deformation. Increasing fold amplitude and wavelength involves both limb segment rotation and hinge migration (Mitra, 2003; Poblet and McClay, 1996). Rotation of the fold limb initially occurs by flexural slip folding but may involve significant internal deformation between locked hinges in the late stages of deformation (Mitra, 2003; Poblet and McClay, 1996). The forelimb of a detachment fold can become faulted as the fold develops, thereby creating a break-thrust structure. Faulting of fold limbs typically occurs due to high strains on the fold limbs during rotation and may be induced by reduced flexural slip efficiency of the competent units, a reduced ductility contrast, or evacuation of the basal ductile unit from around the fold (Mitra, 2003). Variations in detachment fold geometry such as asymmetry and faulting have been related to variations in the initial mechanical stratigraphy and pre-existing structure (Mitra, 2003). Detachment folds may initiate at pre-existing discontinuities or perturbations on the basal detachment such as faults or changes in basement dip.

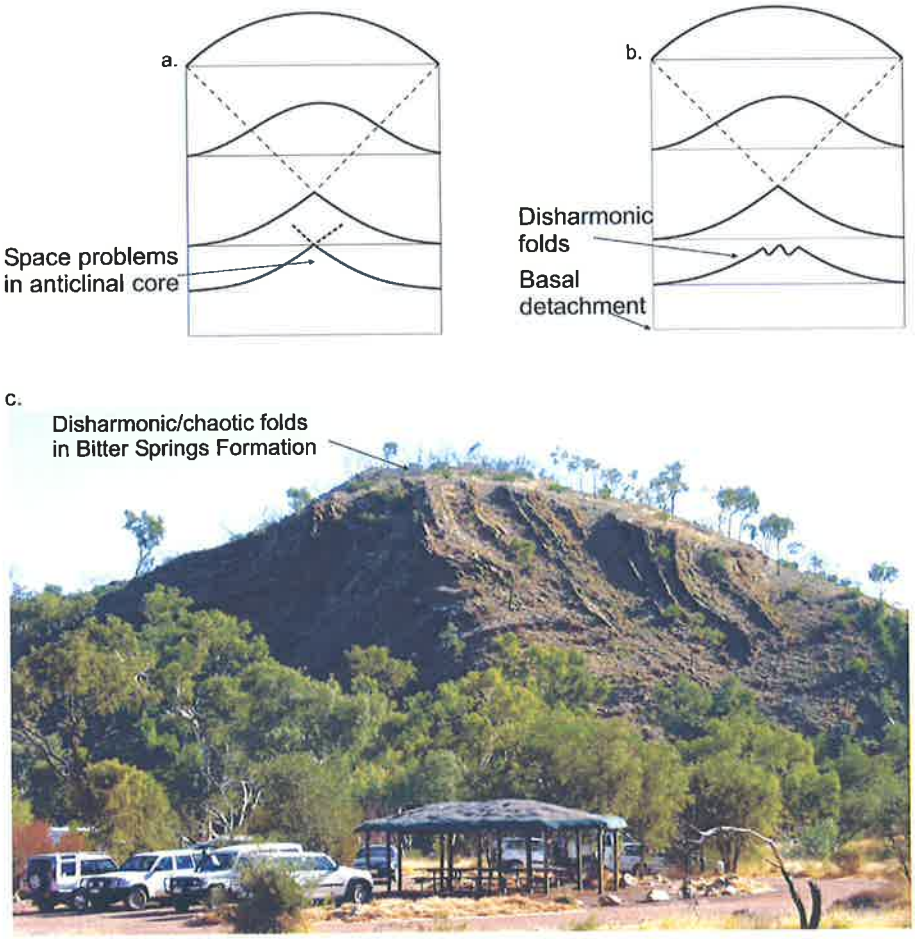

Figure 8.2. Geometry of disharmonic detachment folds. a) Space problems in the core of a concentric fold resulting from convergence of radii of curvature to form a cuspate geometry in the fold core. b) Space problems in the core of the anticline are resolved by disharmonic folding of the incompetent basal unit above the detachment (De Sitter, 1964; Mitra, 2003). c) Example of disharmonic/chaotic folding within the Bitter Springs Formation at the base of the MacDonnell Homocline at Ellery Creek (Fig. 7.2).

8.5 Construction of Regional Cross-sections

Balanced regional cross-sections have been constructed through the Mereenie and Palm Valley fields and are constrained by the models of basement-cover interaction and detachment folding presented in the previous sections. Two additional sections have been constructed to the west and east of Palm Valley to help understand the relationship between the Gardiner Range, James Range and Palm Valley anticlines (Fig. 7.3).

8.5.1 Cross-section inputs

Existing geological maps and seismic, magnetic and well data were integrated using Midland Valley's 2D Move software to construct the sections.

Maps

Scanned copies of the existing 1:250 000 geological map sheets provided the basic framework for section construction (Appendix B). The Mereenie section has been constructed through the Lake Amadeus (Wells et al., 1962) and Mount Liebig (Wells et al., 1961) 1:250 000 sheets. The Gardiner Range, Palm Valley and James Range sections are constructed through the Henbury (Ranford et al., 1963) and Hermannsburg (Shaw et al., 1995) 1:250 000 sheets.

Wells

The cross-sections have been constructed through or near existing petroleum and regional stratigraphic wells as shown on the sections. Table 8.1 shows the wells used in each section.

Section	Well	Distance from section	Source
Mereenie	Undandita 1A	3 km	Santos Ltd
	BMR Mount Liebig 2	13 km	NTGS
	East Mereenie 4	0	NTGS
	East Johnny's Creek 1	16 km	NTGS
Gardiner Range	Tyler 1	8 km	NTGS
	Wallara 1	17 km	NTGS
Palm Valley	Palm Valley 4	0	Santos Ltd
	Wallara 1	11 km	NTGS
James Range	Finke 1	10 km	NTGS
	James Range A	16 km	NTGS

Table 8.1. List of wells used in construction of the cross-sections showing distance from section lines. Stratigraphic markers from the wells were used to constrain the cross-sections.

Seismic Data

The Mereenie section runs along seismic section m83-16 and the Palm Valley section runs along seismic section PV94-4 acquired by Santos Ltd and Magellan Petroleum respectively. Both digital sections were imported into 2D Move and depth-converted using a constant velocity derived from check-shot velocities. The indurated rocks at shallow depth have similar properties to those at reservoir depth, imparting a relatively constant velocity from the surface to the Pacoota Sandstone of 4210 m/s for the Mereenie section (Fig. 8.3) and 4300 m/s for the Palm Valley section. There have been numerous other regional- and prospect-scale seismic surveys acquired in the basin that are not included in this study because of either poor quality or distance for the cross-sections.

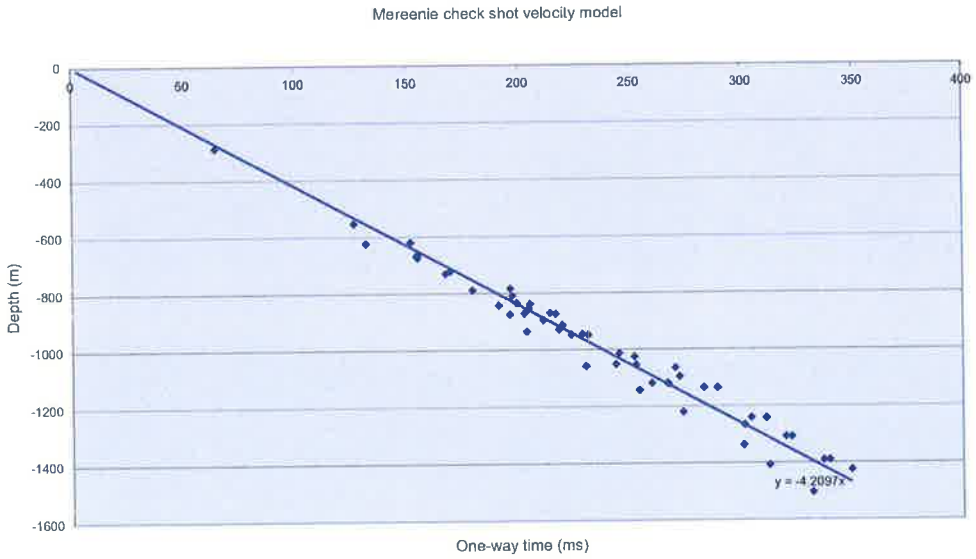

Figure 8.3. Check shot velocity data for all wells in the Mereenie Field. Depth conversion of the Mereenie seismic was performed using a constant velocity of 4210 m/s. A similar near-linear relationship exists over the Palm Valley Field defining a near-constant velocity of 4300 m/s.

Magnetic Data

The depth to magnetic basement along the cross-sections has been constrained using Wellman's (1991) basin-scale depth to magnetic basement map derived from aeromagnetic data. The magnetic basement profile along each section has been transferred directly by overlaying the sections on the basin-scale depth to magnetic basement map (Wellman, 1991).

8.5.2 Limitations of the cross-sections

There are several limitations to the cross-sections which and are briefly described here.

- The James Range section is normal to the James Range and strikes 178°. The section is not normal to the MacDonnell Homocline so a balanced section cannot be constructed through the homocline and the section is thus terminated in the middle of the Missionary Plain (Fig. 8.4).

- The basement culmination at the northern end of the Mereenie section is poorly constrained. Outcrop data is poor and no detailed structural work has been done in the area. Unfortunately, it is beyond the scope of this study to investigate the basement-cover interaction at the northern margin of the Mereenie section as land access is difficult due to native landowner permission issues. The basement culmination has been drawn in accordance with field observations made by others in the Mount Liebig area (Flottmann pers.comm., Santos 2004; Hand pers.comm., University of Adelaide 2004)

- Much of the Missionary Plain and southern ends of the sections are beneath extensive sand cover and the structure remains speculative in these areas.

- Many of the formation names are inconsistent between map sheets and wells and correlation of some formations across the basin is difficult. The cross-sections use key surfaces that separate major groups and have not focused on individual formations, except for the Heavitree Quartzite, Bitter Springs Formation and Pacoota Sandstone.

8.5.3 Assumptions of the cross-sections

Although the cross-sections are constrained by the geological maps and seismic, well and magnetic data, several fundamental assumptions have been made.

1. The basement culmination at the northern end of the Gardiner Range and Palm Valley sections is constructed in accordance with that of Flottmann and Hand (1999).

2. It is assumed that the top of magnetic basement (Wellman, 1991) is the top of basement. However, the values may be too shallow if there are basalt layers within the Proterozoic sequence or the values may be too deep if there is a non-magnetic layer at the top of the basement.

3. It is assumed that the Heavitree Quartzite maintains a relatively consistent thickness in the order of 300–500 m across the basin (Flottmann pers. comm., Santos 2004). Where there is significant discrepancy between the projected depth of the Heavitree Quartzite and the top of magnetic basement, it is assumed that the space is occupied by sedimentary equivalents of the Mount Harris Basalt.

4. The folds within the Proterozoic and Palaeozoic units are interpreted as detachment folds. The Bitter Springs Formation is assumed to have deformed in a non-elastic fashion and the basement and Heavitree Quartzite are assumed not to have been deformed in the foreland fold belt.

5. It is assumed that the upper sequence deformed by parallel folding and can be restored using 2D Move's flexural slip algorithm. The Bitter Springs Formation is interpreted to have deformed non-elastically and can only be restored by area balance methods. All units are line-length balanced except for the Bitter Springs Formation which is area balanced.

6. Where the thickness of a unit changes between two known locations, it is assumed that the change in stratigraphic thickness is uniform over the distance between the known points in the absence of contrary evidence.

7. The pre-erosion thickness of the Pertnjara Group is constrained by maturation and apatite fission track analysis across the basin (Gibson et al., 2004; Jackson et al., 1984; Tingate, 1991).

8. The Pertnjara molasse wedge developed with continued erosion of the basement culmination. The uneroded basement culmination is shown with the Pertnjara molasse wedge for display purposes only.

8.5.4 Mereenie Section

The Mereenie cross-section was constructed through the Mereenie Field with end-points at 703500; 7274300 and 803000; 7388250 (AMG Zone 52). The section runs along seismic line m83-16 and is constrained by four wells; Undandita 1, BMR Mount Liebig 2, East Mereenie 4 and East Johnny's Creek 1. Figure 8.5 shows the Mereenie section at the present day and pre-erosion levels. Figure 8.6 shows the Mereenie section restored to the top of the Pacoota Sandstone using the 2D Move flexural slip algorithm. Figure 8.6 also shows a close-up view of the Mereenie section through seismic section m83-16 and the East Mereenie 4 well.

8.5.5 Gardiner Range Section

The Gardiner Range section is constructed through the eastern end of the Gardiner Range approximately 10 km east of the Areyonga community, with end-points at 213400; 7276900 and 256000; 7395700 (AMG Zone 53). The section is to the immediate west of the Palm Valley Anticline and is constrained by the projection of the Tyler 1 and Wallara 1 wells. Figure 8.7 shows the Gardiner Range section at present day and pre-erosion levels. Figure 8.8 shows the Gardiner Range section restored to the top of the Pacoota Sandstone using the 2D Move flexural slip algorithm.

8.5.6 Palm Valley Section

The Palm Valley cross-section is constructed through the crest of the Palm Valley Anticline with end-points at 243800; 7276400 and 276300; 7394800 (AMG Zone 53). The section is constrained by seismic line PV 94-04, the Palm Valley 4 well and the projection of the Wallara 1 well. Figure 8.9 shows the Palm Valley section at the present day and pre-erosion levels. Figure 8.10 shows the Palm Valley section restored to the top of the Pacoota Sandstone using the 2D Move flexural slip algorithm. Figure 8.10 shows a close-up view of the Palm Valley section through seismic section PV 94-04 and Palm Valley 4.

8.5.7 James Range Section

The James Range cross-section is constructed through the western end of the James Range Anticline with end-points at 287000; 7257400 and 279000; 7355000 (AMG Zone 53). The section is to the immediate east of the Palm Valley Anticline and is constrained by the projection of the James Range A and Finke 1 wells. The section has not been constructed through the MacDonnell Homocline as it is oblique to the homocline. Figure 8.11 shows the James Range section at the present day and pre-erosion levels. Figure 8.12 shows the James Range section restored to the top of the Pacoota Sandstone using the 2D Move flexural slip algorithm.

The following sections discuss key observations made from the cross-sections relating to intracontinental deformation and basin evolution with a specific focus on the Mereenie and Palm Valley structures.

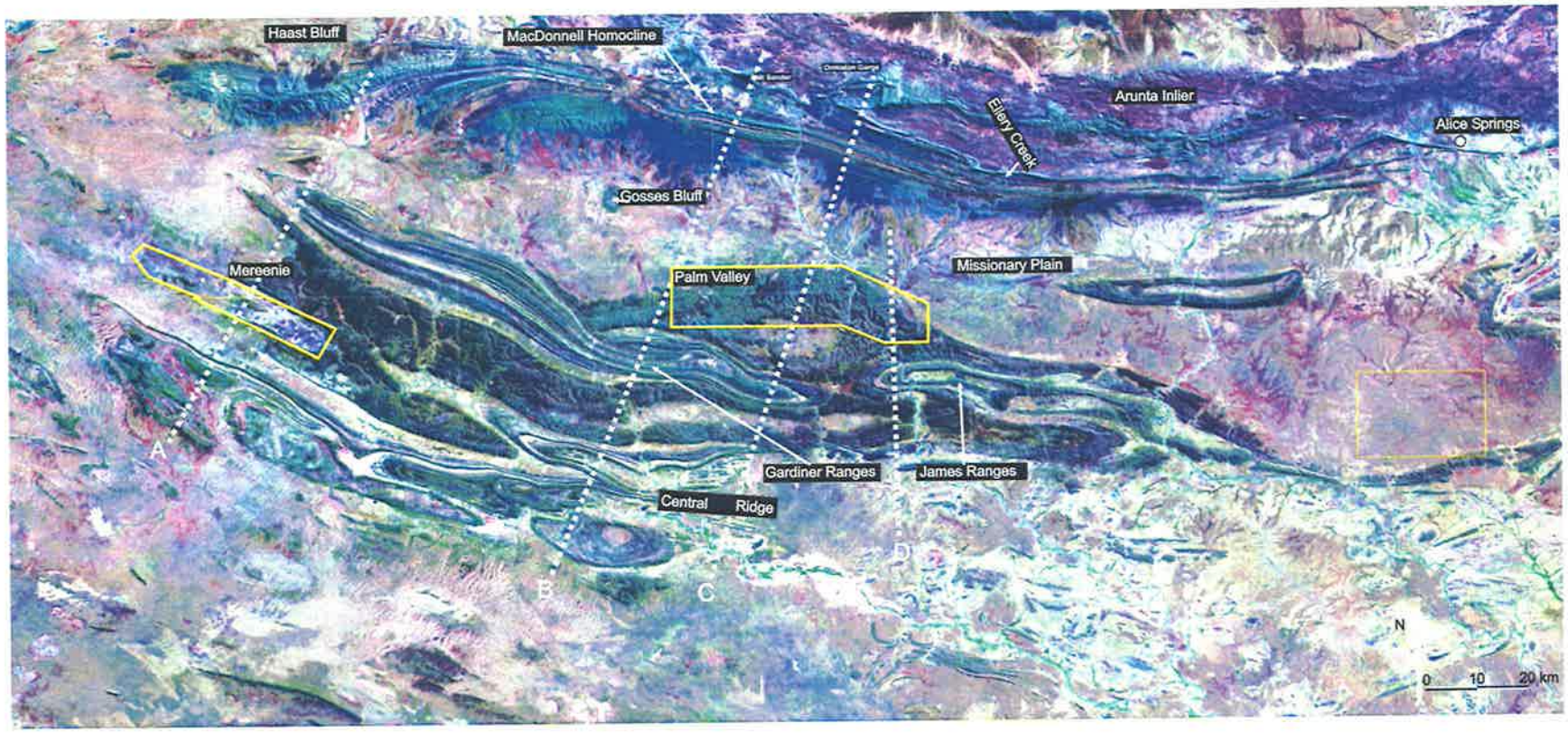

Figure 8.4. Landsat image of the northern Amadeus Basin showing the location of the (A) Mereenie, (B) Gardiner Range, (C) Palm Valley and (D) James Range cross-sections (NASA, 2004). The yellow boxes show the extent of the petroleum production licenses (PPL).

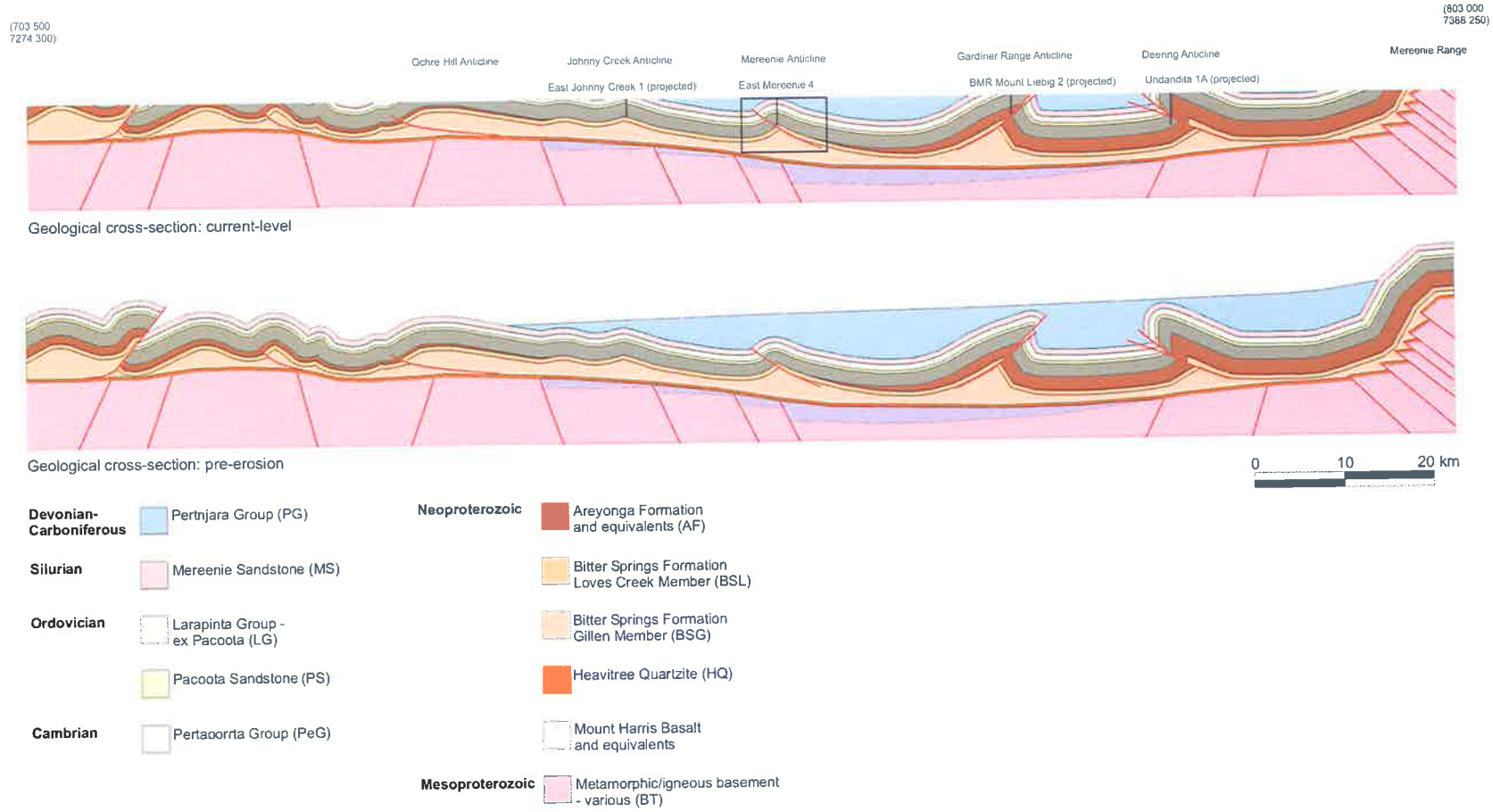

Figure 8.5. The Mereenie regional cross-section showing the contemporary and post-ASO levels. The un-eroded basement culmination and molasse wedge are shown together for display purposes only. The black rectangular outline shown in the current-level cross-section is the outline of the seismic section shown in Figure 8.6.

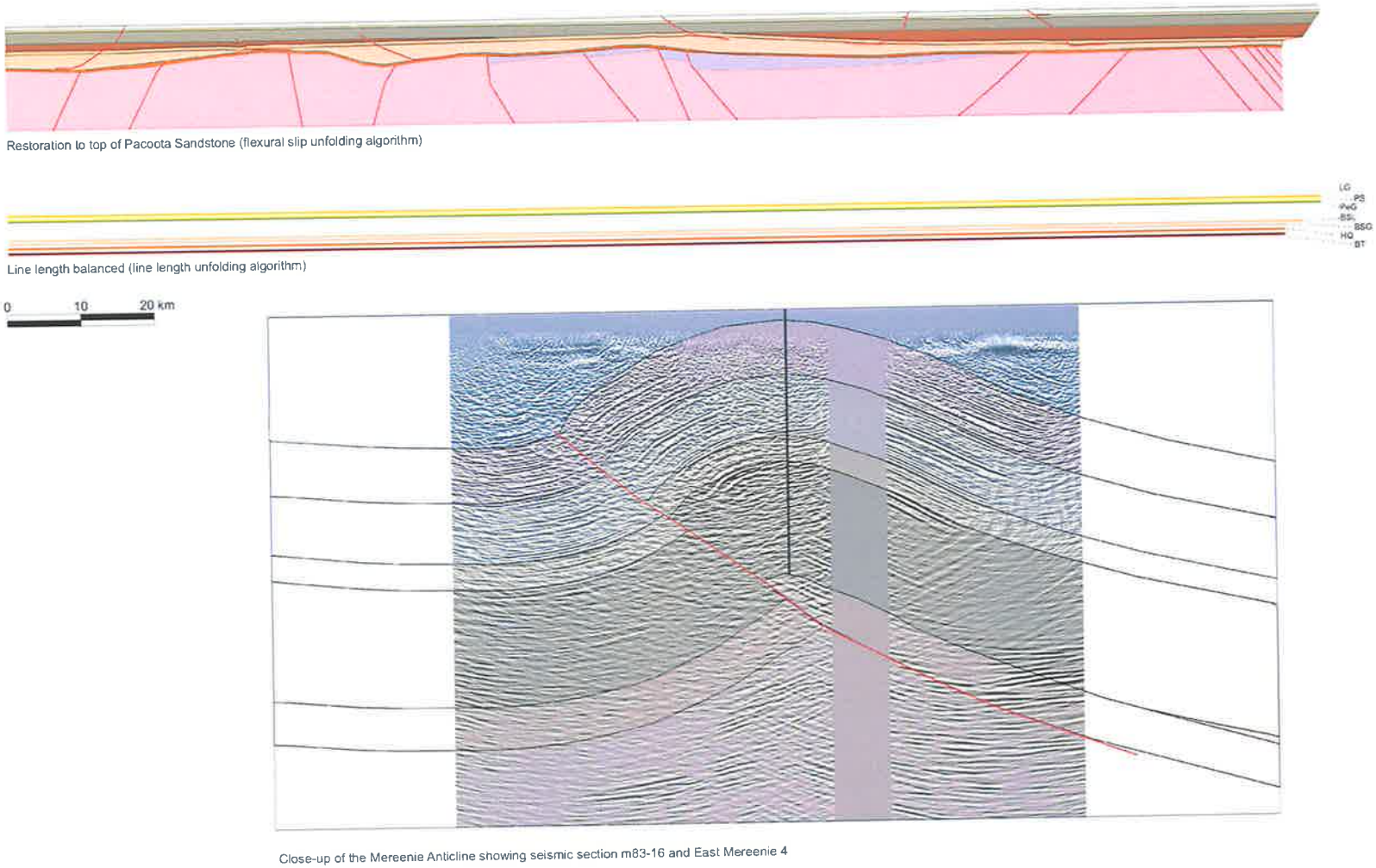

Figure 8.6. Mereenie regional cross-section restorations and close-up of Mereenie Anticline showing seismic section m83-16. The section is restored to the top of the Pacoota Sandstone and is line length balanced. The location and scale of the seismic section is shown in Figure 8.5.

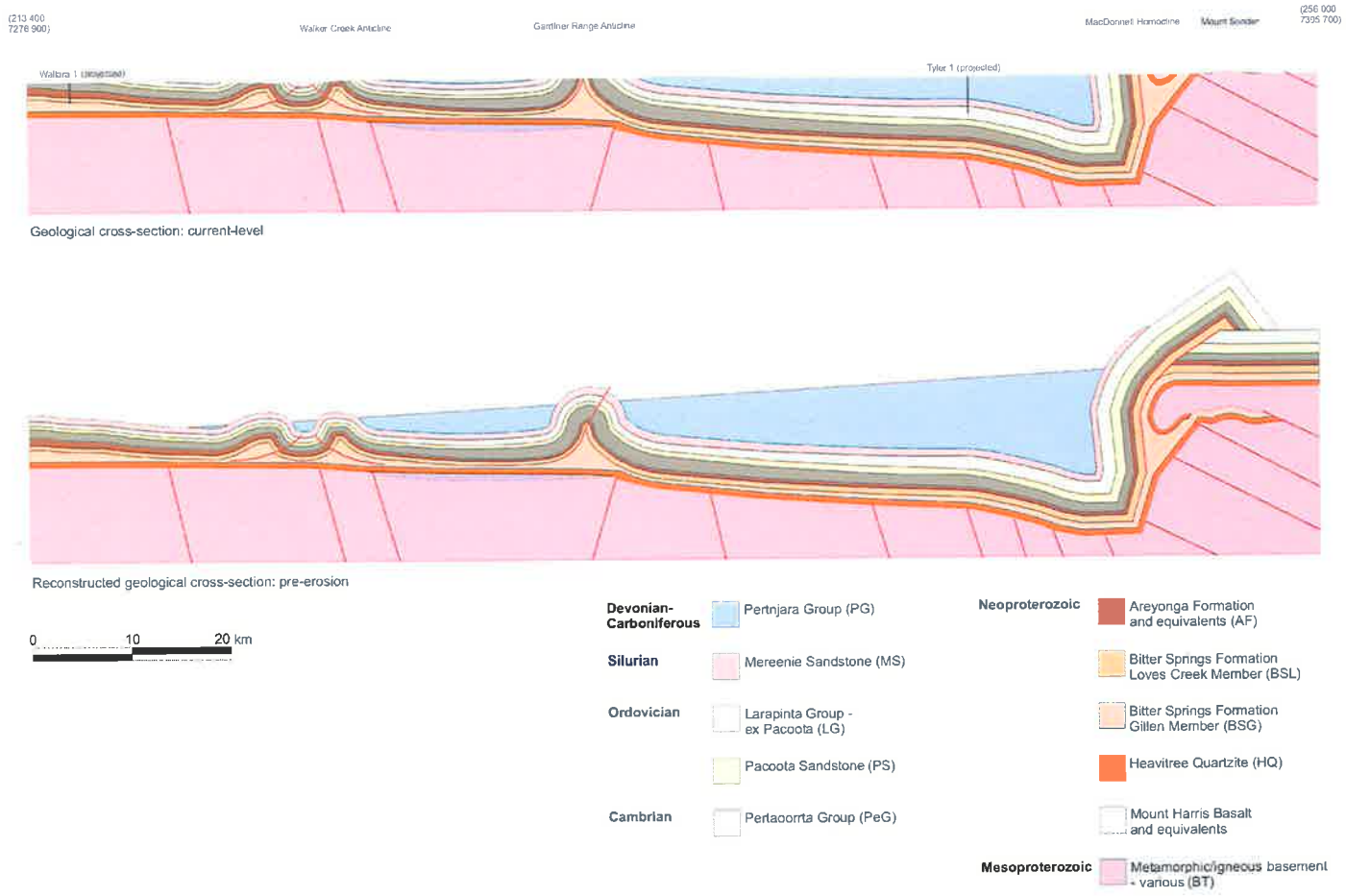

Figure 8.7. Gardiner Range regional cross-section showing the contemporary and post-ASO levels. Note the footwall shortcut faults of the Redbank Shear Zone caused rotation of the basement wedge.

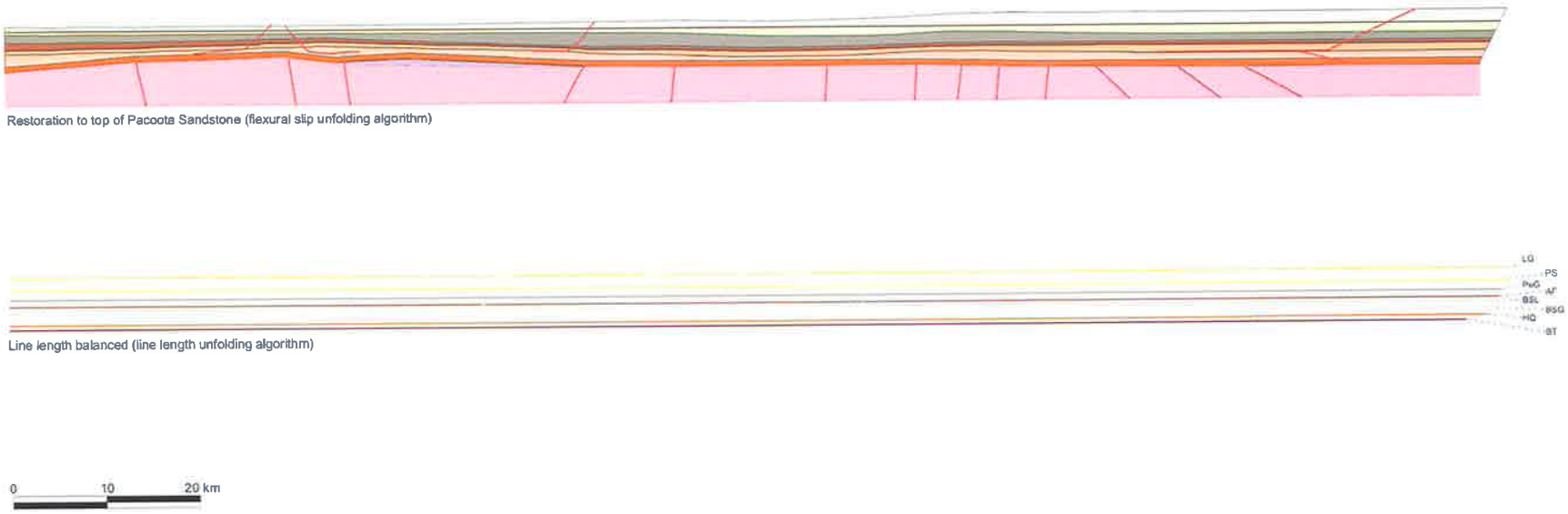

Figure 8.8. Gardiner Range regional cross-section restorations. The section is restored to the top of the Pacoota Sandstone and is line length balanced. The Gillen Member of the Bitter Springs Formation is area balanced.

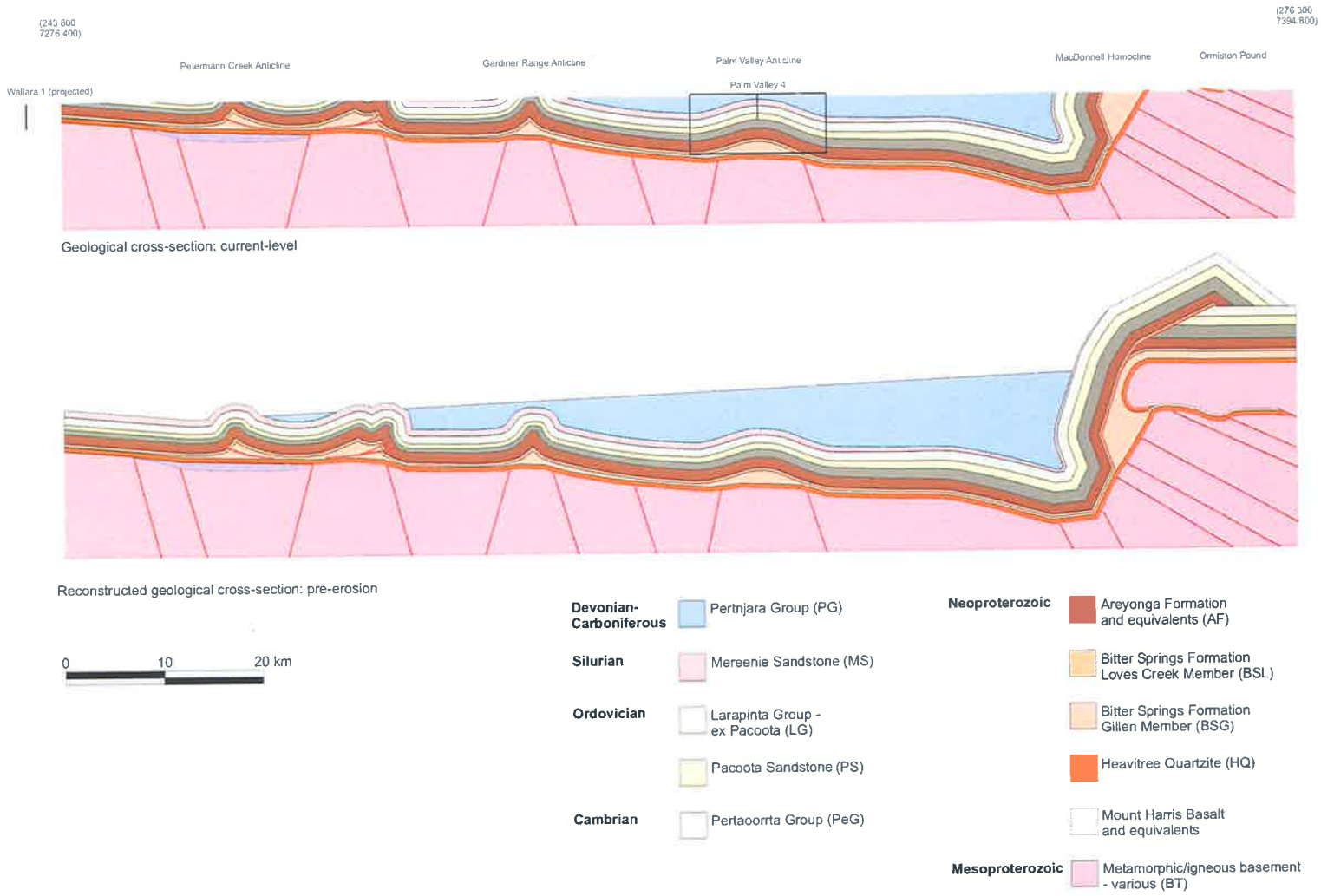

Figure 8.9. The Palm Valley regional cross-section showing the contemporary and post-ASO levels. The black rectangular outline shown in the current-level cross-section is the outline of the seismic section shown in Figure 8.10.

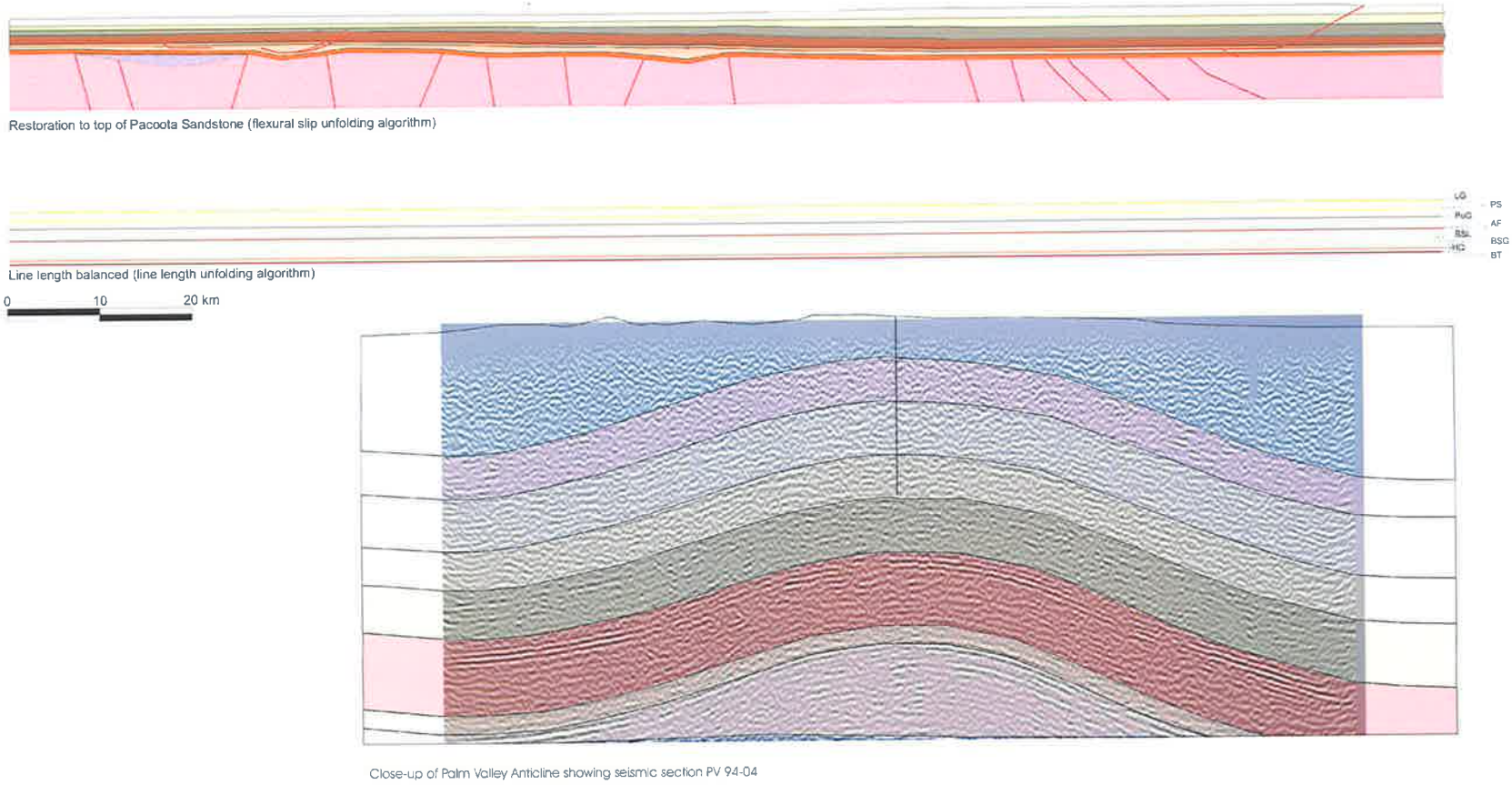

Figure 8.10. The Palm Valley regional cross-section restorations and close-up of the Palm Valley Anticline showing seismic section PV 94-04. The section is restored to the top of the Pacoota Sandstone and is line length balanced. The Gillen Member of the Bitter Springs Formation is area balanced. The location and scale of the seismic section is shown in Figure 8.9.

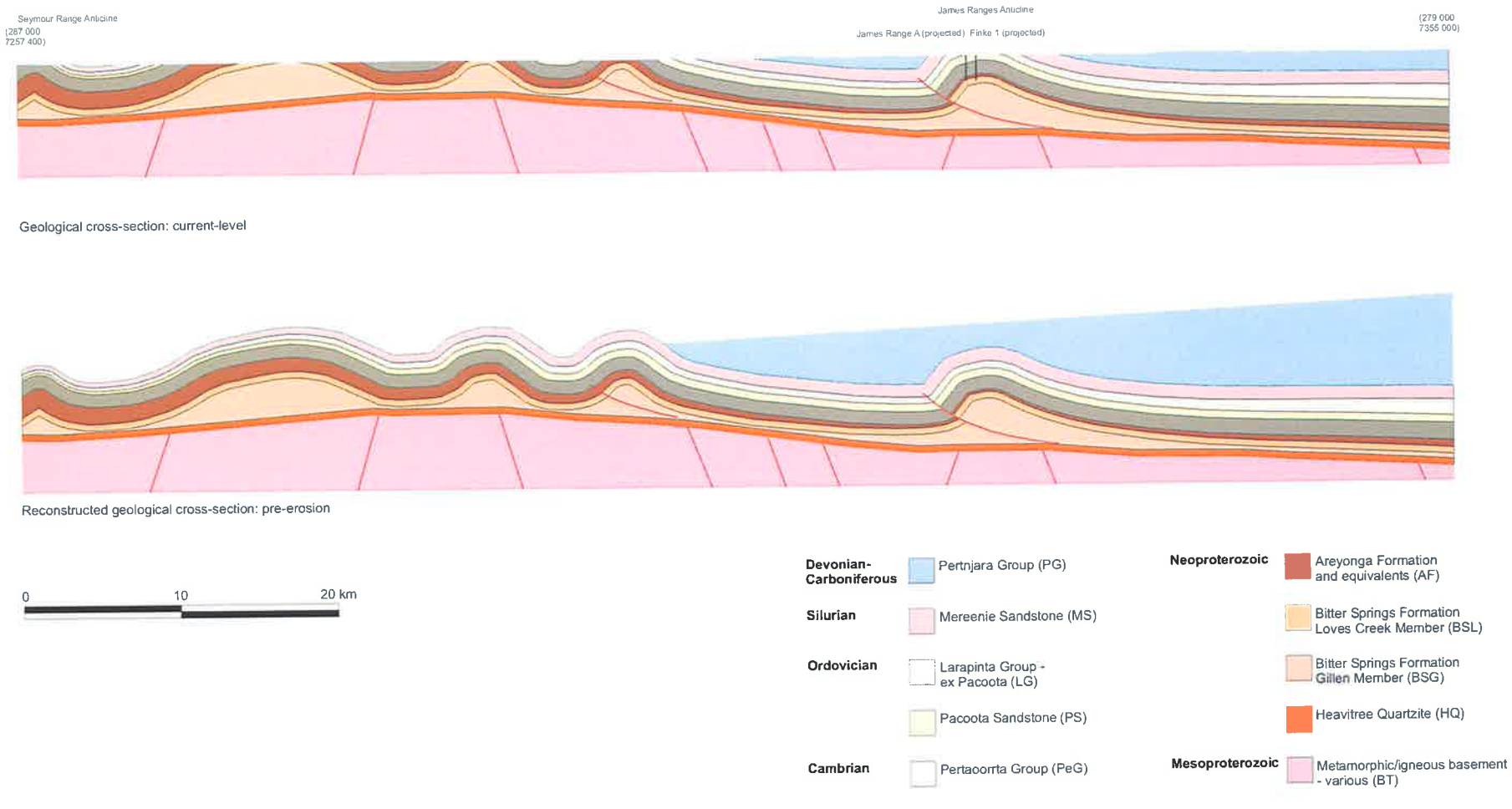

Figure 8.11. The James Range regional cross-section showing the contemporary and post-ASO levels.

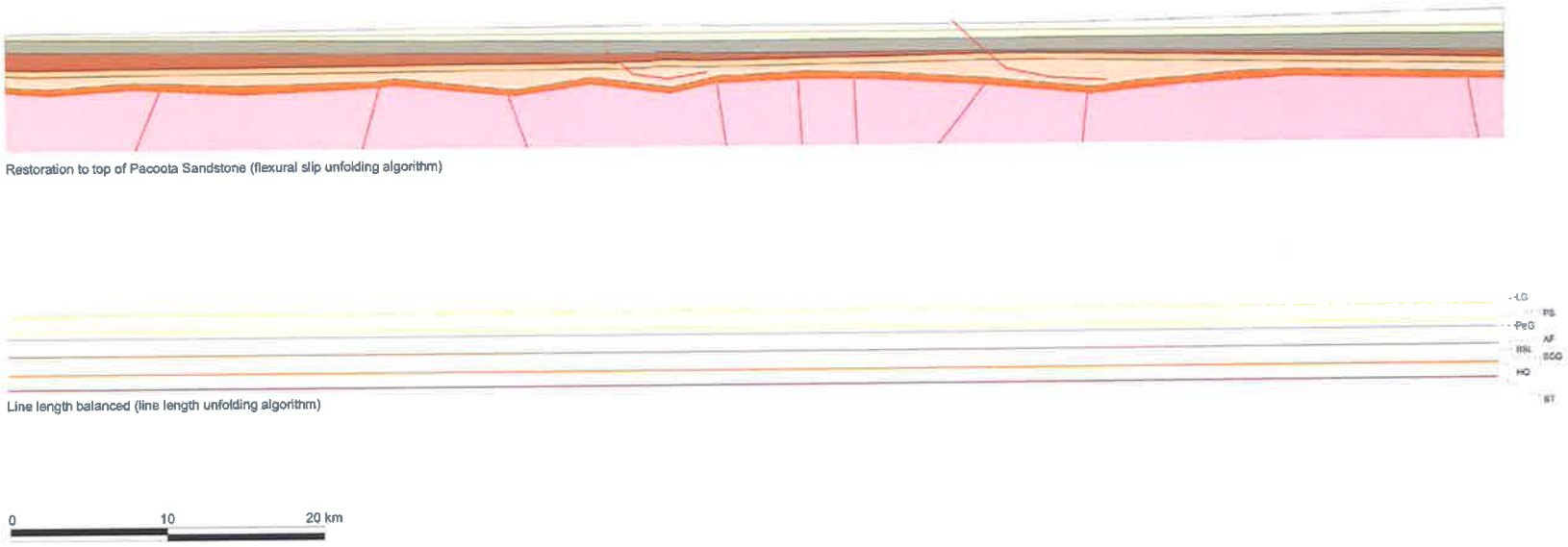

Figure 8.12. James Range cross-section restorations. The section is restored to the top of the Pacoota Sandstone and is line length balanced. The Gillen Member of the Bitter Springs Formation is area balanced.

8.6 Key Observations

8.6.1 Basement-cover interaction

Shortening is relatively consistent along the Mereenie, Gardiner Range and Palm Valley sections. Shortening implied by the Gardiner Range cross-section is in the order of 30 km or 20% over a restored line length of 160 km. This is significantly less than earlier thin-skinned models (Teyssier, 1985) and is of similar magnitude to that proposed by Flottman and Hand (1999).

One of the most notable differences between the Mereenie cross-section and the Palm Valley/Gardiner Range cross-sections is the basement-cover interaction at the northern end of the sections along the MacDonnell homocline. The basement-cover interaction along the Palm Valley and Gardiner Range section is reasonably well constrained (Flottmann and Hand, 1999). However, the basement-cover interaction along the Mereenie section is poorly defined and is constrained by field observations made by others (Flottmann pers. comm., Santos 2004; Hand pers. comm., University of Adelaide 2004). Several lines of evidence, as outlined below, suggest a change in structural style from the Palm Valley and Gardiner Range sections to the Mereenie section.

- The geological map data show basement-cored synformal anticlines at the northern end of the Palm Valley and Gardiner Range sections. The basement-cored synformal anticlines do not occur at the northern end of the Mereenie section.

- The MacDonnell homocline is less developed along the Mereenie section than along the Palm Valley and Gardiner Range sections.

- The top of the magnetic basement has been significantly deflected in front of the homocline along the Palm Valley and Gardiner Range sections yet there is no basement deflection in front of the homocline along the Mereenie section.

- Field observations by others (Flottmann pers. comm., Santos 2004; Hand pers. comm., University of Adelaide 2004) in the Haast Bluff area, near the northern end of the Mereenie cross-section, suggest that the basement and Heavitree Quartzite are repeated by a series of steep, 30°– 45° dipping thrust faults resembling an imbricate stack geometry (Fig. 8.4).

There are several possible explanations for the variation in deformation between the Mereenie and Palm Valley/Gardiner cross-sections; however, it is interpreted here that this variation in deformation is due to a combination of varying intensity of the ASO and the effect of pre-existing structure. The Redbank Shear Zone (RSZ) formed as early as 1500–1400 Ma (Shaw and Black, 1991) and had a major influence on deformation style by focusing deformation and displacement during the ASO. It is reasonable to assume that the structure of the RSZ along the Mereenie cross-section may differ from the Gardiner and Palm Valley cross-sections in the absence of any deep seismic lines through the Haast Bluff area. Significant variation in the RSZ has the potential to impart considerably different structural styles between the Mereenie and Palm Valley sections. Several authors have identified the importance of pre-existing basement-involved structures to orogenesis (Cooper, 1996; Soper and Higgins, 1990). The presence of the RSZ has resulted in the basement-cored wedge geometry instead of the passive-roof-duplex geometry typical of orogens that have no basement involvement (Banks and Warburton, 1986; Cooper, 1996; Flottmann and Hand, 1999).

The top of magnetic basement is significantly deflected in front of the homocline along the Palm Valley and Gardiner Range cross-sections due to the ASO. Basement deflection in front of the homocline is significantly less along the Mereenie cross-section. There are at least three possible explanations for this observation. The first possibility is that the load emplaced along the Mereenie section was significantly less than the load emplaced along the Palm Valley and Gardiner Range cross-sections and did not cause as much deflection of the lithosphere. A smaller emplaced load may be due to decreased intensity of the ASO or variation in the RSZ. The second possibility is that the basement culmination along the Mereenie cross-section was progressively eroded as it was emplaced and was never large enough to generate sufficient load to deflect the lithosphere. In comparison, the basement culmination along the Palm Valley and Gardiner Range cross-sections may have experienced only limited erosion thereby generating sufficient load to deflect the lithosphere. The third possibility is that there were differences in the lithosphere between the Mereenie section and the Palm Valley and Gardiner Range cross-sections resulting in different flexural responses to crustal loading. A combination of the first two possibilities seems most likely.

Molasse sedimentary sequences are deposited in response to orogenic uplift and are sourced from the uplifted area both during and after the orogenic phase. Molasse wedges may be of considerable thickness and have been shown to have a significant effect on deformation dynamics within fold and thrust belts (Dahlen and Suppe, 1988; Molnar and Lyon-Caen, 1988; Storti and McClay, 1995). The formation of molasse wedges increases overburden and therefore the normal stress acting on an underlying thrust fault. Increased normal stress can cause thrust faults to 'lock-up' and new faults develop in front of the molasse wedge (Dahlen and Suppe, 1988; Molnar and Lyon-Caen, 1988). The Pertnjara molasse wedge has had significant influence on the development of the MacDonnell Homocline and foreland folding by preventing

thrust faults propagating through the homocline into the Missionary Plain. The extra overburden of the molasse wedge may have prevented folding of the upper section in front of the homocline (Missionary Plain area) focusing folding near the toe of the wedge.

8.6.2 Foreland folding

Deformation of the foreland in front of the homocline is dominated by thin-skinned folding characterised by detachment folding of the sedimentary cover with a detachment in the Bitter Springs Formation. The detachment folds have developed by elastic, parallel folding of the Late Proterozoic-Silurian sequence and inelastic flow of the Bitter Springs Formation from the syncline hinges into the anticline cores. Some of the anticlines are faulted (e.g. the Mereenie and Gardiner faults) and these faults are interpreted as break-thrusts formed at the late stages of folding. The Heavitree Quartzite and Proterozoic basement below the Bitter Springs Formation detachment have remained undeformed by the thin-skinned folding phase.

Deformation and shortening within fold and thrust belts typically decreases gradually from the hinterland towards the foreland (Davis and Reynolds, 1996; Huiqi et al., 1992). The cross-sections show that the majority of shortening is accommodated in the hinterland and a small amount of shortening of the sedimentary cover is accommodated in the foreland. The Palm Valley and Gardiner Range cross-sections (Figs 8.7, 8.9) show that there is no shortening of either the basement or cover in the Missionary Plain area and that the decrease in shortening from the hinterland to the foreland is not a continuum. It appears that the Pertnjara molasse wedge restricted the location of the most hinterland-ward fold to near the toe of the wedge.

Fold development along the Mereenie section differs slightly to that in the other cross-sections. The most northern anticline along the Mereenie cross-section is the Deering Anticline. The Deering Anticline is ~20 km south of the basement culmination and is strongly foreland-verging and more asymmetric than the other anticlines intersected by the cross-sections. By comparison, the Gardiner Range, Palm Valley and James Range anticlines are ~55 km, 35 km and 45 km respectively from the basement uplift (measured along the cross-section lines). The difference in fold development between the cross-sections is probably due to the different basement-cover interaction and the smaller molasse wedge in front of the homocline along the Mereenie cross-section. The smaller molasse wedge along the Mereenie cross-section would have reduced overburden and allowed folds to develop closer to the homocline and may have allowed basement faults to propagate through the homocline into the foreland.

The thickness of the sedimentary succession above the detachment surface has a significant influence on detachment fold wavelength (Currie et al., 1962; Mitra, 2003; Rowan, 1993). The upper sequence varies from 3.5–4.5 km and the fold wavelength in the Amadeus Basin is generally between 10 and 25 km, defining wavelength-thickness ratios of 3:1–6:1. These values

are similar to those published for the Appalachian Plateau (6:1 to 8:1) and the Wildhorn nappe of the Swiss Alps (4:1) (Mitra, 2003; Rowan, 1993).

Although the first order controls on fold geometry such as deformation intensity and stratigraphic thickness are well understood, the factors that control the exact point of fold initiation and development are less clear. Mitra (2003) concluded that variations in detachment fold geometry such as asymmetry and the presence or absence of faulting are related to the initial mechanical stratigraphy and the pre-existing structure. Pre-existing basement structures may have created irregularities and local discontinuities along the detachment surface or influenced sedimentation by creating localised underlying sediment thickness or thicker salt pods that may act as nucleation sites for detachment folds. Poor quality seismic data across the basin inhibits imaging beneath the salt-bearing Bitter Springs Formation. The magnetic data appear to show some variation beneath the detachment folds; however, the data is too low resolution to conclusively draw a relationship between basement structure and fold location.

Gardiner Range Anticline

The Gardiner Range Anticline is the most laterally extensive fold in the central Amadeus Basin. The anticline is hinterland-verging and strikes northwest–southeast, extending almost 100 km from north of the Mereenie Field to south of the Palm Valley Field (Fig. 8.4). The Mereenie and Gardiner Range cross-sections intersect the anticline at the northwest and southeast ends respectively. Previous interpretation of the deep seismic reflection data suggest up to 30 km of displacement in the middle of the Gardiner Fault, based on apparent stratigraphic repetition beneath the Bitter Springs Formation (Shaw et al., 1991b). However, the seismic data used in the previous interpretations are very poor beneath the Bitter Springs Formation and the interpretation is by no means conclusive. It is kinematically unlikely that 30 km of shortening would occur on a single thin-skinned structure when less than that is accommodated along the entire RSZ. The Gardiner Range cross-section suggests only 30 km of shortening along its entire length. The Gardiner Range Anticline is interpreted here as an asymmetric, faulted detachment fold with maximum shortening probably less than 1 km. Maximum displacement along the fault remains speculative as neither the Mereenie nor Gardiner Range sections intersect the middle of the fault. The faulted detachment fold model presented here accounts for the steep to overturned beds in the footwall of the Gardiner Fault.

James Range Anticline

The James Range Anticline is immediately east of the Gardiner Range and Palm Valley anticlines. The James Range Anticline is a similar structure to the Gardiner Range Anticline, except that it is foreland-verging and unfaulted at outcrop level. The asymmetry of the anticline at the surface suggests that the detachment fold may be breached by a foreland-verging fault at depth.

Palm Valley Anticline

The Palm Valley Anticline is a mildly hinterland-verging fold between the James Range Anticline and the Gardiner Range Anticline. Prospect-scale seismic reflection data shows that there is only minor faulting of the Palm Valley Anticline. The Palm Valley Anticline is interpreted here as an accommodation structure that has balanced displacement between the tips of the foreland-verging James Range and the hinterland-verging Gardiner Range. There is a significant angular unconformity between the outcropping Hermannsburg Sandstone and the seismically imaged Cambro-Ordovician units. The Hermannsburg Sandstone dips no more than 9° at the surface (Shaw et al., 1995) yet the seismic profiles show the Cambro-Ordovician units dip up to 22°, implying much of the anticline had developed prior to deposition of the Hermannsburg Sandstone. Angular unconformities between the Brewer Conglomerate and Hermannsburg Sandstone elsewhere in the basin show that the Palm Valley Anticline had completely developed prior to maximum burial and thus hydrocarbon charge.

Mereenie Anticline

The Mereenie Anticline is approximately 25 km southwest of the Gardiner Range Anticline. The Mereenie Anticline is an asymmetric, foreland-verging, faulted detachment fold. The Pacoota Sandstone dips 45°– 50° and 25°– 30° on the southwest and northeast limbs respectively. The seismic profiles show that the Mereenie Fault does not extend through the entire Mereenie Sandstone and has a maximum throw of ~ 660 m along seismic line m87-01. The seismic and outcrop data show a significant angular unconformity between the Cambro-Ordovician units and the Hermannsburg Sandstone implying that the anticline had largely developed prior to Hermannsburg deposition. Angular unconformities between the Brewer Conglomerate and Hermannsburg Sandstone elsewhere in the basin suggest that the Mereenie Anticline had completely developed prior to maximum burial and thus hydrocarbon charge. The Mereenie Fault developed late in the evolution of the anticline, but prior to maximum burial and final hydrocarbon charge (Figs 8.13, 8.14).

8.7 Hydrocarbon Charge and Trap Formation

There have been several thermal modelling and maturation studies of the Amadeus Basin (Gibson et al., 2004; Jackson et al., 1984; Tingate, 1991). Maturation modelling from the Tyler 1 well (Missionary Plain) indicates that cessation of hydrocarbon generation from the Horn Valley Siltstone coincided with cooling/exhumation during the final stages of the ASO (Gibson et al., 2004). Burial and maturation history plots of the Mereenie Field (Fig. 8.13) show that the Horn Valley Siltstone was buried to approximately 3.5–4 km in the Carboniferous, thus leading to oil/condensate generation (Jackson et al., 1984). Burial and maturation history plots of the Palm Valley Field (Fig. 8.13) show that the Horn Valley Siltstone was buried to approximately 5.5–6 km in the Carboniferous, thus leading to gas generation (Jackson et al., 1984). Deposition of the

Pertnjara molasse wedge was responsible for burial and hydrocarbon generation in the northern Amadeus Basin (Gibson et al., 2004). The Palm Valley and Mereenie structures, therefore, developed pre-charge.

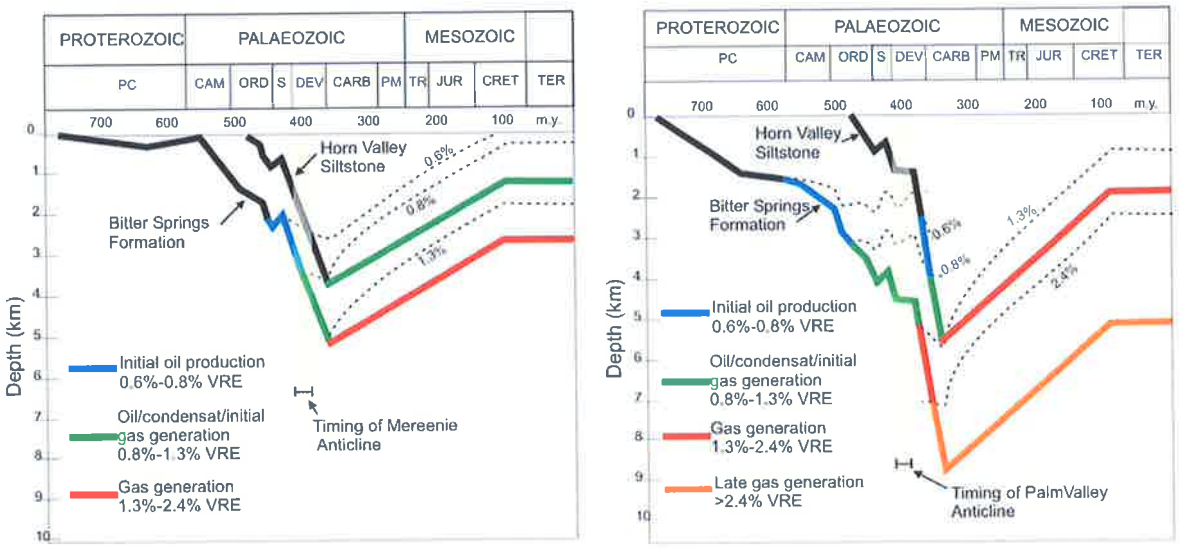

Figure 8.13. Burial and maturation profiles of the Mereenie (left) and Palm Valley (right) fields assuming geothermal gradients of 29°C/km (Jackson et al., 1984). The relative timing of trap formation is also indicated. Note that trap formation and Mereenie faulting was prior to maximum burial and subsequent hydrocarbon charge.

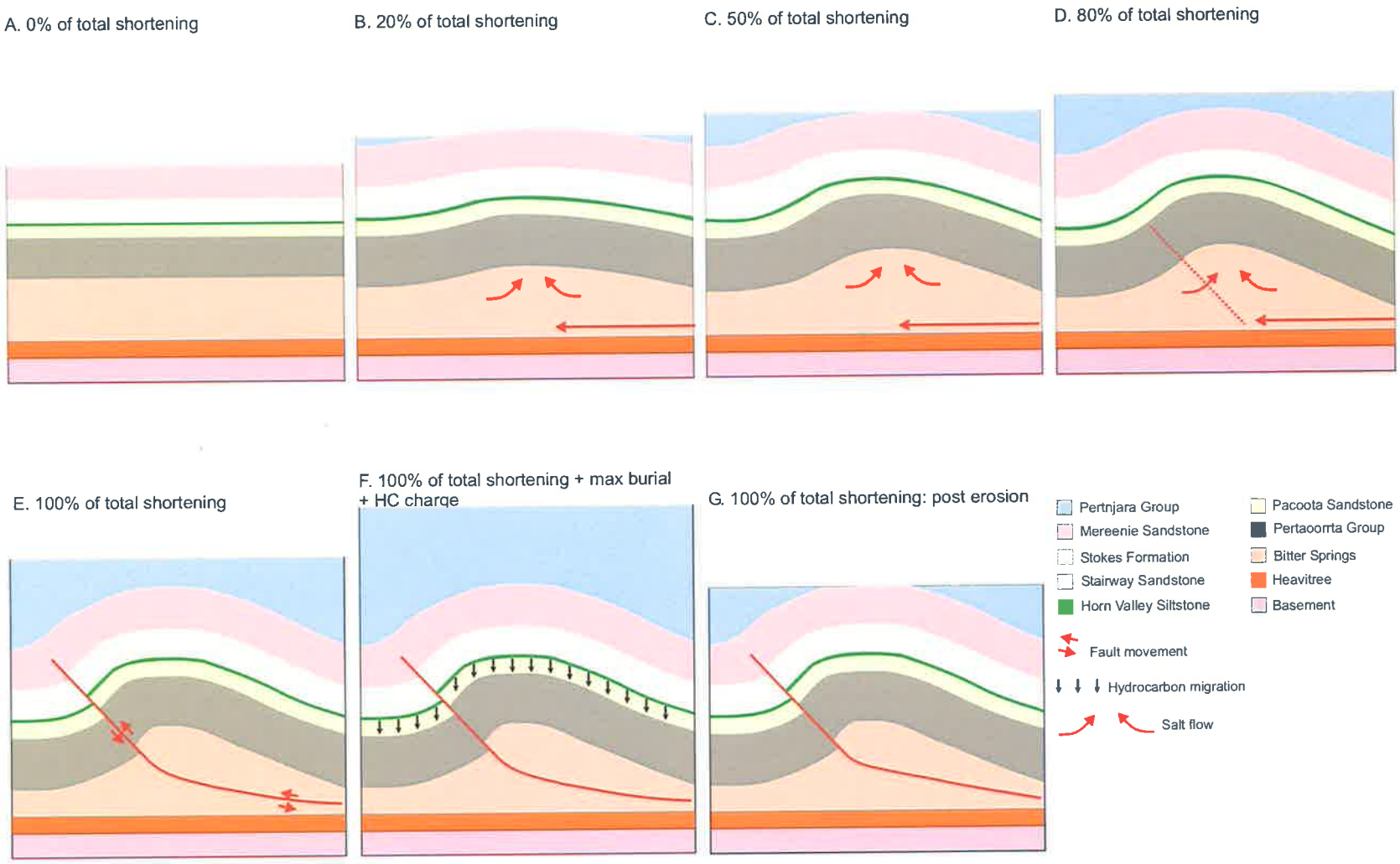

Figure 8.14. Evolution of the Mereenie Anticline constructed from seismic section m83-16 using the 2D Move tri-shear and line-length unfolding algorithms. The anticline is interpreted to have developed as a faulted detachment fold with a detachment in the Bitter Springs Formation. Faulting occurred late in the fold development at approximately 80% shortening. Hydrocarbon charge occurred post-faulting during maximum burial.

8.8 Isostatic Modelling of the Northern Amadeus Basin

The Redbank gravity anomaly (~150 mGal) along the northern margin of the Amadeus Basin is one of the largest gravity anomalies within any continental interior (Watts, 2001) and is of significant interest to the wider geologic community. The cross-sections constructed in this chapter provide an ideal opportunity to investigate this phenomenon and provide insight into intracratonic structural development.

The cross-sections show that a relatively high-amplitude, short-wavelength foreland basin with substantial basement deflection developed in front of the MacDonnell Homocline. The wavelength and amplitude of a foreland basin is a function of the applied thrust load and the elastic properties of the lithosphere (Beaumont, 1981; Jordan, 1981). High-amplitude, short-wavelength foreland basins develop where the lithosphere has low effective elastic thickness (Te) (Jordan, 1981; Watts, 2001). Paradoxically, gravity coherence data indicate that the contemporary effective elastic thickness in central Australia is high, ~ 80-100 km (McKenzie and Fairhead, 1997; Zuber et al., 1989). A possible explanation for this inconsistency between Te inferred from the shape of the foreland basin and from gravity data is that the Te of central Australia was considerably less during the ASO and has since increased to its contemporary thickness.

A considerable heat flow event would have significantly reduced the effective elastic thickness of the lithosphere of the Amadeus Basin. Unfortunately, the pre-ASO tectonic history of the Amadeus Basin remains poorly understood due to poor seismic imaging below the Bitter Springs Formation, erosion and overprinting of structures during the ASO. Recent work suggests that there was an Ordovician rift-like event to the north of the contemporary basin margin, coeval with deposition of the Larapinta Group (Hand, 2004 pers comm; Lee et al., 2002). Such an extensional event may have generated sufficient heat flow to reduce the effective elastic thickness of the lithosphere (Watts, 2001) and may be responsible for the discrepancy between contemporary effective elastic thickness and the geometry of the Amadeus foreland basin.

The isostatic development of the northern Amadeus Basin is modelled here using 2D Move software in order to help constrain the pre-ASO development of central Australia and to account for the discrepancy between contemporary effective elastic thickness and the geometry of the Amadeus foreland basin.

8.8.1 Isostasy and flexure theory

Load changes within the lithosphere due to either contraction or extension are spread regionally due to the strength and rigidity of the lithosphere. The area over which a given load is spread

and the size of the deflection is determined by the flexural properties of the lithosphere (Jordan, 1981; Turcotte and Schubert, 1982; Watts, 2001).

The deflection caused by a load L of width w is given by Equation 8.1.

$$Dx = \sum_{n=0}^{n=w} \frac{Ln.\alpha^3}{8.D} e^{-x/\alpha} \left(\cos\left(\frac{x}{\alpha}\right) + \sin\left(\frac{x}{\alpha}\right) \right)$$

Equation 8.1

$$D = \frac{E.Te^3}{12.(1-v^2)}$$

Equation 8.2

$$\alpha = \left(\frac{4.D}{\rho_m . g} \right)^{1/4}$$

Equation 8.3

8.8.2 Palm Valley isostasy model

Isostatic modelling has been conducted on the Palm Valley cross-section because it is the best constrained cross-section (Flottmann and Hand, 1999). The start-point isostatic model as shown in Figure 8.15 was taken as the Palm Valley cross-section restored to the top Larapinta Group. The load is simplified by assuming a single thrust load emplaced along the Redbank Shear Zone and structures within its footwall. The aim of the isostatic modelling is to load the start-point model via thrust and sedimentary wedge loading then unloading to deflect the top of basement so that it matches the contemporary magnetic basement profile (Wellman, 1991).

8.8.3 Isostatic modelling results

Figure 8.16 shows the isostatic model assuming Te = 88 km. The basement is only slightly deflected and does not match the contemporary geometry of the foreland basin, implying that the Te was significantly less than 88 km during the ASO. Figure 8.17 shows the isostatic model assuming Te = 10 km. The thrust and molasse wedge loads deflect the basement beyond the contemporary basement profile. The model is then unloaded assuming effective elastic thicknesses of 10, 30 and 88 km. Unloading with low Te (i.e. 10 and 30 km) values cause the model to rebound beyond the contemporary profile. The best match is achieved by loading with Te = 10 km and unloading with a Te = 88 km.

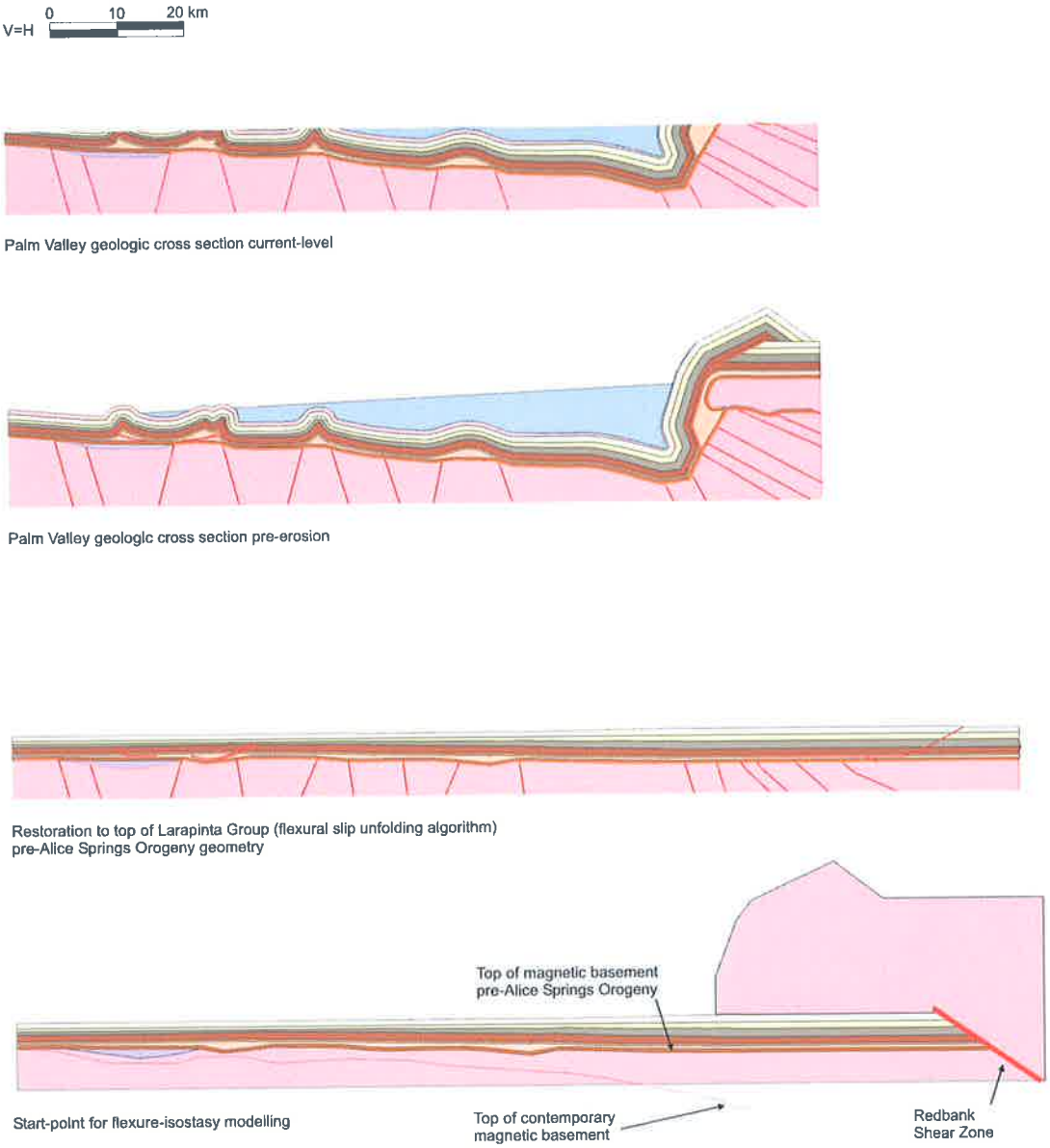

Figure 8.15. The start-point isostatic model (bottom) based on the Palm Valley cross-section restored to top Larapinta Group.

8.8.4 Mereenie isostasy model

Isostatic modelling has been conducted on the Mereenie section using the same elastic properties as the Palm Valley model to compare and contrast the amount of thrust loading and basement deflection between the Mereenie and Palm Valley sections. The aim of the Mereenie isostatic modelling is to help constrain what thrust load is required to cause the observed basement deflection and demonstrate relative orogenic intensity. The start-point isostatic model as shown in Figure 8.20 was constructed from the Mereenie section restored to the top Larapinta Group. The thrust load is simplified by assuming a single load emplaced along a series of imbricate basement faults. The size of the thrust and wedge loads were adjusted via an iterative process to deflect the top of basement so that it matches the contemporary magnetic basement profile (Fig. 8.18).

8.8.5 Isostatic modelling interpretation

The isostatic modelling of the Palm Valley section implies that the effective elastic thickness of the northern Amadeus Basin during the ASO must have been ~ 10 km. The modelling also implies that there must have been significant cooling of the lithosphere prior to unloading to prevent excessive rebound. Low Te values during the ASO may be attributed to elevated heat flow during early Ordovician rifting to the north of the contemporary basin margin (Hand, 2004 pers comm; Lee et al., 2002).

The regional cross-sections show that basement deflection along the Mereenie section is much less than along the Palm Valley section. Isostatic modelling of the Mereenie section shows that the emplaced thrust and wedge loads were significantly smaller along the Mereenie section than along the Palm Valley section. The isostasy modelling implies that the orogenic intensity and subsequent uplift along the Mereenie section were significantly less than along the Palm Valley section.

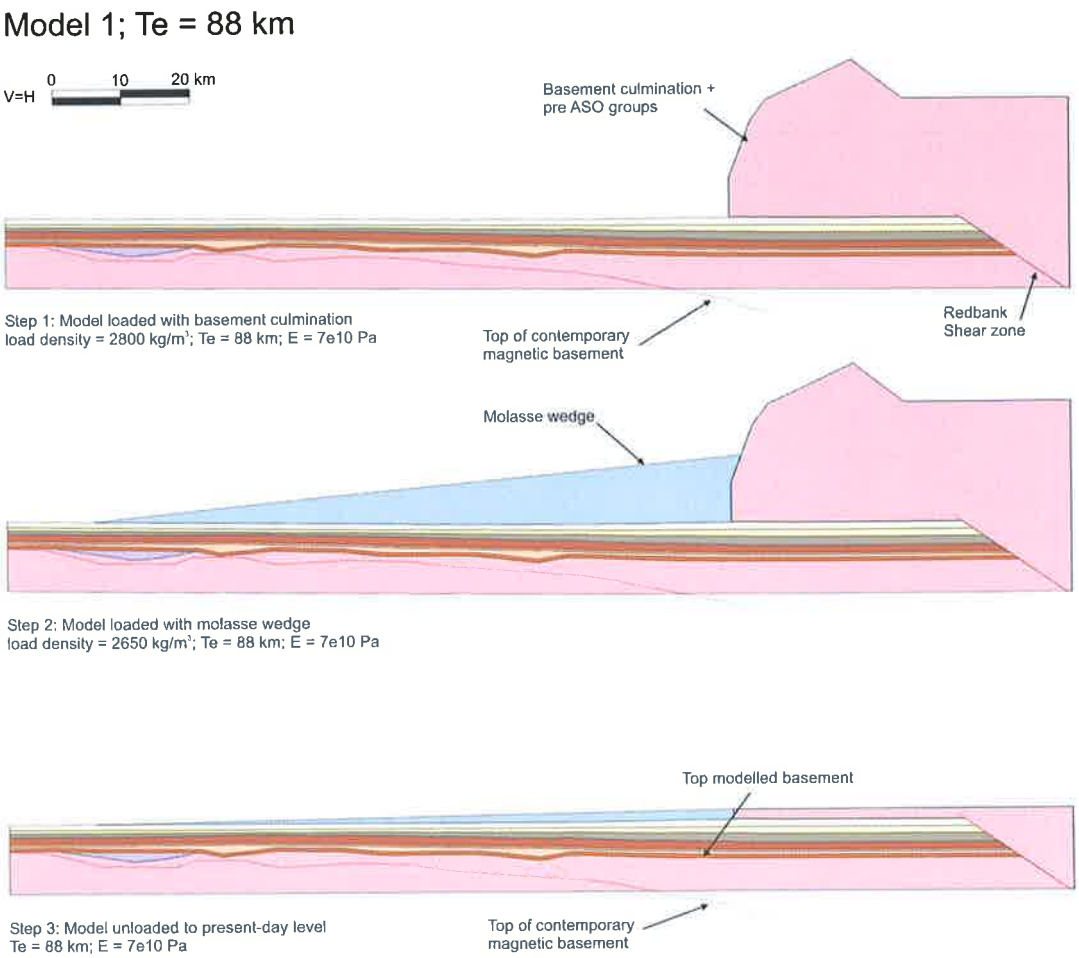

Figure 8.16. Isostatic model showing the effects of thrust and wedge loading of the northern Amadeus Basin with an effective elastic thickness of 88 km. The basement is only mildly deflected and does not match the contemporary magnetic basement. The effective elastic thickness during the ASO must have been significantly less than 88 km to produce the contemporary geometry.

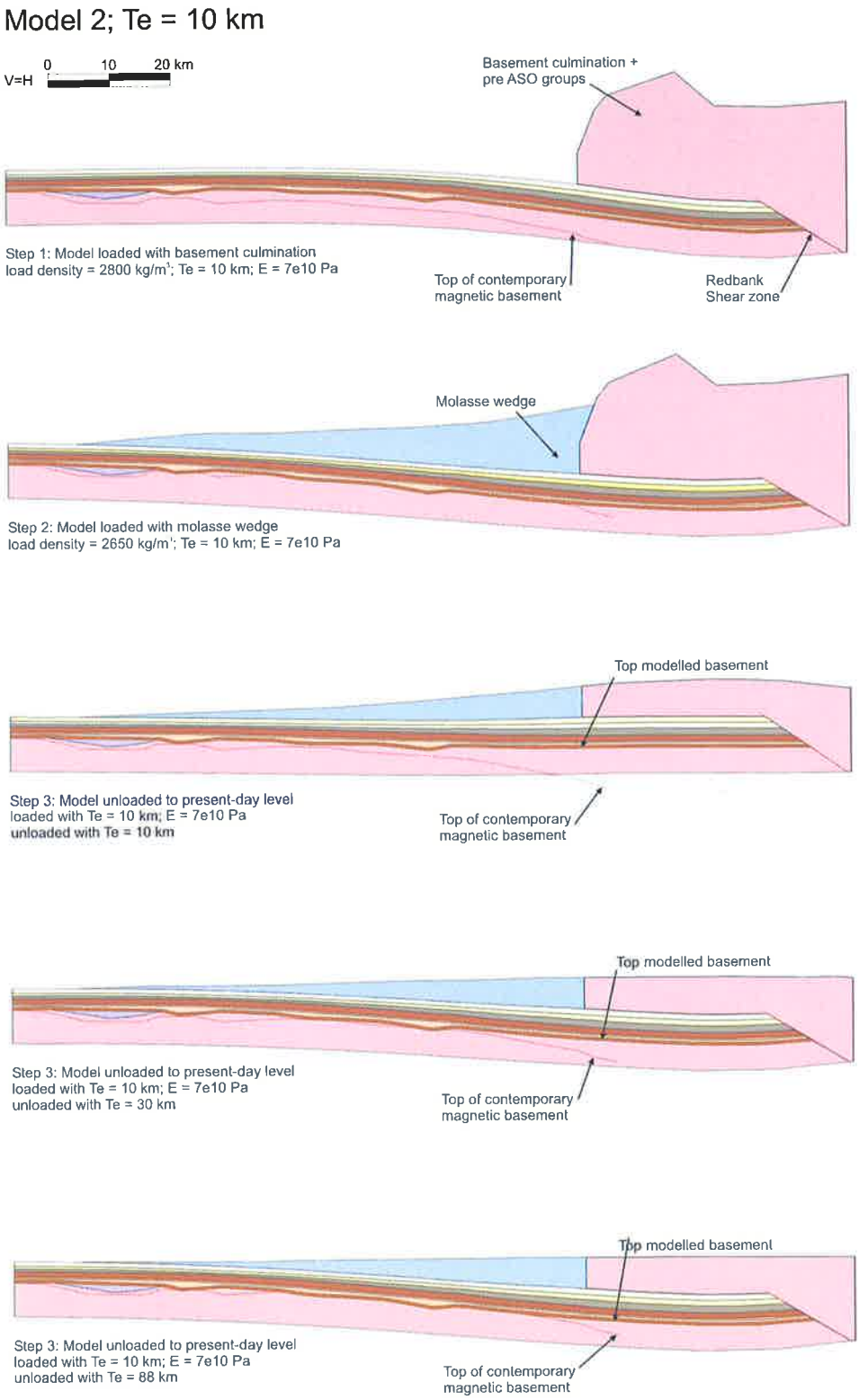

Figure 8.17. Isostatic model showing the effects of thrust and wedge loading with an effective elastic thickness of 10 km. The model is then unloaded with effective elastic thicknesses of 10, 30 and 88 km respectively. The best match is given by loading with Te=10 km and unloading with Te= 88 km.

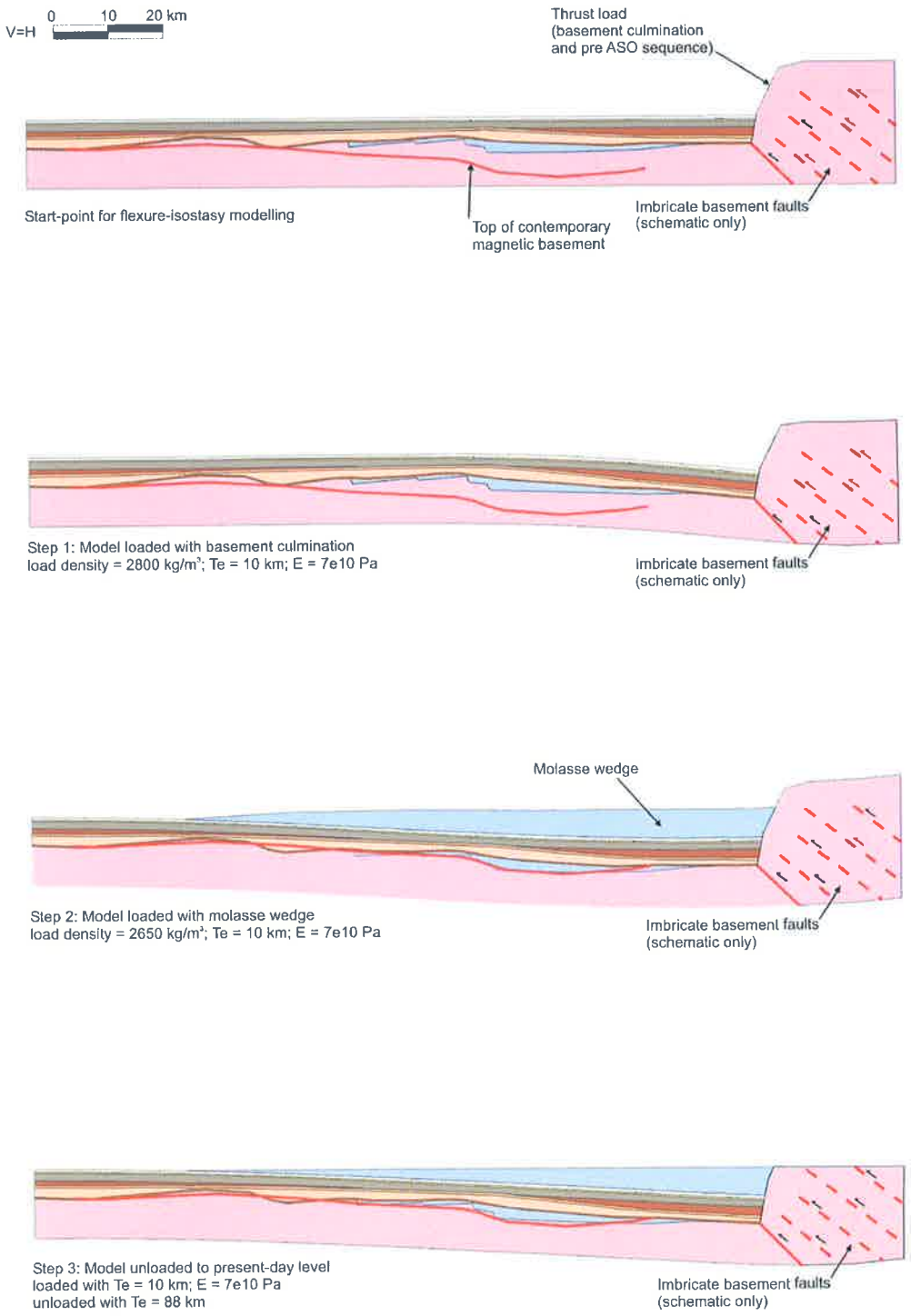

Figure 8.18. Isostatic model constructed along the Mereenie regional cross-section assuming the same elastic properties as the Palm Valley model (loaded with Te = 10 km and unloaded with Te = 88 km). The start-point isostatic model was constructed from the Mereenie section restored to the top Larapinta Group. The thrust load is simplified and includes the basement culmination and the pre ASO sequences. The imbricate basement faults are only schematic.

8.9 Synopsis

This chapter has constrained the structural setting and evolution of the Mereenie and Palm Valley fields. The work provides insight into the pre and syn-ASO structural development of the Amadeus Basin and contributes to the greater understanding of intracratonic structural development.

The cross-sections presented in this chapter show the interaction of a basement-cored wedge with the sedimentary cover in an intracratonic setting. The main displacement zone in the footwall of the RSZ is an ancient crustal discontinuity that has had a long and varied history of compression and extension since as early as 1500 Ma (Flottmann et al., 2004). The RSZ focused intracratonic deformation during the ASO and resulted in the observed basement-cover interaction rather than the formation of a passive-roof-duplex as observed in many orogens with no basement involvement (Banks and Warburton, 1986; Cooper, 1996; Flottmann and Hand, 1999). Shortening across the northern margin of the basin is ~ 30 km, significantly less than the ~110 km implied by thin-skinned models (Marjoribanks, 1976; Teyssier, 1985).

Deformation within the foreland in front of the RSZ is relatively mild and characterised by thin-skinned detachment folding. The Mereenie and Palm Valley anticlines developed as salt-cored detachment folds above a detachment in the Bitter Springs Formation. The Mereenie Anticline has tighter fold limbs than the Palm Valley Anticline and was faulted during the late stages of folding. Movement along the Mereenie Fault was prior to maximum burial, hence fault development is pre-hydrocarbon charge.

Isostatic modelling implies that the effective elastic thickness of the lithosphere was significantly less during the ASO than its contemporary thickness. Ordovician rifting (pre-ASO) and associated heat flow may be responsible for the discrepancy between contemporary effective elastic thickness and the geometry of the foreland along the northern Amadeus Basin. The site of proposed Ordovician extension (Lee et al., 2002) was the site of subsequent inversion during the ASO. The modelled effective elastic thickness of 10 km during the ASO is similar to contemporary intracratonic extensional provinces such as east Africa and the Basin and Range Province (Watts, 2001). The isostasy modelling supports field observations showing that orogenic intensity and subsequent uplift along the Mereenie section were significantly less than along the Palm Valley section.

The following chapters use the structural modelling presented in this chapter to help account for fracture development in the basin (Chapter 9) and to reduce risk associated with the Mereenie sub-thrust play (Chapter 10).

9 Natural Fracturing in the Amadeus Basin

9.1 Background

Natural fractures have a varied influence on hydrocarbon deliverability in the otherwise tight reservoirs of the Amadeus Basin. The Palm Valley Field is a type 2 fractured reservoir where fractures provide essential permeability to the low permeability matrix (Aguilera, 1995; Do Rozario, 1991; Flottmann, 2003). The original gas in place in the Palm Valley fracture network and matrix was estimated as 10.79 Bscf and 834.01 Bscf, respectively, as of 1995 (Aguilera, 1995). The Mereenie Field has experienced significantly less burial and diagenesis than Palm Valley (Fig. 8.13) and is a type 3 fractured reservoir where fractures assist dominantly matrix flow (Flottmann, 2003; Havord, 1991; Jackson et al., 1984). Initial recoverable reserves in the Mereenie Field were estimated at 19 MMSTB of oil and 590 BCF of gas as of 1991 (Havord, 1991). Numerous published and unpublished studies have been conducted on natural fracture development in the Palm Valley Field in order to assist field development (Berry et al., 1996; Do Rozario and Baird, 1987; Milne and Barr, 1990a). Natural fracturing has significantly less influence at Mereenie and has been the subject of only a few unpublished reports directed at enhanced oil recovery and gas cap exploitation (Campagna and Flottmann, 2002; Hillis et al., 1999b). These previous studies do not account for the considerable discrepancy in fracture development between Mereenie and Palm Valley. The controls on natural fracture development may be better understood by studying natural fracture development in both fields with respect to each other. A more thorough understanding of natural fracture development has the potential to improve development drilling, increase reserves and extend the life of both the Mereenie and Palm Valley Fields. The views presented in this chapter are those of the author and do not necessarily reflect those of the Santos-Magellan joint venture. Detailed discussion of field development issues has been omitted from this thesis at the request of the joint venture.

9.2 Previous Studies

9.2.1 Palm Valley

The Palm Valley Anticline has approximately 350 m of topographic relief with deeply incised valleys partly defined by major fracture sets in the outcropping Hermannsburg Sandstone (Milne and Barr, 1990a). A photo-geological study over the outcropping Palm Valley Anticline demonstrates the area is dominated by two major fracture sets: a NNW-striking set, and; an ENE-striking set (Do Rozario and Baird, 1987). The two fracture sets are approximately perpendicular and parallel to the main fold axis respectively (Figs 9.1– 9.3).

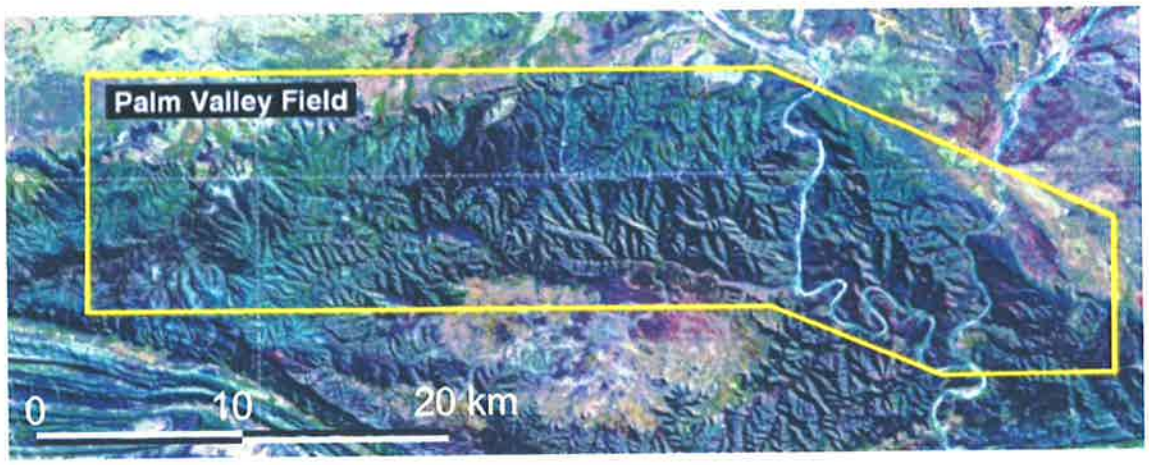

Figure 9.1. Landsat image of the Palm Valley Anticline showing the rugged surface topography defined by the natural fractures (NASA, 2004).

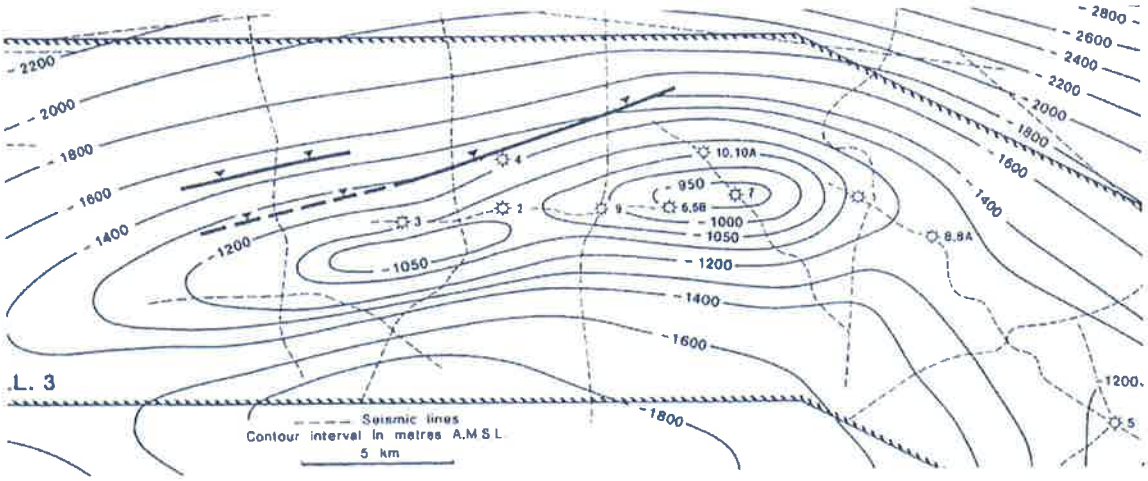

Figure 9.2. Top Pacoota Sandstone depth structure map (m) of the Palm Valley Field (Berry et al., 1996).

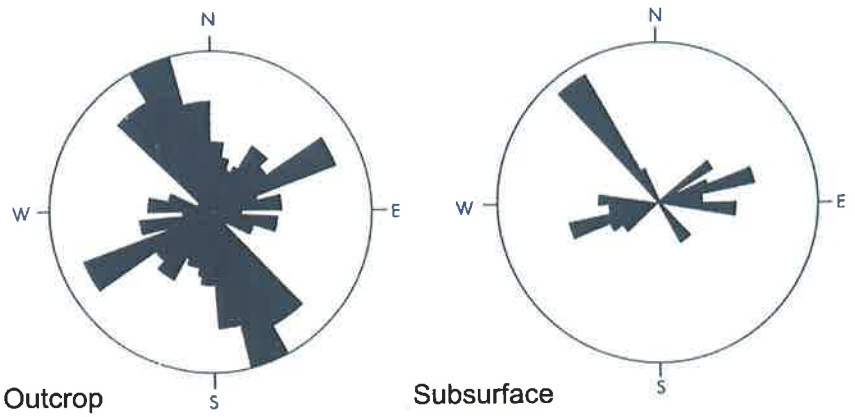

Figure 9.3. Strike of major surface fractures identified by the photo-geologic study compared to subsurface fracture strike (strike backed out from dip-direction) from HDT data (Do Rozario and Baird, 1987).

Oriented core, dip-meter (HDT) and formation microscanner (FMS; Palm Valley 7 only) data have been used to study the Palm Valley fracture network at reservoir depth (Berry et al., 1996; Do Rozario and Baird, 1987; Milne and Barr, 1990a). The studies reveal that high-angle fractures (70°– 90°) are generally confined to the more competent units (i.e. sandstones of the lower Stairway and Pacoota Sandstones and limestones and dolomites of the Horn Valley Siltstone). Low-angle fractures (8°–17°) identified as bedding-plane shear fractures from core and FMS are typically restricted to the shale intervals within the sequence (Berry et al., 1996; Milne and Barr, 1990b). The nature of the high-angle fractures is variable; some are un-mineralised, others are completely mineralised and closed however, most are partially mineralised and are propped open (Fig. 9.4). Previous interpretation of the FMS and HDT data suggest typical maximum fracture aperture in the order of 3 mm although apertures of up to 10 mm are suspected (Do Rozario and Baird, 1987; Milne and Barr, 1990a). Pressure tests show that the Pacoota and lower Stairway Sandstones are in pressure communication (Milne and Barr, 1990a); therefore, some of the open natural fracture networks must extend through the Horn Valley Siltstone (~80 m thick). Analysis of the high-angle fracture orientations shows that there are two major sets: one set striking east-northeast, and one striking north-northwest consistent with those observed in the photo-geological study (Fig. 9.3). There are also smaller, less defined sets as shown in Figure 9.5 (Berry et al., 1996; Milne and Barr, 1990a).

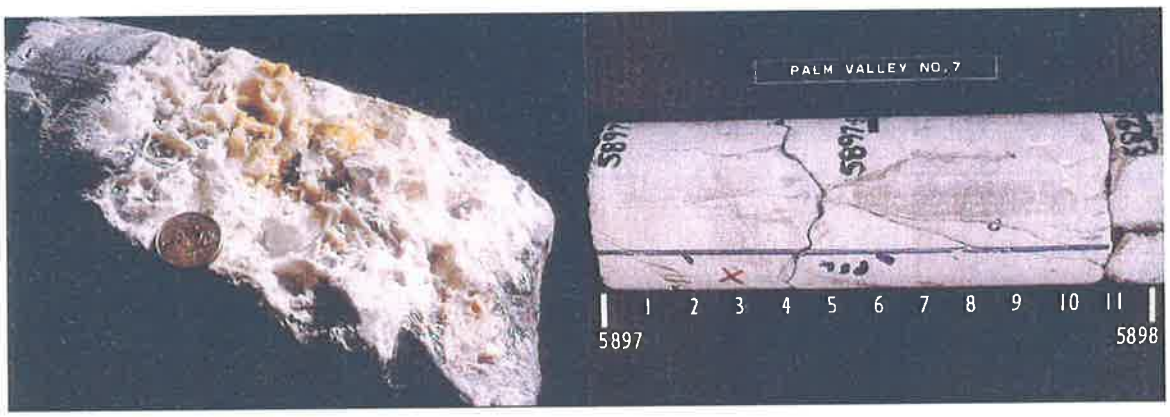

Figure 9.4. Examples of reservoir-level fractures from Palm Valley 7 core (Berry et al., 1996). Fractures at high-angles to S_{Hmax} could contribute to reservoir permeability if they are partially mineralised and propped open by the various fracture-filling mineral phases including barite, ankerite and quartz.

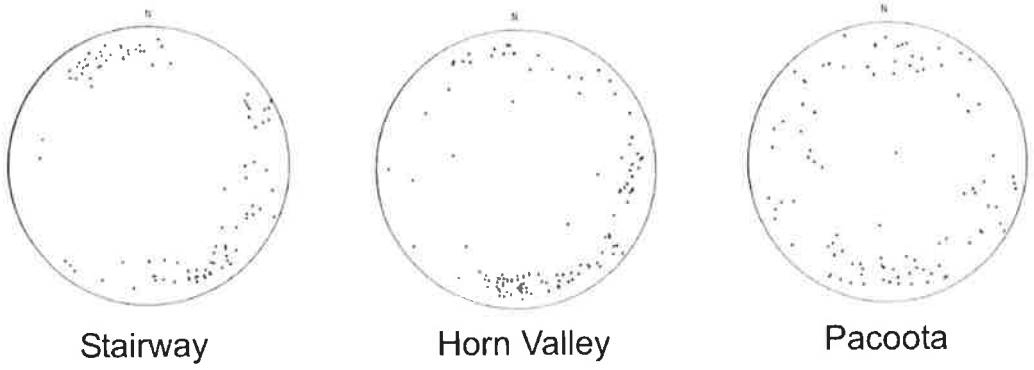

Figure 9.5. Plots of fracture poles recorded at reservoir level from oriented core and FMS data from Palm Valley 7 (Berry et al., 1996).

There is significant variation in fracture development across the field dependent on structural position (Berry et al., 1996; Milne and Barr, 1990a). The high density of fractures in the fold crest (Palm Valley 7) and the fracture orientations relative to the fold structure have led authors to interpret most of the fractures as originating as a result of folding (Berry et al., 1996; Milne and Barr, 1990a). Berry et al. (1996) use a complex model of type 1 and type 2 fold-related fracture assemblages to account for the fracture orientations observed within the field (Fig. 9.6). Their model accounts for the dominant ENE-striking set as extensional/tensile fractures of a type 2 assemblage formed in response to outer-arc flexure during folding about an axis parallel to bedding strike (i.e. crestal extensional fractures). The NNW-striking fractures are modelled as extensional/tensile fractures of a type 1 assemblage formed in response to flexure during folding about an axis perpendicular to bedding strike. The other minor fracture sets are modelled as either left or right lateral shears of type 1 or type 2 assemblages (Berry et al., 1996). The dominant ENE-striking and NNW-striking sets are perpendicular to each other providing essential connectivity between the fracture sets.

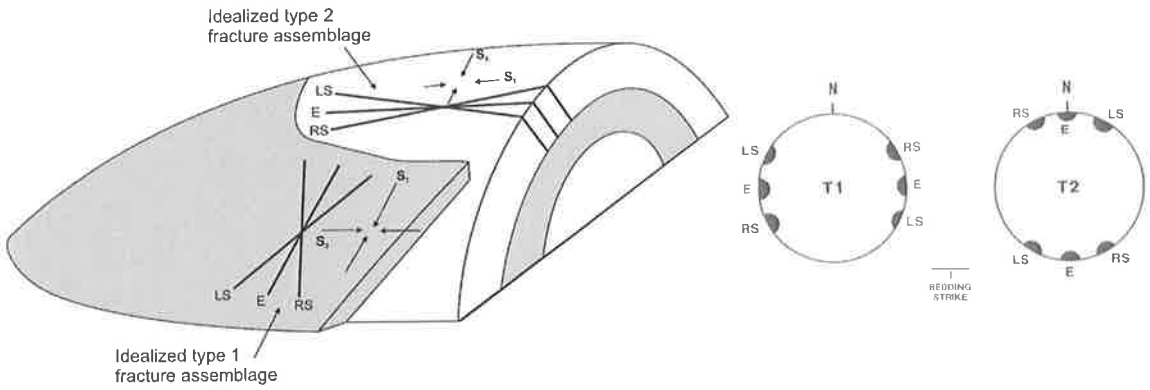

Figure 9.6. Idealised fold-related type 1 and type 2 fracture assemblages relative to strike, dip and surface curvature (left) and idealised stereographic projections of the type 1 and type 2 fracture assemblages at Palm Valley used by previous authors to model the Palm Valley fracture assemblage (Berry et al., 1996; Stearns and Friedman, 1972).

9.2.2 Mereenie

Photo-geological mapping of surface fractures over the Mereenie Field, as undertaken at Palm Valley, is not possible due to the relatively poor outcrop and extensive sand cover over the field (Fig. 9.7). Subsurface fractures in the Mereenie Field have been measured using 9006 m of FMS logs from 16 wells (Hillis et al., 1999b). Hillis et al. (1999) interpreted a total of 371 electrically conductive and resistive fractures in the FMS data. The fractures are typically high angle, dipping between 60°– 90° and define two major sets: a NNW-striking set and a WNW-striking set. The two sets are at a small angle to the trend of anticline fold axis (Figs 9.8, 9.9). The two main fracture sets are interpreted to be fractures of a type 2 fracture assemblage related to outer-arc flexure during folding about an axis parallel to bedding strike (Hillis et al., 1999b). There are also small faults and fault-related fractures in wells close to the main Mereenie Fault (East Mereenie 38) (Hillis et al. 1999). Previous studies have been limited because all wells with FMS data are off-crest oil rim wells and there are no crestal wells with fracture data to calibrate fracture development with structural position.

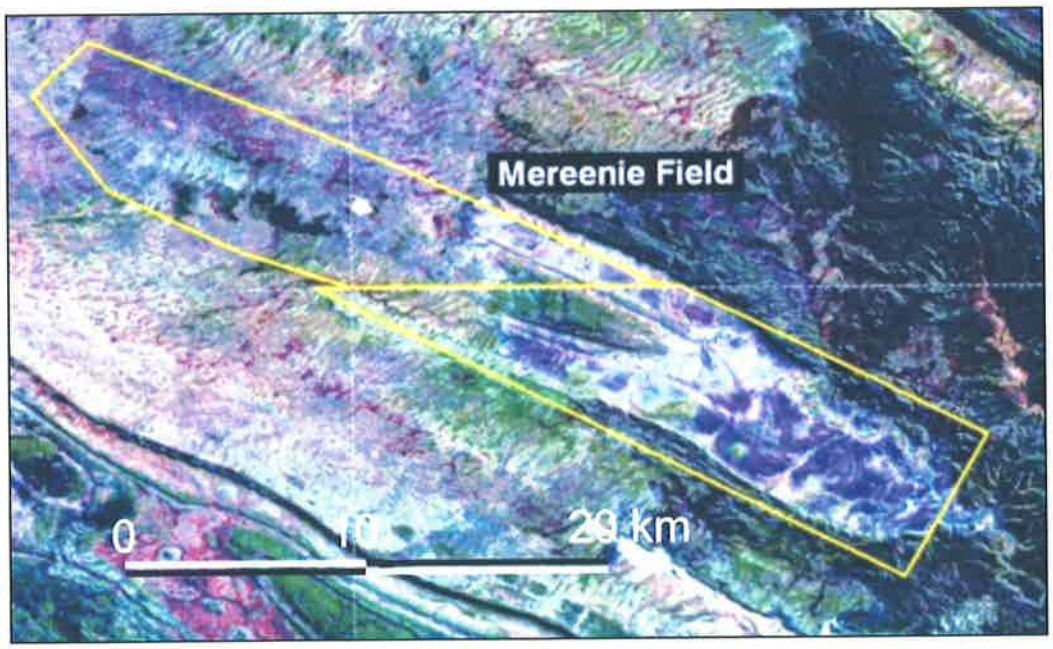

Figure 9.7. Landsat image over the Mereenie Field (NASA, 2004).

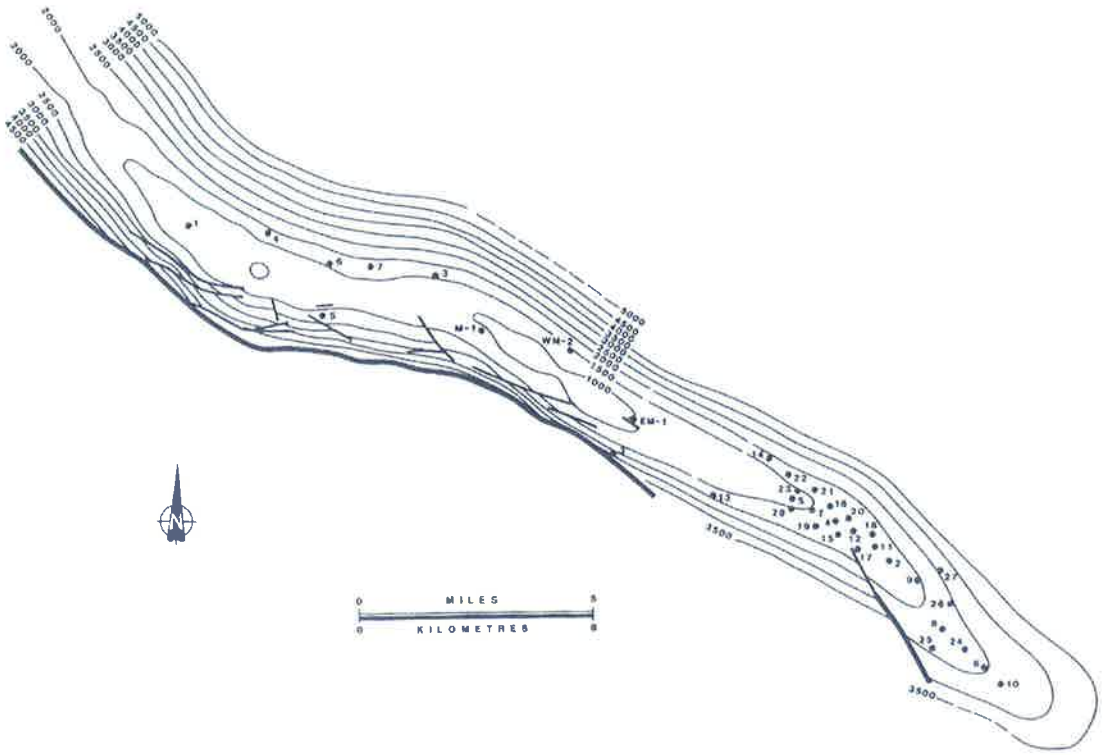

Figure 9.8. Top Pacoota Sandstone depth structure map (feet) of the Mereenie Field (Havord, 1991).

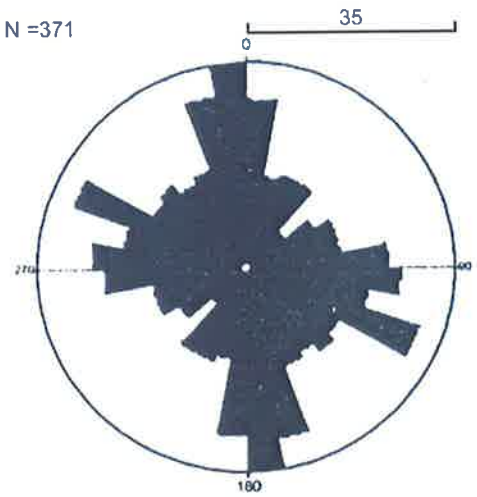

Figure 9.9. Rose plot of all fracture strikes interpreted from FMS data in the Mereenie Field, a total of 371 fractures were interpreted (Hillis et al., 1999b).

9.3 Comparison of Natural Fracturing in the Palm Valley and Mereenie Fields

The previous studies have been successful in identifying the importance of fractures in both fields, linking outcrop observations to reservoir level and identifying the importance of mechanical stratigraphy. The problem with these models is that many of the predicted fracture sets, namely left and right lateral shear fractures of both assemblage types are either absent or poorly defined

and there is no evidence (to the best of the author's knowledge) to suggest that the fractures at appropriate orientations are in fact shear fractures (i.e. slickenlines or offset). Furthermore, the studies do not account for the discrepancy in natural fracture development between the Palm Valley and Mereenie Fields.

There are several similarities and differences between the natural fracture systems at Mereenie and Palm Valley. The following are the key similarities.

- The fracture systems are generally high angle dipping between 60°– 90°.
- The fractures are predominantly fold-related with a dominant set approximately parallel to the fold axis, interpreted as crestal extensional fractures.
- The fracture population is influenced by the mechanical stratigraphy with high-angle fractures more frequent in competent intervals (sandstones) and bedding-plane shear fractures in the shales.

The following are the key differences:

- The fracture system in the Palm Valley Field is considerably more intense than in the Mereenie Field. Fracture densities never exceed one per metre in the Mereenie Field yet the most productive intervals in the Palm Valley Field have fracture densities in the order of 30 per metre (Berry et al., 1996; Hillis et al., 1999b). However, fracture density in the crestal areas of the Mereenie anticline is unclear due to a lack of crestal wells with information on fracture occurrence.
- The Palm Valley fracture network is dominated by two sets perpendicular to each other, providing good connectivity (Fig. 9.3). The Mereenie fracture network is dominated by two sets at a small angle to each other, thereby limiting connectivity (Fig. 9.9).
- The Palm Valley fracture network has a dominant set striking perpendicular to the main east-west fold axis providing good fracture connectivity (based on HDT data from Palm Valley 6B). Pressure and terference testing show that the fast direction is parallel to the fold axis (Berry, 2004. pers comm). There are virtually no fractures that strike perpendicular to the Mereenie fold axis.

There are several possible explanations to account for the differences in fracture development between Mereenie and Palm Valley:

- differences in the rheological properties of the reservoir rocks at the time of fracturing;
- differences in the pressure history of the two fields;
- differences in structural style and evolution of the two fields;
- differences in bulk strain;
- any combination of the above.

Fracture modelling, reservoir management and the prediction of permeability sweet spots in both fields may be improved if the reasons for the discrepancy in fracturing between the two fields are recognised. The following sections compare the structural geometry and the structural, burial and pressure histories of the two fields in order to assess this issue.

9.4 Rheology

The rheology of a sedimentary sequence has a critical influence on natural fracture development and is a function of the elastic properties of each sedimentary layer and the stacking pattern of the sequence (Cooke and Underwood, 2001; Rijken and Cooke, 2001; Underwood et al., 2003). Studies from both the Palm Valley and Mereenie Fields demonstrate the importance of the different rheological properties of different layers, having shown that fractures are more abundant in the competent sandstone intervals than the shale intervals (Berry et al., 1996; Hillis et al., 1999b). The stratigraphic sequence from the Pacoota Sandstone to the Stairway Sandstone is relatively consistent at Palm Valley and Mereenie (Benbow and Lawson, 1967; Walker and Berry, 1993). Hence, any small differences in the sequence are not considered significant enough to account for the considerable difference in fracture development in the two fields.

Deep burial and consequent diagenesis can significantly change the rheology of a sedimentary sequence. The Palm Valley Field has been buried approximately 2 km deeper than the Mereenie Field (Fig. 8.13), resulting in more advanced diagenesis and porosity reduction. Rock strength testing has been previously conducted on all suitable samples from the Palm Valley cores to determine the mechanical properties of the reservoir rocks (Stearns et al., 1996). Appendix F shows a multi-stage stress-strain test conducted on a Palm Valley Pacoota Sandstone sample at confining pressures of 5000, 7500 and 10 000 psi (Stearns et al., 1996). Equations 9.1 and 9.2 are used to derive the cohesive strength and coefficient of friction from the stress-strain data (Table 9.1).

$$S_n = 0.5(S_1+S_3) - 0.5(S_1-S_3)\,COS2\theta \qquad \text{Equation 9.1}$$

$$S_s = 0.5(S_1-S_3)\,SIN2\theta \qquad \text{Equation 9.2}$$

Additional stress-strain testing was conducted as part of this study in order to compare rheological properties between Mereenie and Palm Valley. A multi-stage stress-strain test was conducted on a Pacoota Sandstone sample from 1435.09 m in East Mereenie 4. The test was conducted under similar confining pressures to replicate the test conditions of the Palm Valley tests (Appendix F). Equations 9.1 and 9.2 are used to derive the cohesive strength and coefficient of friction from the stress-strain data (Table 9.1).

The stress-strain testing shows that the Pacoota Sandstone has similar mechanical properties at Mereenie and Palm Valley and that differing rheology is thus unlikely to be responsible for the variation in fracture development between the two fields. In-situ elastic properties are typically a function of maximum burial and they do not necessarily reflect the mechanical properties at the time of fracturing if fracturing occurred prior to maximum burial, which is highly likely in this instance. However, most of the difference in maximum burial depth between Palm Valley and Mereenie is due to deposition of the Pertnjara Group after folding and fracturing and there is no evidence to suggest that Palm Valley was buried significantly deeper than Mereenie at the time of folding and fracturing.

Field	Formation	C_o	μ	T*
Palm Valley	Pacoota Sandstone	58.8 MPa	0.81	~29.4 MPa
Mereenie	Pacoota Sandstone	55 MPa	0.79	~27.5 MPa

Table 9.1. Rock mechanical properties derived from multi-stage stress-strain testing on Pacoota Sandstone samples from the Mereenie and Palm Valley Fields (Stearns et al., 1996). * Tensile strength (T) is estimated as $0.5*C_o$.

9.5 Pore Pressure

Pore pressure has a critical influence on natural fracture development. An increase in pore pressure reduces effective stress and moves the Mohr circle towards the failure envelope, thereby increasing the propensity for fracturing. Formation test data shows that both the Mereenie and Palm Valley fields were hydrostatically pressured pre-development (Aguilera, 1995; Havord, 1991); however, if significant palaeo-overpressure occurred at Palm Valley, this may account for the discrepancy in fracturing between the two fields. There are a number of observations that suggest Palm Valley and Mereenie may have experienced different pressure histories. Figure 9.10 shows a sand dyke and associated breccia within the Pacoota Sandstone at Glen Helen Gorge implying substantial palaeo-overpressure in the northern Amadeus Basin ~25 km north of Palm Valley (Maltman and Bolton, 2003).

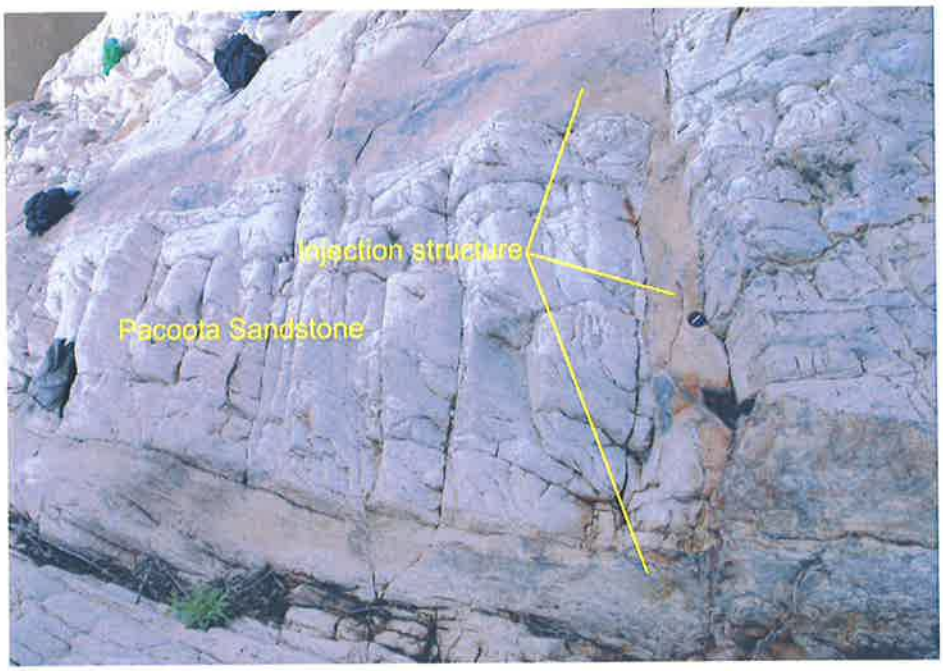

Figure 9.10. Sedimentary injection structure within the Pacoota Sandstone in Glen Helen Gorge implies palaeo-overpressure in the northern Amadeus Basin ~25 km north of Palm Valley. The clastic dyke comprises sandstone clasts of the Pacoota Sandstone within a sandstone matrix.

Figure 9.11. Flow banding (left) and brecciation (right) within the injection structure shown in Figure 9.10.

Overpressure may be generated in a number of ways, including disequilibrium compaction, tectonic compression, kerogen maturation and gas generation (Osborne and Swarbrick, 1997). Maturation of kerogen to oil and subsequent cracking to gas is accompanied by fluid volume expansion that can generate overpressure in a closed system (Barker, 1990; Osborne and Swarbrick, 1997). Overpressure may have developed at Palm Valley via this mechanism because deep burial has pushed the reservoir through the oil window and well into the gas window (~6 km max) (Fig. 8.13). In comparison, the Mereenie Field has never been buried past the oil window (~4 km max), limiting gas cracking and consequent fluid volume expansion.

Disequilibrium compaction overpressures develop when the rate of fluid expulsion from the pore spaces cannot keep up with compaction due to rapid burial. Disequilibrium compaction commonly occurs in shale prone sequences subjected to rapid burial (Mann and Mackenzie, 1990; Osborne and Swarbrick, 1997). As discussed in Section 7.2.3, evidence suggests that the Pertnjara Group was deposited very rapidly along the northern margin of the basin with burial rates up to 0.5–1 km/Myr in the Brewer Conglomerate inferred along the northern margin over the Missionary Plain (Gibson et al., 2004; Jones, 1991). Palm Valley is closer to the orogenic front and may have experienced deeper and more rapid burial resulting in elevated fluid pressures compared to Mereenie.

Disequilibrium compaction-type overpressure may also be induced via tectonic compression/elevated horizontal stresses (Osborne and Swarbrick, 1997; Sleep and Blanpied, 1992). The cross-sections presented in Chapter 8 show that orogenic intensity was greater along the Palm Valley cross-section that at Mereenie and that any tectonically induced overpressure would probably be greater at Palm Valley than at Mereenie. Furthermore, the Palm Valley structure is unfaulted and may have been more capable of sealing overpressure than the faulted Mereenie Anticline which may have leaked due to fault-valve processes (Sibson, 1990; Sleep and Blanpied, 1992). The same fault-valve processes may have prevented the retention of overpressure at Palm Valley once fracturing occurred.

In conclusion, it is possible that preferential overpressure development at Palm Valley has influenced the intensity of natural fracturing with respect to Mereenie. However, there are no definitive data with which to prove this hypothesis.

9.6 Structural Style

The structural modelling and cross-sections presented in Chapter 8 show that the Palm Valley and Mereenie anticlines are similar structures. Both anticlines formed as detachment folds above the Bitter Springs Formation during the Alice Springs Orogeny. However, there are several significant differences between the two structures (Table 9.2). The Palm Valley Anticline is essentially unfaulted with only minor offset at reservoir level and is more symmetric with maximum limb dips of ~22°. The Mereenie Anticline has a faulted forelimb forming a break-thrust geometry and is a more advanced, asymmetric structure with forelimb and backlimb dips of ~45° and ~25° respectively. The top Pacoota Sandstone structure maps show that there is also significant difference between the structures parallel to the main fold axes. The Mereenie structure is a southeast plunging cylindrical fold with four-way closure created by minor plunge at the northwest end of the structure and minor saddles along the fold crest (Fig. 9.8). The Palm Valley structure has significantly greater plunge along the anticlinal noses, defining a much more dome-like geometry comprising two prominent domes separated by a saddle (Fig. 9.2).

	Mereenie	Palm Valley
Fold style	Detachment fold	Detachment fold
Fold geometry	Faulted, gently plunging cylindrical	Minor faulting, domes and connecting saddle
Symmetry	Asymmetric	Symmetric
Maximum forelimb dip	45°	22°
Maximum back limb dip	25°	22°
Plunge eastern nose	2.3°	3.3°
Plunge western nose	0.7°	1.9°

Table 9.2. Comparison of the Mereenie and Palm Valley structural geometries. The Mereenie Anticline is a tighter structure in the direction perpendicular to the fold axis, but the Palm Valley Anticline is more dome-like and is tighter in the direction parallel to the main fold axis.

9.6.1 Curvature analysis

Surface curvature has been used by numerous authors as a proxy for fold-related fracture density with varying degrees of success (Hennings et al., 2000; Lisle, 1994; Masaferro et al., 2003). Curvature analysis was originally restricted to 2D curvature (due to technical limitations), commonly referred to as normal curvature (Harris et al., 1960; Narr, 1991). Normal curvature analysis determines the rate of change of bedding dip around a fold. However, flexural slip folds do not necessarily require strain within the folded surfaces and fracturing is not necessary to accommodate folding even in tight cylindrical folds (Lisle, 1994). In contrast, any surface subject to double curvature, such as a dome or saddle, cannot form without a component of stretching or contraction of the surface, thereby inducing strain and promoting fracturing (Lisle, 1994). Recently developed techniques of curvature analysis can assess 3D curvature, referred to as Gaussian curvature, over a surface grid. Gaussian curvature is defined as the product of the two greatest curvatures (k_1 and k_2) measured along two orthogonal curves (Fig. 9.12). Gaussian curvature has been shown to be a good proxy for fold-related fractures in a number of studies (Hennings et al., 2000; Lisle, 1994; Masaferro et al., 2003; Wynn and Stewart, 2003).

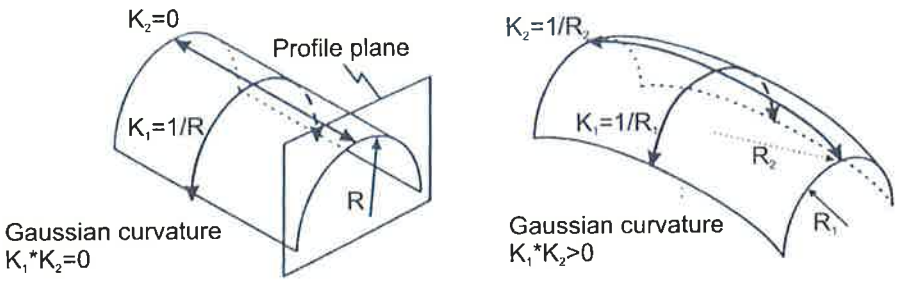

Figure 9.12. Gaussian curvature is defined as the product of the two principal curvatures, k_1 and k_2 measured along two orthogonal curves through point k. A gentle dome will have greater Gaussian curvature than a tight cylindrical fold despite the cylindrical fold having greater 2D curvature perpendicular to the fold axis (Lisle, 1994; Wynn and Stewart, 2003).

Surface grids of the top of the Pacoota Sandstone have been created over the Mereenie and Palm Valley anticlines during previous studies by integrating 2D seismic data with surface

geology projected to the top Pacoota Sandstone level (Flottmann, 2003). Normal and Gaussian curvature analysis of both grids has been conducted in this study using the Midland Valley 3D Move software. An inherent problem with this approach is the absence of 3D seismic data resulting in uncertainty and smoothing between the 2D lines over both grids. In addition, the Mereenie grid is constrained by more closely spaced and better quality seismic lines than the Palm Valley grid. The Mereenie grid was smoothed to a similar resolution to the Palm Valley grid to allow a more rigorous comparison between the two grids. The Palm Valley grid covers 1065 km^2 and is defined by 6664 points and 12 948 triangles each ~0.08 km^2. The Mereenie grid covers 281 km^2 and was resampled so that it is defined by 1709 points and 2855 triangles each ~0.1 km^2.

Figures 9.13 and 9.14 show normal curvature maps of the Mereenie and Palm Valley grids with the same colour scale for comparison purposes. Normal curvature is particularly high along the Mereenie fold crest and forelimb and is generally an order of magnitude higher than that over the Palm Valley Anticline (Table 9.3) (Appendix G). Normal curvature analysis suggests that the Mereenie Anticline is more prone to fold-related fracturing because the mean normal curvature over the Mereenie grid (5.56×10^{-2}) is an order of magnitude greater than it is over the Palm Valley grid (8.11×10^{-3}). Fold-related fractures predicted by normal curvature analysis would be most dense along the Mereenie fold axis and forelimb; however, this is not supported by well data from the Mereenie forelimb.

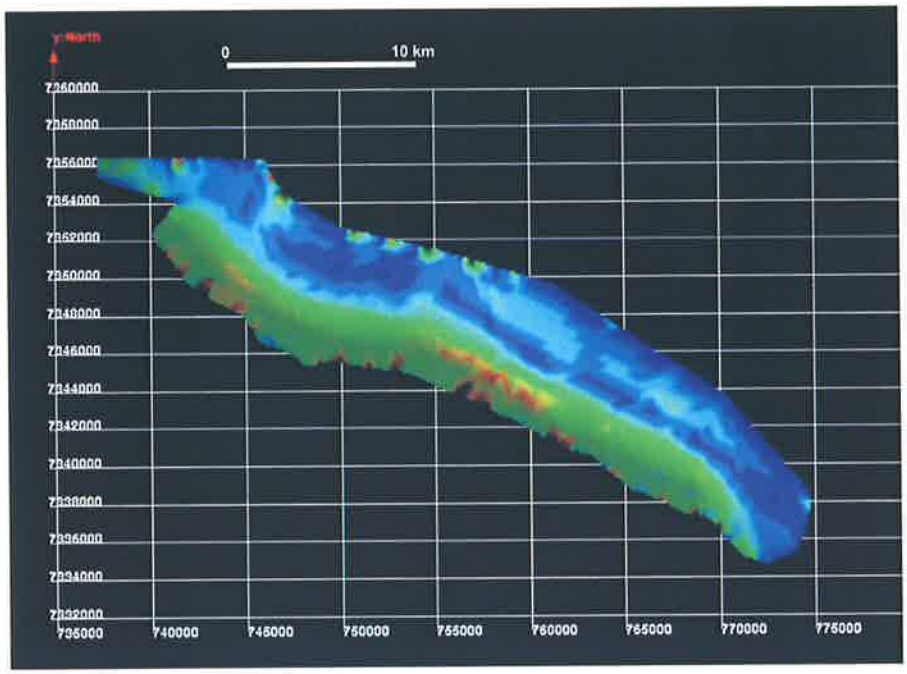

Figure 9.13. Normal curvature map of the top Pacoota Sandstone over the Mereenie Anticline. Normal curvature is greatest along the fold crest and steep forelimb. Red indicates areas of high normal curvature and blue indicates areas of low normal curvature. Background grid is 5 km * 2 km.

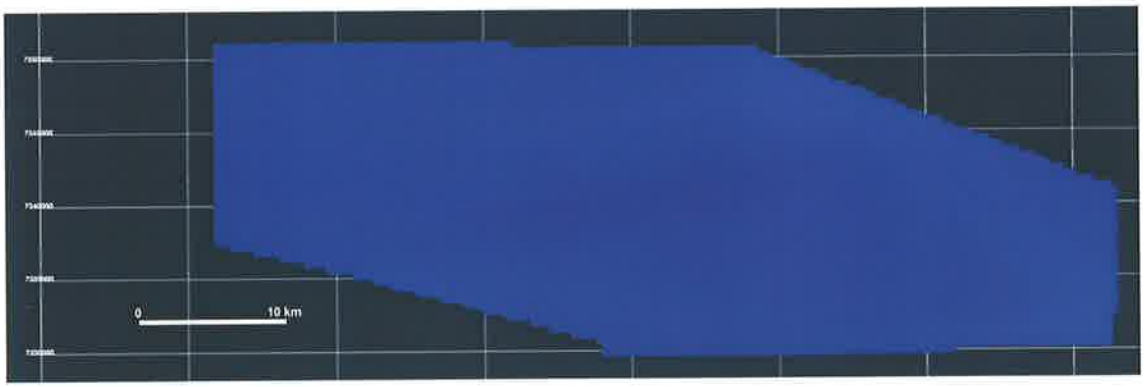

Figure 9.14. Normal curvature map of the top Pacoota Sandstone over the Palm Valley Anticline with the same colour scale as the Mereenie map. Mean normal curvature over the Palm Valley grid is approximately an order of magnitude less than that over the Mereenie grid. Background grid is 10 km * 5 km.

Figures 9.15 and 9.16 show Gaussian curvature maps of the Mereenie and Palm Valley grids with the same colour scale for comparison purposes. Gaussian curvature has been calculated over both structures using a calculation-grid size of 400 m * 400 m. An unexpected result of the analysis is that the mean Gaussian curvature over the Mereenie grid (1.53×10^{-3}) is an order of magnitude greater than that over the Palm Valley grid (1.33×10^{-4}) despite the Palm Valley structure being more dome shaped than the cylindrical Mereenie structure. Hence, first-pass

analysis of the Gaussian curvature results suggests Mereenie should be more prone to fold-related fracturing than Palm Valley.

Figure 9.17 presents histograms of the Gaussian curvature calculated at each point over both grids. The histograms show distinct differences in the distribution of Gaussian curvature between the two fields. The Gaussian curvature distribution over the Mereenie grid is characterised by some high-value outliers ($>|0.002|$) and a high percentage of points with zero Gaussian curvature (75.2%, Table 9.3). The high-value outliers in the Mereenie distribution create a skewed range in the data because the vast majority of values are zero. The outliers significantly influence the value of mean Gaussian curvature and obscure the colour scale of the Gaussian curvature maps. The distribution of Gaussian curvature at Palm Valley has a far lower percentage of high-value outliers and has a lower percentage of zero values, suggesting that Gaussian curvature is more even over the Palm Valley structure. The percentage of non-zero points appears to be more reflective of the general fold form than the maximum or mean values of Gaussian curvature over the grid.

The cause and significance of the high-value Gaussian curvature outliers at Mereenie is unclear. The outliers would most likely be distributed as linear trends along the seismic lines if they were caused by sampling; however, this is not the case. If a point has high normal curvature, even a small amount of curvature in the perpendicular direction produces high Gaussian curvature. The areas of high Gaussian curvature over the Mereenie grid correspond with the areas of high normal curvature, implying the high-value outliers are real and are a function of multiplication effects in the areas of high normal curvature. As most of the points at Mereenie have zero Gaussian curvature (due to multiplication by zero), any high-value points significantly skew the population.

The Gaussian curvature distributions in both fields have been trimmed to between -0.002 and 0.002 to remove the effect of high-value outliers $>|0.002|$. Mean Gaussian curvature has been recalculated for the trimmed distributions (Table 9.3) and is an order of magnitude greater over the Palm Valley grid (1.09×10^{-4}) than over the Mereenie grid (1.7×10^{-5}). The histograms and mean Gaussian curvature calculated from the trimmed distributions suggest that the Palm Valley Anticline should have more fold-related fracturing than the Mereenie Anticline. Figures 9.18 and 9.19 show that Gaussian curvature is more widely and evenly distributed over Palm Valley.

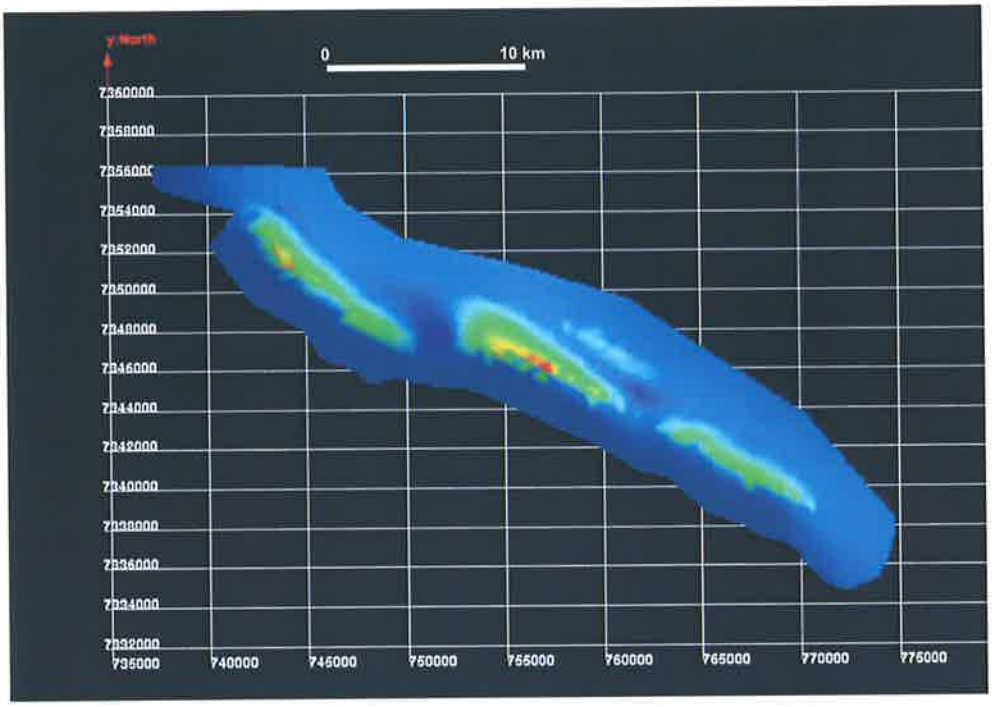

Figure 9.15. Gaussian curvature map of the top Pacoota Sandstone over the Mereenie Anticline.

Figure 9.16. Gaussian curvature map of the top Pacoota Sandstone over the Palm Valley Anticline at the same scale as the Mereenie map.

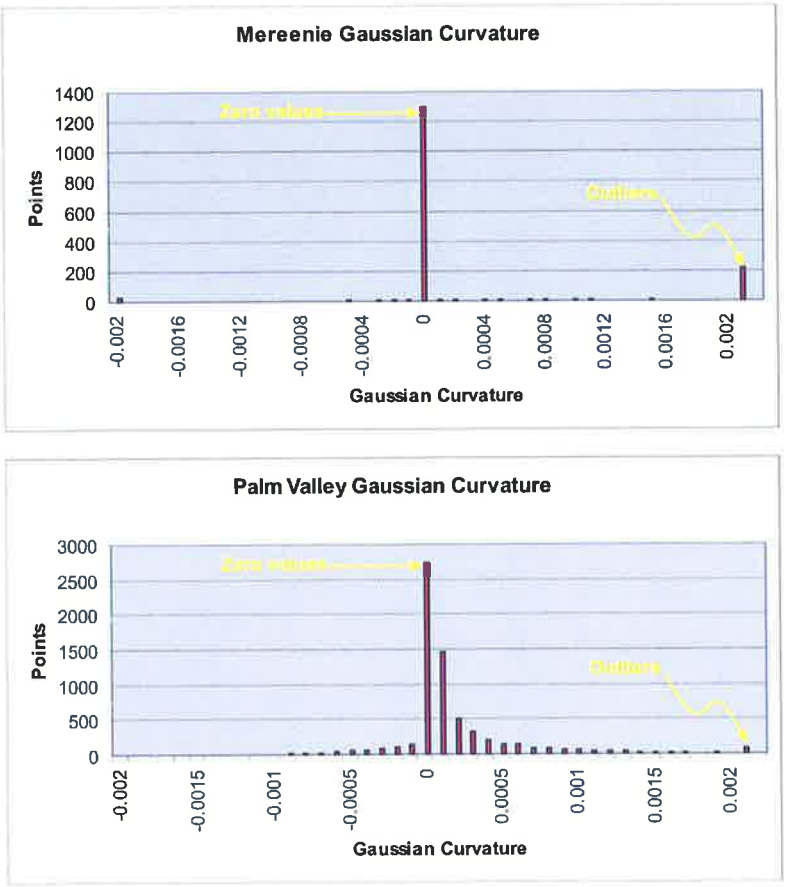

Figure 9.17. Histograms of Gaussian curvature over the Mereenie and Palm Valley Fields (bin size 0.0001) using the same surface grids as for normal curvature. 75.2% of values over the Mereenie grid are zero compared to only 27.9% zero values over the Palm Valley grid. There are significant outliers in the Mereenie distribution that strongly influence the mean Gaussian curvature values. Mean Gaussian curvature has been calculated with the data trimmed to between -0.002 and 0.002 to remove the effect of outliers (Table 9.3).

	Points	Mean	Median	St Dev	% = 0	% > 0	% < 0
Mereenie Normal	1709	5.56×10^{-2}	3.71×10^{-2}	5.04×10^{-2}	NA	NA	NA
Mereenie Gaussian	1709	1.53×10^{-3}	0	5.33×10^{-3}	**75.2%**	18.8%	6%
Gaussian (-ve values)	103	-1.46×10^{-3}	-7.86×10^{-4}	5.43×10^{-3}	NA	NA	NA
Gaussian (+ve & zero)	1606	1.72×10^{-3}	0	5.48×10^{-3}	NA	NA	NA
Gaussian trimmed (-0.002 - 0.002)	1461	$\mathbf{1.70 \times 10^{-5}}$	**0**	3.10×10^{-4}	**87.9%**	6.9%	5.2%
Palm Valley Normal	6664	8.11×10^{-3}	6.46×10^{-3}	5.83×10^{-3}	NA	NA	NA
Palm Valley Gaussian	6664	1.33×10^{-4}	1.00×10^{-6}	4.20×10^{-4}	**27.9%**	50.6%	21.5%
Gaussian –ve values	1434	-1.74×10^{-4}	-4.60×10^{-5}	2.60×10^{-4}	NA	NA	NA
Gaussian +ve values & zero	5230	2.18×10^{-4}	3.30×10^{-5}	4.20×10^{-4}	NA	NA	NA
Gaussian trimmed (-0.002 - 0.002)	6590	$\mathbf{1.09 \times 10^{-4}}$	$\mathbf{1 \times 10^{-6}}$	3.60×10^{-4}	**28.2%**	50.1%	21.8%

Table 9.3. Summary of the normal and Gaussian curvature distributions over the Mereenie and Palm Valley grids. Mereenie has a significantly higher mean Gaussian curvature; however, it is strongly affected by outliers. Palm Valley has a higher mean Gaussian curvature when the distributions are trimmed to between –0.002 and 0.002 to remove the effect of outliers. Palm Valley has a significantly lower proportion of non-zero values reflecting greater Gaussian curvature over much of the structure.

Gaussian curvature is indeed a good proxy for fracture intensity in the Palm Valley Field with a good correlation between well performance and Gaussian curvature. Figure 9.20 shows the location of wells in the field relative to Gaussian curvature. All of the production wells occur in areas of high Gaussian curvature and all three of the non-producing wells (typically, well tested at rates too small to measure) occur in areas of zero or near-zero Gaussian curvature. The relationship between Gaussian curvature and fracture intensity in the Mereenie Field is less clear because most of the wells (with fracture data) have been drilled off-crest to develop the oil rim and are not in areas of high Gaussian curvature along the fold crest. Correlation between Gaussian curvature and fracture intensity/well performance in the Mereenie Field may be assessed once crestal wells are drilled to develop the gas cap. Crestal wells drilled to develop the Mereenie gas cap are anticipated to intersect higher densities of fold-related fractures than the off-crest oil wells.

The curvature analysis presented here suggests that Gaussian curvature is a good proxy for fold-related fractures and that the percentage of non-zero values is most representative of the general fold form. However, curvature analysis is field-specific and values from one field cannot be directly correlated to fracture intensity in another field. The results of any curvature analysis must be calibrated with fracture or production data from wells in the same field before any link can be established between curvature and fracturing.

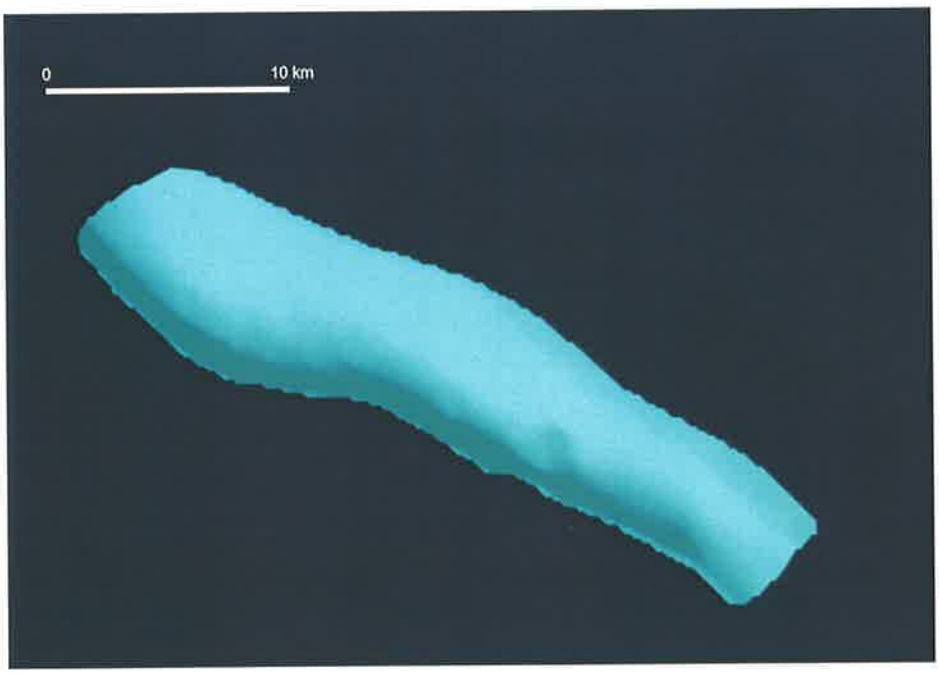

Figure 9.18. Gaussian curvature map of the top Pacoota Sandstone over the Mereenie Anticline with the colour range limited to between -0.002 and 0.002 to remove the effects of the high-value outliers. Dark blue represents –0.002 and red represents –0.002. The light blue shade present over most of the anticline represents Gaussian curvature of zero.

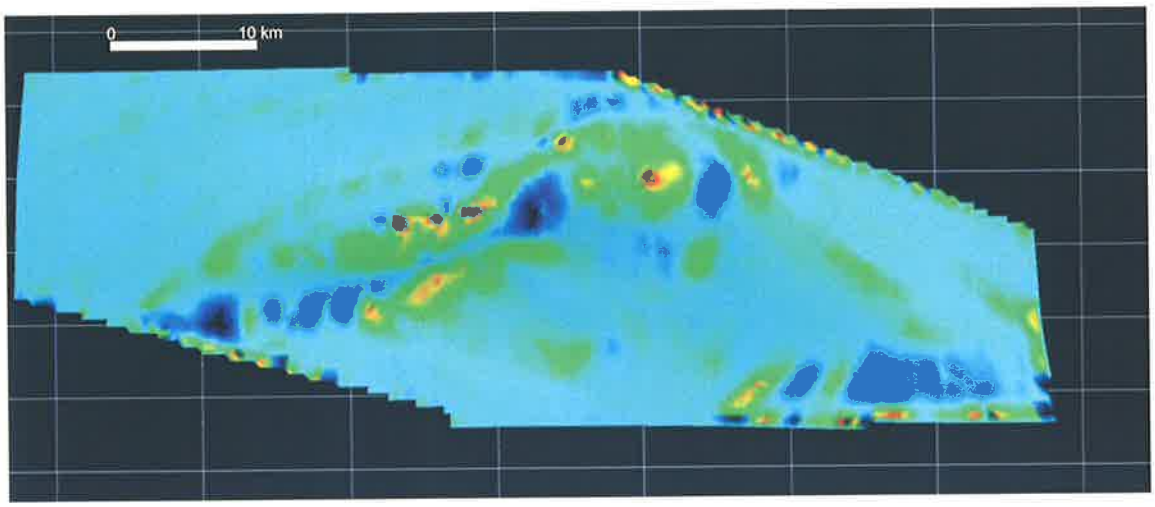

Figure 9.19. Gaussian curvature map of the top Pacoota Sandstone over the Palm Valley Anticline well locations with the colour range limited to between -0.002 and 0.002 to remove the effects of the high-value outliers. Dark blue represents –0.002 and red represents –0.002. The light blue shade present over much of the anticline represents Gaussian curvature of zero. Note that areas of significant Gaussian curvature are more evenly distributed over the Palm Valley Anticline than over the Mereenie Anticline.

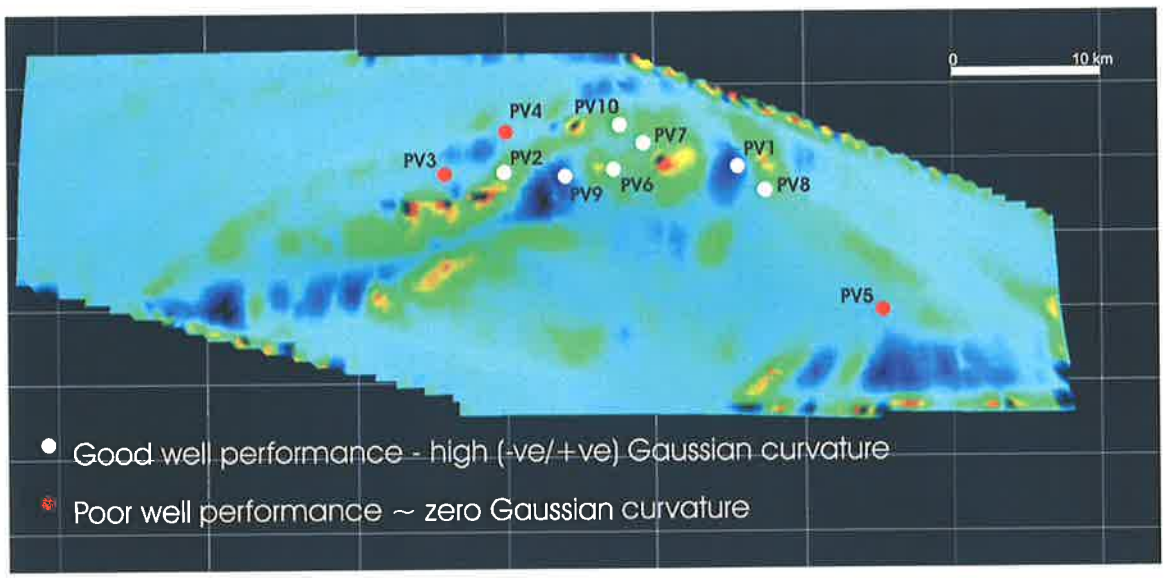

Figure 9.20. Gaussian curvature map over the Palm Valley Field showing the location of performing and non-performing wells. The non-producing wells occur in areas of zero or near zero Gaussian curvature and the producing wells occur in areas of high Gaussian curvature.

9.7 Regional Fractures (at Depth)

The previous sections have discussed local, fold-related fractures. The fold-related fractures at reservoir level in the Palm Valley Field are strongly reflected in the surface morphology over the Palm Valley Anticline (Figs 9.1, 9.3) and it appears that many of the natural fractures in both the Palm Valley and Mereenie Fields are a result of localised fold-related flexure. However, inspection of landsat images, aerial photographs and outcrops suggests that there is an additional phase of fracturing in the Amadeus Basin, which, to the best of the author's knowledge, has not been previously published. The surface morphology of the MacDonnell, Gardiner and James Ranges is dominated by a series of small valleys at remarkably consistent spacing of 500–1500 m (Figs 9.21–9.23). The valleys are perpendicular to strike and are responsible for the unique appearance of the ranges and their famous tourist appeal. The regularly spaced valleys are restricted to the Pertaoorrta and Larapinta Groups and do not occur in the Neo Proterozoic or Devonian Pertnjara Group.

Outcrop observations and the consistent nature of the valley system suggest that fracture swarms may control valley development (Figs 9.21–9.23). The regionally pervasive fracture swarms are not restricted to specific anticlines and occur along straight crested ridges suggesting they are not fold-related. The fractures typically strike perpendicular to bedding, ranging from north–south over the James Range to northeast–southwest over the northern Gardiner Range. Little information about the fractures can be determined from surface ornamentation or mineralisation because the valleys typically have moderately steep slopes covered in rubble due to the ancient landscape. The fractures are not restricted to individual beds and are quite pervasive within the latest Proterozoic to Ordovician section. The occurrence of the fractures in the latest Proterozoic to Ordovician section suggests that the fractures responsible for the surface geomorphology may occur at reservoir level and may therefore affect reservoir permeability.

Figure 9.24 shows valley/fracture swarm spacing in the Pacoota Sandstone mapped from aerial photographs on two traverses along the MacDonnell and Gardiner–James Ranges. A single, averaged fracture spacing value has been assigned for each 1:50 000 aerial photograph. The fracture spacing decreases from the east-southeast (where it is ~500 m) to the west-northwest (where it is ~>1200 m) along both the MacDonnell and Gardiner–James traverses (Fig. 9.24). Although the aerial photographic survey does not cover the Gardiner Range as far west as Mereenie, projection of the trends shown in Figure 9.24 suggests that regional fracture spacing is significantly greater at Mereenie (~>1500 m) than at Palm Valley (~ 550 m). These values are supported by outcrop observations over the Mereenie Anticline that suggest a spacing of major fracture swarms between 1300 and 4000 m (Campagna and Flottmann, 2002).

Most pervasive, regional, steeply dipping fracture sets are interpreted as being a result of uplift and unloading. This may be an appropriate model where the steeply dipping fractures are restricted to the upper few hundred metres of the crust (Engelder, 1985; Twiss and Moores, 1992). Indeed, such was the interpretation of the Scotia and Goonyella Riverside examples presented earlier in this thesis. However, the field observations do not support an unloading model for the regional fractures in the Amadeus Basin because they are restricted to the Pertaoorrta and Larapinta groups and do not occur in the Neoproterozoic or syn-ASO Pertnjara Group despite ~2-5 km of unloading (Gibson et al., 2004).

Figure 9.21. The regularly spaced valleys are controlled by pervasive fractures as demonstrated by this example in the Pacoota Sandstone and Goyder Formation at Glen Helen Gorge viewed towards the south. The valleys like the one shown here are mappable from aerial photography.

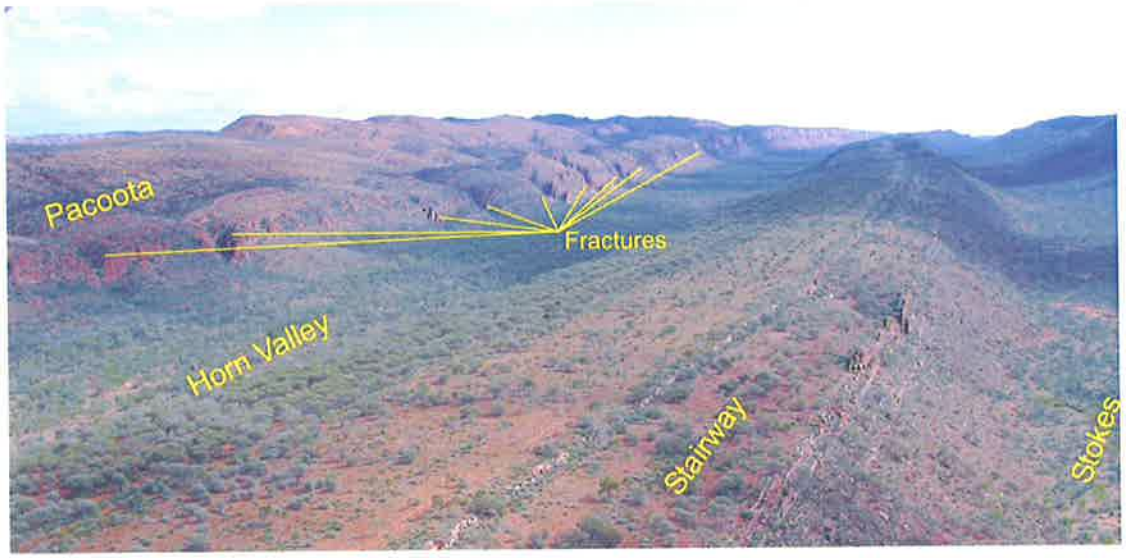

Figure 9.22. The fracture-controlled regular valley system responsible for the unique appearance of the MacDonnell Ranges directly east of Glen Helen Gorge, viewed towards the northeast from the air.

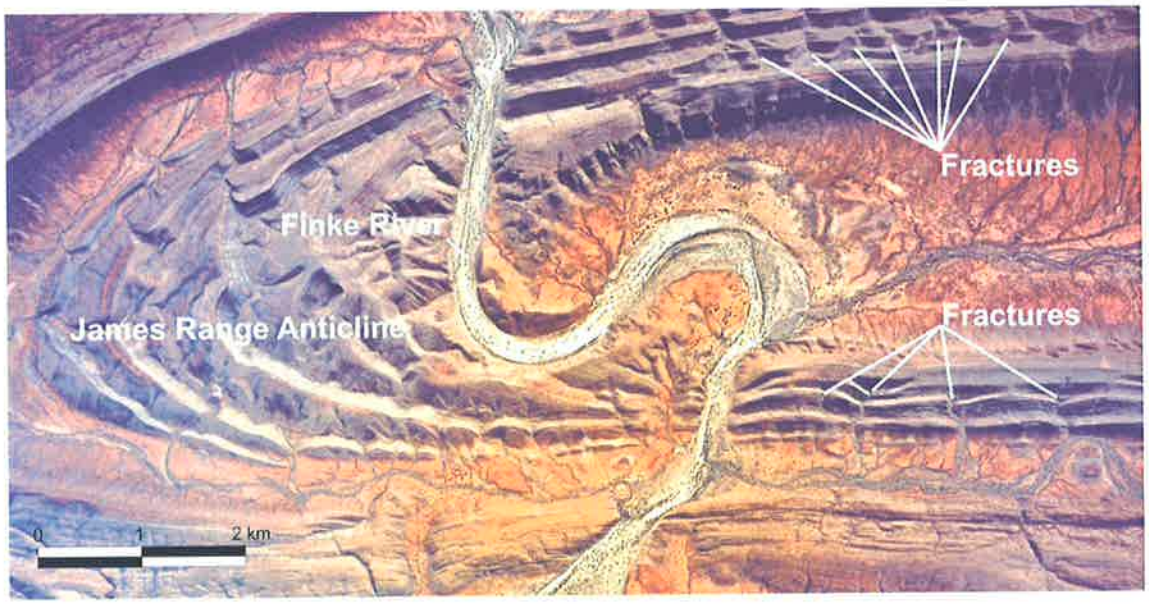

Figure 9.23. Aerial photographic expression of the regional fracture systems over the James Range Anticline. Note that the Finke River cuts through the anticline suggesting the contemporary drainage had established prior to folding.

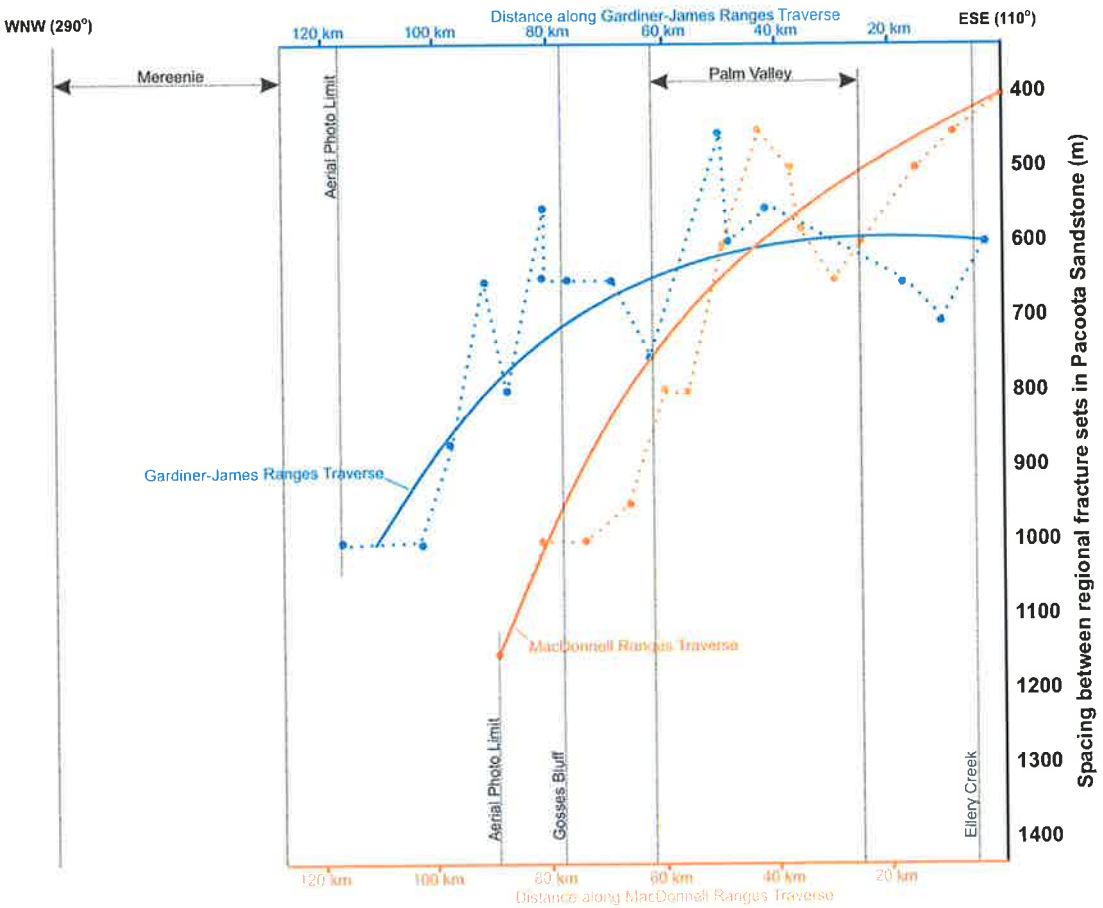

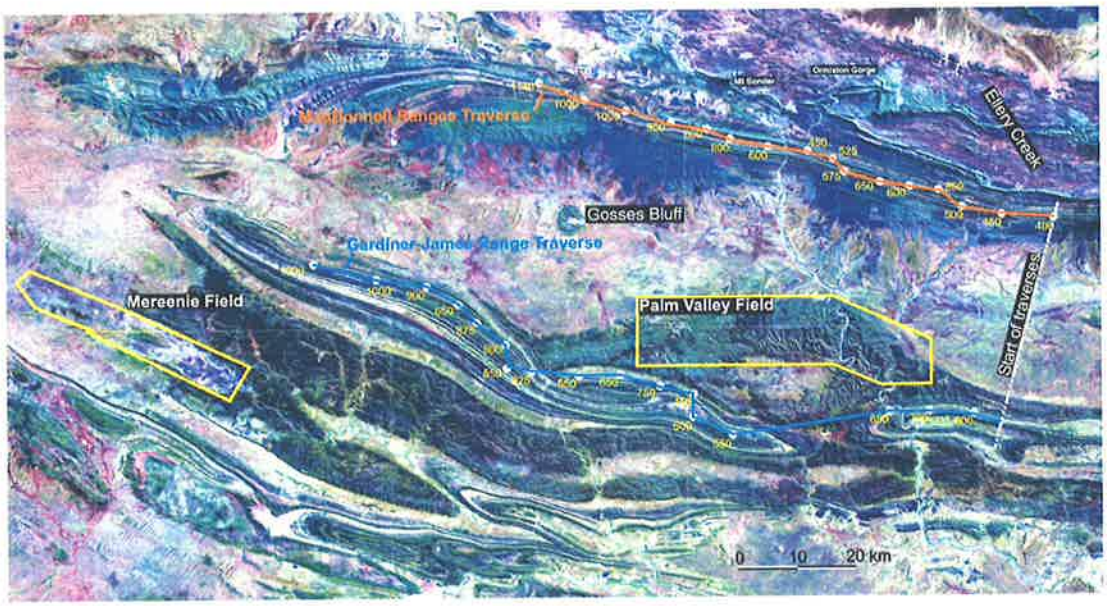

Figure 9.24. Regional fracture spacing in the Pacoota Sandstone mapped from the 1:50 000 aerial photographs; one value of fracture spacing has been assigned per photograph. The traverses are along the MacDonnell Ranges and Gardiner–James Ranges (bottom) and end at the northwest limit of the aerial photographic surveys. The spacing of the regional fracture swarms typically increases from east-southeast to west-northwest.

9.7.1 Regional orogenic-related fracture analogues

The regional fracture system of the Amadeus Basin, which is normal to bedding strike and thus parallel to the ASO shortening direction, is consistent with fracture systems in foreland basins of North and South America (Bell and Babcock, 1986; Scheidegger, 1983; Winslow, 1983) and of Europe (Becker, 1989; Dunne and North, 1990). The regional fractures described by these authors form parallel to the regional maximum horizontal stress associated with orogenic activity and appear to be directly related to orogenic intensity (Fig. 9.25). Lateral gradients in fracture intensity have been demonstrated between flat-lying fractured strata and adjacent folded strata containing the same fracture set (normal to fold axis) in front of the Appalachian and Andes mountains (Dean et al., 1979; Winslow, 1983). The fractures are interpreted to have formed in the flat-lying strata in front of the orogenic front (parallel to shortening direction) prior to their incorporation into the fold and thrust belts (Dean et al., 1979; Lorenz et al., 1991; Winslow, 1983). The regional fracture set in the Amadeus Basin appears similar: it is parallel to ASO shortening and occurs in the folded pre-ASO Pertaoorrta and Larapinta Groups, but not in the syn-ASO Pertnjara Group.

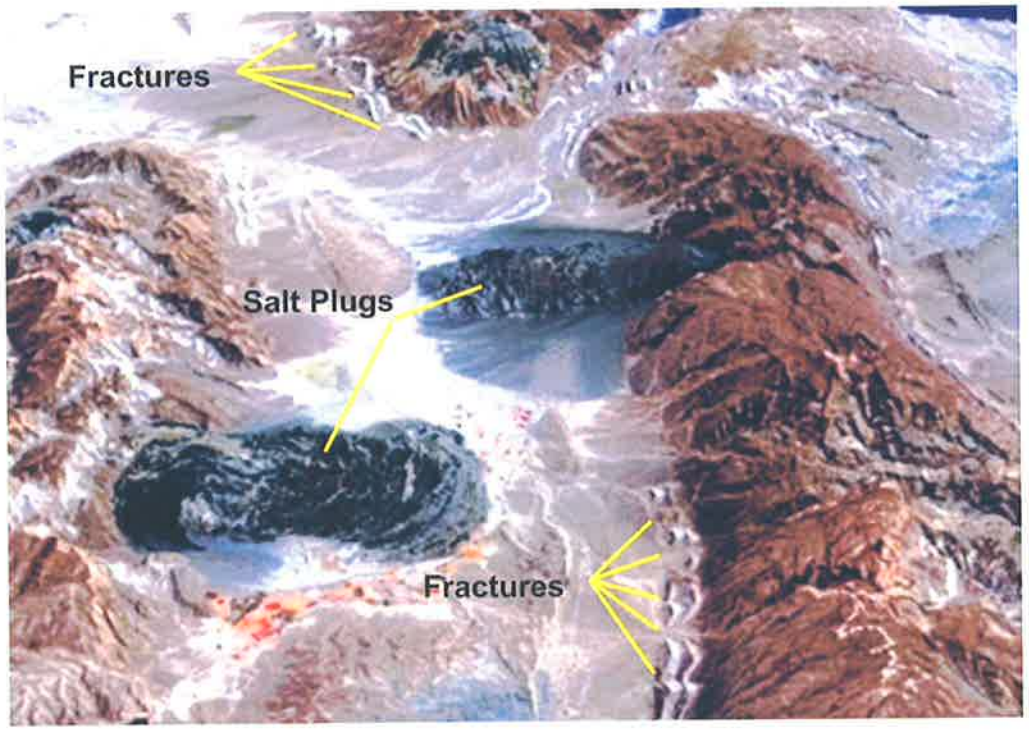

Figure 9.25. Satellite image showing salt plugs expelled from the core of detachment folds in a carbonate sequence in the southern Zagros Mountains, Iran (Space.com, 2004). Note the regular regional fracture sets striking approximately perpendicular to the fold axes. The regional fracture sets and detachment folds shown here are interpreted to be similar to those of the northern Amadeus Basin (Fig. 9.24).

Lorenz et al. (1991) present a model for the formation of steeply dipping regional fractures at depth in the Cretaceous Mesaverde Group of the Piceance Basin, Colorado, in front of a Laramide uplift (Lorenz and Finley, 1991). Their analysis shows that a set of regional fractures parallel to regional shortening formed at maximum burial (36–40 Ma) during a pulse of regional

Laramide compression (Lorenz and Finley, 1991). The proposed mechanism requires high differential horizontal stress and pore pressure that approaches, but does not and cannot exceed, the least principal stress. Local tensile stresses are formed around flaws and micro-cracks in the rock, parallel to the far-field maximum compressive stress as the anisotropy and magnitude of the stresses increases. Tensile fractures then form and propagate in the plane of maximum and intermediate principal stress and can occur up to hundreds of kilometres beyond an orogenic front in the absence of folding or flexure (Lorenz and Finley, 1991; Lorenz et al., 1991). These regional fractures are responsible for high-rate gas wells within the Piceance and San Juan basins (Lorenz and Finley, 1991; Teufel and Herrin, 2003).

The mechanism of formation of regional, orogen-normal fractures at depth presented by Lorenz et al. (1991) may account for the regional fractures observed in the Amadeus Basin. The spacing of these fractures in the Amadeus Basin is related to orogenic intensity (Fig. 9.24). The cross-sections presented in Chapter 8 show that orogenic intensity decreases westward from the Palm Valley cross-section to the Mereenie cross-section. Figure 9.24 shows that regional fracture spacing increases westward from ~500 m along the Palm Valley cross-section to ~>1500 along the Mereenie cross-section and can be directly correlated to orogenic intensity. Any palaeo-overpressure at the longitude of Palm Valley would also have contributed to the preferential formation of regional fractures in the Palm Valley area.

9.7.2 Significance of regional fracture swarms in the Amadeus Basin

If the pervasive regional fractures seen in the Amadeus Basin occur at reservoir level they may have a significant impact on permeability in the Palm Valley and Mereenie reservoirs for the following reasons.

- The regional fractures are suitably oriented within the in-situ stress field to be open and hydraulically conductive (S_{Hmax}~010°) (Berry et al. 1996; Hillis et al. 1998).

- The regional fractures are at a high angle to the dominant crestal fold-related fractures, thereby potentially providing good fracture connectivity.

- The regional fractures are pervasive and are not bed-bound, thereby plumbing the entire reservoir by providing connectivity between the bed-bound, fold-related fractures and different reservoir intervals.

9.7.3 Evidence for regional fracture swarms in the Palm Valley Field

There is compelling evidence that the pervasive regional fracture swarms occur at reservoir level in the Palm Valley Field and dominate well performance where present. Pressure tests in the Palm Valley Field indicate that the Pacoota Sandstone and Stairway Sandstone (below and above the Horn Valley Siltstone respectively) are in pressure communication (Milne and Barr, 1990b). The most likely explanation for this observation is that a pervasive fracture network extends through the Horn Valley Siltstone that is some 80 m thick and connects the Pacoota Sandstone and Stairway Sandstone. It seems unlikely that the localised bed-bound, fold-related fractures would provide such connectivity. Indeed the previous studies have shown that the small, bed-bound fractures typically occur in the sandstones and are not well developed in the shales/siltstones (Berry et al., 1996; Hillis et al., 1999b). The pressure communication between the Pacoota Sandstone and Stairway Sandstone is more likely due to the pervasive regional fracture swarms extending through the entire Horn Valley Siltstone.

The Palm Valley 6 well was drilled as a crestal well and subsequently plugged due to low flow rates, despite intersecting many small fractures. Palm Valley 6 was then side tracked and Palm Valley 6B achieved a flow rate of 137 MMSCFD which is an Australian onshore record (Milne and Barr, 1990b). The high rate from Palm Valley 6B is attributed to the intersection of a large, effective fracture(s) and undepleted reservoir pressure (Berry, 2004. pers comm). The significant difference in flow rates between Palm Valley 6 and Palm Valley 6B is attributed to two factors: 1) Palm Valley 6B was deviated and therefore intersected more near-vertical fractures and; 2) the fractures intersected by the two wells had different orientations and may be of a different type (Milne and Barr, 1990b). The HDT data show that natural fractures in Palm Valley 6 predominantly strike east-northeast and they are interpreted as crestal fold-related fractures. The HDT data show that the natural fractures intersected by Palm Valley 6B predominantly strike north-northwest and they may be either fold-related or the pervasive regional fractures. It is not possible to determine whether the fractures intersected by Palm Valley 6B are fold-related or part of a more pervasive regional fracture swarm based on orientation alone, in addition the HDT data is considered unreliable (Berry, 2004. pers comm). However, the gas flow influx pattern in Palm Valley 6B is characterised by sudden, large increases in influx suggesting the intersected fracture(s) is large and effective. Such a fracture is more likely a pervasive regional fracture swarm than a bed-bound fold-related fracture set. In addition, the fractures are parallel to the mapped regional fractures in the James and Gardiner Ranges (based on the HDT data).

9.7.4 Evidence for regional fracture swarms in the Mereenie Field

It is unclear whether the regional fracture swarms occur at reservoir level in the Mereenie Field as there are no deviated wells in the field. If regional fractures occur at reservoir level in the Mereenie Field they may provide permeability sweet spots for both oil-rim and gas-cap wells, although they would probably have less overall impact than those at Palm Valley because they

are likely to be more widely spaced. The aerial photographic mapping suggests that regional fracture spacing increases to more than 1500 m around the Mereenie Field (Fig. 9.24). The concept of regional fractures at reservoir level could be tested by future development drilling with deviated wells perpendicular to the regional fracture strike and at an appropriate spacing.

9.8 Synopsis

There are at least two generations of natural fracturing in the Amadeus Basin that are important to reservoir development: 1) fold-related fractures and; 2) previously undocumented regional, orogenic-related fractures. Many of the fold-related fractures are at a high angle to S_{Hmax} and may be stress-insensitive and remain open and hydraulically conductive due to the high rock strength and mineralisation (Berry et al., 1996; Hillis et al., 1998). The fold-related fractures are typically bed-bound, and are more closely spaced, providing access to the low permeability matrix while the regional fractures are more pervasive and plumb the entire reservoir by connecting the smaller fold-related fractures and the individual reservoir intervals.

The fold-related fractures may be predicted by modelling the fold geometry with Gaussian curvature. Areas of high fracturing and good well performance in the Palm Valley Field correlate with areas of high Gaussian curvature. The relationship between Gaussian curvature and fracturing within the Mereenie Field is less clear as most existing wells are off-crest oil rim wells. Any relationship between fold form and fracture development in the Mereenie Field may be tested once crestal wells are drilled to develop the gas cap. The quality of the input data and resolution of grid sampling have a significant effect on curvature analysis and hinders direct comparison of curvature between different fields/grids. The analysis presented in this chapter shows that curvature analysis is field-specific and curvature values from one field cannot be directly correlated to fracture intensity in another field. The results of any curvature analysis need to be calibrated with fracture or production data from within the field and cannot be calibrated to data from another field. Direct comparison of curvature values between fields would be most successful where the structures are completely constrained by 3D seismic. This issue is unlikely to be isolated to the Amadeus Basin and the findings of the curvature analysis presented in this chapter may be applied to other exploration and development programs in similar situations.

The regional orogenic-related fractures are a previously undocumented phenomenon within the Amadeus Basin, and are interpreted to have a significant impact on well performance. The regional fractures are pervasive and effectively plumb the Palm Valley Field by connecting the bed-bound, fold-related fractures and different reservoir intervals. The analysis presented in this chapter shows a clear relationship between orogenic intensity and regional fracture spacing. The structural analysis presented in Chapter 8 shows a decrease in orogenic intensity from the Palm

Valley cross-section to the Mereenie cross-section. Figure 9.24 shows spacing of regional fracture swarms increases westward from ~ 550 m over Palm Valley to >1500 m over Mereenie.

The effect of overpressure and rock mechanical properties on fracture development in the two fields remains somewhat ambiguous. There does not appear to be a significant variation in rock mechanical properties between the two fields. Both fields were normally pressured pre-development. However, there is evidence that the Palm Valley Field may have been subject to higher palaeo-overpressure than the Mereenie Field, although the extent of any palaeo-overpressure in Palm Valley remains unclear.

The findings of this chapter have specific application to the development of the Mereenie and Palm Valley fields and to petroleum exploration and development in similar provinces. The most productive wells in both fields are expected to occur in locations where the pervasive regional fractures intersect zones of dense fold-related fractures or where there are large reservoir-effective crestal fractures (as currently targeted). The regional fracture swarms occur independently of seismically resolvable structures but may be predicted at reservoir level at Mereenie and Palm Valley by extrapolating outcrop information. However, in other regions where outcrop information is unavailable, seismic methods such as AVO and AVAZ may be useful in locating regional fracture swarms where high quality 3D seismic is an option.

The following chapter uses the structural modelling presented in Chapter 8 to assess and reduce risk associated with the Mereenie sub-thrust play.

10 Mereenie Sub-thrust Assessment

10.1 Background

Exploration wells have tested the crests of most major anticlines in the northern Amadeus Basin, with the only economic accumulations occurring at the Mereenie and Palm Valley fields. The 'sub-thrust play' provides further exploration potential but has only been tested at one location in the basin. Magellan Petroleum drilled the Undandita wells in 1988 along the Deering Anticline some 50 km northeast of Mereenie (Fig. 8.5). The wells intersected the Carmichael thrust fault and various minor faults between 500 and 1100 m. The wells found oil and gas shows in the Arumbera Sandstone and the Pacoota Sandstone within the footwall of the Carmichael Fault (NTGS, 2003).

The Mereenie Field is within the hangingwall of the Mereenie Fault. The Mereenie Anticline strikes northwest-southeast and is approximately 40 km long and 4 km wide. Oil and gas are produced from stacked marine to shoreline sandstones of the Pacoota Sandstone with vertical closure ~ 300 m (Havord, 1991). More than half the initial oil reserves have been produced and the field is in decline. The sub-thrust play has the potential to increase reserves within the Mereenie Field and is an attractive near-field exploration target due to existing infrastructure and an upcoming development drilling campaign.

The charge history and top seal condition of the Mereenie sub-thrust play are considered to be similar to the Mereenie Field itself and are thus not the critical risk factors for the play. The critical risk factors for the sub-thrust play are:

- the structural development and geometry of the Mereenie Anticline with regard to charge history;
- the presence of fault-dependant footwall closure;
- the integrity of the fault seal.

The 2D restoration of the Mereenie Anticline presented in Figure 8.16 is based on seismic line m83-16 near the middle of the Mereenie Field (Fig. 10.1) and uses the 2D Move trishear and line length unfolding algorithms. There are four distinct stages in the fold development.

1. The fold developed as a detachment fold with parallel folding in the outer layers and disharmonic folding within the Bitter Springs Formation as ductile material migrated into the fold core. Subsequent initiation of syn-tectonic sedimentation marks the base of the Pertnjara Group.

2. Continued migration of the Bitter Springs Formation into the fold core became more difficult as the fold evolved resulting in a 'break-thrust' developing at approximately 80% of the overall shortening. The majority of the fold form had established prior to faulting.

3. Final movement occurred along the Mereenie fault to accommodate the remaining 20% of shortening (i.e. the last 20%) with continued deposition of the Pertnjara Group.

4. Continued deposition of the Pertnjara Group resulted in maximum burial and hydrocarbon charge.

The Mereenie Fault is considered to have developed pre-charge due to the dynamic lag between basement uplift/fold formation and maximum burial/hydrocarbon charge. Footwall closure and fault seal are thus the critical risk factors for sub-thrust trap integrity and are assessed in following sections of this chapter.

10.2 Mereenie Footwall Closure

The greatest limitation to this study is the poor quality of seismic data over the footwall of the Mereenie Fault. Figure 10.1 shows the 2D seismic grid used in this study, the Mereenie Fault and existing wells. The absence of strike-lines to tie the dip-lines within the footwall creates a large degree of uncertainty in any structural interpretation. In addition, the footwall of the fault is at the end of the dip-lines and its imaging may be influenced by migration effects altering its true geometry and creating further uncertainty. Figure 10.2 shows the variation in throw along the Mereenie Fault derived from the depth-converted seismic data. The graph shows that displacement decreases exponentially from 660 m on seismic section m87-01 towards the fold tip. The throw gradient follows a consistent trend along strike implying that the seismic interpretation in the footwall is at least valid.

The depth-converted seismic interpretation was gridded using Badley's Traptester software to produce depth to structure figures (Figs 10.3, 10.4). Figure 10.3 provides a 3D perspective of the Mereenie Field viewed towards the northwest. Figure 10.4 show that footwall saddles occur directly across the fault from the hangingwall saddles. This is consistent with the structural modelling that suggests most of the fold form developed prior to faulting. Therefore, hangingwall saddles are not fault-dependent and should coincide with footwall saddles. Areas in the footwall adjacent the West Mereenie and East Mereenie hangingwall saddles are therefore the most prospective. The 2D seismic data indicates that there may be as much as 150 m of vertical closure within these areas (Fig. 10.4).

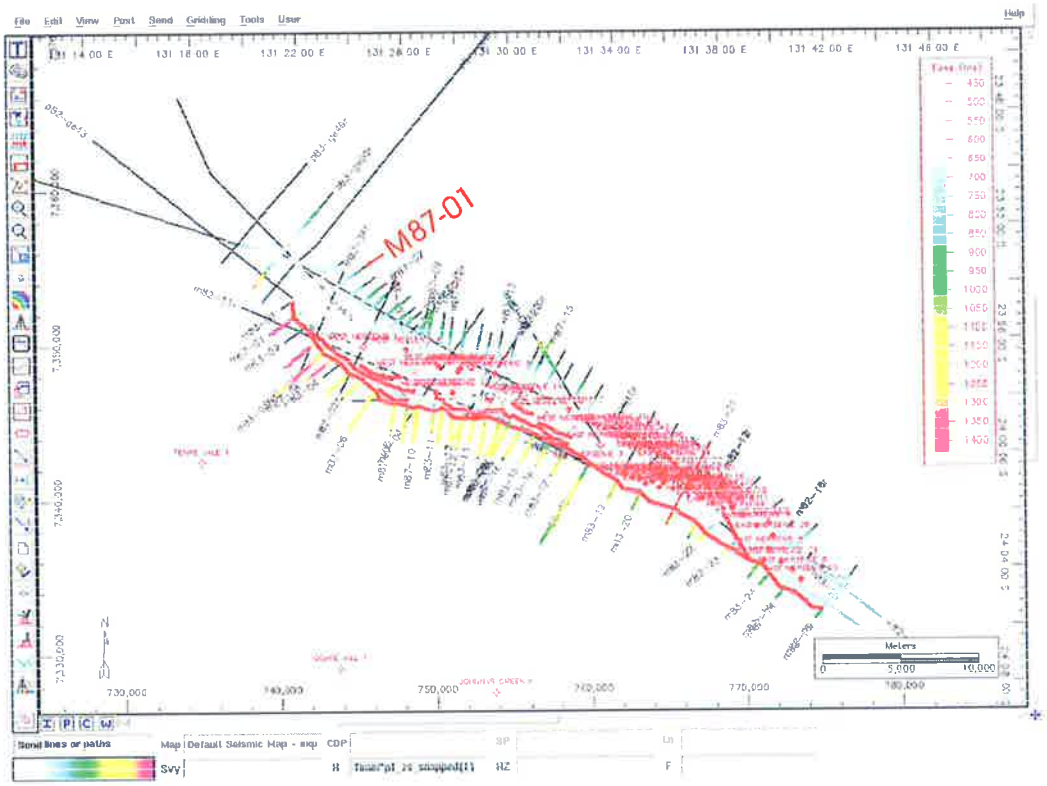

Figure 10.1. The Mereenie 2D seismic grid used in this study. The Mereenie Fault is shown with existing wells. Note there are no tie lines in the footwall of the fault.

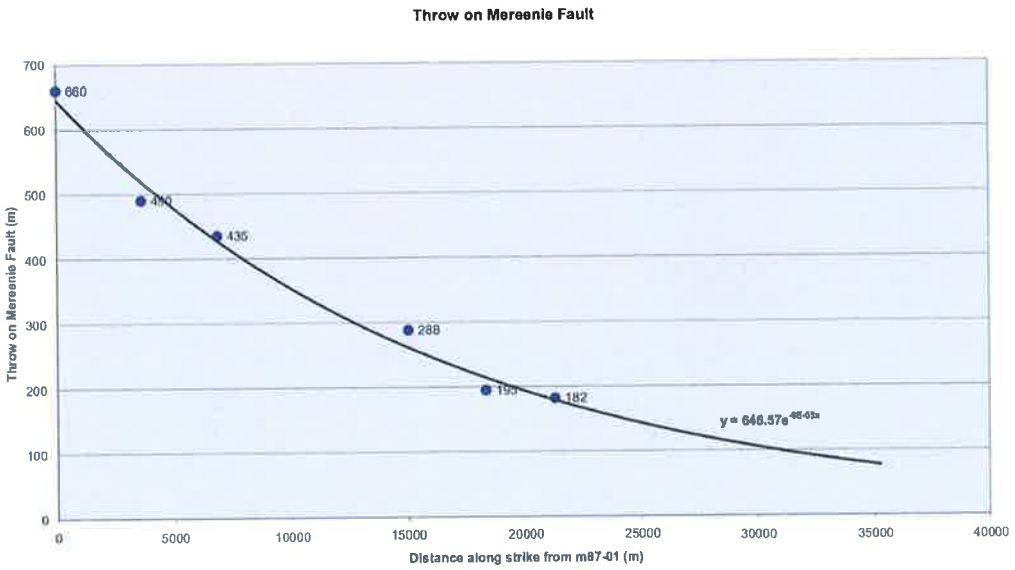

Figure 10.2. Variation of fault throw along the Mereenie Anticline. Fault throw decreases exponentially from 660 m on seismic line m87-01 southwest towards the fold tip.

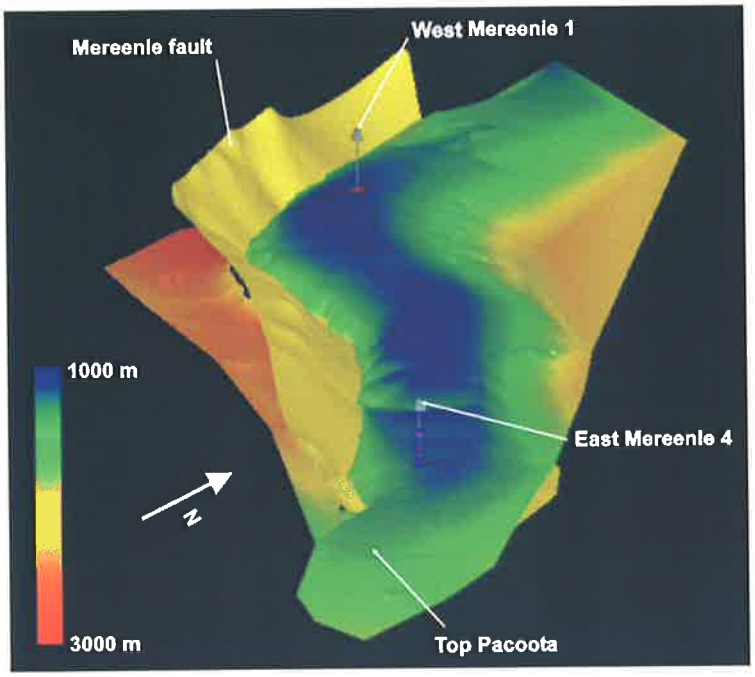

Figure 10.3. Perspective view of the Mereenie Field showing the north-dipping Mereenie fault (yellow), the top of the Pacoota Sandstone and the East Mereenie 4 and West Mereenie 1 wells. The portion of anticline shown here is approximately 40 km long.

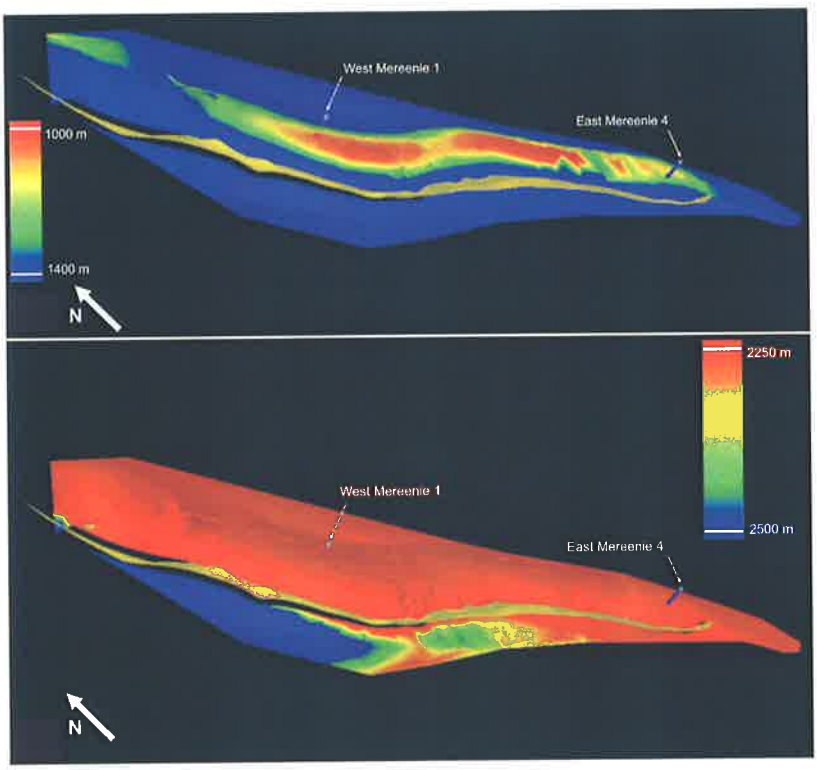

Figure 10.4. 3D depth to structure figures of the top Pacoota Sandstone. The top figure is coloured to highlight four-way closure in the hangingwall and the bottom figure is coloured to highlight four-way closure in the footwall. Footwall closure occurs immediately opposite hangingwall closure. The portion of anticline shown here is approximately 40 km long.

10.3 Fault Seal Analysis

Since the Mereenie Fault is pre-charge and saddles have been identified in the footwall, fault seal integrity is the critical issue to sub-thrust integrity as it is required for four-way closure of the footwall saddles. Several factors have been identified as critical to fault seal assessment. These are: across fault lithologic juxtaposition relationships (Allan, 1989; Smith, 1966; Yielding et al., 1997); fault damage zone sealing potential (Knipe et al., 1998; Yielding, 2002; Yielding et al., 1997); and post-charge fault reactivation (Jones and Hillis, 2003; Mildren et al., 2002b; Wiprut and Zoback, 2002). A complete assessment of fault seal potential must assess all of these issues. This study uses Badley's Traptester software to examine these issues as described in the following sections.

The fault seal assessment presented here is a standalone study to coincide with an upcoming drilling campaign. Accurate fault seal analysis requires 3D seismic data over the prospect. However, this study is limited by the widely spaced 2D seismic data that is available. The fault seal analysis has also been simplified by only considering two of the Mereenie wells due to the consistent stratigraphy across the field (Fig. 10.5). Nonetheless, the fault seal analysis presented herein provides an assessment of the critical factors influencing fault seal and the prospectivity of the Mereenie sub-thrust play.

10.4 Rock Properties

In the case of a sub-thrust play, the shale content of the rocks within and below the reservoir needs to be known in order to assess fault seal potential via juxtaposition and fault damage processes. The gamma-ray logs are considered to provide a reasonable estimate of shale content within the Pacoota Sandstone and overlying units and have been previously used for lithology determination and correlation (Havord, 1991). However, no previous work has addressed the petrophysical properties of the Cambrian units below the Pacoota Sandstone within the Mereenie Field. Core gamma and particle size analysis were conducted on a core sample of the underlying Goyder Formation from West Mereenie 1 to determine the relationship between clay content and gamma response within the Cambrian section.

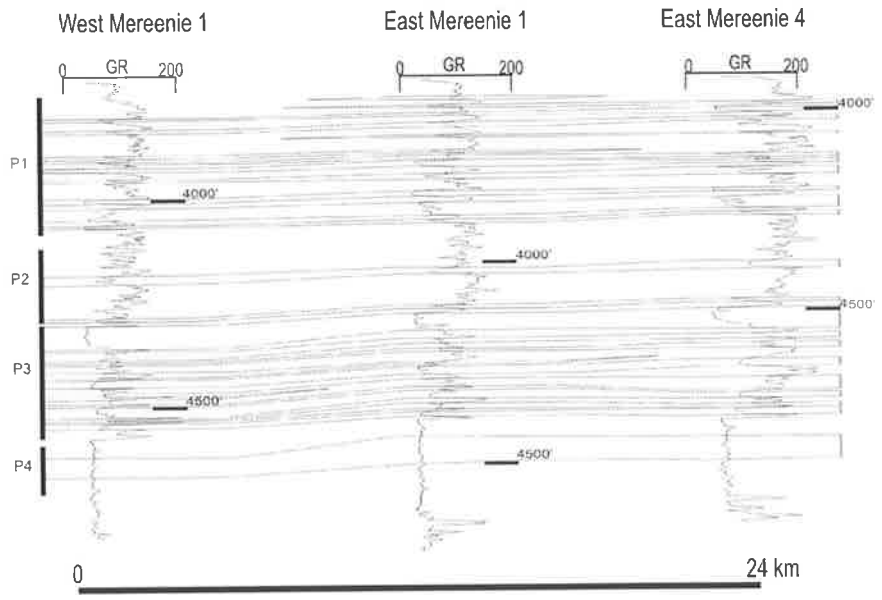

Figure 10.5. Gamma log correlation of the Pacoota Sandstone along the crest of the Mereenie Anticline. Note the consistent log character and thickness of most Pacoota sands along the 24 km section between West Mereenie 1 and East Mereenie 4 (Havord, 1991). Neither neutron nor multi-spectral gamma logs were acquired in the Mereenie wells.

10.4.1 Core gamma

Gamma-ray logs may be used to quantify shale volume, but there are several potential pitfalls associated with this procedure e.g. (Rider, 2000). Some minerals present in sandstones, including K-feldspar, carbonates and evaporates, may contain anomalously high amounts of radioactive elements producing high gamma-ray values thus masking the true clay content. Core gamma-ray testing was conducted on selected core from West Mereenie 1 to assess the ability of the gamma-ray log to predict shale volume within the Goyder Formation as described in Appendix C (Fig. 10.6).

Clean sandstones within the cored interval produced the lowest gamma counts (sample B; Fig. 10.6) and the siltstone layers produced gamma highs (sample A; Fig. 10.6). At first pass, the gamma log appears to be an accurate indicator of clay content. The relationship between core gamma and clay content is investigated further with particle size analysis as described in the following section.

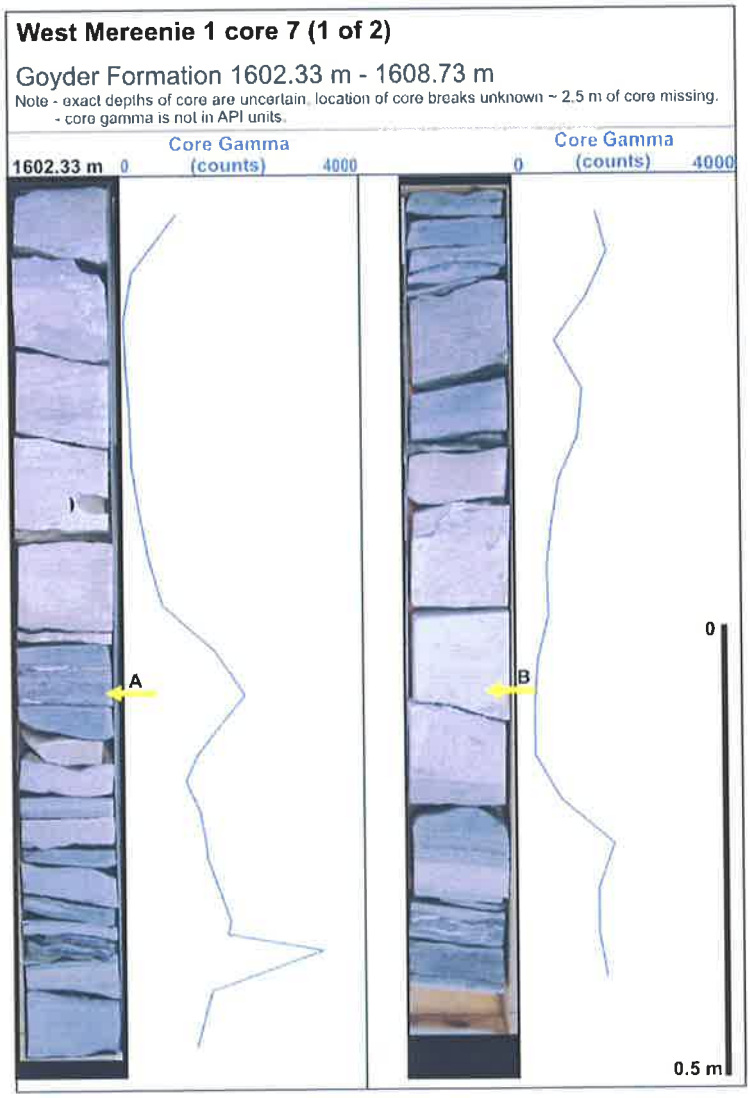

Figure 10.6. Core photos and corresponding core gamma-ray logs of the Goyder Formation in West Mereenie 1. Gamma spikes are associated with the most shaly layers. Note that the core gamma log is not in API units.

10.4.2 Particle size analysis

Particle size analysis was conducted on select samples of the Goyder Formation from West Mereenie 1 corresponding to core gamma lows and spikes (Table 10.1). The particle size analysis, as described in Appendix D, determines the fraction of a disaggregated sample < 2 μm and is assumed to be an accurate measure of clay content (Dewhurst et al., 2002). The sandstone samples B and D have the lowest gamma counts and have clay contents of 2.9% and 2.7% respectively. The siltstone samples A and C correspond to spikes in the core gamma log and have clay contents of 13.5% and 15.8% respectively. The particle size analysis and core gamma log results show that the down-hole gamma log is an effective indicator of shale volume within the Goyder Formation (Fig. 10.7). A fundamental assumption can be made that the range of clay content values over the cored interval is representative of the entire Goyder Formation.

Sample ID	A	B	C	D	E	F
(Depth)	(1602.82 m)	(1605.58 m)	(1605.94 m)	(1606.50 m)	(1677.26 m)	(1677.44 m)
Lithology	Siltstone	Sandstone	Siltstone	Sandstone	Limestone	Limestone
Gamma*	2112	250	1725.5	141	807.5	284
% < 2 μm	13.5%	2.9%	15.8%	2.7%	4.8%	4.6%

Table 10.1. Particle size analysis of the Goyder Formation from West Mereenie 1 and core gamma counts. Samples A and B are shown in Figure 10.6; samples C, D and E are shown in Appendix C.

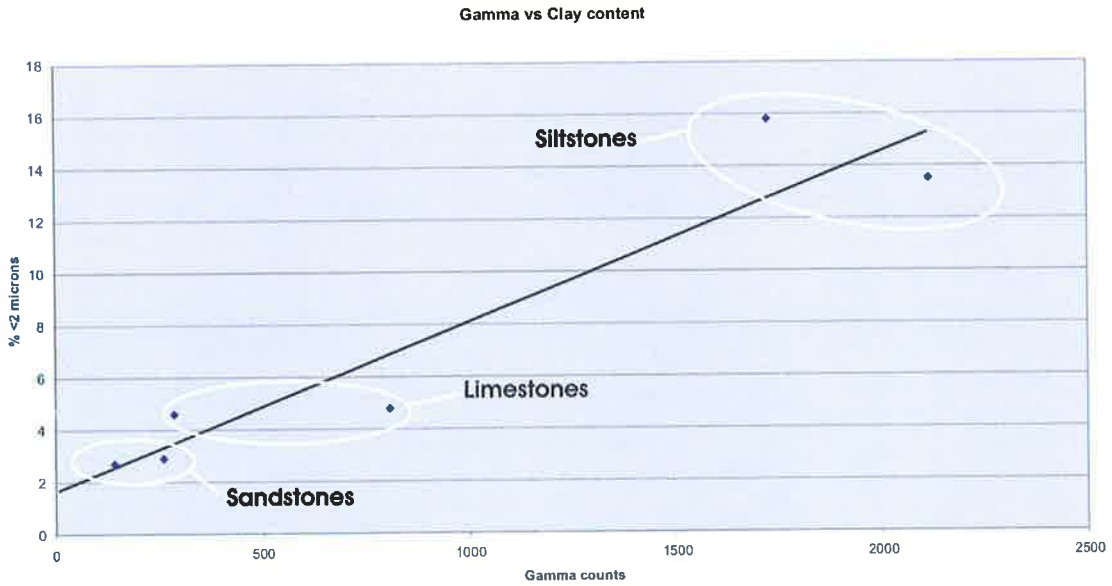

Figure 10.7. Plot of % <2 μm vs. gamma counts from core gamma logging. The consistent relationship indicates that down-hole gamma-ray is a satisfactory indicator of clay content within the Goyder Formation.

10.4.3 Shale volume

The East Mereenie 4 well is the only well in the field drilled through the entire Goyder Formation and terminates in the Bitter Springs Formation. An estimate of the shale volume from the Stairway Sandstone to the Bitter Springs Formation was derived from the East Mereenie 4 gamma log (Fig. 10.8). The maximum gamma-ray value over the entire logged interval is assumed to represent 100% shale (shale line) and the minimum gamma-ray value is assumed to be 0% shale (sand line). All gamma-ray values are then assigned a percentage of shale (Vshale%) assuming a nonlinear relationship of increasing shale volume with increasing gamma values as described by Equations 10.1 and 10.2 (Rider, 2000).

$$Vsh = 0.33(2^{2vsh^*} - 1)$$ Equation 10.1

$$Vsh^* = \frac{GR(\text{log value}) - GR(min)}{GR(max) - GR(min)}$$ Equation 10.1

Where: GR(max) = 100% shale and GR(min) = 0% shale.

The values derived from the shale volume calculation over the Goyder Formation are consistent with the particle size analysis presented in Table 10.1. A Vshale curve was produced in Traptester using this relationship and is shown in Figure 10.8. The Pacoota Sandstone is shaliest at the top (P1 and P2) with thin sand layers. The base of the Pacoota Sandstone (P3 and P4) is very sandy and has very few shale/siltstone lenses. Figure 10.8 shows that the Goyder Formation is typically a sandy sequence with a background shale volume of approximately 2–10% with thin, intermittent siltstone bands approximately 0.5–1 m thick of 15–20% shale. The Cambrian section is very sandy and there is no significant shale interval between the Pacoota Sandstone and Bitter Springs Formation.

10.4.4 MICP

Mercury injection capillary pressure testing (MICP) was conducted on samples A–D to determine their cross-fault sealing potential for use in the juxtaposition analysis. The MICP curves and a description of the test procedure are included in Appendix E. The MICP analysis (Table 10.2) shows that the dominant sandstone lithotype has an entry pressure of 60–00 psia implying that it is capable of holding back an oil column of only 2–4 m (based on published data for the Pacoota Sandstone; Table 10.2) (Havord, 1991). The intermittent siltstone layers in the Goyder Formation have entry pressures >10 000 psia and are thus capable of holding back an oil column in excess of the structural closure height; however, they are not potential juxtaposition seals due to their limited thickness.

Sample ID (Depth)	B (1605.58 m)	D (1606.50 m)	A (1602.82 m)	C (1605.94 m)
Lithology	Sandstone	Sandstone	Siltstone	Siltstone
% < 2 μm	2.9%	2.7%	13.5%	15.8%
Porosity	11.1%	6.7%	0.3%	0.8%
Entry pressure (Hg-air)	60 psia	100 psia	> 10 000 psia	>10 000 psia
Entry pressure (oil-brine)*	1.07 psia	1.79 psia	>180 psia	>180 psia
Maximum column height (m)*	2 m	4 m	>400 m	>400 m

Table 10.2. MICP test results of samples A-D within the Goyder Formation of West Mereenie 1. Calculations based on:

- oil density = 0.784 g/cm^3 (49 API);
- brine density = 1.05 g/cm^3;
- Pacoota Sandstone reservoir displacement pressure = 10 psia (Hg/air)(Havord, 1991);
- interfacial tension = 5 dynes/cm (Schowalter, 1979), and;
- bottom hole temperature = 140 °F.

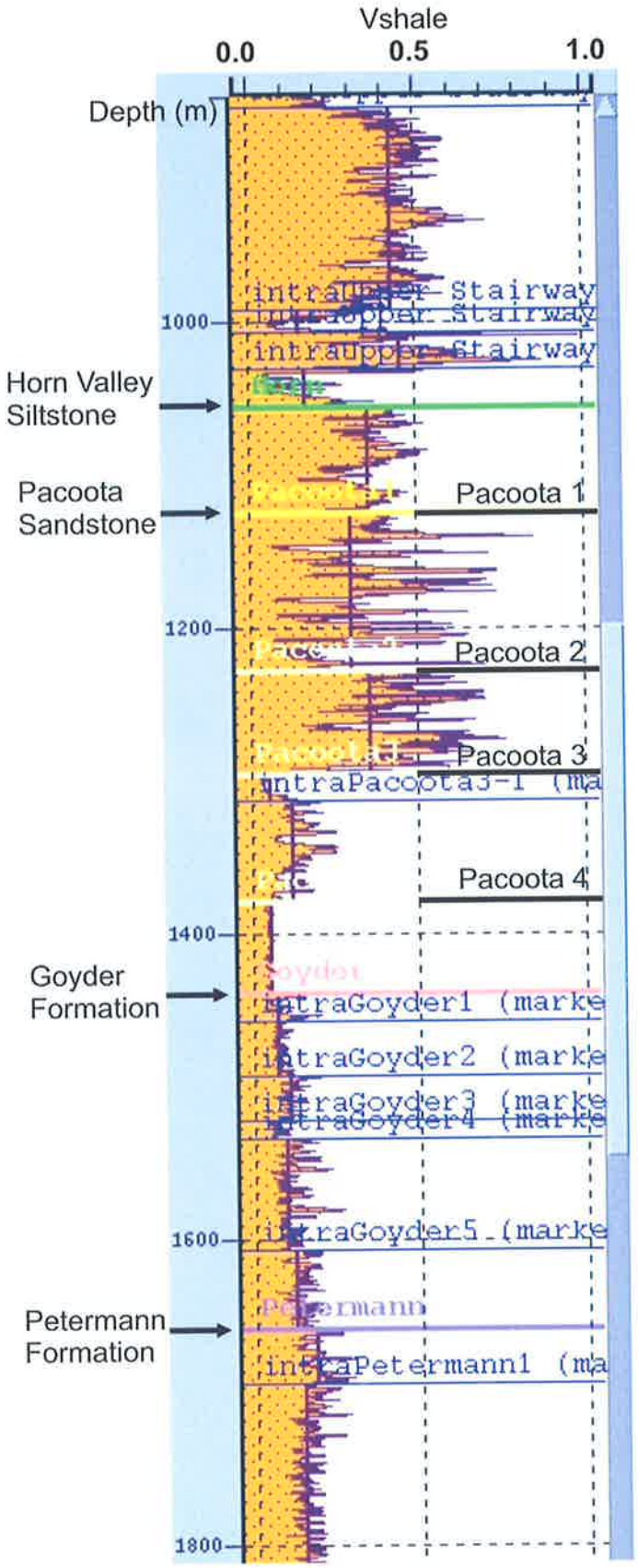

Figure 10.8. Shale volume curve (Vshale) created from the East Mereenie 4 gamma log. Note that the pre-Pacoota section is very sandy with only a few intermittent siltstone lenses.

10.5 Juxtaposition

The Vshale curve was used to subdivide the Pacoota Sandstone into 41 intraformational beds/isochores and the underlying Goyder Formation into six intraformational beds/isochores (Bouvier et al., 1989). Beds/isochores with an average Vshale of <15% were assigned to the sand lithotype, beds with 15–35% Vshale were assigned to a siltstone lithotype and beds with >35% Vshale were assigned to the shale lithotype.

Juxtaposition modelling requires knowledge of both hangingwall and footwall stratigraphy. Stratigraphic data does not exist for the Mereenie footwall as it remains undrilled. Hence, a 'pseudo well' that replicates the hangingwall stratigraphy at East Mereenie 4 was created at an arbitrary location in the footwall for use in the juxtaposition analysis. Work by previous authors demonstrates the relative consistency in stratigraphic thickness and log character along the length of the Mereenie hangingwall, as shown in Figure 10.5 (Havord, 1991). It is assumed that this stratigraphic consistency extends across the fault. This is a reasonable assumption since there is no growth observed on seismic sections across the Mereenie Fault.

All the intraformational surfaces in East Mereenie 4 and the pseudo well were projected onto the fault surface to create fault-isochore intersections. The modelling process was set so that each isochore in the footwall and hangingwall maintained a constant thickness and remained parallel to the interpreted seismic surfaces.

Figures 10.9 and 10.10 show the mapped juxtaposition relationships for the slipped interval on the fault plane and show that within the footwall, all of the Pacoota sandstones are juxtaposed against either hangingwall sandstone or thin siltstone layers, thus providing poor juxtaposition seal. The MICP analysis suggests that the maximum hydrocarbon column that may be supported via juxtaposition sealing by Goyder Formation sandstones in the hangingwall is in the order of 2–4 m. However, the fault itself may still be an effective seal despite poor juxtaposition seal. There are many published examples of sealing faults with sandstone on sandstone juxtaposition (Labaume et al., 2000; Naruk et al., 2003). The following sections address the seal potential of the fault plane and damage zone.

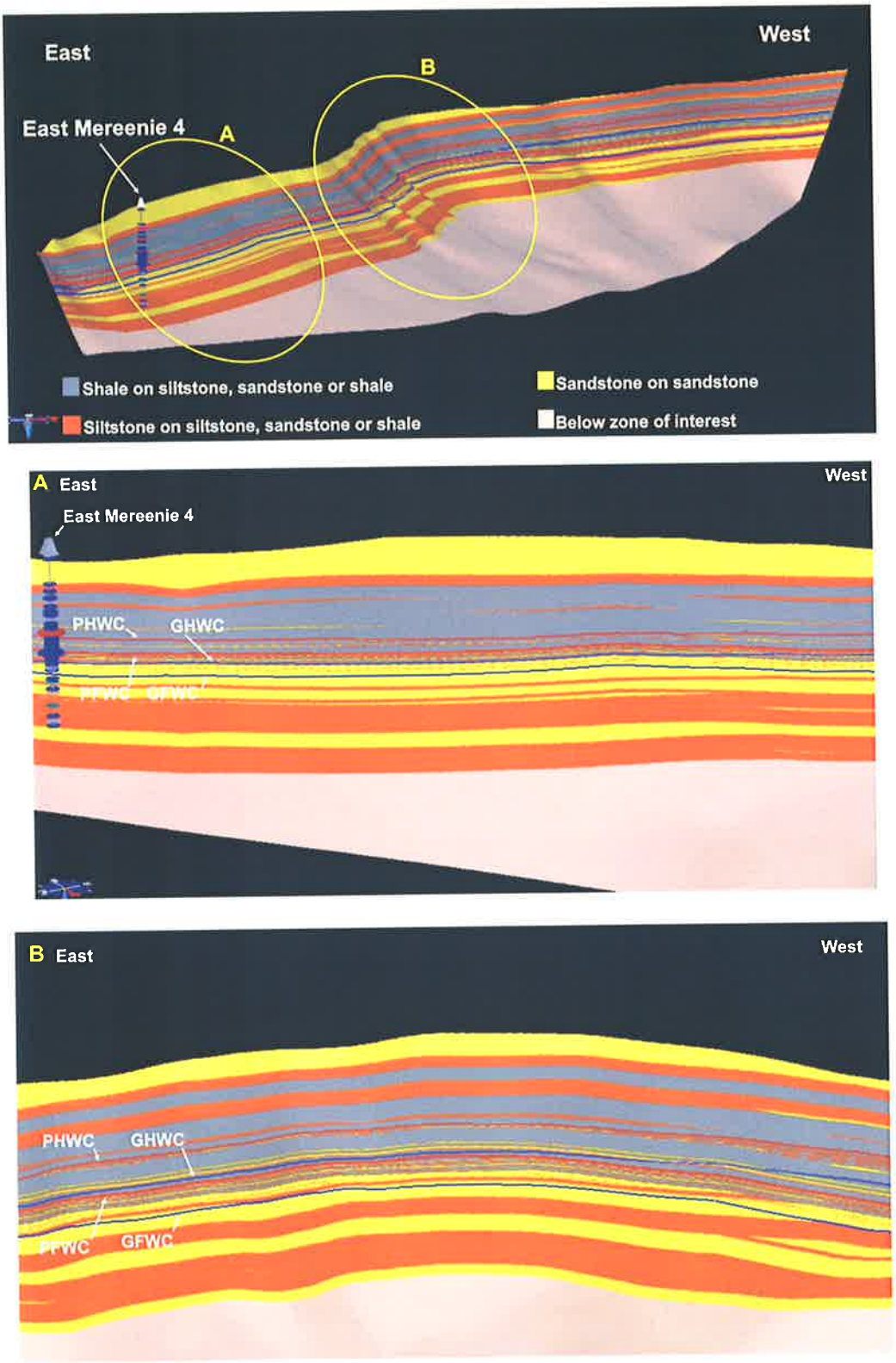

Figure 10.9. Juxtaposition modelling on the Mereenie fault viewed from the north and close-ups of (A) the East Mereenie and (B) West Mereenie saddles. The hangingwall and footwall cut-offs of the Pacoota Sandstone are marked by the red lines (PHWC, PFWC). The hangingwall and footwall cut-offs of the Goyder Formation are marked by the blue lines (GHWC, GFWC). The portion of the fault shown here is approximately 40 km long.

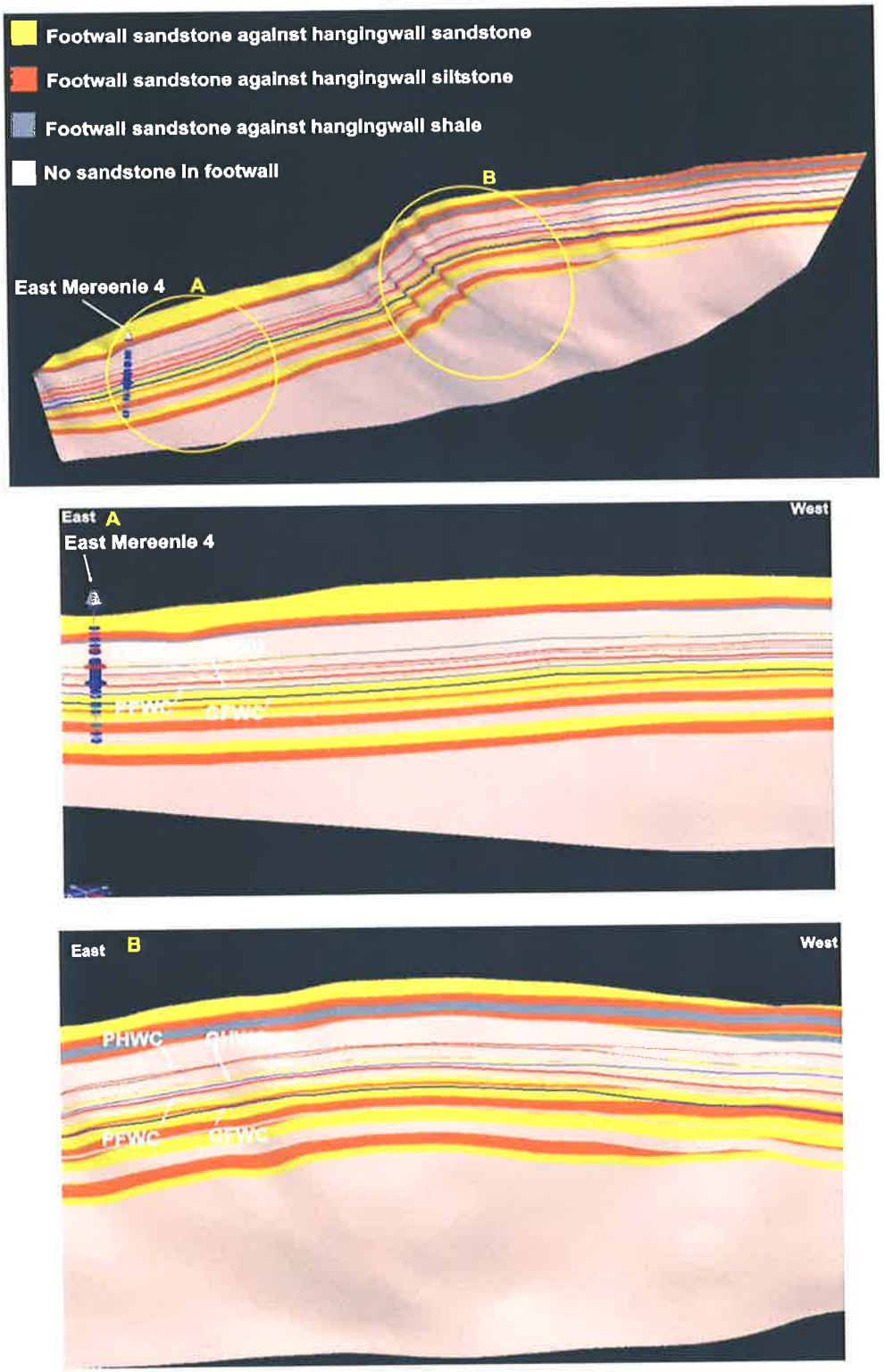

Figure 10.10. Juxtaposition relationships for the slipped interval on the fault plane, coloured according to juxtaposition relationships relative to sandstone intervals in the footwall and close-ups of (A) the East Mereenie and (B) West Mereenie saddles. Note that all the sandstones within the Pacoota Sandstone in the footwall are juxtaposed against either sandstone or siltstones within the hangingwall thus providing poor juxtaposition seal. The portion of the fault shown here is approximately 40 km long.

10.6 Fault Rock Properties – Membrane Seal

Faults with sandstone-on-sandstone juxtaposition that retain hydrocarbon columns are considered to be sealing due to fault rock properties (Fisher and Knipe, 1998; Knipe et al., 1998; Labaume et al., 2000). Faults may act as effective seals due to the fault rock itself, irrespective of juxtaposition sealing. Fault rocks in porous siliciclastic rocks often have lower porosity and permeability and higher capillary entry pressure than the host rocks (Sperrevik et al., 2002). The changes in rock properties in fault rocks occur due to a variety of processes including porosity collapse, grain size reduction, mixing of phyllosilicate minerals with framework grains and mineralisation and fluid flow along the fault zone (Antonellini and Aydin, 1994; Fisher and Knipe, 1998). The fault processes and fault rock types along the Mereenie Fault are unconstrained as none of the Mereenie wells intersect the main fault. The properties and thus sealing potential of the Mereenie fault has been assessed using samples collected from other faults in the Amadeus Basin, published literature, and Badley's Traptester software.

10.6.1 Shale gouge

The fault zone processes and the petrophysical properties of fault rocks are highly dependent on the host rock and the temperature and pressure history (Fisher and Knipe, 1998; Yielding et al., 1997). The fault zone process of clay smear involves the entrainment of clay or shale into the fault plane thereby increasing the capillary entry pressure of fault rocks. The Shale Gouge Equation (Yielding et al., 1997) and similar methodologies (Fulljames et al., 1996; Lindsay et al., 1993) provide a method to quantify the amount of phyllosilicate minerals entrained in the fault rock and therefore predict the sealing potential of clay fault rocks. The shale gouge ratio method (SGR) is integrated into Traptester providing a quantitative method to assess fault rock properties from mixing of lithologies where clay smear is the dominant process. The method has been calibrated with oil-field data throughout the world (Bretan et al., 2003; Yielding et al., 1997); however, it has been developed principally with provinces such as the North Sea in mind. SGR is calculated in Traptester using Equation 10.3 where: Vsh is the shale content of a sample; Δz is the bed thickness, and; T_h is the fault throw.

$$SGR = \frac{\sum Vsh * \Delta z}{T_h} \qquad \text{Equation 10.3}$$

Figure 10.11 displays calculated SGR along the Mereenie Fault. The SGR rapidly decreases from around 30% at the top Pacoota footwall cut-off to around 5% at the top Goyder footwall cut-off. The SGR is typically in the range 5–10% over the best reservoir intervals in the Pacoota Sandstone (Pacoota 3 and Pacoota 4 reservoirs). SGR values of 15–20% are considered by many authors to represent the threshold between non-sealing and sealing behaviour of faults in mixed clastic sequences without diagenetic overprinting (Bretan et al., 2003; Yielding, 2002;

Yielding et al., 1997). Therefore, potential fault seal along the Mereenie Fault due to clay smear is considered poor. However, the SGR methodology does not address the processes of mineralisation or cataclasis along sandstone on sandstone faults. It has been demonstrated some sandstone-on-sandstone faults with low SGR can be sealing due to cataclasis or mineralisation (Labaume et al., 2000).

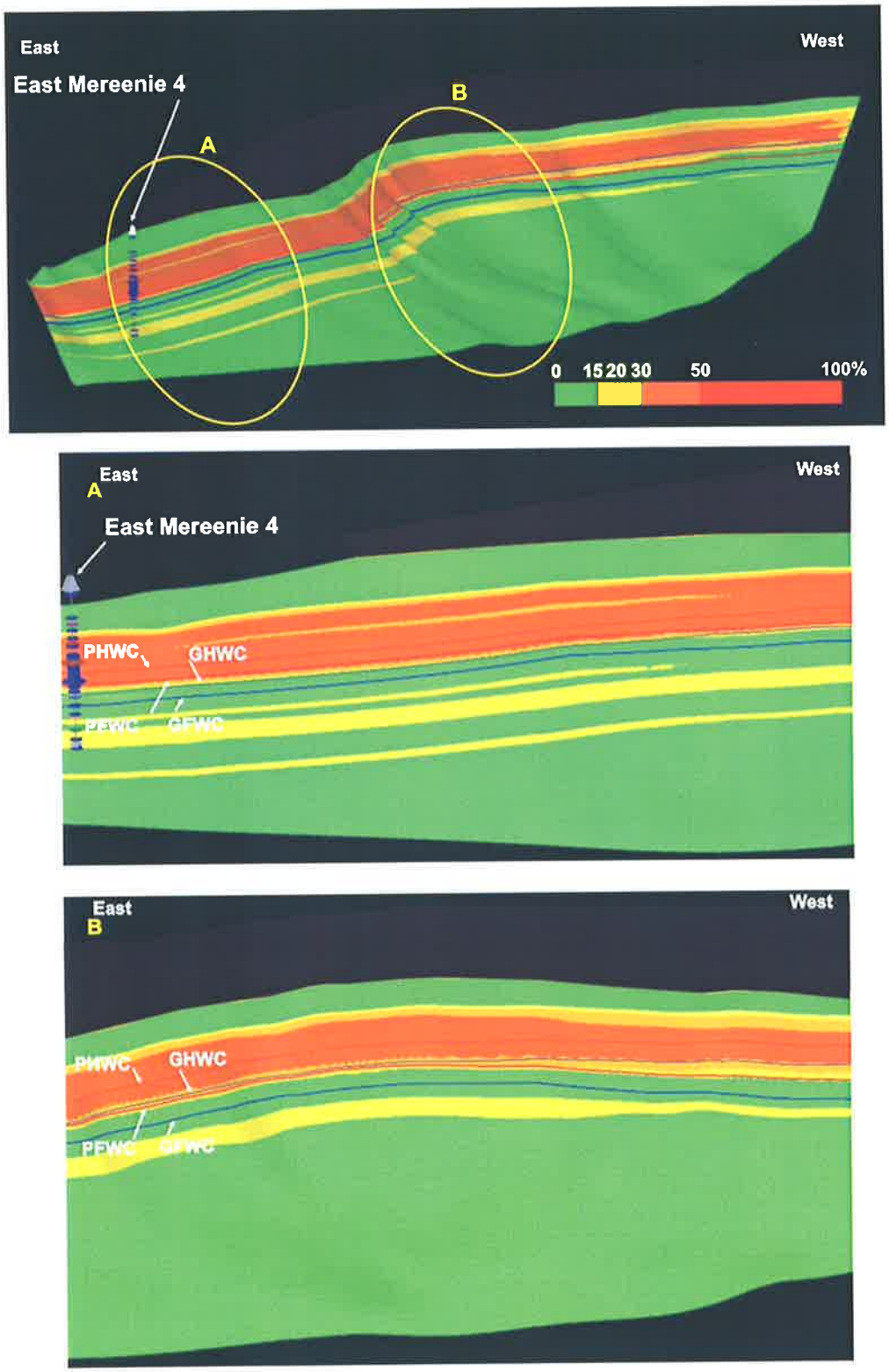

Figure 10.11. Shale gouge ratio (SGR) on the Mereenie fault viewed from the north and close-ups of (A) the East Mereenie and (B) West Mereenie saddles. The hangingwall and footwall cut-offs of the Pacoota Sandstone are marked by the red lines (PHWC, PFWC). The hangingwall and footwall cut-offs of the Goyder Formation are marked by the blue lines (GHWC, GFWC). The portion of the fault shown here is approximately 40 km long.

10.6.2 Cataclasis

Cataclasis is a process of rock deformation accommodated by micro-fracturing, rotation, translation, crushing and granulation of mineral grains and pore collapse (Aydin and Johnson, 1983). Cataclasites typically display higher capillary entry pressures than host rocks and may provide effective fault seals where there is sandstone-on-sandstone juxtaposition and low SGR (Labaume et al., 2000; Naruk et al., 2003). Significant advances in the understanding of cataclasis have been made, but to the author's knowledge, there are no published methods for quantifying cataclasite development in fault zones (Antonellini and Aydin, 1994; Fisher et al., 2004; Sperrevik et al., 2002).

The development of cataclasite in sandstone on sandstone faults is related to the initial porosity of the sandstone and stress conditions at the time of deformation (Engelder, 1974). Sandstones deformed under low mean effective stress relative to the hydrostatic yield strength tend to dilate during deformation, limiting cataclasite development (Antonellini and Aydin, 1994). If the mean effective stress conditions at the time of deformation are high compared to the hydrostatic yield strength, compaction tends to occur, promoting the formation of cataclasite (Engelder, 1974; Sperrevik et al., 2002). Cataclasis is thus more likely to develop along thrust faults (relatively high mean stress) than along normal faults (relatively low mean stress). Geochemical evidence from both normal fault (Fisher et al., 2004) and thrust fault (Labaume et al., 2000) settings show that significant quartz cementation occurs when cataclasites form above 80°– 90°C dramatically increasing cataclasite seal potential. The quartz cement is typically locally derived and is not dependent on fluid flow along the fault (Fisher et al., 2004). Although the reservoir temperature at the time of faulting is unclear, it is quite possible that reservoir temperatures exceeded 90°C some time during faulting (Jackson et al., 1984). These published findings suggest that the Mereenie Fault may have well-developed, quartz-cemented cataclasite along the fault surface.

10.6.3 Mineralisation

It is also feasible that membrane seal may occur due to mineralisation of the fault resulting in an impermeable barrier. Previous work in the Amadeus Basin has shown that fluids derived from the Bitter Springs Formation have mineralised the Carmichael Fault and fractures in the Palm Valley Field (Berry et al., 1996; Hamilton et al., 1991; Pontifex, 2001). Fractures in the Palm Valley reservoirs are propped open with ankerite, barite and quartz mineralisation precipitated from fluids sourced from the Bitter Springs Formation (Berry et al., 1996; Hamilton et al., 1991). It is important to note that the open fractures at Palm Valley are tensile, not shear fractures (faults).

The Undandita 1A well is the only test of the sub-thrust play in the Amadeus Basin and core samples have been taken of the fault rock (Pontifex, 2001). Mineralogical studies of the fault rock show poikilitic, intergranular anhydrite with microcrystalline dolomite (Fig.10.12), suggesting

fluid flow from the Bitter Springs Formation and mineralisation along the Carmichael Fault. The Mereenie and Carmichael are similar faults emanating from the Bitter Springs Formation, hence mineralisation along the Mereenie Fault is likely and may be a potential sealing mechanism.

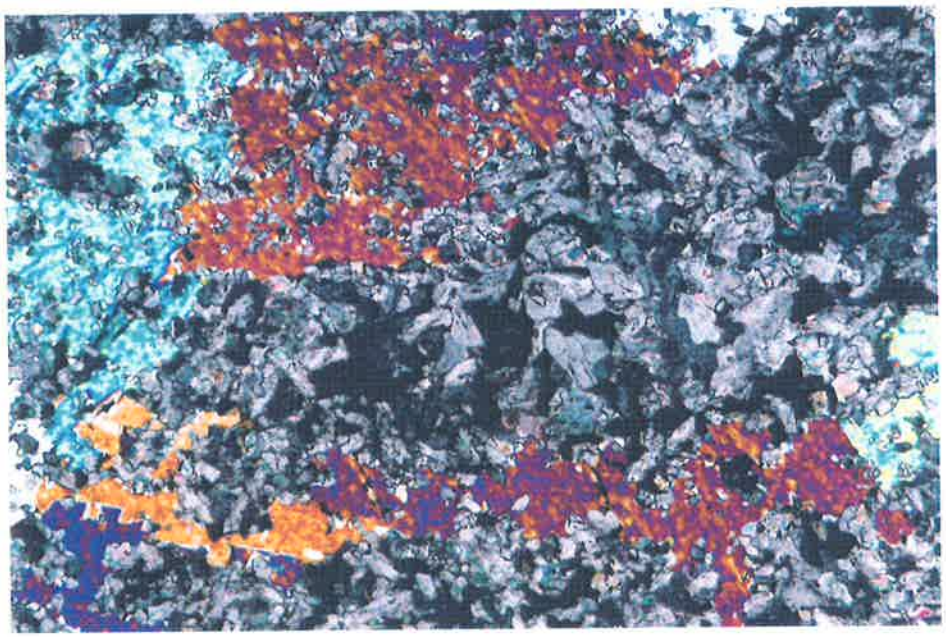

Figure 10.12. Mineralisation along the Carmichael Fault showing poikolitic anhydrite with microcrystalline dolomite. The sample shown is from 752 m in Undandita 1A (Pontifex, 2001). The field of view is approximately 2 mm wide.

10.7 Reactivation Assessment

Intact juxtaposition or membrane fault seals may be breached by post-charge reactivation (Jones and Hillis, 2003; Mildren et al., 2002b; Wiprut and Zoback, 2002). The risk of fault reactivation may be quantified by the increase in pore pressure (ΔP) required to induce failure along a fault plane of given orientation within the contemporary stress field. The FAST technique provides a method to calculate ΔP over a fault surface of known geometry given knowledge of in-situ stress and fault rock parameters (Mildren et al., 2002a). The FAST algorithm is incorporated into Traptester as the 'slip stability' function and has been used to assess the reactivation potential of the Mereenie Fault. The implementation of the FAST technique within Traptester is limited since it does not allow the user to vary fault rock properties and assumes $\mu = 0.6$ and $C = 0$.

10.7.1 In-situ stress

The in-situ stress tensor is required to calculate ΔP and assess reactivation risk. The in-situ stress tensor for the Mereenie Field has been documented by previous studies as summarised below (Hillis and Mildren, 1995; Hillis et al., 1999b). There is substantial variation especially in horizontal stress across the Mereenie Field. Traptester can only calculate reactivation potential

using a single gradient for each principal stress, thus field-wide averages of the principal stresses at reservoir depth have been used.

Vertical stress

The vertical stress over East Mereenie was calculated by integrating density log data with sonic log and check-shot data using the Nafe-Drake velocity/density transform (Ludwig et al., 1970). The vertical stress/depth relations for East and West Mereenie are given by Equation 10.4 and 10.5 (Hillis and Mildren, 1995).

$$\text{East Mereenie: } Sv = \frac{(0.94786 \ln h + 17.96242)h}{1000} \qquad \text{Equation 10.4}$$

$$\text{West Mereenie: } Sv = \frac{(0.84682 \ln h + 17.98300)h}{1000} \qquad \text{Equation 10.5}$$

A field-based average of 24.9 MPa/km (1.1 psi/ft) at reservoir depth has been adopted for use in Traptester calculations of reactivation risk.

Minimum horizontal stress

The magnitude of minimum horizontal stress has been constrained by mini-fracture test closure pressures. S_{hmin} magnitudes are extremely variable across the Mereenie Field ranging from gradients of 11.1 MPa/km to 23.3 MPa/km (Hillis et al., 1999b). The general trend is an increase in minimum horizontal stress gradient along the strike of the structure from 11.1 MPa/km to 23.3 MPa/km from the more depleted East Mereenie to the less depleted West Mereenie end of the field. Minimum horizontal stress appears to decrease with pore pressure depletion although the exact relationship is not well constrained (Hillis et al., 1999b). It is considered that the values obtained for West Mereenie are more representative of virgin/un-depleted conditions and an average of these values of 19.5 MPa/km (0.86 psi/ft) has been used in Traptester calculations of reactivation risk.

Maximum horizontal stress

The maximum horizontal stress has been constrained based on the occurrence of drilling-induced tensile fractures (DITFs) and frictional limits to stress. Where DITFs are observed, a lower bound to the maximum horizontal stress in un-depleted conditions is given by Equation 10.6 (Hillis et al., 1999b):

$$S_{Hmax} \geq 3_{Shmin} - P_P - P_W \qquad \text{Equation 10.6}$$

The maximum horizontal stress gradient in West Mereenie 9 was calculated as 40.3 MPa/km (1.78 psi/ft) (Hillis et al., 1999b) and this value has been used in Traptester calculations of reactivation risk. Hence the stress regime for undepleted (hydrostatic) pore pressure is one of a strike-slip stress regime where, $S_{Hmax}>S_v>S_{hmin}$.

Maximum horizontal stress orientation was determined by analysis of image log data. The mean breakout orientation across the field is 124° mean hence, S_{Hmax} orientation = 034°(Hillis et al., 1999b).

10.7.2 Slip stability

Figure 10.13 and 10.14 show the reactivation risk (slip stability) of the Mereenie fault plotted as ΔP. Figure 10.13 shows poles of the Mereenie Fault plotted on a structural permeability and Mohr diagrams and imply low reactivation risk within the in-situ stress tensor. As expected the ΔP values increase with depth from 5 MPa near the surface to over 40 MPa at 4 km depth. ΔP at the level of the Pacoota Sandstone is in the order of 20 MPa (Fig. 10.14). The gradual increase in ΔP with depth equates to a ΔP gradient of approximately 10 MPa/km suggesting low reactivation risk within the in-situ stress field. Sections of the fault striking more east-west have slightly higher ΔP values due to their orientation relative to the in-situ stress tensor; however, they are still considered at relatively low risk of reactivation.

Slip stability as applied only assesses reactivation risk within the contemporary stress field. The assumption that ΔP as calculated provides an accurate assessment of post-charge reactivation risk is reasonable only if the contemporary stress field is representative of the stress fields to which the fault has been subjected post-charge. Where there has been a significant change in the stress tensor post-charge (e.g. via plate readjustment), the risk of reactivation for differing palaeo-stress regimes has not been assessed. It is possible that there has been significant plate readjustment and variation of the stress field in central Australia post-charge.

Structural modelling based on field, map (Shaw et al., 1995; Wells et al., 1961) and seismic interpretation reveals that very few, if any, thrust faults in the northern Amadeus Basin intersect the Pertnjara Group (Figs 8.5, 8.16) (Appendix B). The modelling implies that there is very limited if any thrust fault movement post-Pertnjara and thus final movement along the Mereenie fault is likely to be pre-charge. These observations, together with the slip stability modelling, imply that the risk of fault seal failure due to post-charge fault reactivation is low.

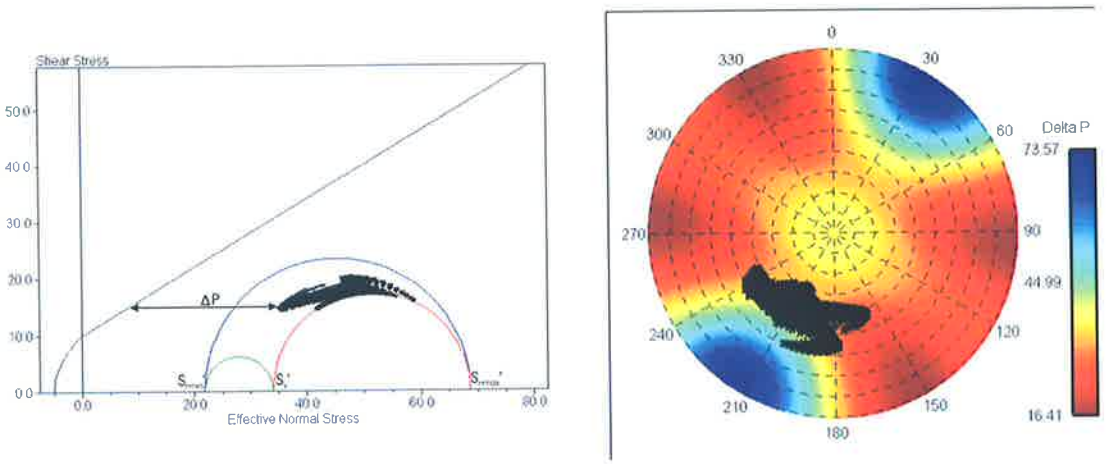

Figure 10.13. Mohr diagram (left) structural permeability diagram (right) showing poles of the Mereenie fault at 2250 m. ΔP at reservoir level (2250 m) is in the order of 20–30 MPa and reactivation within the in-situ stress field is considered low.

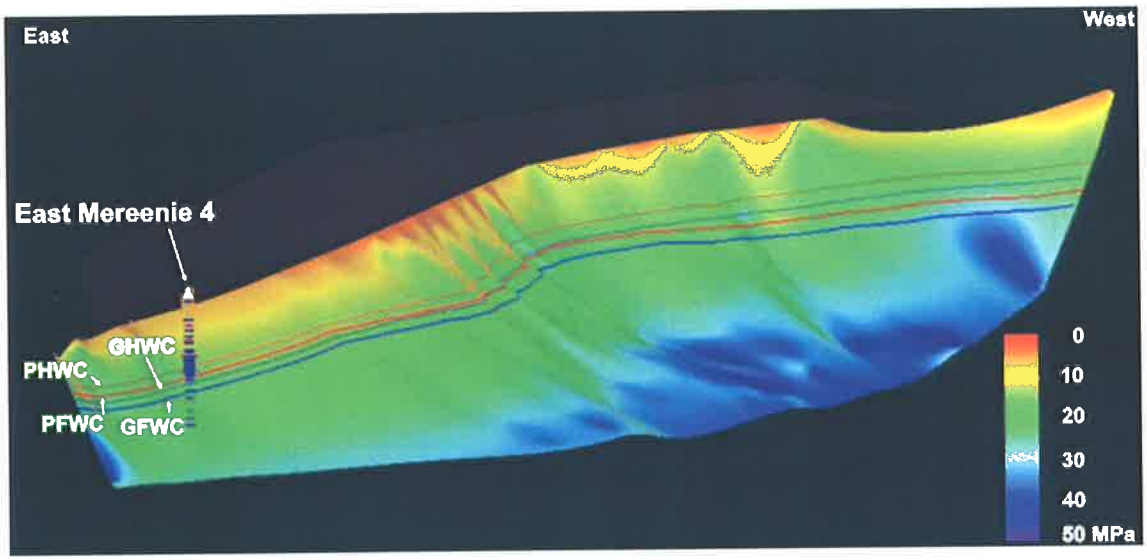

Figure 10.14. Reactivation potential (slip stability) of the Mereenie fault. ΔP at reservoir level (2250 m) is in the order of 20–30 MPa and reactivation within the in-situ stress field is considered low. The portion of the fault shown here is approximately 40 km long.

10.8 Mereenie Sub-thrust Fault Seal Risking

The structural modelling presented in previous sections shows that the Mereenie Anticline is a faulted detachment fold formed during the ASO and that the Mereenie Fault formed prior to hydrocarbon charge. Provided the Mereenie fault formed pre-charge, and there is footwall closure, the critical risk to the Mereenie sub-thrust play is fault seal to provide footwall four-way closure. The overall risk of fault breach is assessed here based on the premise and quantitative elicitation presented by Jones and Hillis (2003). They argue that a fault is sealing if there is juxtaposition or damage sealing and if it has not been reactivated. The integrated probability of fault seal (FS) can be expressed by Equation 10.7 where: a is the probability of membrane seal;

b is the probability of juxtaposition seal and; c is the probability of fault reactivation (Jones and Hillis, 2003).

$$FS = \{1-[(1-a)(1-b)]\} \times (1-c) \qquad \text{Equation 10.7}$$

10.8.1 Uncertainty

Uncertainty may be incorporated into the risk analysis to reflect the completeness and technical limitations of the data set. The uncertainty (U) associated with each aspect of fault seal risk may be calculated by the summation of the uncertainty of each critical parameter (nw) divided by the total number of parameters (n) as shown in Equation 10.8 (Jones and Hillis, 2003). The uncertainty is then used to provide an upper and lower bound of risk for each aspect of fault seal.

$$U = [1-(\Sigma nw/n)] \times 100 \qquad \text{Equation 10.8}$$

Table 10.3 presents the parameters used in the fault seal assessment and uncertainty analysis. The numerical values presented for probability and uncertainty in Table 10.3 are as per the Sherman-Kent scale for eliciting and quantifying confidence judgements (Jones and Hillis, 2003; Meyer and Brooker, 1991).

	Risk	Upper	Lower	Uncertainty
Quartz rich sediments				1.0
High mean stress				0.9
Temp>80-90°C				0.3
Fault connected to Bitter Springs				0.7
Syn-tectonic fluid flow				0.3
Membrane uncertainty				36%
Membrane (a)	**0.70**	**0.95**	**0.45**	
Fault zone architecture				0.6
Fault throw				0.5
Sedimentary architecture				0.7
Juxtaposition uncertainty				40%
Juxtaposition (b)	**0.10**	**0.14**	**0.06**	
Stress regime				0.8
Failure envelope				0.6
3-D fault geometry				0.7
Reactivation uncertainty				30%
Reactivation (c)	**0.30**	**0.21**	**0.39**	
Probability of fault sealing	**0.51**			
Upper integrated risk	**0.76**			
Lower integrated risk	**0.29**			

Table 10.3. Parameters used for fault seal risking.

10.8.2 Mineralisation and Cataclasis

The method presented by Jones and Hillis (2003) is based on fault rock sealing due to shale gouge. Analysis presented in this chapter shows that shale gouge values between the Pacoota and Goyder footwall cut-offs is less than 15% and that sealing by shale gouge is highly unlikely (Bretan et al., 2003). It is more likely that the fault is sealed via either cataclasis or mineralisation sourced from the Bitter Springs Formation. Several critical parameters have been identified that may influence the potential for fault seal due to cataclasis or mineralisation and were discussed in sections 10.6.2 and 10.6.3. As discussed in those sections, the author knows of no techniques for quantifying the probability of seal development due to cataclasis or mineralisation of the fault plane. However, given the factors discussed in sections 10.6.2 and 10.6.3 it is considered likely (P = 0.7) that either one of these processes would create fault seal.

10.8.3 Sub-thrust seal risk

Table 10.3 summarises the probability of fault sealing with the upper and lower integrated risks. The calculated probability of 0.51 implies that the probability of fault sealing is intermediate to

moderate. The upper integrated risk of 0.76 implies that the possibility of fault sealing is likely to very likely. The lower integrated risk of 0.29 implies that the possibility of fault sealing is very unlikely to unlikely as per Table 10.4.

Probability	Seal Condition	Probability	Seal Condition
1	Certain	0.4	Moderately unlikely
0.9	Extremely likley	0.3	Unlikely
0.8	Very likely	0.2	Very unlikely
0.7	Likely	0.1	Extremely unlikely
0.6	Moderately likely	0	Impossible
0.5	Intermediate		

Table 10.4. The probability of fault sealing may be quantified and elicited. A probability of one means fault seal is certain and a probability of zero means fault seal is impossible (Jones and Hillis, 2003).

The fault seal risking shows that the probability of fault sealing is intermediate and thus the Mereenie sub-thrust play provides an attractive near-field exploration target provided other criteria such as volumetric estimates are satisfied. The sub-thrust play could be tested by a multi-objective development well during the upcoming drilling campaign to offset cost and risk.

11 Concluding Statement

The aim of this thesis was to progress our knowledge of natural fracturing and relevant structural geological concepts within the Bowen and Amadeus basins in order to assist development drilling, improve reservoir management, increase the reserves and extend the life of the Scotia, Mereenie and Palm Valley fields.

11.1 Scotia Study

The study presented in Chapter 2 of this thesis identifies the importance of in-situ stress and natural fracturing to gas deliverability in the Scotia Field. Areas of relatively low horizontal stress are critical for successful hydraulic fracture completions and natural fractures provide access to the low permeability matrix of the reservoir. The majority of reservoir level fractures formed in association with shortening during the Triassic Hunter Bowen Orogeny and are therefore not present in the overlying, outcropping Jurassic-Cretaceous units of the Surat Basin. The density of reservoir level fractures interpreted from image logs is directly correlated with structural position over the Burunga Anticline with most fracturing along the crest and forelimb of the fold. The fractures in outcrop have different strikes, dips and surface ornamentation to those at reservoir level, they are typical of tensile joint sets and formed during post-Cretaceous uplift and unloading. The unloading joints preserved in outcrop are restricted to a few hundred metres from the surface and do not exist at reservoir level in the Scotia Field.

The orientation and magnitude of the in-situ stress field at Scotia is generally consistent with that documented by the Australian Stress Map (Hillis et al. 1998; Hillis et al. 1999). The in-situ stress tensor is characterised by high S_{Hmax} and varies between strike-slip and reverse-stress regimes across the field. Structural permeability diagrams show that fractures striking between north-northeast are most suitably oriented to be hydraulically conductive within the in situ stress field and fractures striking northwest–southeast are the least likely to be open and hydraulically conductive. Hydraulic fracture completions are not effective in areas of the Scotia Field characterised by high mean stress, particularly where a reverse-stress regime exists (Flottmann et al. 2002; Johnson et al. 2002). Scotia 15 is an area of high mean stress and a hydraulic fracture treatment was relatively unsuccessful with the well currently flowing only ~0.3 MMCFD despite intersecting one of the most naturally fractured zones of the reservoir. Conversely, successful hydraulic fracture treatments were achieved in Scotia 10 and 14, in areas of relatively low mean stress (strike-slip regime) and the wells currently produce at relatively high rates (2.5 MMCFD).

11.2 Goonyella Riverside Study

The Goonyella Riverside study presented in Chapters 3–6 of this thesis presents an analogue study for the Scotia Field and others in similar settings. The study identifies the key controls on natural fracture development within a coal measure succession and links different fracture sets to specific tectonic events to which the Scotia Field has also been subjected. The Goonyella Riverside study provides insight into the deformation mechanisms and stress distribution within a coal measure succession and highlights the variable behavior of different lithologies.

Cleat development at Goonyella Riverside is a function of coal composition. Low ash, vitrinite rich layers have closely spaced cleats in the order of 5 mm whereas high ash, inertinite rich layers have cleat spacings in the order of 20–150 mm. The face cleat direction is relatively consistent in the Goonyella Riverside area (i.e. east-west ± 15°) and reflects the direction of maximum horizontal stress at the time of coal diagenesis. The work presented in this thesis shows that cleat orientation may be predicted pre-drill by the orientation of seismically resolvable structures if they formed under the same stress orientations. In accordance with basic Andersonian theory, cleats should generally strike perpendicular to thrust faults and parallel to normal faults if the structures formed under the same stress orientations. It is therefore imperative to understand the structural relationships and timing between burial, diagenesis (cleat formation) and emplacement of seismically resolvable structures. Coal cleat development is a primary control on the economic viability of coal seam methane projects as it influences reservoir permeability and well completions/stimulations (Gray 1987; Johnson et al. 2002; Zuber and Boyer 2002). However, it is difficult to model discrete coal cleats from image log data because they are below image log resolution. An alternative method for coal cleat modelling may be the prediction of coal type using sequence stratigraphic approaches to predict vitrinite-rich intervals (Bocking pers. comm., Bocking and Associates 2003).

Porosity reduction along fault cores may reduce permeability perpendicular to the fault whereas fracturing within the damage zone may increase permeability parallel to the fault in both coal and sandstone reservoirs. A single thrust fault has accounted for almost half the ground water entering the underground exploration adit at Goonyella Riverside due to flow along the damage zone of the fault. The spacing of fault-related fractures in the damage zone is controlled by both rheology and the proximity to the fault core. Fault-related fracturing is significantly greater within the sandstone-prone interval than within the coal-prone interval due to variations in rheological properties between the different units and their interaction with each other. The top and base of the coal seams are effective zones of mechanical decoupling and bedding plane slip along the coal-rock interface accommodates much of the strain applied during thrusting. Consequently, damage zones are less developed in the coal-prone interval as bedding plane slip has accommodated a large portion of the thrust-induced strain. Damage zones in coal-prone

intervals may contribute less to permeability sweet-spots than similar faults in coal-free intervals. In addition, lateral ramps of the thrust faults may act as flow baffles or barriers and compartmentalise reservoirs where there has been porosity reduction in the fault core.

The stresses measured in the inter-seam rock at Goonyella Riverside are consistent with those presented for the northern Bowen Basin in the Australian stress map (Hillis et al., 1999; Hillis et al., 1998). The inter-seam rock is characterised by a reverse-stress regime with S_{Hmax} oriented 020°. The Goonyella Middle Seam has significantly lower horizontal stress magnitudes than the inter-seam rock and is characterised by a normal-stress regime with S_{Hmax} also oriented 020°. The partitioning of stress between the coal and inter-seam is attributed to the regionally high horizontal stress and differences in mechanical properties between the coal and inter-seam, namely the elastic modulus. The stress partitioning between coal and inter-seam observed at Goonyella Riverside is expected to occur in similar lithologic and high-stress environments. Conventional hydraulic fracture completions that treat large intervals of wellbore may be ineffective in similar settings for a number of reasons. High background stress can cause high initiation and propagation pressures that may prevent successful completion and/or damage the reservoir. Even if a hydraulic fracture is successfully propagated away from the wellbore, it may propagate in the lowest stress intervals and may not treat the sandstones if they are subjected to stresses above background levels. A more appropriate strategy may be the use of pinpoint fracture completion technology (Schlumberger, 2004; Thompson et al., 2002).

The effect of pore pressure on stress in the coal and inter-seam is unclear due to limited testing and differences in the test methods at virgin and dewatered conditions. The acquired data implies the stress tensor is coupled with pore pressure in both the coal and inter-seam. P_P-S'_{Hmax} coupling in the inter-seam rock would result in a decrease of differential stress with a decrease in pore pressure whereas $P_P - S'_{hmin}$ coupling in the coal seams via matrix shrinkage would cause a differential stress increase with pore pressure reduction that could potentially induce failure during reservoir depletion. The contact between coal seams and overlying strata is a mechanically weak layer along which slip can readily occur and may provide complications during drilling and completion of hydrocarbon wells including stuck pipe and damaged casing (Johnson et al. 2002). $P_P - S'_{hmin}$ coupling may exacerbated these problems during reservoir development. Fracture susceptibility diagrams show that the face cleats in the coal seams are not suitably oriented to be hydraulically conductive within the in-situ stress field and this scenario is not isolated to Goonyella Riverside. Regional studies show that the dominant face cleat orientation in the Bowen Basin is east-west ± 30° (Pattison et al., 1996) and that the S_{Hmax} azimuth is approximately 030°N (Hillis et al., 1999). The most prospective areas with regard to cleat permeability in the basin will occur where cleats are most suitably oriented for reactivation (i.e. cleats ~060° and S_{Hmax} ~030°).

11.3 Amadeus Basin Study

The study presented in Chapters 7–10 examines the structural geology of the Amadeus Basin in order to assist development of the Mereenie and Palm Valley fields. Regional cross-sections presented in Chapter 8 demonstrate the basement-cover interaction along the northern margin of the basin. The main orogenic displacement zone, the Redbank Shear Zone (RSZ), is an ancient crustal discontinuity with a long and varied history of compression and extension since ~1500 Ma (Flottmann et al. 2004). The RSZ focused deformation during the Alice Springs Orogeny (ASO) resulting in a basement cored wedge rather than a passive-roof-duplex typical of orogens without basement involvement (Banks & Warburton 1986; Cooper 1996; Flottmann & Hand 1999). The cross-sections imply ~30 km of shortening across the northern margin of the basin, significantly less than the ~110 km implied by previous thin-skinned models (Marjoribanks 1976; Teyssier 1985). Isostatic modelling of the northern margin of the Amadeus Basin implies that the effective elastic thickness of the lithosphere was significantly less during the ASO than the contemporary thickness. The modelled thickness of 10 km during the ASO is similar to contemporary intracratonic extensional provinces such as east Africa and the Basin and Range Province (Watts 2001). Ordovician rifting (pre-ASO) and associated heat flow may be responsible for the discrepancy between contemporary effective elastic thickness and the short wavelength of northern Amadeus foreland. The site of proposed Ordovician extension (Lee et al. 2002) is also the site of subsequent inversion during the ASO. The isostasy modelling supports field observations showing that orogenic intensity and subsequent uplift along the Mereenie section were significantly less than along the Palm Valley section. Deformation within the foreland, in front of the RSZ is relatively mild and is characterised by thin-skinned detachment folding. The Mereenie and Palm Valley anticlines developed as salt-cored detachment folds above a detachment in the Bitter Springs Formation. The Mereenie Anticline has tighter fold limbs than the Palm Valley Anticline and was faulted during the late stages of folding at ~80% of total shortening forming a break-thrust type structure.

There are at least two generations of natural fracturing in the Amadeus Basin that are important to reservoir development: 1) fold-related fractures and; 2) regional, orogenic-related fractures. Many of the fold-related fractures are at a high angle to S_{Hmax} and are stress-insensitive due to the high rock strength and mineralisation (Berry et al. 1996; Hillis et al. 1998). The fold-related fractures are typically bed-bound, and are more closely spaced, providing access to the low permeability matrix while the regional fractures are more pervasive and plumb the entire reservoir by connecting the smaller fold-related fractures and the individual reservoir intervals. The fold-related fractures may be predicted by modelling the fold geometry with Gaussian curvature and a good correlation exists between high Gaussian curvature and well performance in the Palm Valley Field. The relationship between Gaussian curvature and fracturing within the Mereenie Field is less clear as most existing wells are off-crest oil rim wells. This study shows that curvature analysis is field-specific and the results of any curvature analysis need to be

calibrated with fracture or production data from within that field. The work presented in Chapter 9 shows a clear relationship between orogenic intensity and regional fracture spacing with regional fracture swarms becoming more closely spaced with increased orogenic intensity. The most productive wells in both fields are expected to occur in locations where the pervasive regional fractures intersect zones of dense fold-related fractures or where there are large reservoir-effective crestal fractures (as currently targeted). The regional fracture swarms may be predicted at reservoir level at Mereenie and Palm Valley by extrapolating outcrop information. In fields where outcrop information is unavailable, seismic methods such as AVO and AVAZ may be useful in locating regional fracture swarms where high quality 3D seismic is available.

The study also uses the structural modelling presented in Chapter 8 to evaluate the Mereenie sub-thrust play. The structural modelling shows that the Mereenie Anticline is a faulted detachment fold formed during the ASO and that the Mereenie Fault formed prior to hydrocarbon charge. Provided the Mereenie fault formed pre-charge, and there is footwall closure, the critical risk to the Mereenie sub-thrust play is fault seal to provide footwall four-way closure. Fault seal risk along the Mereenie Fault has been assessed in Chapter 10 by evaluating juxtaposition, damage zone and reactivation seal risk. The mapped juxtaposition relationships for the slipped interval on the fault plane show that within the footwall, all of the Pacoota sandstones are juxtaposed against either hangingwall sandstone or thin siltstone layers, providing poor juxtaposition seal. MICP analysis suggests that the maximum hydrocarbon column that may be supported via juxtaposition sealing is in the order of 2–4 m.

Despite poor juxtaposition seal potential, the fault core and damage zone may still provide an effective seal. The shale gouge ratio (SGR) has been calculated along the Mereenie Fault and is typically in the range 5–10% over the best reservoir intervals in the Pacoota Sandstone. SGR values of 15–20% are considered by many authors to represent the threshold between non-sealing and sealing behaviour (Yielding et al. 1997; Yielding 2002; Bretan et al. 2003). However, the SGR methodology does not address the processes of mineralisation or cataclasis along sandstone on sandstone faults and it has been demonstrated some sandstone-on-sandstone faults with low SGR can be sealing (Labaume et al. 2000). Cataclasite may provide a potential sealing mechanism along the fault considering reservoir temperatures probably exceeding 90°C some time during faulting and that mean stress during faulting was relatively high in terms of cataclasite development. Mineralisation along the fault sourced from the Bitter Springs Formation may also provide a potential sealing mechanism. Mineralogical studies of rock from the Undandita 1A well show poikilitic, intergranular anhydrite with microcrystalline dolomite suggesting fluid flow from the Bitter Springs Formation and mineralisation along the Carmichael Fault (Pontifex 2001). The Mereenie and Carmichael faults are similar emanating from the Bitter Springs Formation suggesting similar mineralisation may occur along the Mereenie Fault.

The reactivation risk (slip stability) of the Mereenie Fault was examined using the in-situ stress tensor. ΔP increases with depth from 5 MPa near the surface to over 40 MPa at 4 km depth and is ~20 MPa at the level of the Pacoota Sandstone. The gradual increase in ΔP with depth equates to a ΔP gradient of approximately 10 MPa/km suggesting low reactivation risk within the in-situ stress field. Slip stability as applied only assesses reactivation risk within the contemporary stress field. Where there has been a significant change in the stress tensor post-charge (e.g. via plate readjustment), the risk of reactivation for differing palaeo-stress regimes has not been assessed. Structural modelling based on field, map (Wells et al. 1961; Shaw et al. 1995) and seismic interpretation reveals that very few, if any, thrust faults in the northern Amadeus Basin intersect the Pertnjara Group. These observations, together with the slip stability modelling, imply that the risk of fault seal failure due to post-charge fault reactivation is low. The overall risk of fault seal breach via juxtaposition, damage zone or reactivation has been assessed on the premise and quantitative elicitation presented by Jones and Hillis (2003). The fault seal risking shows that the probability of fault sealing is intermediate and that the Mereenie sub-thrust play provides an attractive near-field exploration target provided other criteria such as volumetric estimates are satisfied. The sub-thrust play could be tested by a multi-objective development well during the upcoming drilling campaign to offset cost and risk.

Appendix A

Natural Fracture Logs: Goonyella Riverside Underground Area

The fracture logs are derived from the interpretation of 18 image logs acquired over the Goonyella Riverside underground area. The logs show the orientation and density of low, moderate and high angle fractures in the different mechanical units. The BMA ID next to the facies log is the name assigned by BMA to individual sand bodies and coal seams correlated between wells.

Borehole 40958

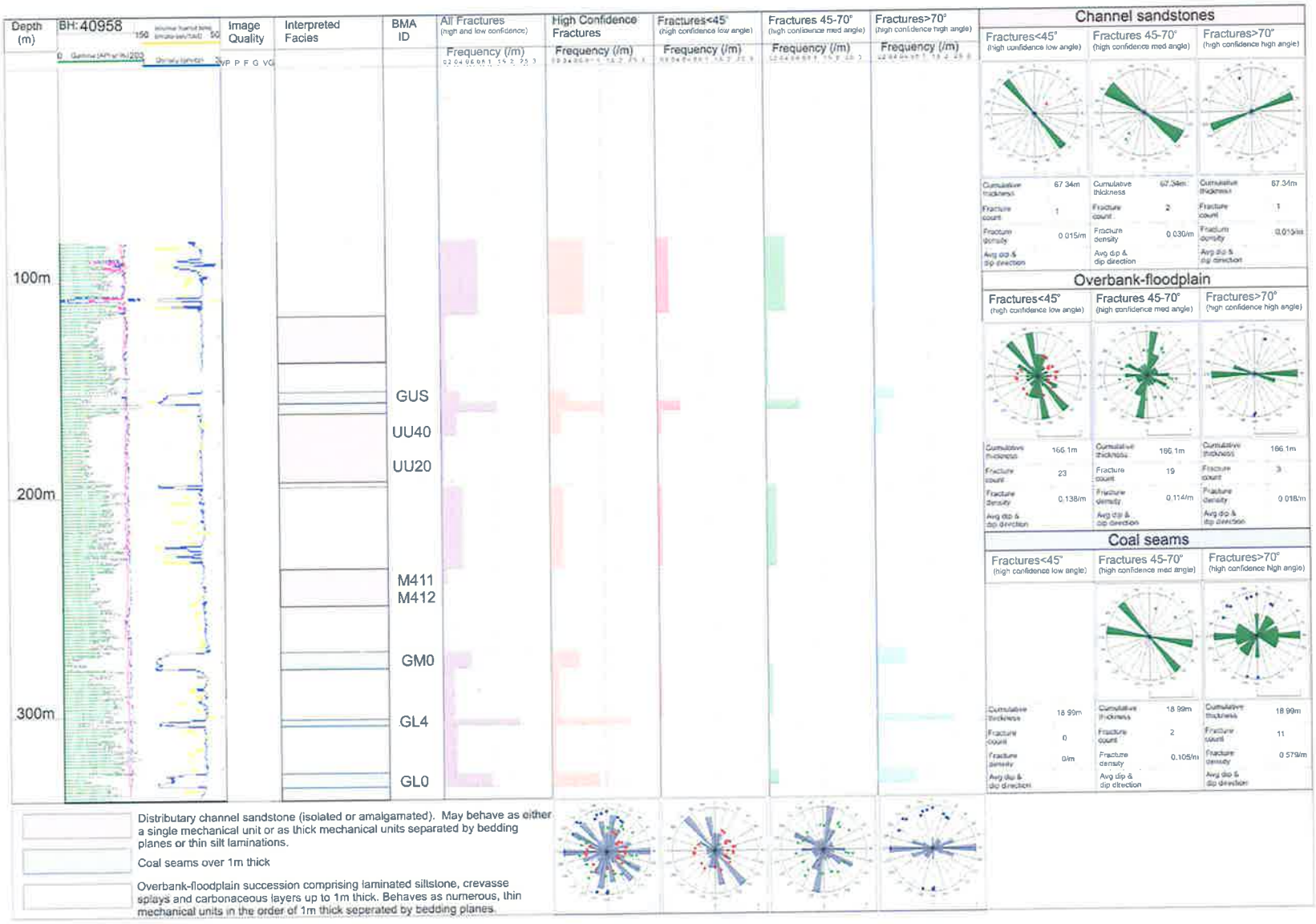

Borehole 40984

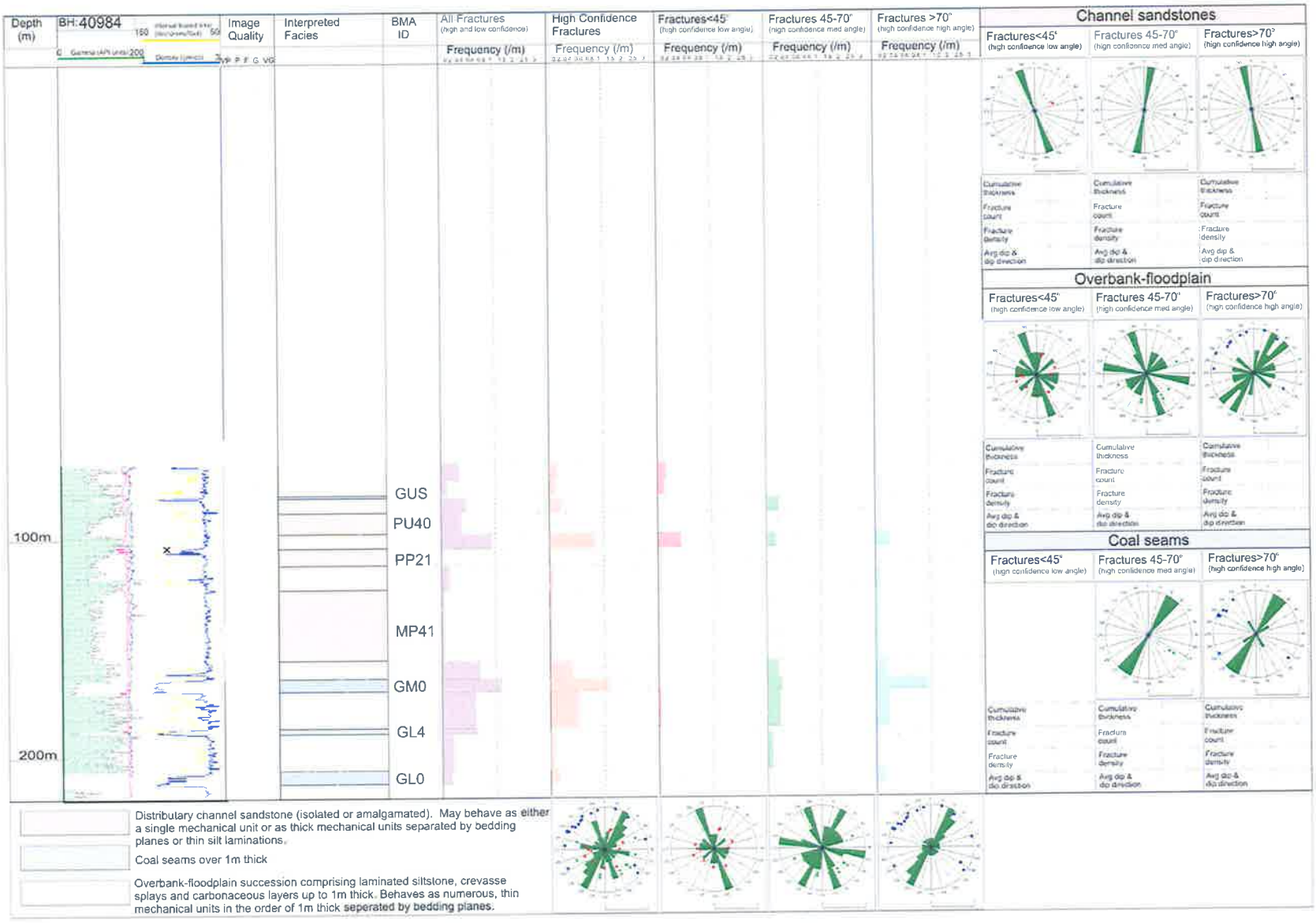

Borehole 40993

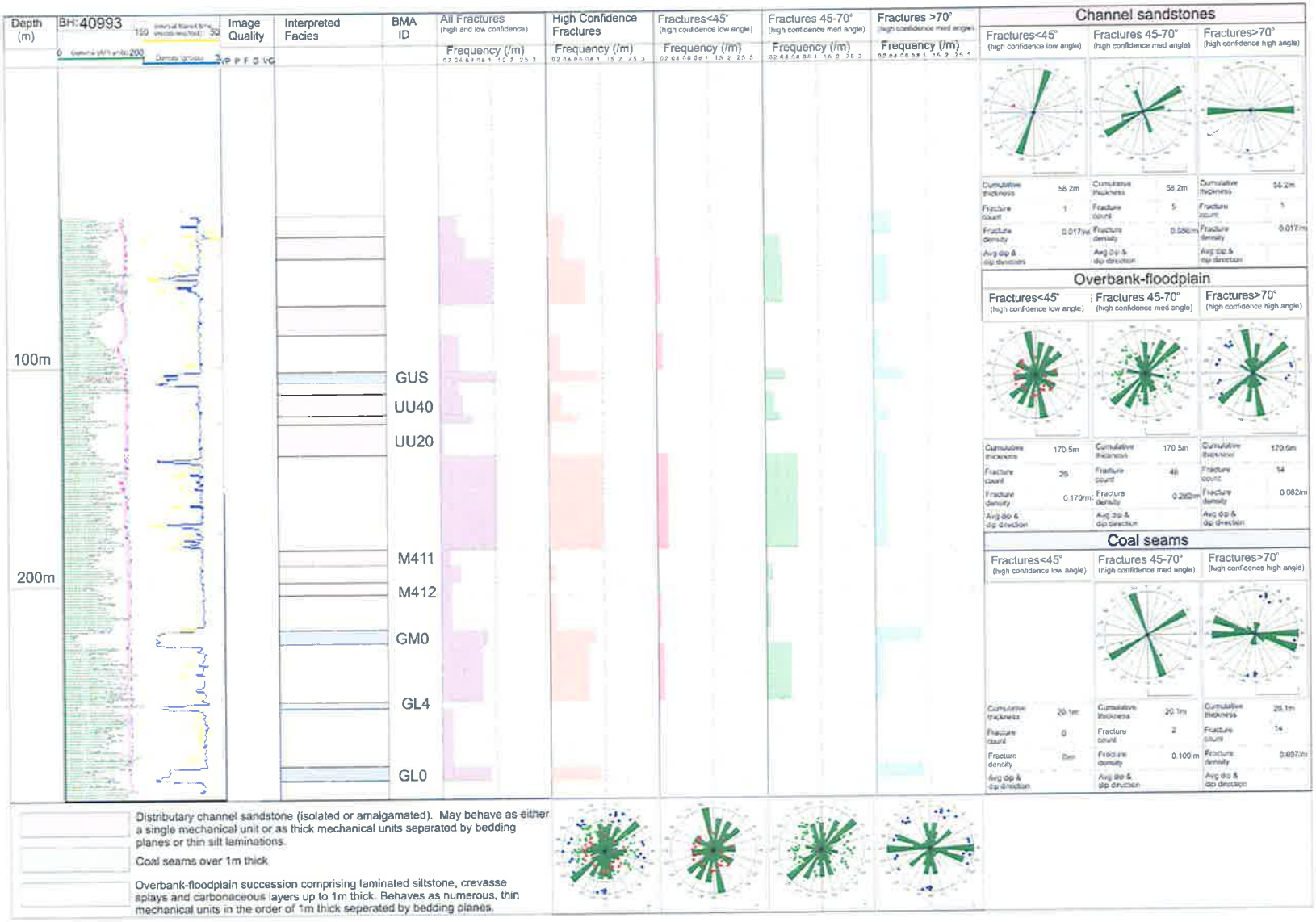

Borehole 40994

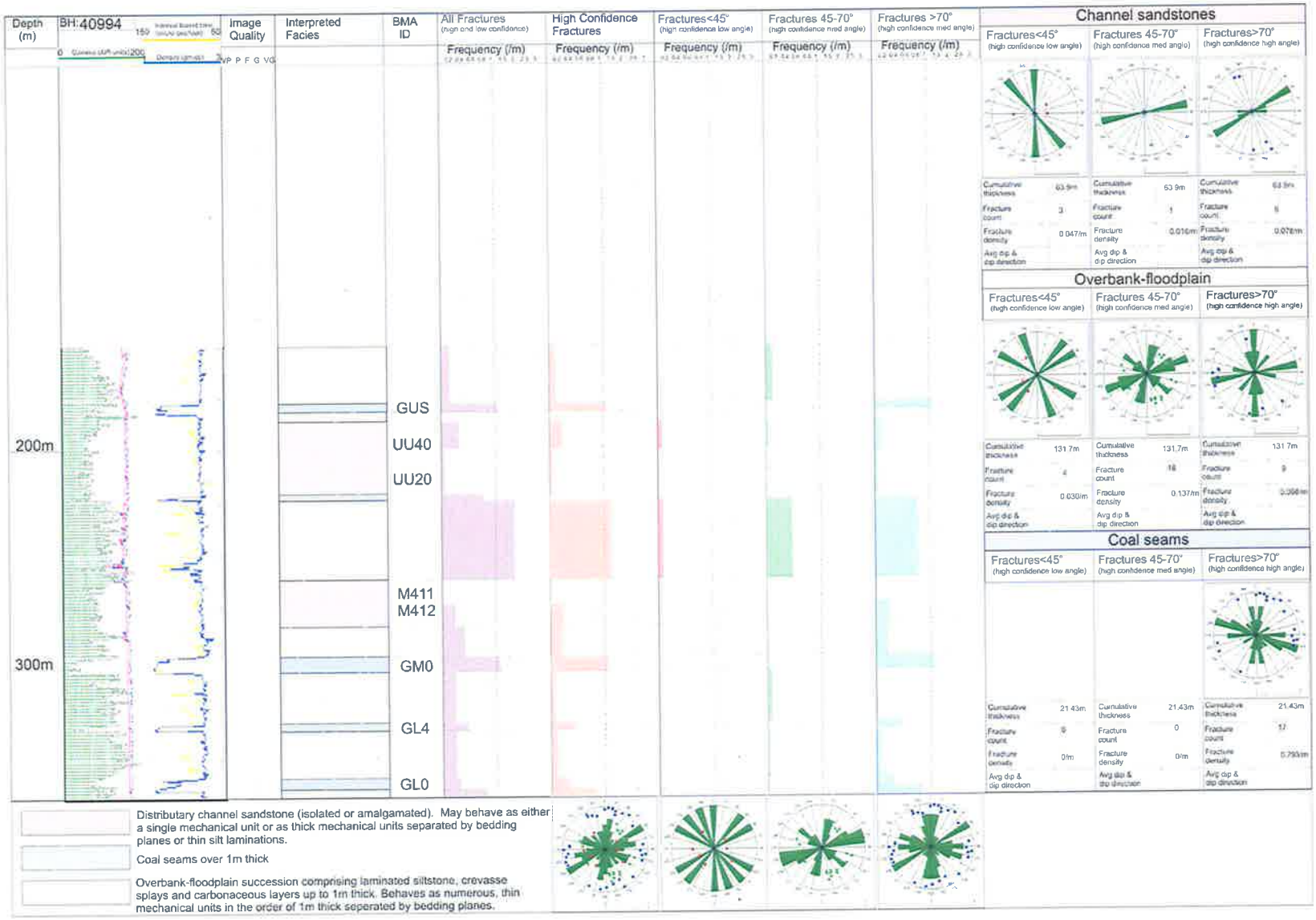

Borehole 40995

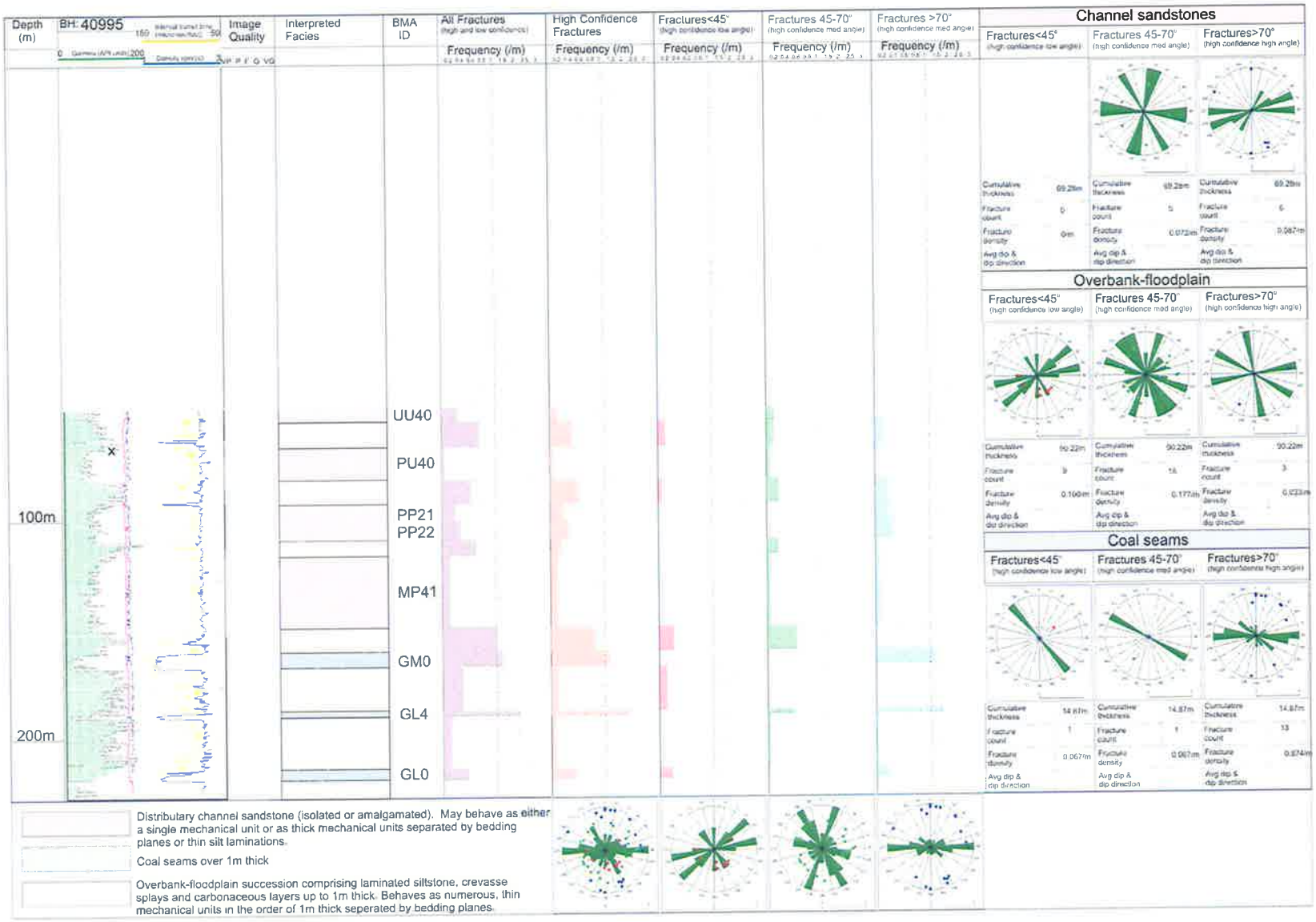

Borehole 40996

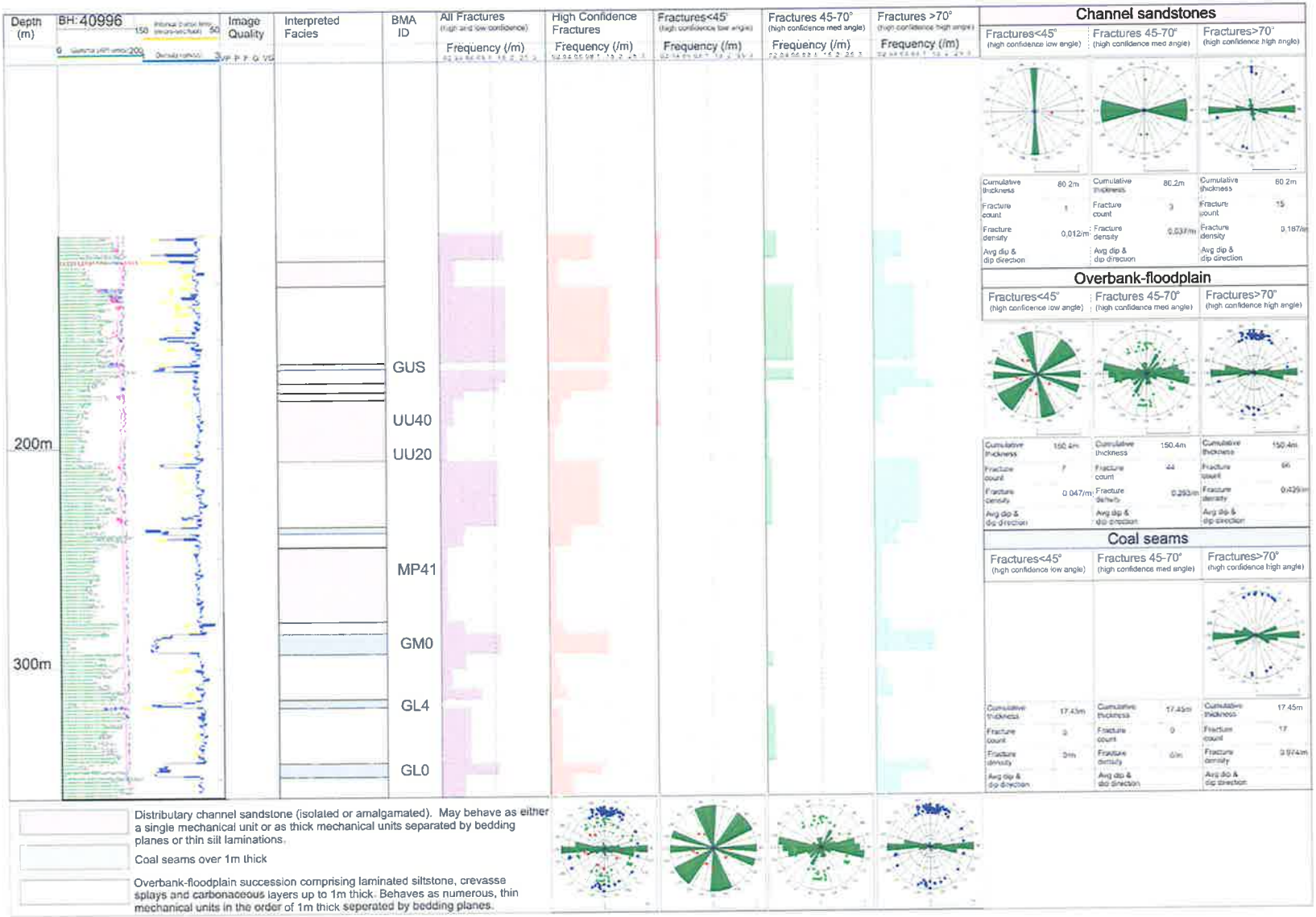

Borehole 40997

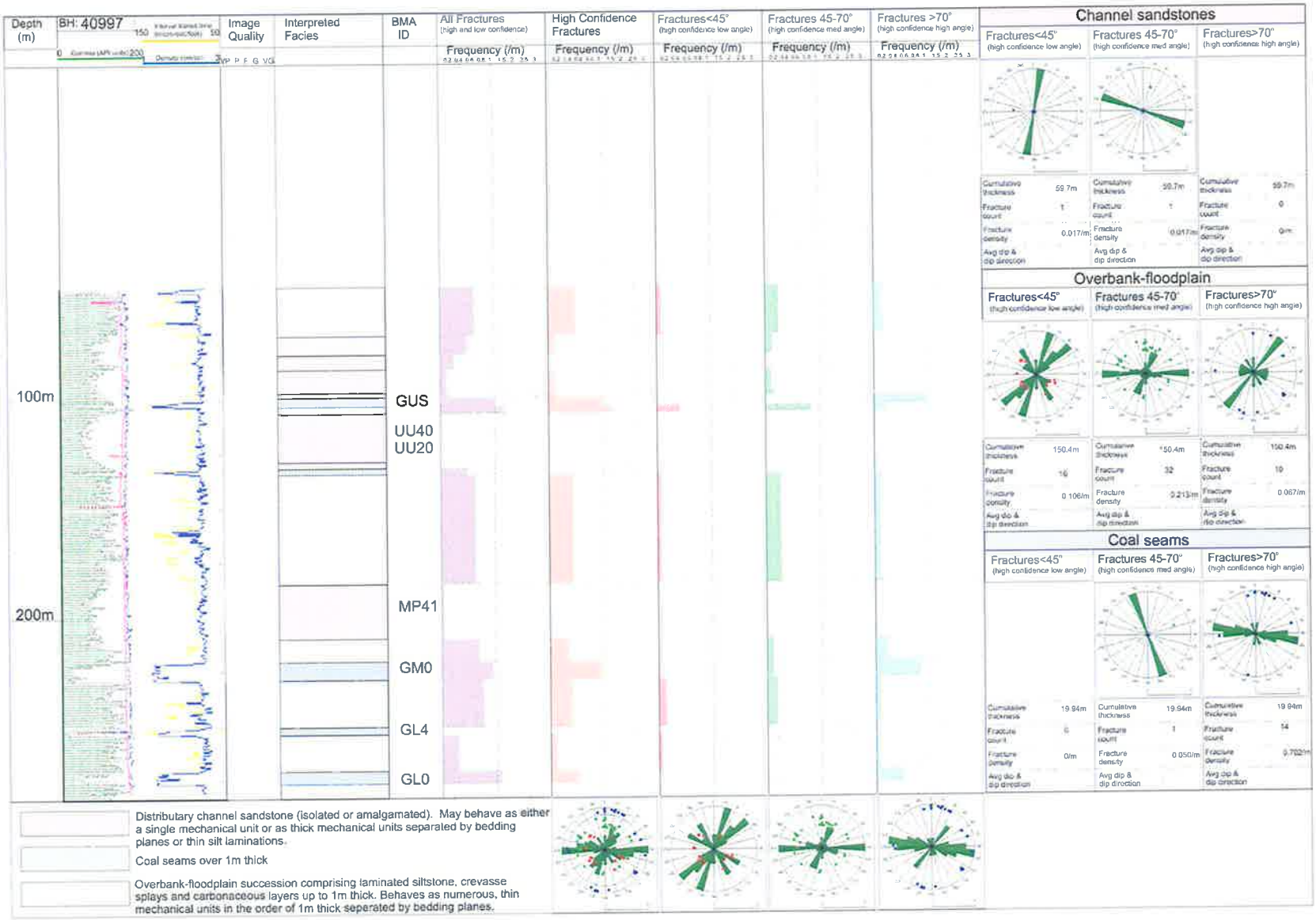

Borehole 40998

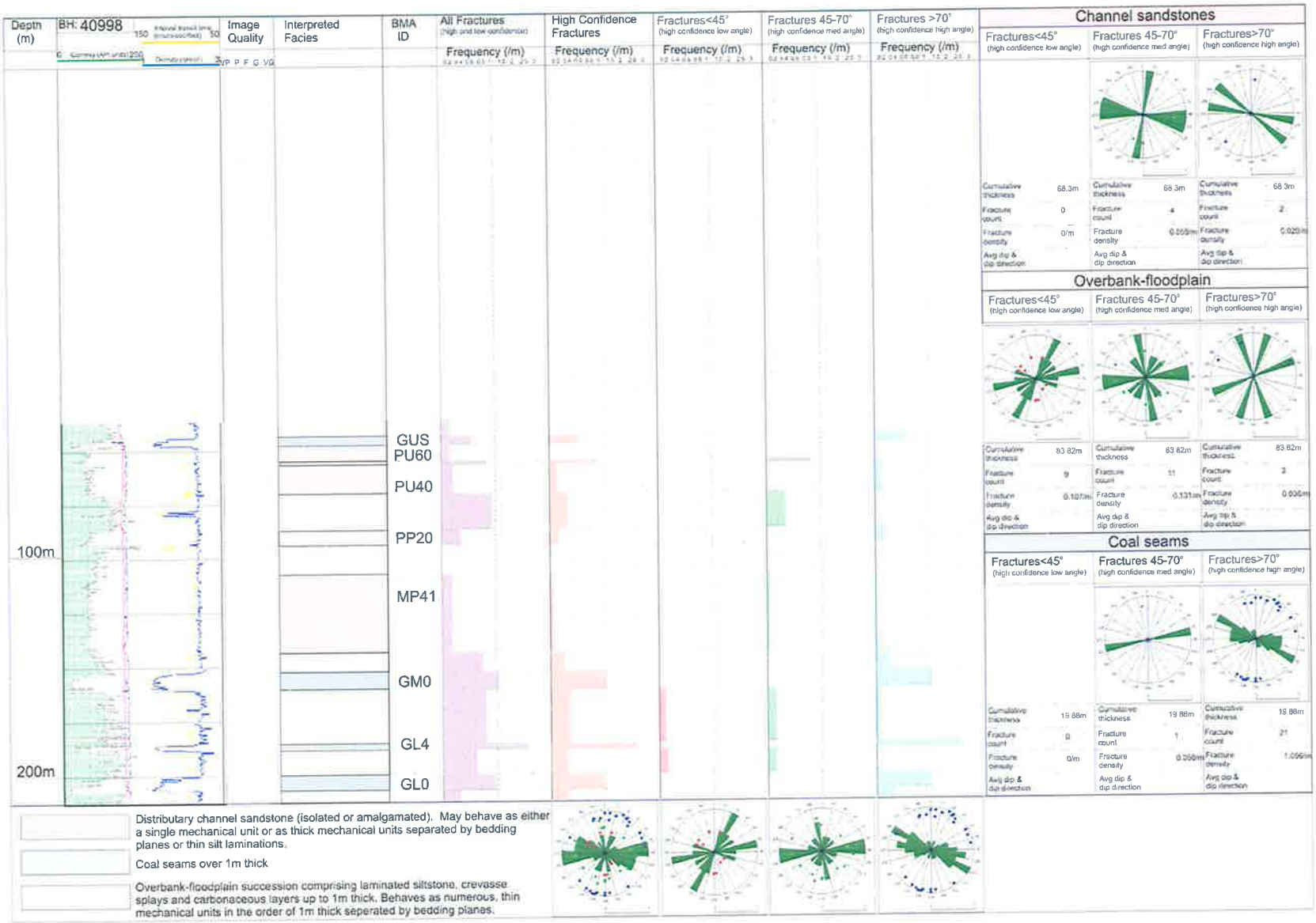

Borehole 41242

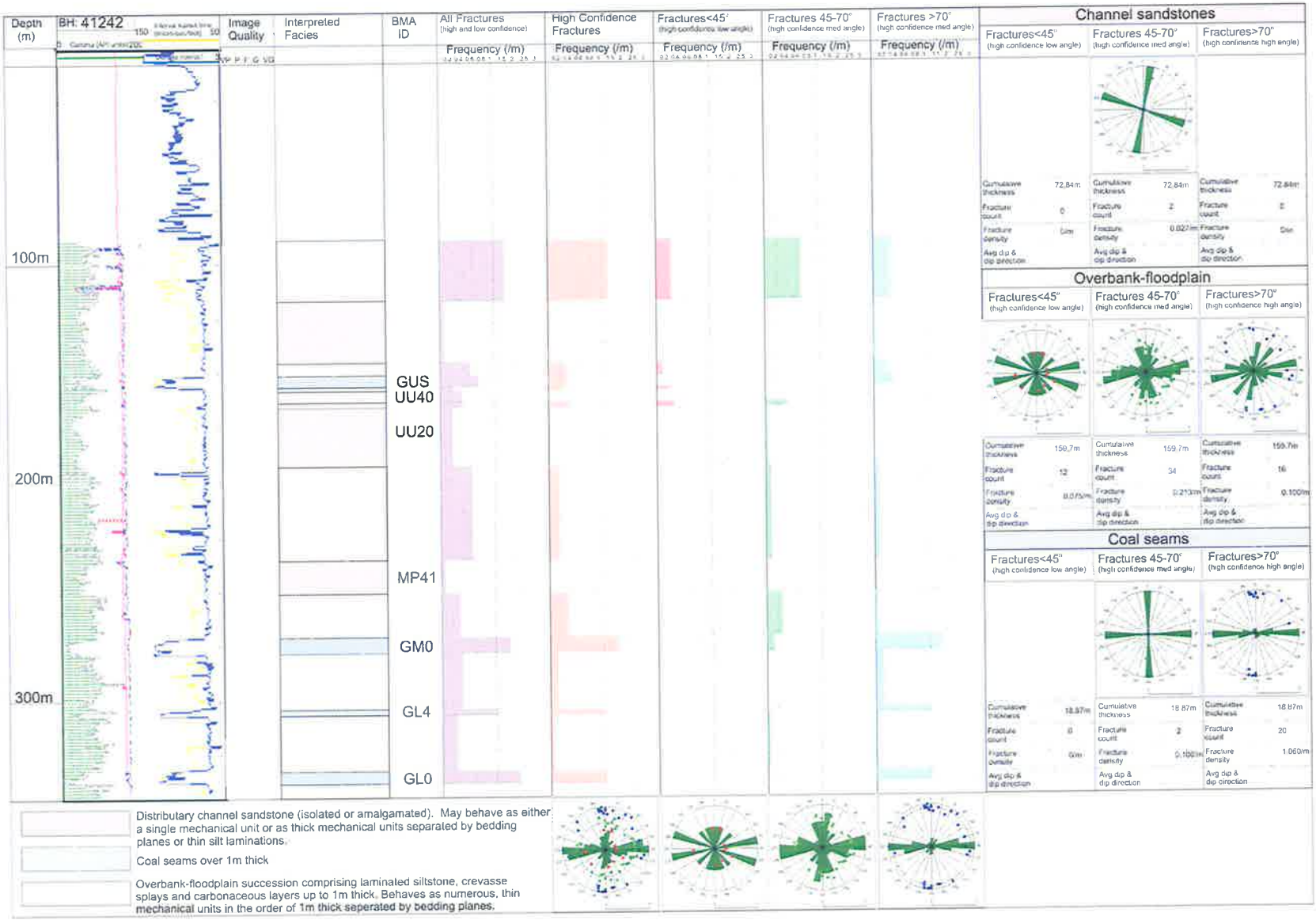

Borehole 41243

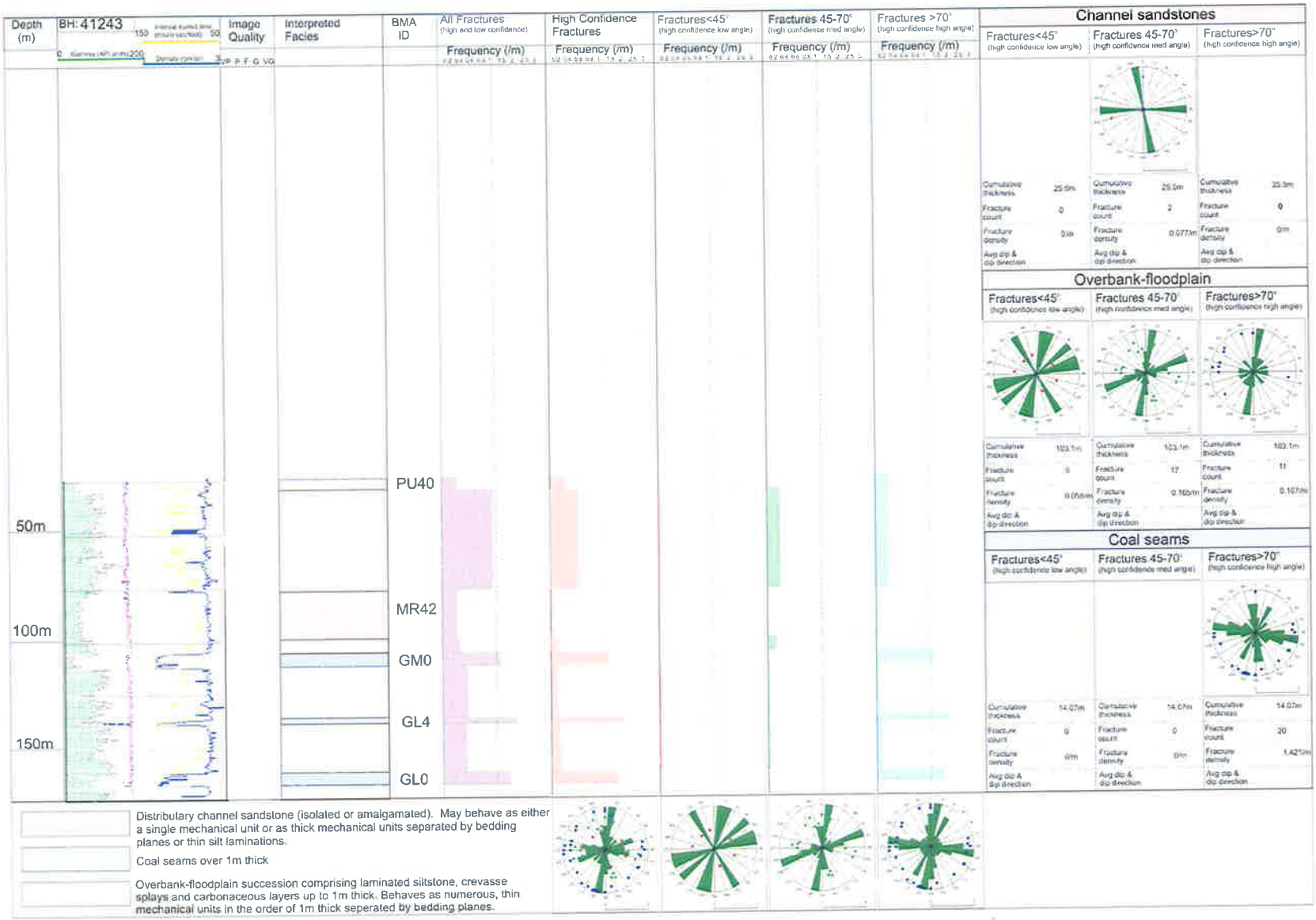

Borehole 41605

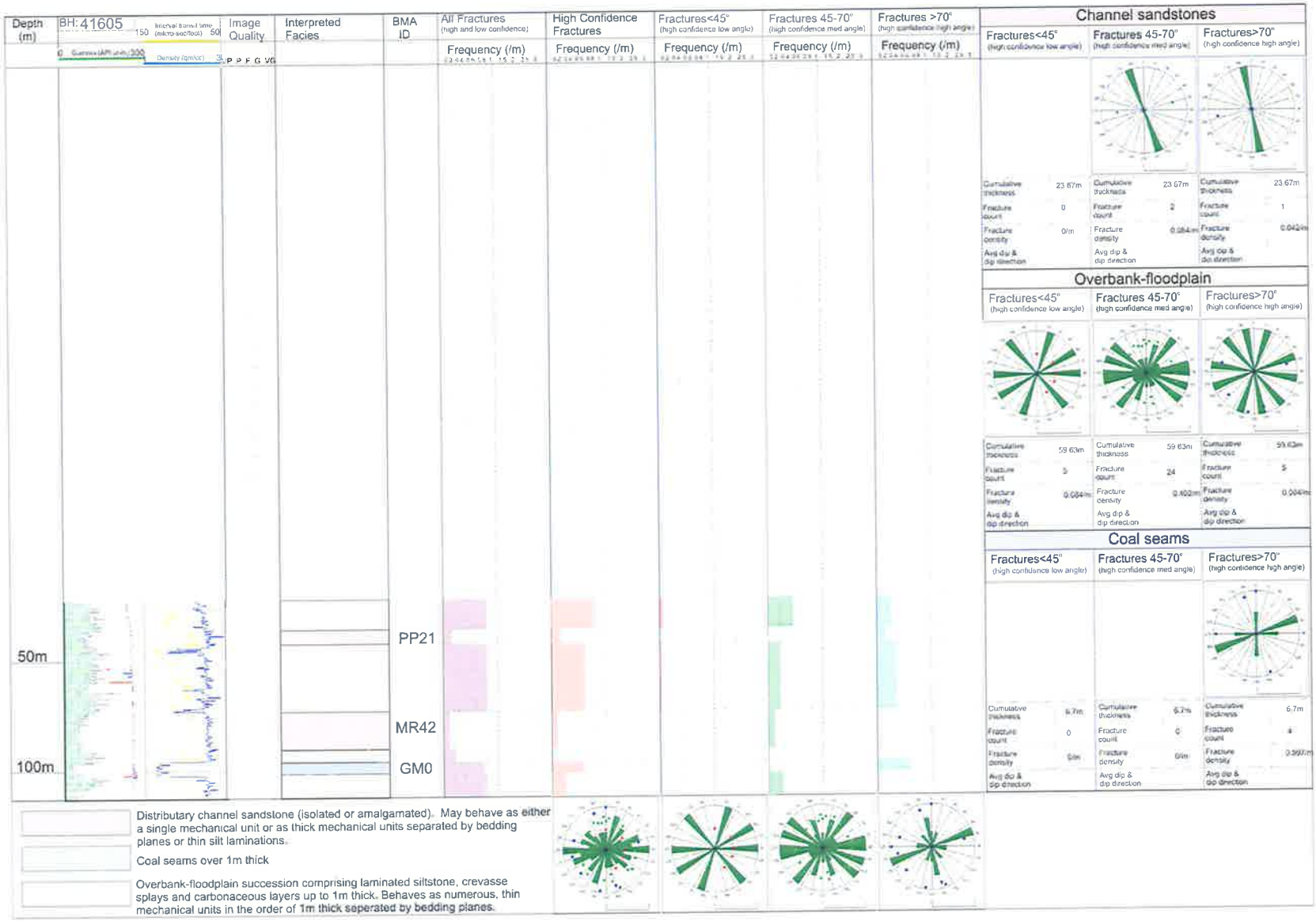

Borehole 41868

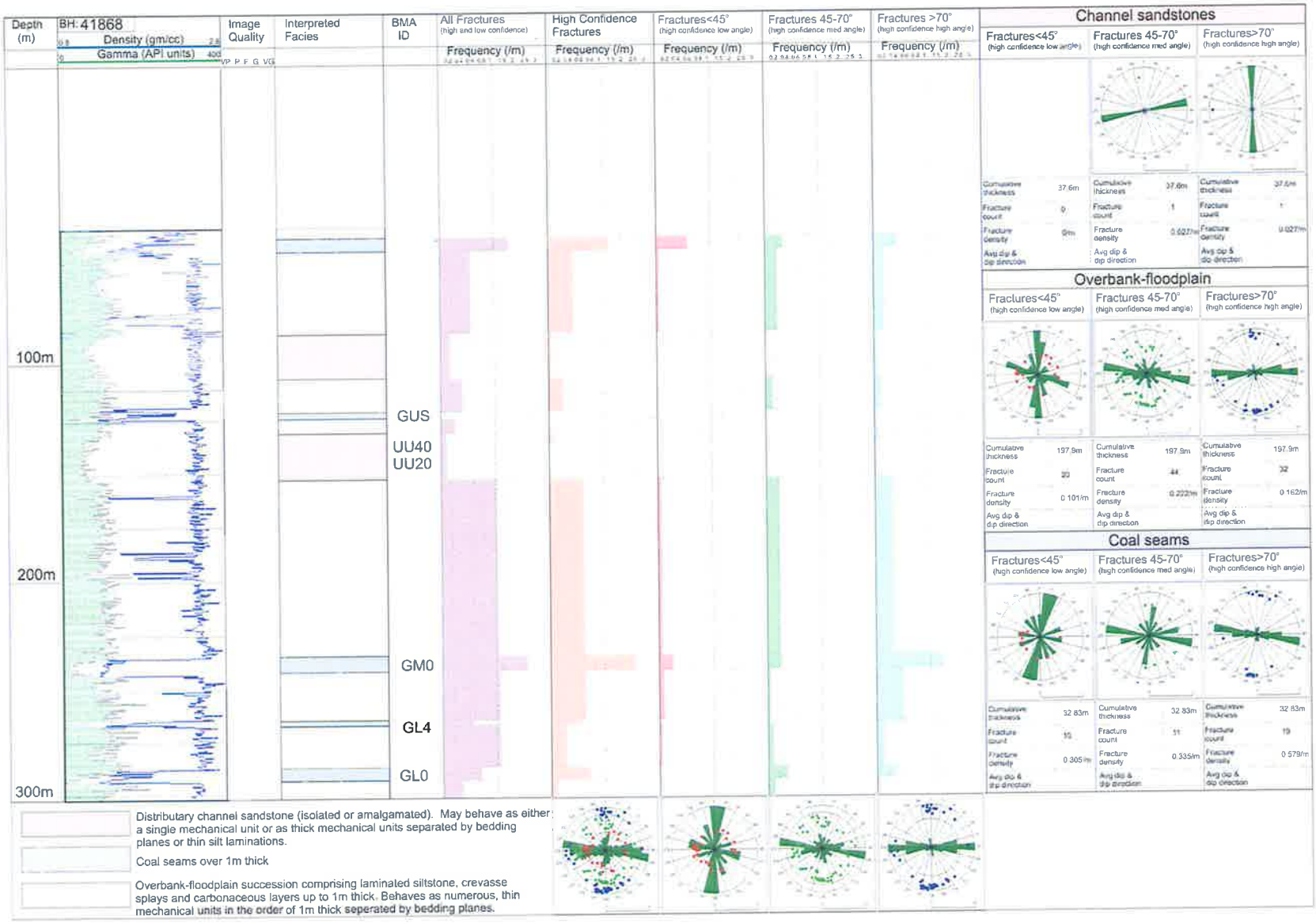

Borehole 41869

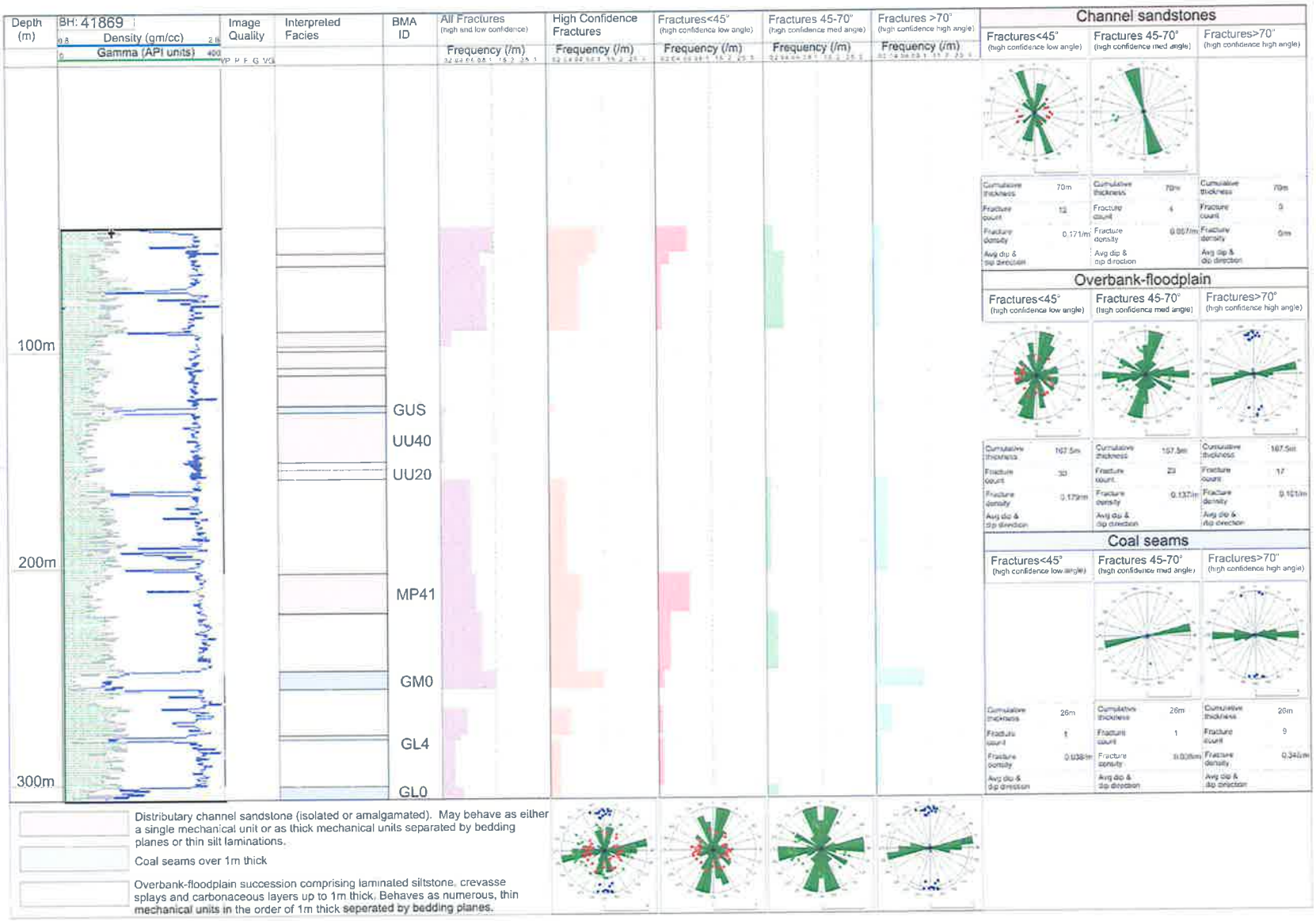

Borehole 41870

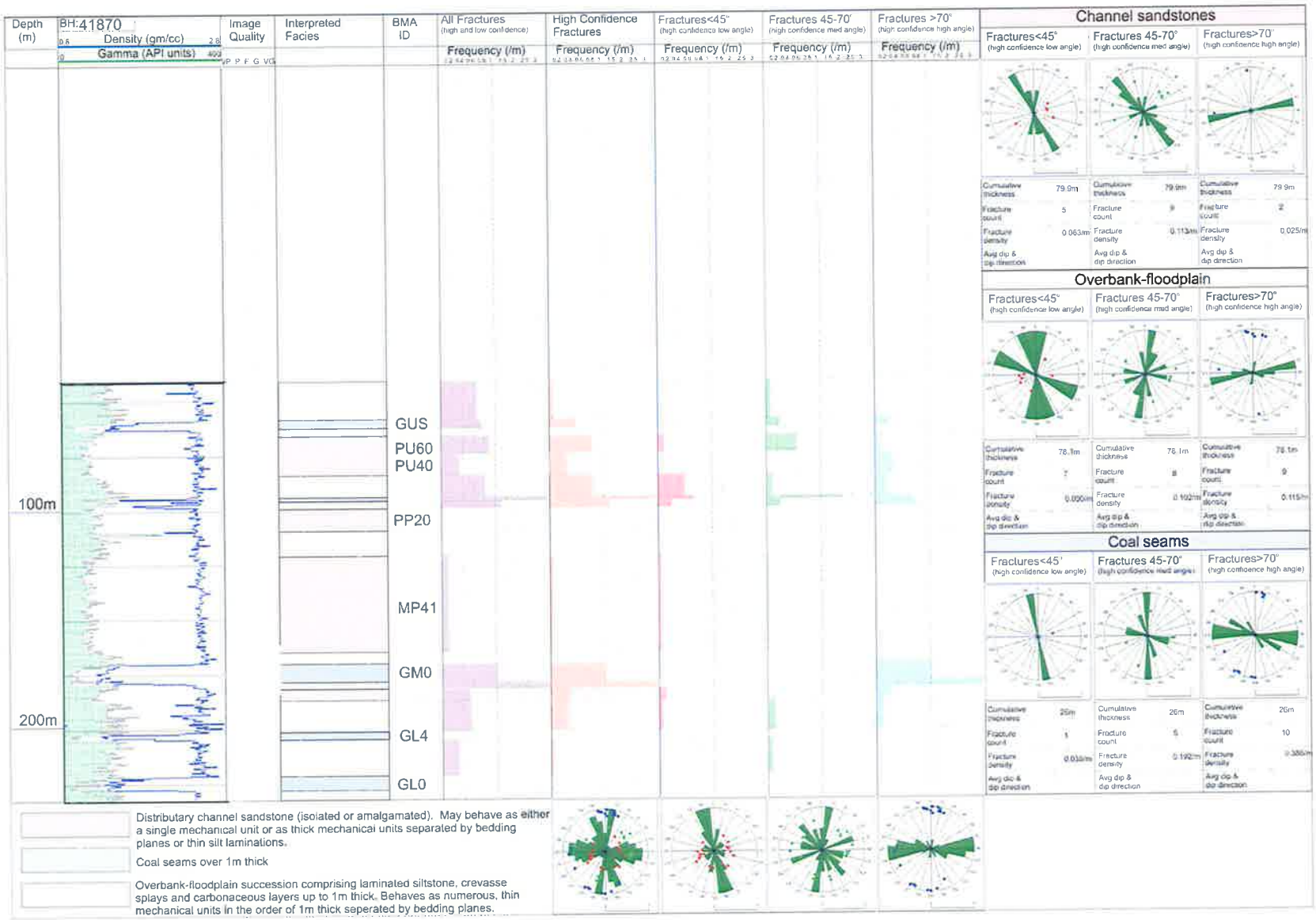

Borehole 41871

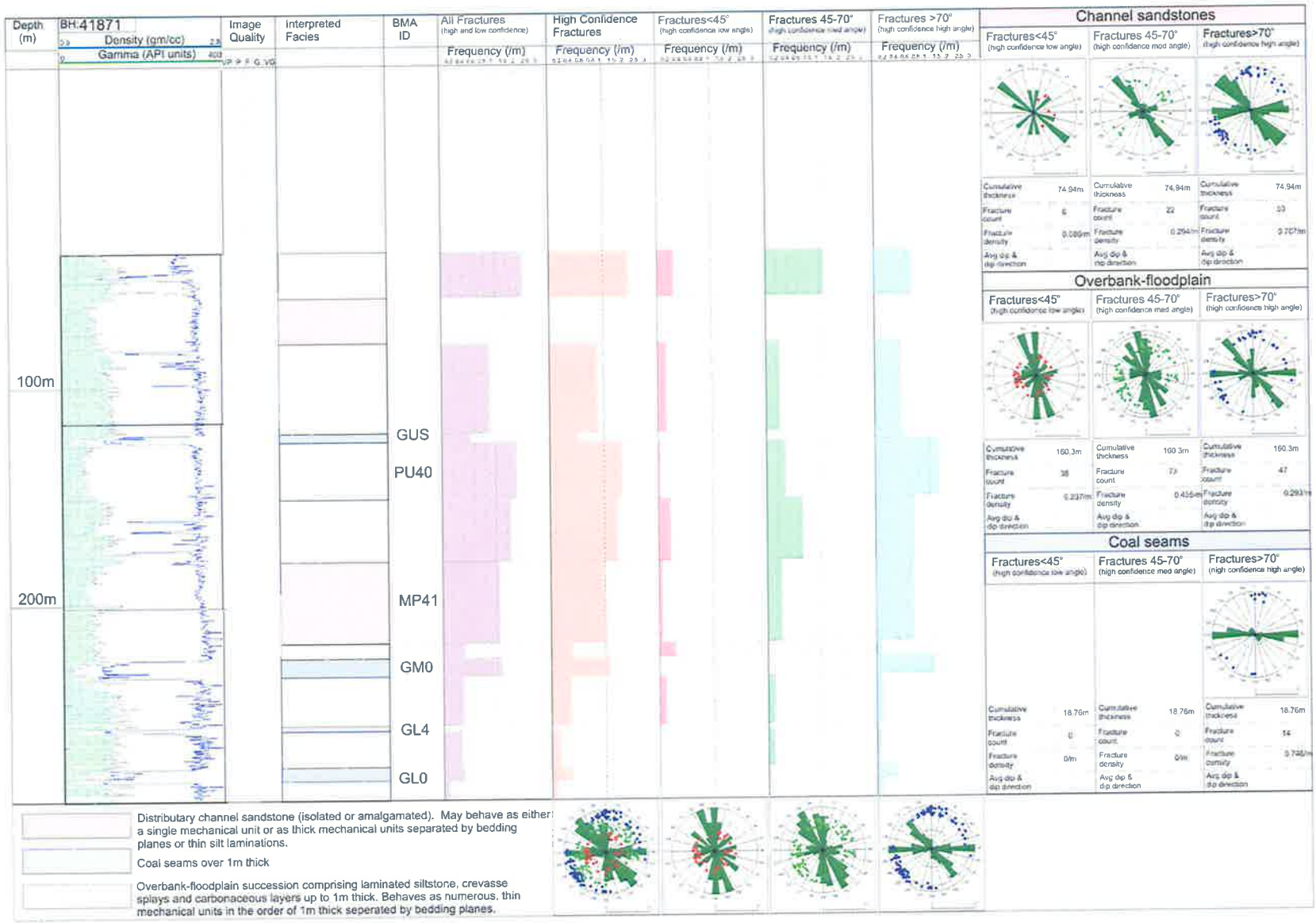

Borehole 41872

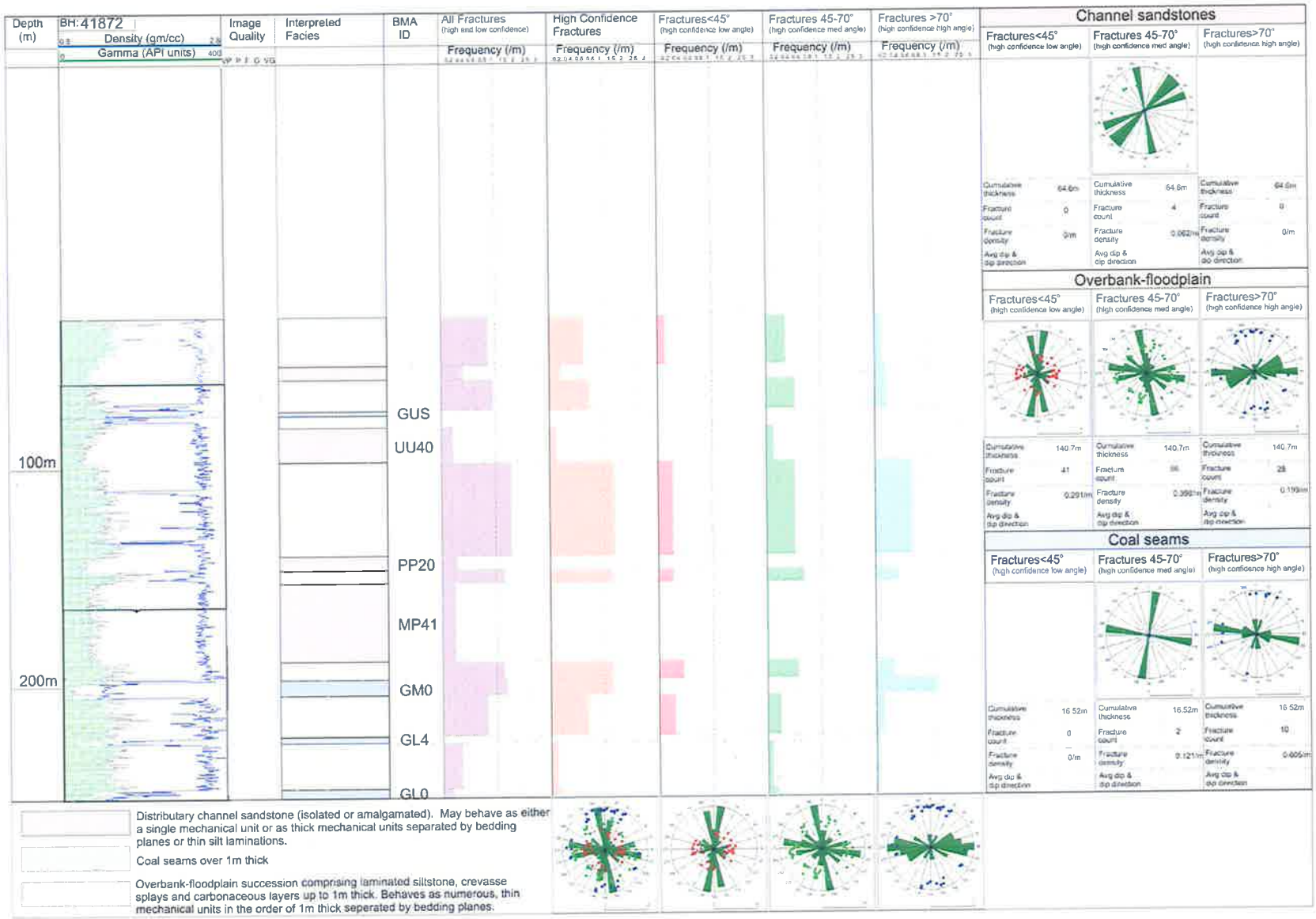

Borehole 41879

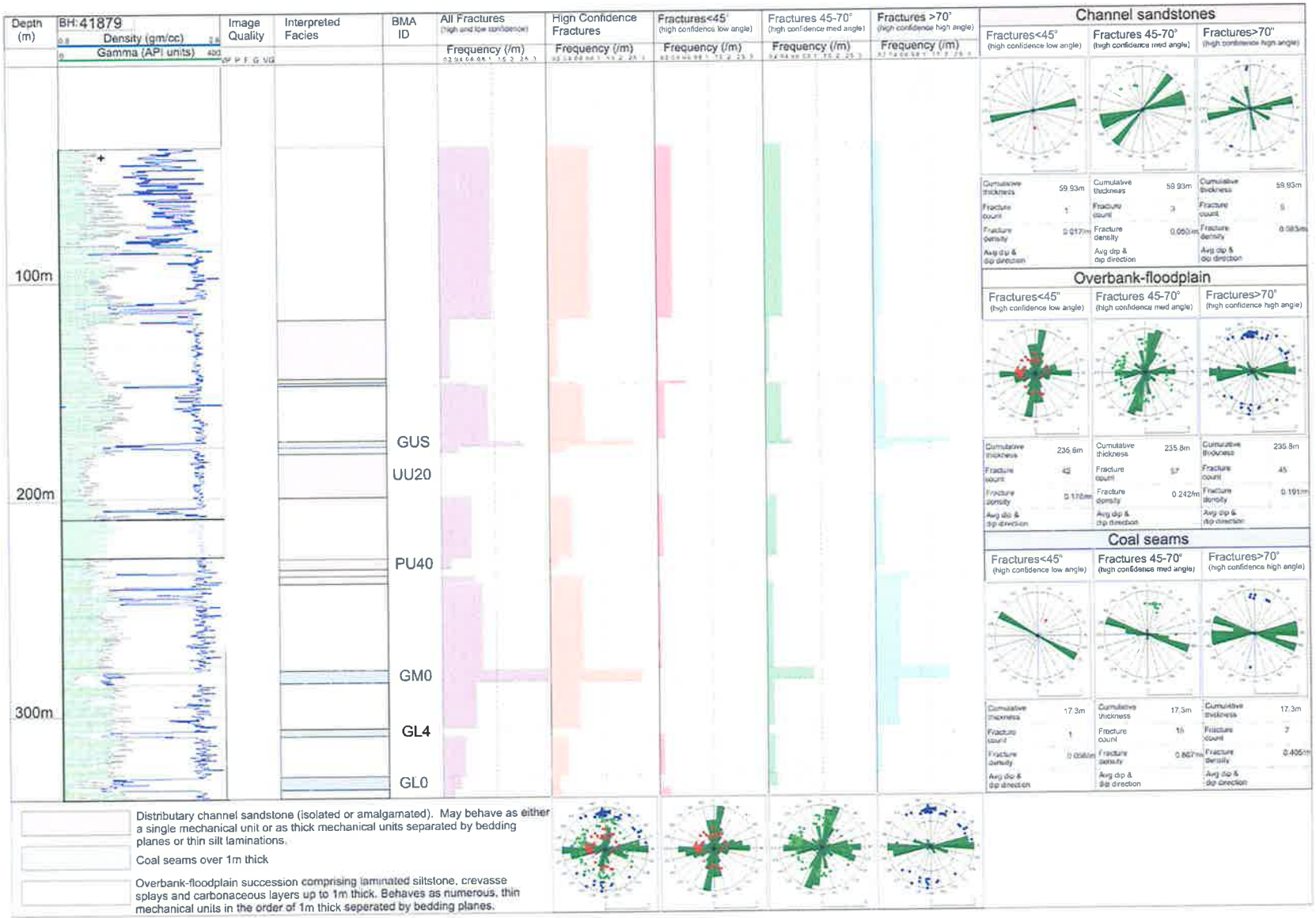

Borehole 41884

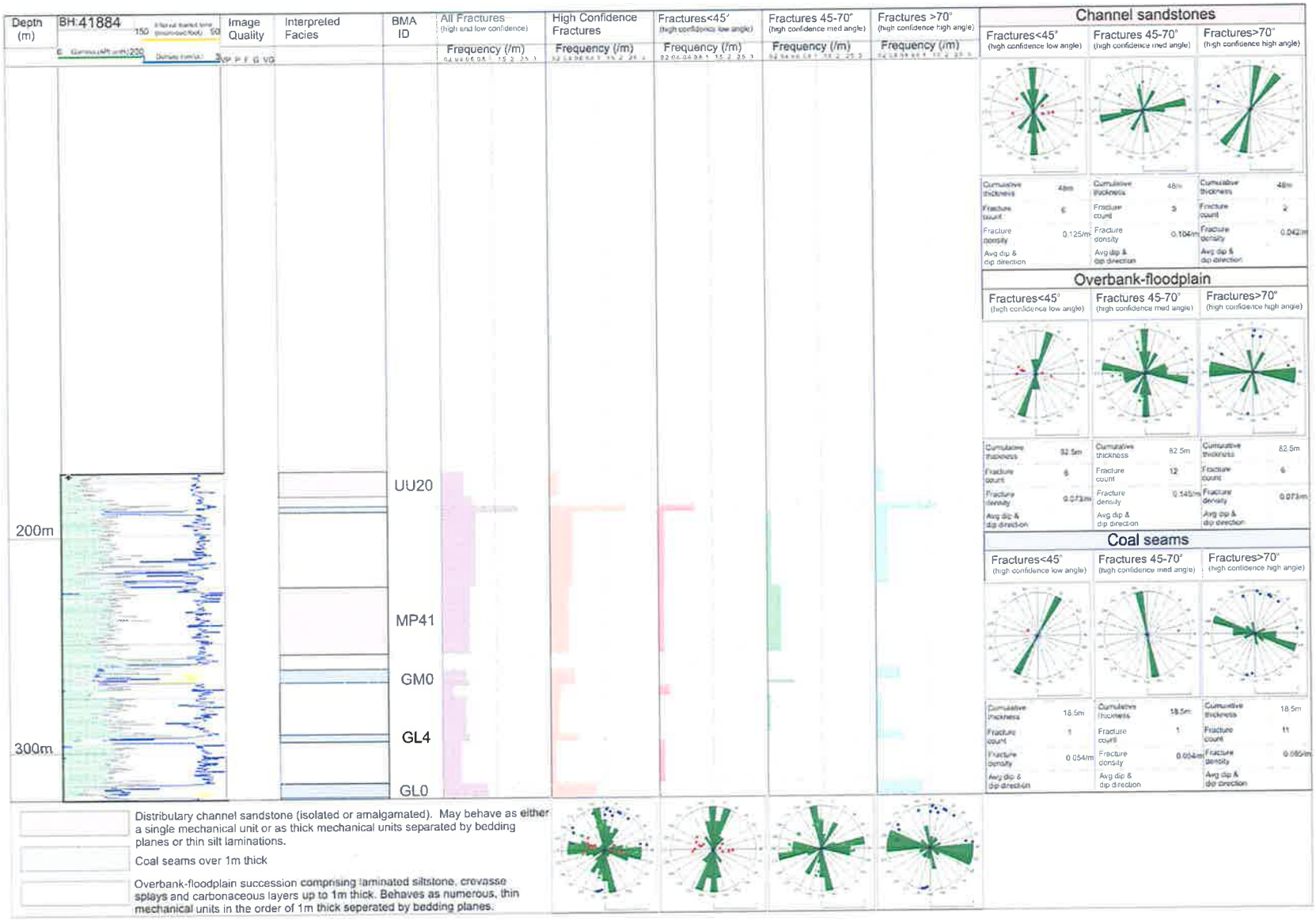

Appendix B

Regional Geology Maps

The regional cross-sections presented in this thesis were constructed from the 1:250 000 geology maps. The Mereenie section was constructed from the Mount Liebig and Lake Amadeus maps. The Gardiner Range, Palm Valley and James Range sections were constructed from the Hermannsburg and Henbury maps.

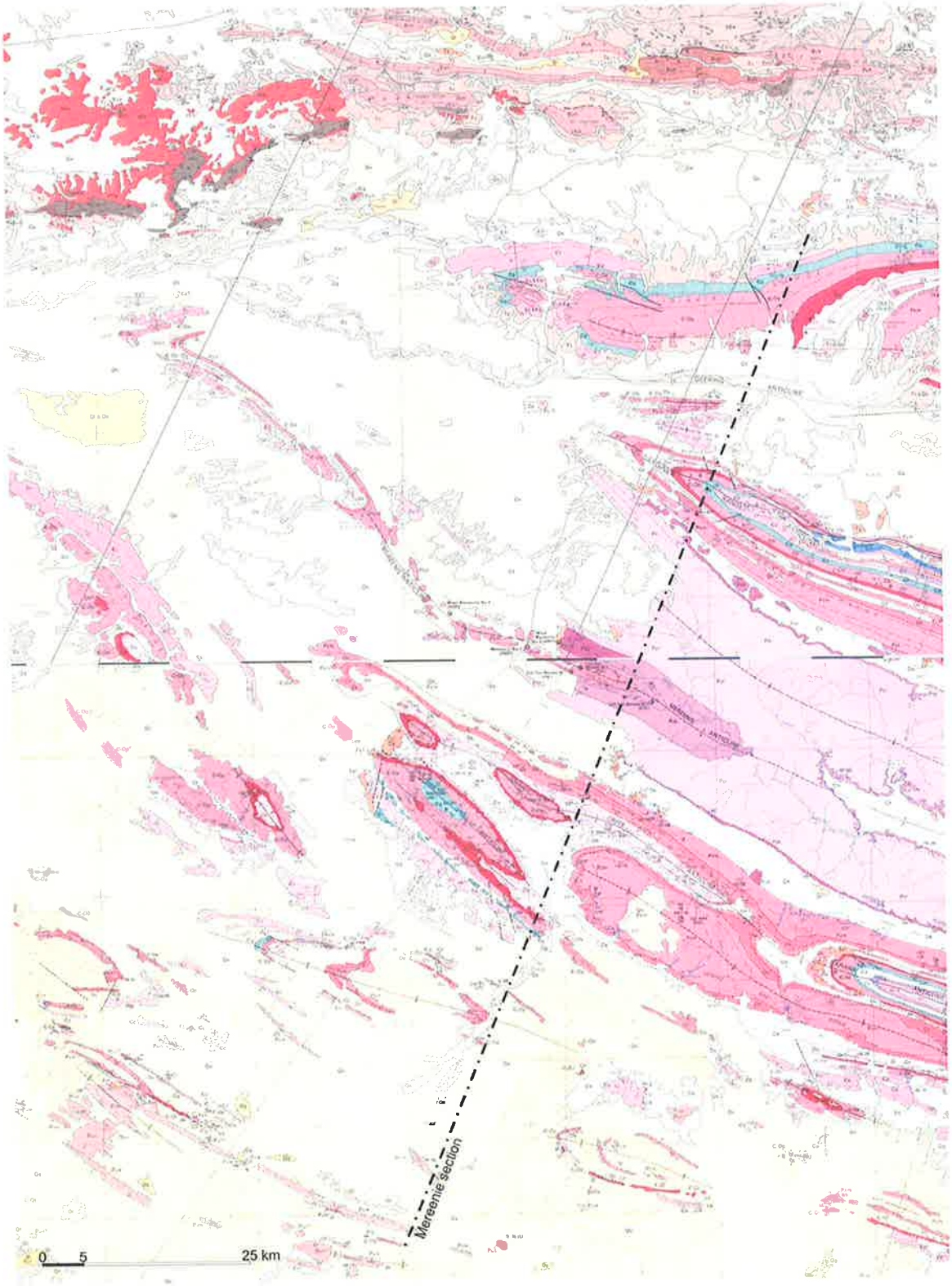

The Mereenie regional section has been constructed from the Mount Leibig (top) and Lake Amadeus (bottom) 1:250 000 map sheets.

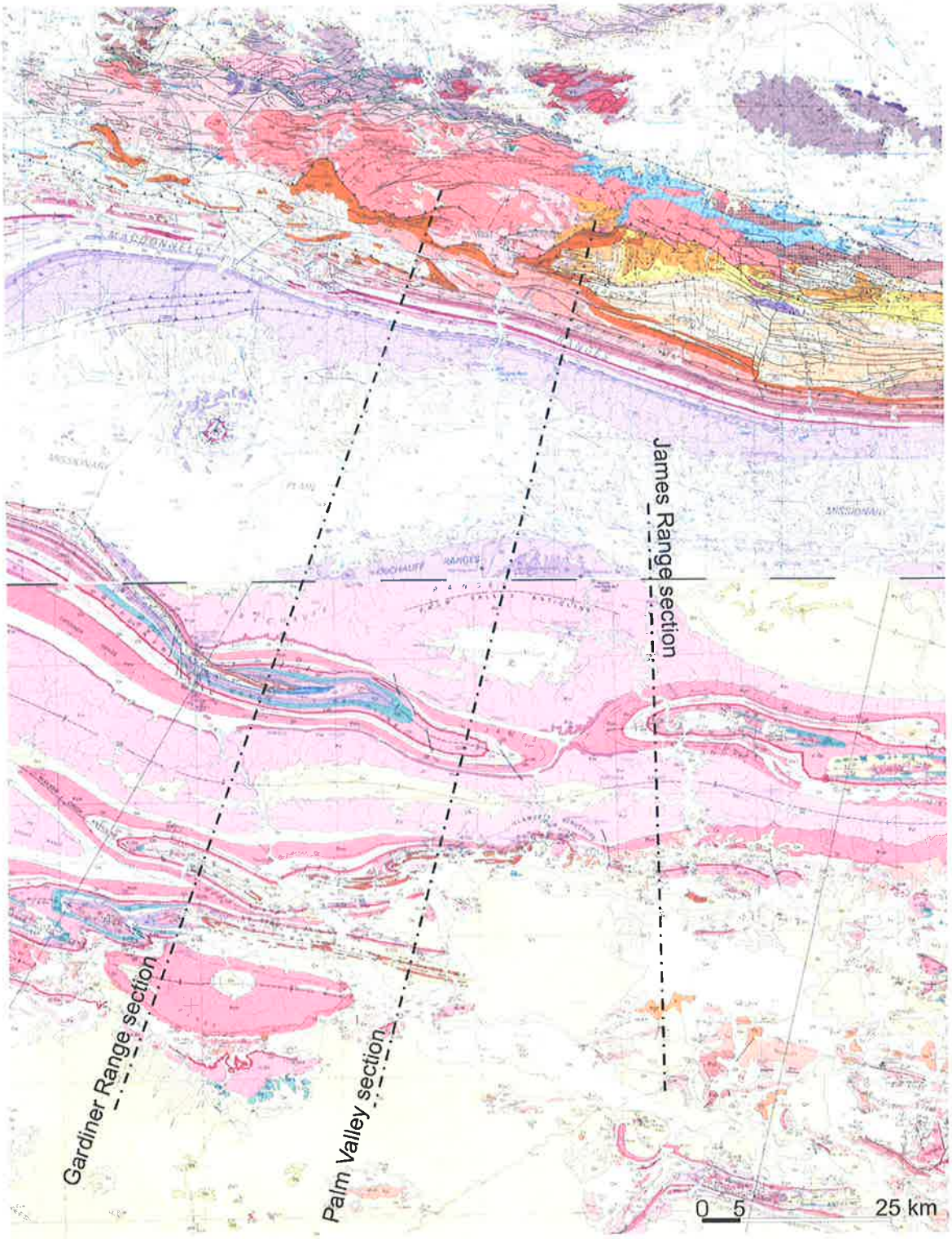

The Gardiner Range, Palm Valley and James Range regional sections have been constructed from the Hermannsburg (top) and Henbury (bottom) 1:250 000 map sheets.

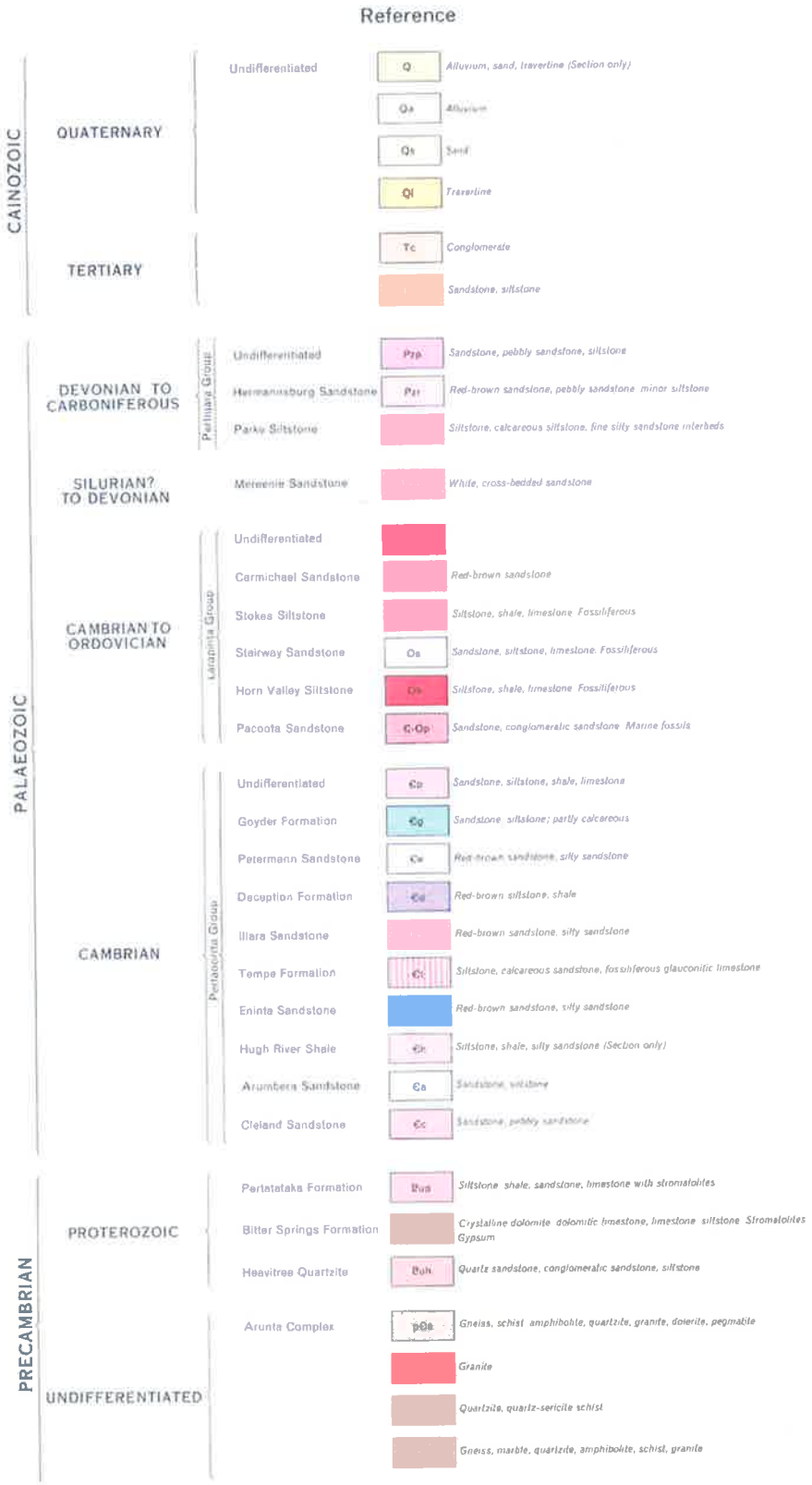

Key for the Mount Liebig map sheet. Note that there are minor variations in colouring and nomenclature between the different map sheets.

Appendix C

Core Gamma Testing: West Mereenie 1

Basic core gamma testing was conducted on core samples of the Goyder Formation to confirm a relationship between gamma-ray response and clay content and thereby produce a reasonable Vshale log from down-hole gamma log data for use in the fault seal analysis. Thorough core gamma testing was not possible due to budget constraints and only a small amount of core could be tested. The following figure shows the multi-spectral core gamma logging tool in operation. Measurements were taken at ~50 mm intervals with care taken to avoid core breaks. The lead cylinder as shown, minimises environmental contributions to gamma radiation; however, some background contribution is unavoidable using this technique. The core gamma work conducted as part of this study only provides a relative gamma count; the logs are not in API units and cannot be directly correlated to down-hole measurements.

Core gamma logging unit in operation

Sample of a siltstone layer.

Sample of cross-bedded sandstone.

West Mereenie 1 core 7 (2 of 2)

Goyder Formation 1602.33 m - 1608.73 m

Note - exact depths of core are uncertain, location of core breaks unknown ~ 2.5 m of core missing.
- core gamma is not in API units.

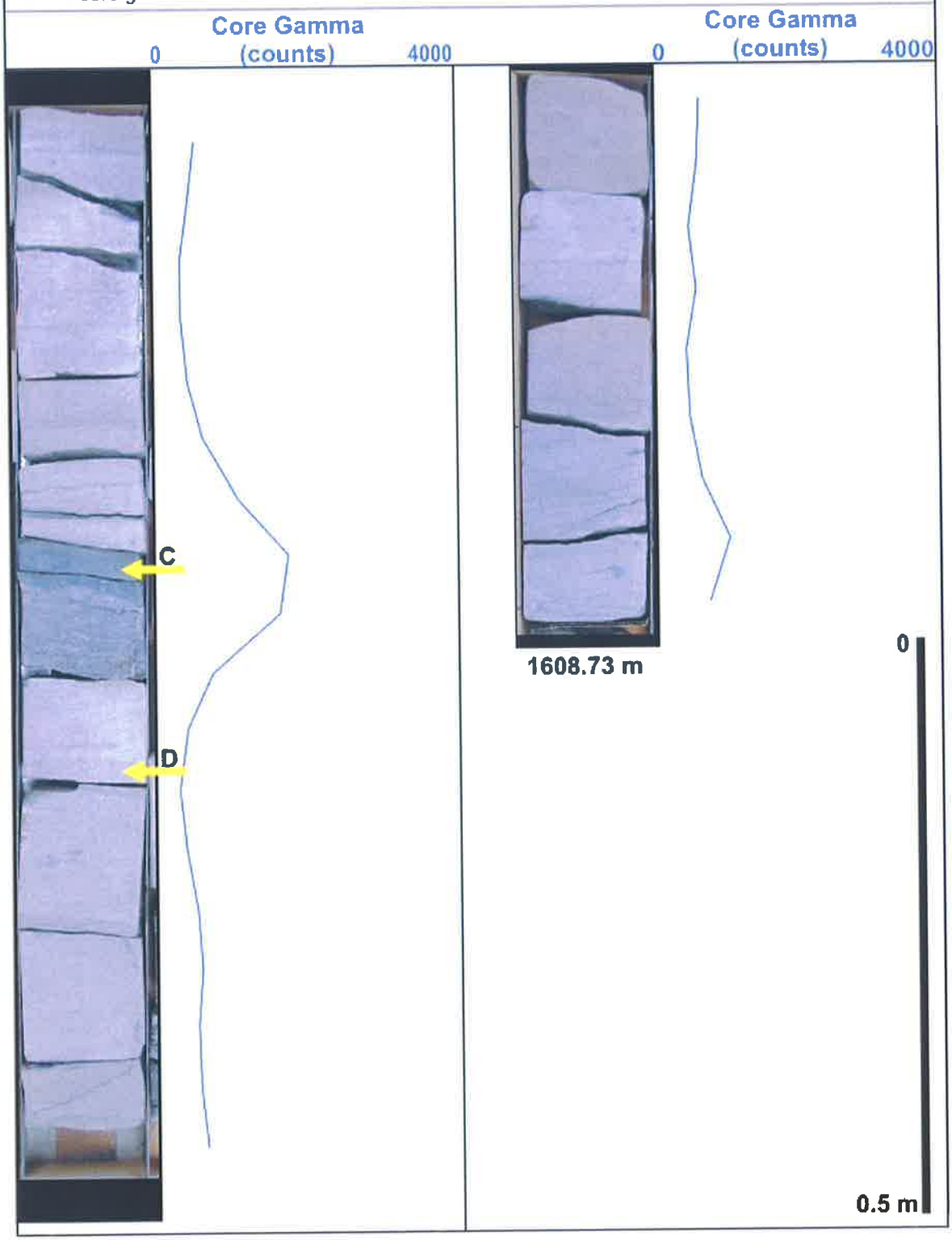

West Mereenie 1 core 8 (1 of 1)

Goyder Formation 1677.01 m - 1677.62 m

Note - core gamma is not in API units.

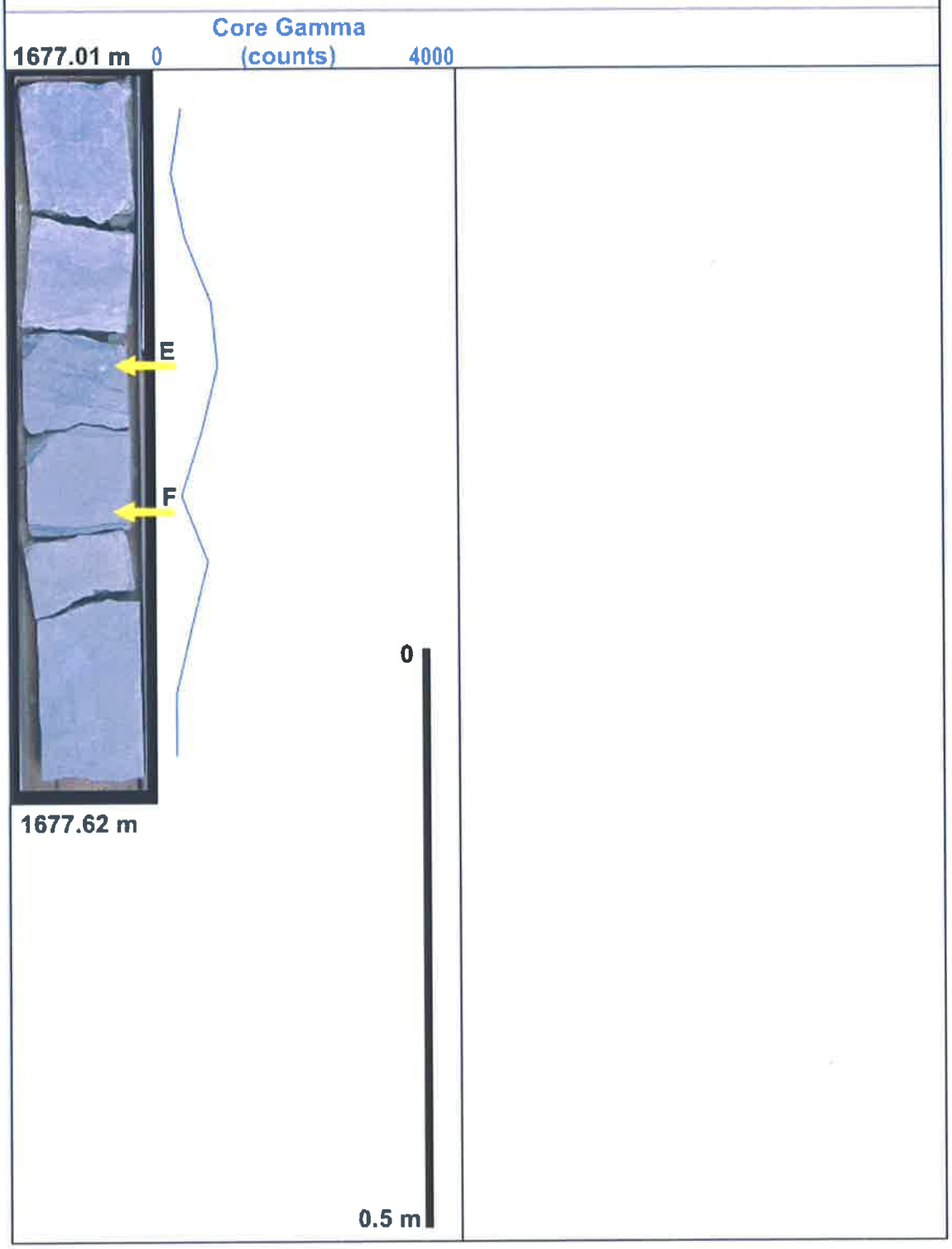

Appendix D

Clay Content Testing: West Mereenie 1

Clay content testing was conducted on four samples from the Goyder Formation by CSIRO Land and Water. The tests were used to calibrate core gamma response to clay content and thereby produce a reasonable Vshale log for the Mereenie sub-thrust fault seal analysis. MICP tests were then conducted on each sample (Appendix E) to assess maximum potential hydrocarbon column heights as part of the assessment of the Mereenie sub-thrust play.

The fraction of a sample less than 2 μm is considered to be an accurate estimate of clay content. A description of the procedure for clay content testing by CSIRO follows:

Approximately 10g of each sample were shaken for 10 minutes with 10ml of a 10% solution of sodium hexametaphosphate and deionised water. The slurries were repeatedly dispersed (using ultrasonic agitation) and centrifuged to recover all of the <2μm fractions. Both fractions were flocculated with NaCl followed by calcium saturation twice (using 1M CaCl2), washed with deionized water then alcohol and oven dried at 60°C.

Borehole	Depth (feet)	Lithology (visual)	%<2 μm
West Mereenie 1	5258'7"	Siltstone	13.5
West Mereenie 1	5268'10"	Siltstone	15.8
West Mereenie 1	5267'8"	Sandstone	2.9
West Mereenie 1	5270'8"	Sandstone	2.7

Appendix E

MICP Results: West Mereenie 1

The sealing capacity of a rock sample can be determined from the pore size distribution using mercury porosimetry known as MICP (Downey, 1984; Purcell, 1949; Schowalter, 1979). The MICP testing in this study was conducted on two sandstone samples and two siltstone samples of the Goyder Formation using a Micrometrics Autopore-III porosimeter (Bentley, 2000). The tested samples were cut into a cube approximately 1 cm^3, thoroughly cleaned, epoxy resinated on five of the six faces and then oven dried at 60°C for 72 hours prior to testing. Each sample was tested to a maximum of 60 000 psia to derive the threshold and entry pressures as shown in the following charts. As pressure increases, the mercury porosimeter senses the intrusion volume of mercury by the change in capacitance between the mercury column and a metal sheath surrounding the stem of the penetrometer. As the mercury column shortens, the pressure and volume data are continuously acquired by an attached computer. The results have been used in conjunction with published information on the Pacoota Sandstone to determine maximum potential hydrocarbon column heights due to juxtaposition seal as part of the assessment of the Mereenie sub-thrust play (Havord, 1991; Schowalter, 1979).

Laboratory air/mercury pressures may be converted to the brine/hydrocarbon system allowing seal capacity and column heights to reflect reservoir conditions. The following modification of Jurin's law (Washburn, 1921) gives the capillary pressures (P_c) required to intrude pore throats of diameter d for the air-mercury system:

$$P_c d = 4 \gamma \cos \theta$$

Where γ is interfacial tension and θ is the contact angle between fluid and solid measured through the denser phase (Vavra et al., 1992). The values for the air-mercury system can then be converted to the reservoir brine-hydrocarbon system (P_{bh}) using:

$$P_{bh} = P_c (\gamma_h \mathrm{Cos}\theta_h) / (\gamma \mathrm{Cos}\theta)$$

Where γ_h and $\mathrm{Cos}\theta_h$ are the interfacial tension and contact angle for the rock-brine –hydrocarbon system. The maximum hydrocarbon column height each rock type can hold before seal leakage (Hmax) is given by:

$$H_{max} = P_{DS} - P_{DR}/(\rho_b - \rho_{hc}) * 0.433$$

Where P_{DS} is the brine/hydrocarbon displacement pressure of the seal, P_{DR} is the brine/hydrocarbon displacement pressure of the reservoir, ρ_b is the brine density and ρ_{hc} is the hydrocarbon density (Dewhurst et al., 2002; Schowalter, 1979).

Initial pressure increases result in mercury entering surface voids and any fractures that may be within the sample and is termed the conformance. Any conformance is subtracted from the final calculations of pore volume. The entry pressure is the pressure at which mercury begins to penetrate the pores of a rock. Threshold pressure is considered to be the pressure at which a continuous filament of mercury extends through the sample. Threshold pressure is determined from the lower inflection point on the capillary pressure curve or the large gradient increase on the first derivative of the capillary pressure curve.

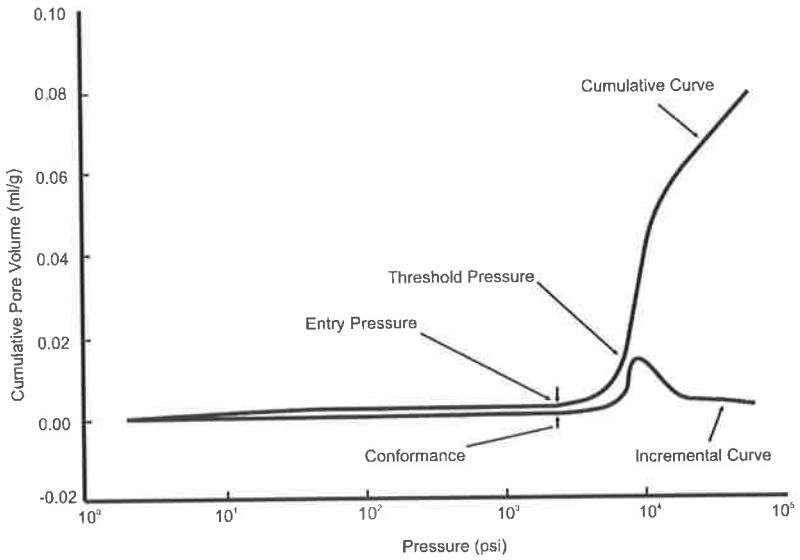

Example of a mercury injection capillary pressure curve displaying location of entry pressure, threshold pressure and conformance (Dewhurst et al., 2002).

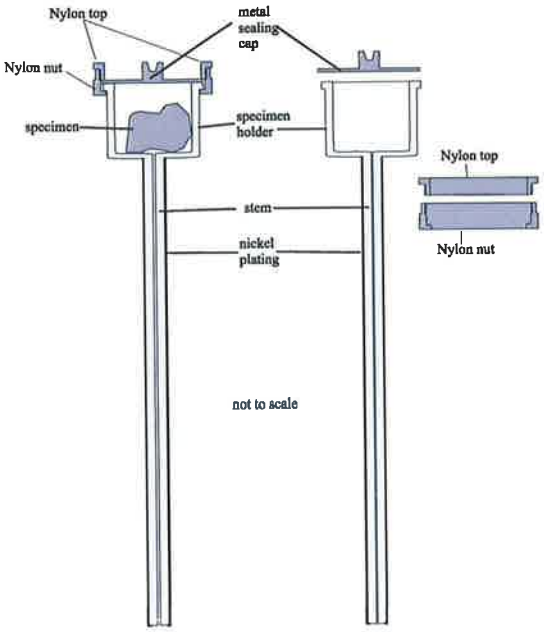

Left; the Micromeritics Autopore 9410 mercury injection porosimeter. Right; schematic view of an assembled penetrometer and the component parts (Bentley, 2000).

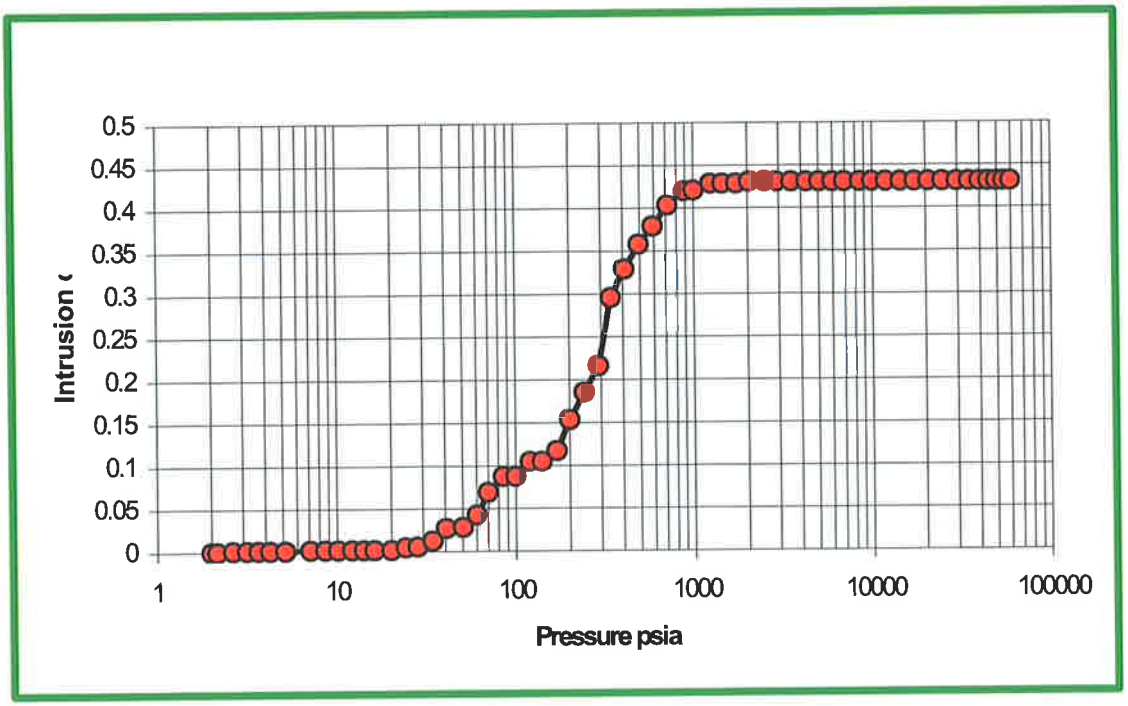

West Mereenie 1

5267'8"

Goyder Formation

Porosity = 11.07%

Density = 2.7959 g/cc

Sandstone

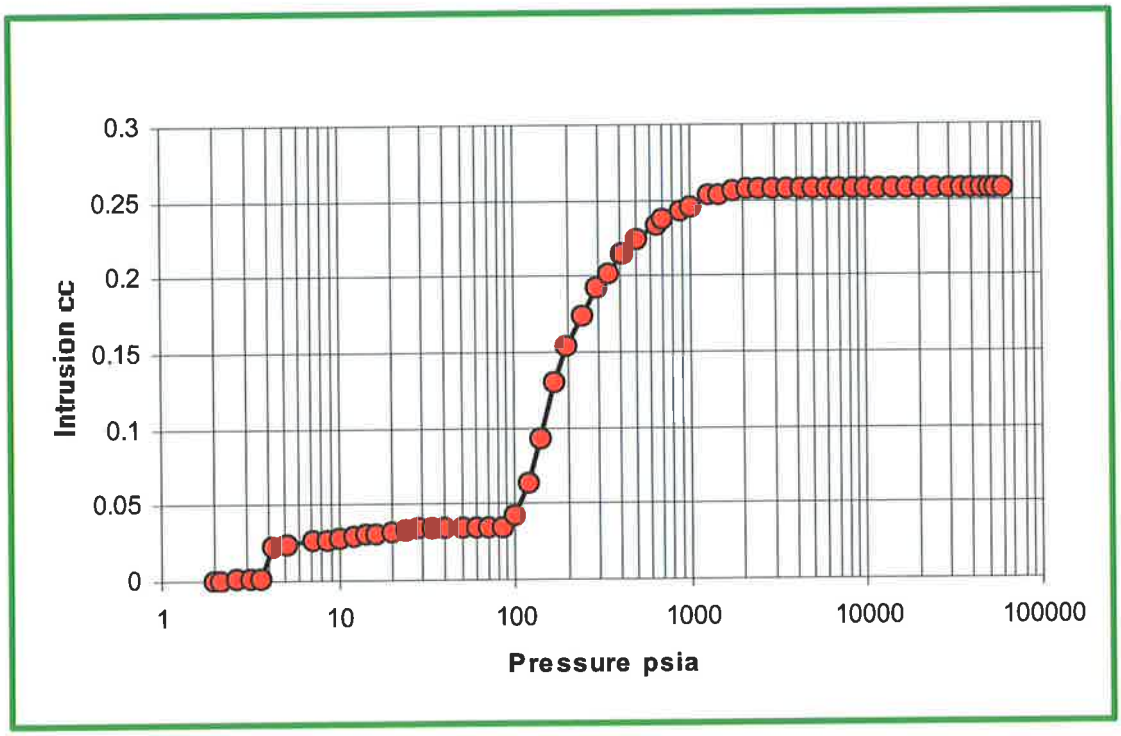

West Mereenie 1

5270'8"

Goyder Formation

Porosity = 6.7262%

Density = 2.6681 g/cc

Sandstone

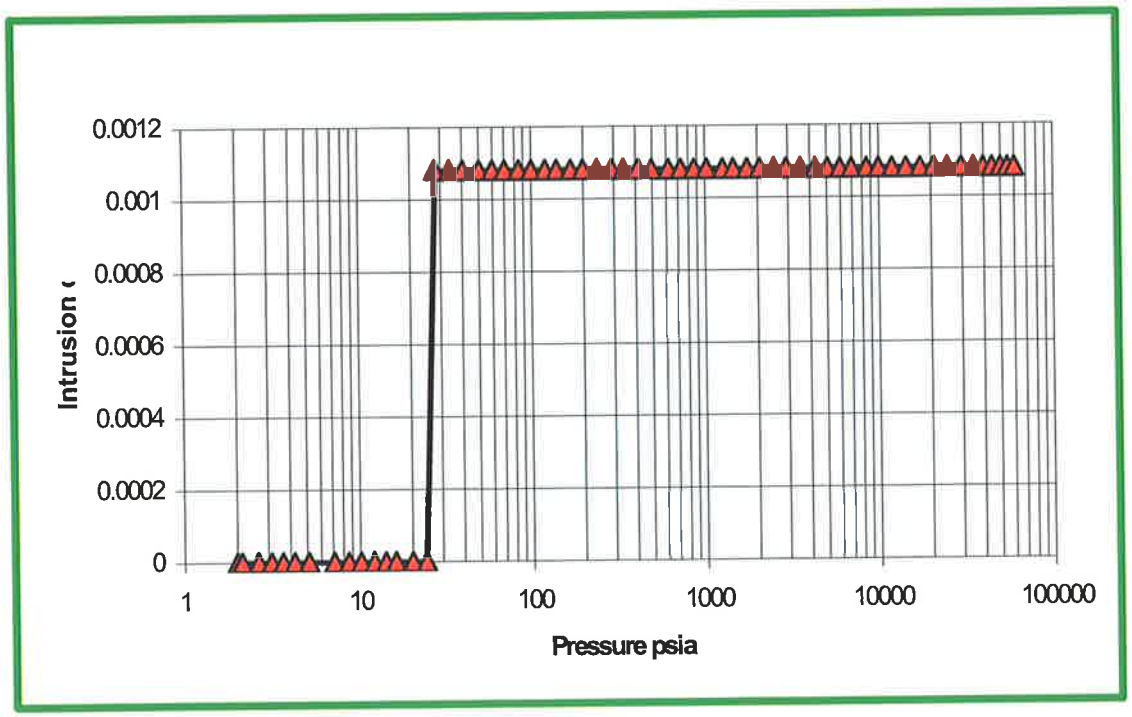

West Mereenie 1
5258'7"
Goyder Formation

Porosity = 0.0980%
Density = 2.6979 g/cc
Siltstone

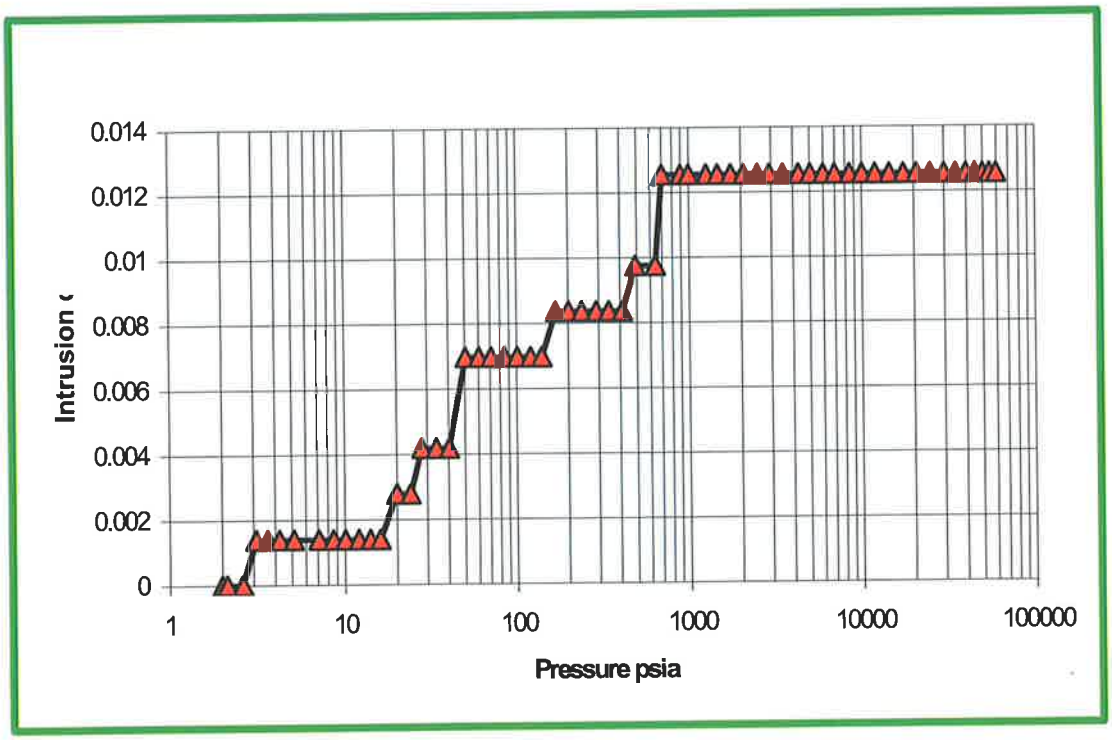

West Mereenie 1
5268'10"
Goyder Formation

Porosity = 0.3100%
Density = 2.6892 g/cc
Siltstone

Appendix F

Stress-Strain Testing of the Pacoota Sandstone: Mereenie and Palm Valley

Stress-strain testing has previously been conducted on Pacoota Sandstone samples from the Palm Valley Field (Stearns et al. 1996). Triaxial testing of Pacoota Sandstone samples from the Mereenie Field has been conducted as part of this study in order to compare mechanical properties of the Pacoota Sandstone between Mereenie and Palm Valley.

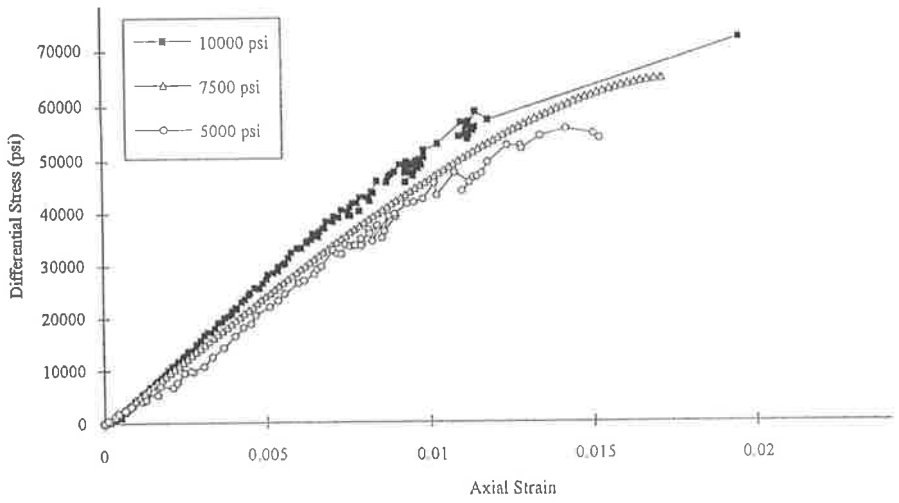

Multi-stage triaxial test results from a Pacoota Sandstone sample from Palm Valley tested at confining pressures of 5000, 7500 and 10000 psi (Stearns et al., 1996).

The following equations have been used to derive the cohesive strength and coefficient of friction from the stress-strain data (Table 9.1).

$S_n = 0.5(S_1+S_3) - 0.5(S_1-S_3)\ COS2\theta$

$S_s = 0.5(S_1-S_3)\ SIN2\theta$

CSIRO Confidential Report No. 04-050

August, 2004

Triaxial Testing of Quartzites from the Mereenie Field, Amadeus Basin

David N. Dewhurst

For Further information contact:

Dr Dave Dewhurst

CSIRO Petroleum

ARRC, 26 Dick Perry Ave,

Kensington, WA 6151, Australia

Telephone: +61-8-6436 8750

Email: david.dewhurst@csiro.au

SUMMARY

Triaxial tests were performed on two samples of quartzite from East Mereenie-4 in the Mereenie field, located in the Amadeus Basin, Northern Territory in order to compare them with previous strength tests run on samples from the nearby Palm Valley gas field. The quartzites tested from the Mereenie field are extremely strong rocks and were too strong to be tested at the confining pressures requested. Single stage triaxial tests were run at lower confining pressures in order to estimate a failure envelope for these samples. The cohesive strength of the quartzites was ~55 MPa with a friction coefficient of 0.79. Assuming a linear failure envelope, estimations were then made of peak strength for samples at the levels of confining pressure initially requested for these tests. These strengths ranged from ~340-450 MPa for the confining pressure range of ~34.5-69.0 MPa (5000-10,000 psi). Although the East Mereenie-4 samples are extremely strong, they are shown to be just slightly weaker than the equivalent rocks from the Palm Valley gas field.

INTRODUCTION

Triaxial tests were performed on two samples of quartzite from East Mereenie-4 in the Mereenie field, located in the Amadeus Basin, in the Northern Territory in order to compare them with previous strength tests run on samples from the nearby Palm Valley gas field (Stearns et al., 1996). The samples were extremely hard, low porosity, high density white quartzites, speckled with occasional red crystals that appear to be siderite.

TESTING EQUIPMENT

The rig used for shale testing comprises a high stiffness load frame, a triaxial cell and systems for cell and pore pressure control. Long-term stability of the control systems and instrumentation transducers is crucial for testing low permeability materials. The rig has full independent control of pore pressure, confining pressure and axial load, to the tune of 70 MPa, 70 MPa and 150 tonnes respectively. The inner diameter of the cell is considerably larger than the sample, allowing the installation of internal instruments such as a load cell, radial and axial displacement transducers, acoustic transducers and temperature sensors to directly measure sample response. The sample stack assembly includes:

- A specimen mounted between top and base platens, encased in a flexible, impermeable Viton membrane (0.75 mm thick), separating the confining fluid from the specimen.

- Two steel platens housing ultrasonic P- and S-wave elements with provision for pore pressure measurement at both ends of the specimen. Shallow grooves are engraved on the platen surfaces to distribute pore fluid evenly and allow testing without using a porous disk. The diameter of the platens is the same as that of the specimen (within ±0.05mm).

- Two diametrically positioned linear variable differential transformers (LVDT) clamped on the top and bottom platens to measure axial displacements.

- A load cell located underneath the bottom platen.

Long term stability of the cell and pore pressure systems is assured by using computer-controlled stepping motor pumps equipped with an uninterruptible power supply. Cell and pore pressure can be maintained within ±5 kPa of the target pressure over a period of a few months. With tests spanning extensive time periods, changes in temperature can be significant and may have considerable effects on the test results, particularly on pore pressure measurements. The cell and the loading frame are well insulated and the temperature control system is capable of maintaining a constant temperature within ±0.5°C over a period of a few months. The tests in this report were performed at room temperature. Cylindrical plugs of nominal 38 mm diameter and 76 mm length were provided. The tests were run in the

dry state in order to directly compare them with previous triaxial tests run on dry samples from the Palm Valley gas field (Stearns et al., 1996).

TEST PROCEDURE

Standard triaxial tests were run on two separate samples at different confining pressures (10 MPa, 15 MPa) to determine the geomechanical properties and failure envelopes for these two rocks (designated EM4/4708 and EM4/4717). Having achieved the desired confining pressure, the sample was loaded axially at a standard rate (0.2% of length per hour, equivalent to strain rate of ~ 5.5×10^{-7} s^{-1}), while stress and strain changes were monitored. Due to the presence and position of an ultrasonic array, it is not possible to use radial strain gauges during these tests.

RESULTS

The rocks tested here initially proved too strong for the initial confining pressures requested (5000, 7500 and 10,000 psi, equivalent to 34.48, 51.71 and 68.95 MPa). As such, the rocks were subjected to confining pressure of 34.48 MPa and axial stress to 300 MPa before it was realised that we would be unable to break them. However, the rocks

SAMPLE	EM4/4708	EM4/4717
Depth	4708'6"	4717'3"
ρ_b (g cm^{-3})	2.449	2.546
$(\sigma_1' - \sigma_3')_f$ (MPa)	275.82	259.50
P_f(MPa)	0 (dry)	0 (dry)
σ_3' (MPa)	15.00	10.00
σ_1' (MPa)	290.82	269.50
2θ	51.5°	51.5°
σ_f' (MPa)	67.25	59.00
τ_f (MPa)	108.08	101.55

Table 1. Stress conditions at failure for the East Mereenie-4 quartzites.

proved to be almost completely elastic, in that very little permanent deformation was recorded on unloading. While not an ideal situation for accuracy of tests results in that the samples may have been weakened, their elastic behaviour suggests that any such weakening is likely to be minor. Maximum axial stresses that could be safely tested were ~350 MPa. Low confining pressures were used in order to break the rocks at axial stresses below this level. This is not ideal on two counts as the points of failure on the failure envelope are very closely spaced and additionally, there are only two points with which to define the failure envelope. Ideally, four or more points would be preferred for this. Stress conditions at failure for these two samples are outlined in Table 1 above. The maximum and minimum principal stresses (σ_1 and σ_3 respectively) are determined directly during the test from axial loads and confining pressures. As pore pressure (P_f) is zero (samples were tested dry), the effective principal stresses are identical to the total stresses in this case. The angle between the failure surface and the maximum principal stress direction (θ) is measured directly on the sample after completion of the test and is an average of two

measurements (52° and 51°). The effective normal (σ'_f) and shear (τ_f) stresses on the failure surfaces were calculated from standard equations below:

$$\sigma'_f = \tfrac{1}{2}(\sigma'_1 + \sigma'_3) - \tfrac{1}{2}(\sigma'_1 - \sigma'_3)Cos2\theta \quad (1)$$

$$\tau_f = \tfrac{1}{2}(\sigma'_1 - \sigma'_3)Sin2\theta \quad (2)$$

Together with the values of the principal stresses, these values were used to define the failure envelope for these samples:

$$\tau = 54.85 + 0.79\sigma'_n \quad (3)$$

The cohesive strength of 54.85 MPa is extremely high compared to most reservoir rocks and the friction coefficient is at the high end of the range of 0.60-0.85 defined by Byerlee (1978) for a range of sedimentary, igneous and metamorphic rock types. These features are likely related to burial and cementation of these rocks. Mohr circles and the failure envelope for these rocks are shown in figure 1 below.

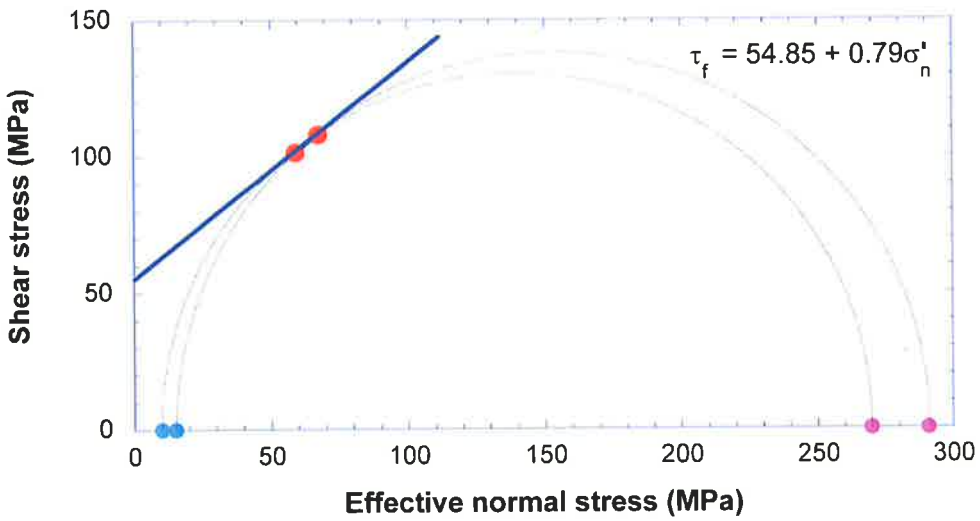

Figure 1. Mohr circles and failure envelope derived from triaxial tests on two samples of quartzite from the East Mereenie-4 well.

The initial aim of these tests was to determine the strength of these rocks at confining pressures of 5000, 7500 and 10,000 psi (34.48; 51.71 and 68.95 MPa). As this was not possible due to the constraints of the load cell and platens (see above), strengths at these confining pressures have been estimated from the failure envelope derived. The main assumption in these calculations is that the failure envelope remains linear across the whole stress range (up to 68.95 MPa). This may not be a good assumption as it is well known that rocks can become ductile and that failure envelopes can curve at high confining pressures. This means that the differential stress estimates presented below would be too high. On the basis that the assumption of linearity holds, then the differential stress at failure for high confining pressures can be calculated by inserting equations 1 and 2 above into equation 3. For example, for a confining pressure of 34.48 MPa (5000 psi), then:

$$\sigma'_f = \tfrac{1}{2}(\sigma'_1 + 34.48) - \tfrac{1}{2}(\sigma'_1 - 34.48)Cos51.5$$

so $\sigma'_f = 0.19\sigma'_1 + 27.95$ (4)

and:

$$\tau_f = \tfrac{1}{2}(\sigma'_1 - 34.48)Sin51.5$$

so $\tau_f = 0.39\sigma'_1 - 13.51$ (5)

We know from equation 3 above that:

$$\tau = 54.85 + 0.79\sigma'_n$$

Hence, inserting equations 4 and 5 into equation 3, we get:

$$0.39\sigma'_1 - 13.51 = 54.85 + 0.79(0.19\sigma'_1 + 27.95)$$

so $0.24\sigma'_1 = 90.44$ MPa

and $\sigma'_1 = 376.84$ MPa.

Then to get the differential stress at failure, the confining pressure (34.48 MPa) must be subtracted, so as such, for a confining pressure of 34.48 MPa (5000 psi) and rounding to the nearest integer:

$\sigma_1' - \sigma_3' = 342$ MPa.

Similar calculations can be performed for the higher levels of confining pressure required for these tests at 51.71 and 68.95 MPa (7500 and 10,000 psi). The results of these calculations for the Mereenie field samples are displayed in the table below alongside those from the Palm Valley field taken from Figure 1 in Stearns et al., (1996) in order to compare strength data.

Confining Pressure (MPa/psi)	Differential Stress at Failure (MPa)	
	East Mereenie-4	Palm Valley
34.48/5000	342	377
51.71/7500	399	435
68.95/10,000	456	493

Table 2. Comparative differential stress at failure for different confining pressure conditions for the Mereenie and Palm Valley fields.

As can be seen from Table 2, the strength estimates for samples from East Mereenie-4 are slightly lower than those derived from the measurements made by Stearns et al., (1996) on the rocks from the Palm Valley gas field.

CONCLUSIONS

The quartzites tested from the Mereenie field are extremely strong rocks and were too strong to be tested at the confining pressures requested. Single stage triaxial tests were run at lower confining pressures in order to estimate a failure envelope for these samples. Assumptions and limitations here include that the two samples were lithologically similar and that the failure envelope was based only on two points derived during these tests. The cohesive strength of the quartzites was ~55 MPa with a friction coefficient of 0.79. Assuming a linear failure envelope, estimations were then made of peak strength for samples at the levels of confining pressure initially requested for these tests. These strengths ranged from ~340-450 MPa for the confining pressure range of ~34.5-69.0 MPa (5000-10,000 psi). Although the East Mereenie-4 samples are extremely strong, they are shown to be just slightly weaker than the equivalent rocks from the Palm Valley gas field.

Appendix G

Gaussian and Normal Curvature Histograms: Mereenie and Palm Valley

Normal and Gaussian curvature have been calculated from grids over the Mereenie and Palm Valley fields using Midland Valley 3D Move software. The grids are at approximately the same resolution defined by 1709 points over Mereenie and 6664 points over Palm Valley. The histograms below show the distribution of normal and Gaussian curvature over both fields. Mereenie is a tighter structure and thus has higher normal curvature. Palm Valley is a more dome shaped structure and has generally higher Gaussian curvature than Mereenie. Outliers within the Mereenie distribution significantly effect mean and median calculations of Gaussian curvature. The outliers in the Mereenie distribution are due to; 1) locally high curvature along the tight fold crest, and; 2) possible sampling issues.

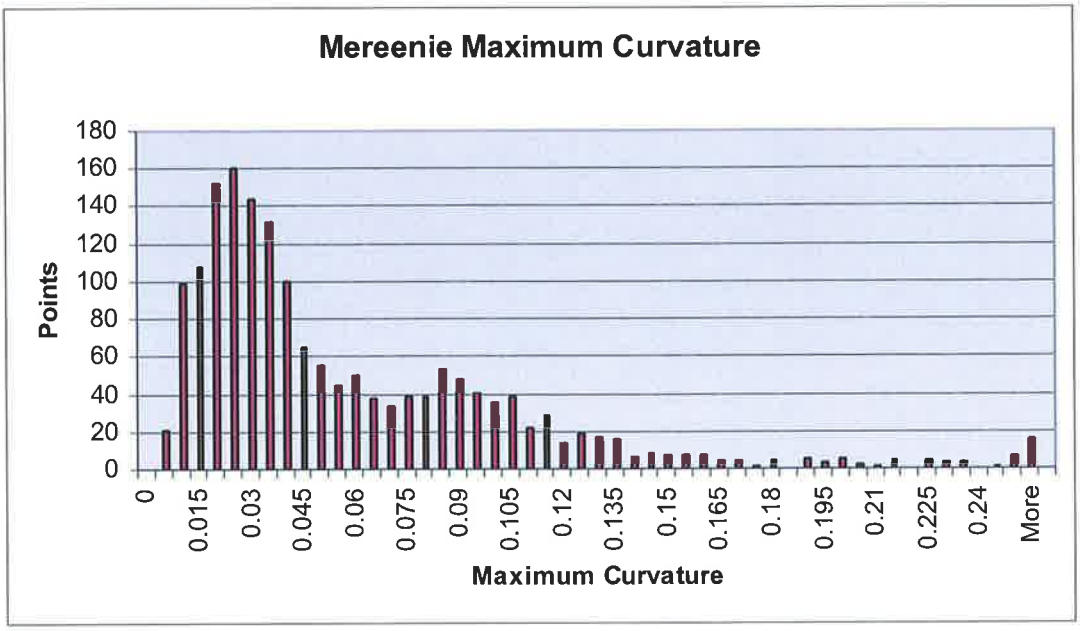

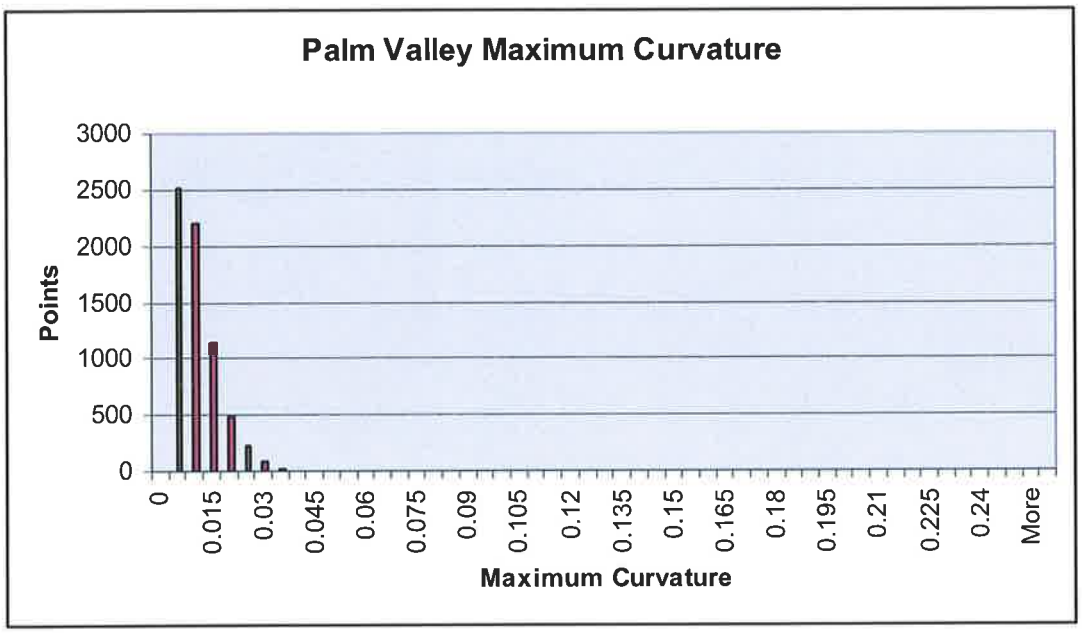

Histograms of normal (maximum) curvature over the Mereenie (top) and Palm Valley (bottom) fields (bin size 0.005). Curvature over both fields has been calculated using Midland Valley 3D Move software. The grid resolution over both fields is approximately equal with 1709 points over the Mereenie grid and 6664 points over the Palm Valley grid. Mereenie is a tighter structure than Palm Valley and therefore has significantly greater normal curvature.

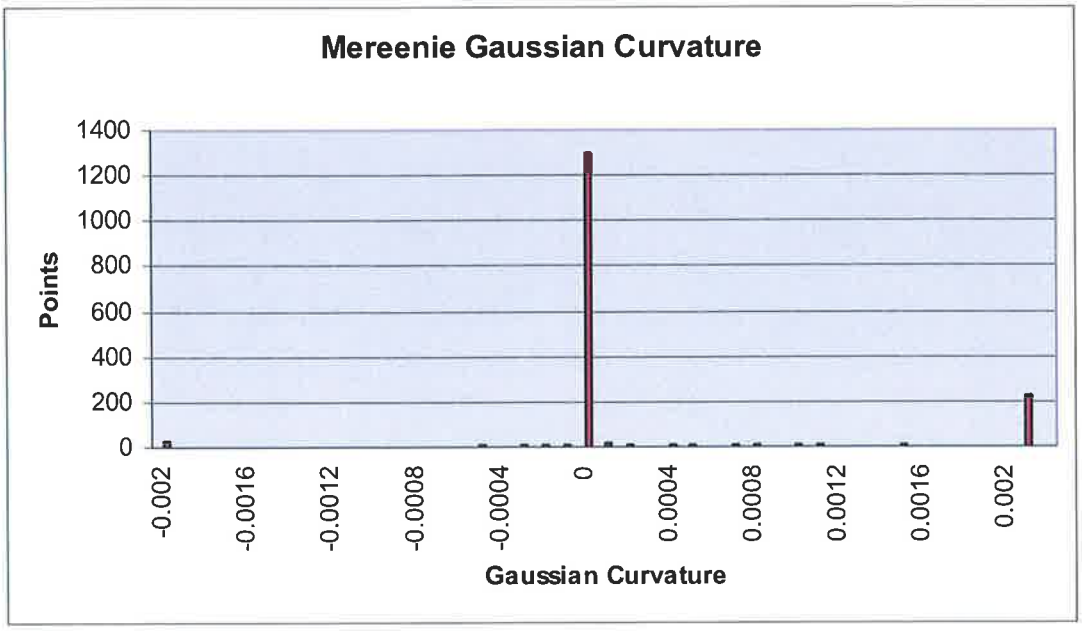

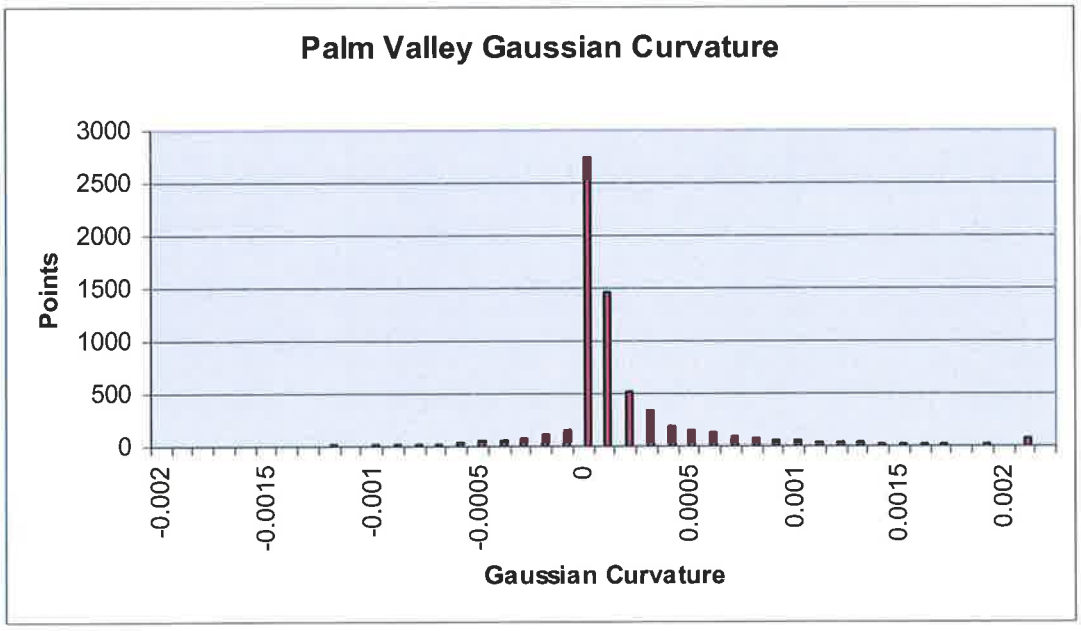

Histograms of Gaussian curvature over the Mereenie and Palm Valley fields (bin size 0.0001) using the same grids as for normal curvature. 75.2% of values over the Mereenie grid are nil compared to only 27.9% over the Palm Valley grid. There are also a significant amount outliers in the Mereenie distribution that strongly influence mean and median calculations.

References

Addis, M. A., 1997, Reservoir depletion and its effect on wellbore stability evaluation: International Journal of Rock Mechanics and Mining Sciences, v. 34, p. 3-4.

Aguilera, R., 1995, Naturally Fractured Reservoirs: Tulsa, PennWell Publishing Company, 522 p.

Allan, U. S., 1989, Model for hydrocarbon migration and entrapment within faulted structures: AAPG Bulletin, v. 73, p. 803-811.

Allmendinger, R. W., 1998, Inverse and forward modeling of trishear fault-propagation folds: Tectonics, v. 17, p. 640-656.

Allmendinger, R. W., 2003, Trishear research at Cornell, http://www.geo.cornell.edu/RWA/trishear/default.html.

Amadei, B., and O. Stephansson, 1997, Rock Stress and its Measurement: Cambridge, Chapman and Hall, 490 p.

Anderson, R. E., 1951, The Dynamics of Faulting and Dyke Formation with Applications to Britain: Edinburgh, Oliver and Boyd, 206 p.

Antonellini, M., and A. Aydin, 1994, Effect of faulting on fluid flow in porous sandstones: petrophysical properties: AAPG Bulletin, v. 78, p. 355-377.

Aydin, A., and A. M. Johnson, 1983, Analysis of faulting in porous sandstones: Journal of Structural Geology, v. 5, p. 19-31.

Baker, J. C., C. R. Fielding, P. De Caritat, and M. M. Wilkinson, 1993, Permian evolution of sandstone composition in a complex back-arc extensional to foreland basin. the Bowen Basin, Eastern Australia: Journal of Sedimentary Petrology, v. 63, p. 881-893.

Banks, C., J., and J. Warburton, 1986, "Passive-roof" duplex geometry in the frontal structures of the Kirthar and Sulaiman mountain belts, Pakistan.: Journal of Structural Geology, v. 8, p. 229-237.

Barker, C., 1990, Calculated volume and pressure changes during the thermal cracking of oil to gas in reservoirs: AAPG Bulletin, v. 74, p. 1254-1261.

Barton, C. A., D. Moos, and M. D. Zoback, 1997, In-situ stress measurements can help define local variations in fracture hydraulic conductivity at shallow depth: The Leading Edge, v. 16, p. 1653-1656.

Barton, C. A., M. D. Zoback, and D. Moos, 1995, Fluid flow along potentially active faults in crystalline rock: Geology, v. 23, p. 683-686.

Beaumont, C., 1981, Foreland basins: Geophysical Journal of the Royal Astronomical Society, v. 65, p. 291-329.

Becker, A., 1989, Detached neotectonic stress field in the northern Jura Mountains, Switzerland: Geologische Rundschau, v. 72, p. 459-475.

Becker, A., and M. R. Gross, 1996, Mechanism for joint saturation in mechanically layered rocks: an example from southern Israel: Tectonophysics, v. 257, p. 223-237.

Bell, J. S., 1996a, In situ stresses in sedimentary rocks (part 1): measurement techniques: Geoscience Canada, v. 23, p. 85-100.

Bell, J. S., 1996b, In situ stresses in sedimentary rocks (part 2): applications of stress measurements: Geoscience Canada, v. 23, p. 135-153.

Bell, J. S., and E. A. Babcock, 1986, The stress regime of the Western Canadian Basin and implications for hydrocarbon production: Bulletin of Canadian Petroleum Geology, v. 34, p. 364-378.

Benbow, D. D., and W. Lawson, 1967, East Mereenie No. 4 Well completion report, Exoil (N.T.) Pty Ltd (unpublished).

Bentley, C., 2000, Operating instructions for the Micromeritics Autopore 9410 Mercury Injection Porosimeter, Adelaide, University of South Australia, p. 1-24.

Berry, M. D., D. W. Stearns, and M. Friedman, 1996, The development of a fractured reservoir model for the Palm Valley gas field: APPEA Journal, v. 36, p. 82-103.

Bouvier, J. D., C. H. Kaars-Sijpesteijn, D. F. Kluesner, C. C. Onyejekwe, and R. C. Van der Pal, 1989, Three-dimensional seismic interpretation and fault sealing investigations, Nun River field, Nigeria: AAPG Bulletin, v. 73, p. 1397-1414.

Bradshaw, J., 1991, Description and depositional model of the Chandler Formation: a Lower Cambrian evaporite and carbonate sequence, Amadeus Basin, central Australia, *in* R. J. Korsch, Kennard, J. K., ed., Bureau of Mineral Resources Bulletin 236: Geological and geophysical studies in the Amadeus Basin central Australia, p. 227-244.

Bradshaw, J. D., and P. R. Evans, 1988, Palaeozoic tectonics, Amadeus Basin, Central Australia: APEA Journal, v. 28, p. 267-282.

Bretan, P., G. Yielding, and J. Jones, 2003, Using calibrated shale gouge ratio to estimate hydrocarbon column heights: American Association of Petroleum Geologists Bulletin, v. 87, p. 397-413.

Byerlee, J. D., 1978, Friction of rocks: Pure Applied Geophysics, v. 116, p. 615-626.

Caine, J. S., J. P. Evans, and C. B. Forster, 1996, Fault zone architecture and permeability structure: Geology, v. 24, p. 1025-1028.

Callow, I. P., and E. H. Briese, 2002, Groundwater inflow assessment - initial development Goonyella longwall development project (unpublished), p. 15.

Camacho, A., W. Compston, M. McCulloch, and I. McDougall, 1997, Timing and exhumation of eclogite facies shear zones, Musgrave Block, central Australia: Journal of Metamorphic Geology, v. 15, p. 735-751.

Campagna, D., and T. Flottmann, 2002, Field study of natural fractures in the Mereenie and Palm Valley fields, Northern Territory, central Australia (unpublished), Santos Ltd, p. 18.

Casey, D. A., 2000, Permeability Report BHP Coal, Boreholes 41870 & 41884 Goonyella Coal Mine (unpublished), Multiphase Technologies Pty. Ltd., p. 8.

Chanchani, S. K., M. D. Zoback, and C. Barton, 2003, A case study of hydrocarbon transport along active faults and production-related stress changes in the Monterey Formation, California, *in* M. Ameen, ed., Fracture and In-Situ Stress Characterization of Hydrocarbon Reservoirs, Geological Society of London. Special Publication 209, p. 17-26.

Chipperfield, S., 2004, After-closure analysis to identify naturally fractured reservoirs: SPE 90002.

Clarke, D., 1979, Heavitree Quartzite stratigraphy and structure near Alice Springs, N.T. (unpublished), Northern Territory Geological Survey, MBR 79/23.

Close, D., I. Scrimgeour, M. Hand, T. Flottmann, and C. Edgoose, 1998, A structural overview of the intracratonic Petermann Orogeny in the Northern Territory: Geologic Society of Australia, v. 49, p. 86.

Coblentz, D. D., M. Sandiford, R. M. Richardson, S. Zhou, and R. R. Hillis, 1995, The origins of the intraplate stress field in continental Australia: Earth and Planetary Science Letters, v. 133, p. 299-309.

Coblentz, D. D., S. Zhou, R. R. Hillis, R. M. Richardson, and M. Sandiford, 1998, Topography, boundary forces, and the Indo-Australian intraplate stress field: Journal of Geophysical Research, v. 103, p. 919-931.

Colmenares, L. B., and M. D. Zoback, 2002, A statistical evaluation of intact rock failure criteria constrained by polyaxial test data for five different rocks: International Journal of Rock Mechanics and Mining Sciences, v. 39, p. 695-729.

Cooke, M. L., P. N. Mollema, D. D. Pollard, and A. Aydin, 2000, Interlayer slip and joint localization in the East Kaibab Monocline, Utah: field evidence and results from numerical modelling, *in* J. W. Cosgrove, and M. S. Ameen, eds., Forced folds and fractures, Geological Society of London. Special Publication 169, p. 23-49.

Cooke, M. L., and C. A. Underwood, 2001, Fracture termination and step-over at bedding interfaces due to frictional slip and interface debonding: Journal of Structural Geology, v. 23, p. 223-238.

Cooper, M., 1996, Passive-roof duplexes and pseudo-passive-roof duplexes at mountain fronts: a review: Bulletin of Canadian Petroleum Geology, v. 44, p. 410-421.

Couples, G. D., H. Lewis, and G. P. W. Tanner, 1998, Strian partitioning during flexural-slip folding, *in* M. P. Coward, T. S. Daltaban, and H. Johnson, eds., Structural geology in reservoir characterization, Geological Society of London. Special Publication 127, p. 149-165.

Cowie, P., A., Knipe, R, J., Main, I, G., 1996, Introduction to the special issue: Journal of Structural Geology, v. 18, p. 1996.

Cullen, A. B., and J. D. Pigott, 1989, Post-Jurassic tectonic evolution of Papua New Guinea: Tectonophysics, v. 162, p. 291-302.

Cumella, S. P., S. Laubach, O. Ortega, A. Makowitz, and P. Rijken, 2002, Natural fracture and diagenetic controls on producibility of low permeability, Upper Cretaceous Williams Fork Formation sandstones, Piceance Basin, Colorado (abs), http://aapg.confex.com/aapg/hu2002/techprogram/paper_45136.htm.

Currie, J. B., H. W. Patnode, and R. P. Trump, 1962, Development of folds in sedimentary strata: Geological Society of America Bulletin, v. 73, p. 655-674.
Dahlen, F. A., and J. Suppe, 1988, Mechanics, growth and erosion of mountain belts: Geologic Society of America Special Paper, v. 218, p. 161-178.
Dahlstrom, C. D. A., 1969, Balanced cross sections: Canadian Journal of Earth Sciences, v. 6, p. 743-757.
Davis, D. M., and T. Engelder, 1985, The role of salt in fold and thrust belts: Tectonophysics, v. 119, p. 67-88.
Davis, G. H., and S. J. Reynolds, 1996, Structural Geology of Rocks and Regions: New York, John Wiley and Sons Inc, 776 p.
De Sitter, L. V., 1964, Structural Geology: New York, McGraw-Hill.
Dean, S. L., B. R. Kulander, and R. E. Williams, 1979, Regional tectonics, systematic fractures and photolinears in southeastern West Virginia: Proceedings of the 2nd International Conference on Basement Tectonics, p. 10-53.
Deckelman, J. A., 1991, Recognition of a fluvial facies in the Pacoota Sandstone and its implications for petroleum exploration, *in* R. J. Korsch, and J. K. Kennard, eds., Bureau of Mineral Resources Bulletin 236: Geological and geophysical studies in the Amadeus Basin central Australia, p. 285-301.
Dewhurst, D. D., R. M. Jones, and M. D. Raven, 2002, Microstructural and petrophysical characterisation of Muderong Shale: application to top seal risking: Petroleum Geoscience, v. 8, p. 371-383.
Dickins, J. M., and E. J. Malone, 1973, Geology of the Bowen Basin, Queensland: Bureau of Mineral Resources, Geology and Geophysics, Bulletin, v. 130, Bureau of Mineral Resources.
Do Rozario, R. F., 1991, The Palm Valley Gas Field, Amadeus Basin, central Australia, *in* R. J. Korsch, and J. K. Kennard, eds., Bureau of Mineral Resources Bulletin 236: Geological and Geophysical Studies in the Amadeus Basin Central Australia, p. 477-492.
Do Rozario, R. F., and B. W. Baird, 1987, The detection and significance of fractures in the Palm Valley gas field: APPEA Journal, v. 27, p. 264-280.
Downey, M. W., 1984, Evaluating seals for hydrocarbon accumulations: AAPG Bulletin, v. 68, p. 1752-1763.
DuBois, D. P., 2004, Jonah Field - development of a Rocky Mountain gas giant, http://www.wy.blm.gov/fluidminerals04/presentations/NFMC/059/DeanDubois_files/frame.htm.
Dunne, W. M., and C. P. North, 1990, Othogonal fracture systems at the limits of thrusting: an example from southwestern Wales: Journal of Structural Geology, v. 12, p. 207-215.
Eberhard, M., and M. Mullen, 2003, The effect of completion methodologies and production in the Jonah Field: SPE 84959.
Edgoose, J., 2000, Hydraulic fracture sediment stress measurement programme boreholes 41869 and 41871: report to BHP Coal Pty Ltd (unpublished), Multiphase Technologies Pty Ltd, p. 3.
Elliot, L. G., 1993, Post-Carboniferous tectonic evolution of eastern Australia: APEA Journal, v. 1993, p. 215-236.
Elphinstone, R., and J. D. Gorter, 1991, As the worm turns: implications of bioturbation on source rocks of the Horn Valley Siltstone, *in* R. J. Korsch, and J. K. Kennard, eds., Bureau of Mineral Resources Bulletin 236: Geological and geophysical studies in the Amadeus Basin central Australia, p. 317-332.
Enever, J. R., 1990, In situ stress measurements in the Bowen Basin and their implications for coal mining and methane extraction: Bowen Basin symposium 1990, p. 106-109.
Enever, J. R., 1993, Case studies of hydraulic fracture stress measurement in
Australia, *in* J. Hudson, A., ed., Comprehensive Rock Engineering, p. 497-532.
Enever, J. R., M. A. Bocking, and I. H. Clark, 1994a, The application of in-situ stress measurement and numerical stress analysis to coalbed methane exploration in Australia: SPE 28780, p. 373-381.
Enever, J. R., and R. G. Jeffrey, 2000, The relationship between stress in coal and rock: Pacific Rocks 2000, p. 409-414.
Enever, J. R., R. J. Walton, and C. R. Windsor, 1994b, Stress regime in the Sydney Basin and its implications for excavation design and construction: Tunnelling conference, p. 49-59.
Engelder, T., 1985, Loading paths to joint propagation during a tectonic cycle: an example from the Appalachian Plateau, U.S.A.: Journal of Structural Geology, v. 7, p. 459-476.
Engelder, T. J., 1974, Cataclasis and the generation of fault gouge: Geologic Society of America Bulletin, v. 85, p. 1515-1522.
Erslev, E. A., 1991, Trishear fault-propagation folding: Geology, v. 19, p. 617-620.
Esterle, J., and R. Sliwa, 2002, Supermodel 2000 Bowen Basin, CSIRO Exploration and Mining, p. 196.

Evans, K. F., T. Engelder, and R. A. Plumb, 1989, Appalachian stress study 1. A detailed description of in situ stress variations in Devonian shales of the Appalachian Plateau: Journal of Geophysical Research, v. 94, p. 7129-7154.
Fergusson, C. L., 1991, Thin-skinned thrusting in the northern New England Orogen, central Queensland, Australia: Tectonics, v. 10, p. 797-806.
Fielding, C. R., A. J. Falkner, J. Kassan, and J. J. Draper, 1990, Permian and Triassic depositional systems in the Bowen Basin: Bowen Basin Symposium 1990, p. 21-25.
Fielding, C. R., R. Sliwa, R. J. Holcombe, and A. T. Jones, 2001, A new Palaeogeographic synthesis for the Bowen, Gunnedah and Sydney basins of eastern Australia: PESA Eastern Australian Basin Symposium, v. 2001, p. 269-279.
Fielding, C. R., C. J. Stephens, J. Kassan, and R. J. Holcombe, 1995, Revised palaeogeographic maps for the Bowen Basin, central Queensland, *in* I. L. Follington, J. W. Beeston, and L. H. Hamilton, eds., Bowen Basin Symposium 1995: Mackay, p. 7-15.
Finch, R. W., J. L. Skees, W. W. Aud, J. L. Johnson, C. Esphahanian, and J. T. Hansen, 1996, Evolution of completion and fracture stimulation practices in the Jonah Field, Sublette County, WY: SPE 36734.
Fisher, Q. J., and R. J. Knipe, 1998, Fault sealing processes in siliciclastic sediments, *in* G. Jones, Fisher, Q, J., Knipe, R, J., ed., Faulting, fault sealing and fluid flow in hydrocarbon reservoirs, The Geological Society of London. Special Publication 147, p. 117-134.
Fisher, Q. J., R. J. Knipe, and R. H. Worden, 2004, Microstructures of deformed and undeformed sandstones from the North Sea: implications for the origins of quartz cement in sandstones, *in* R. Worden, and S. Morad, eds., Quartz cement: origin and effects on hydrocarbon reservoirs, v. Special Publication, Internation Association of Sedimentology.
Flottmann, T., 2003, Natural Fractures and Fractured Reservoirs (unpublished), Santos, p. 161.
Flottmann, T., and M. Hand, 1999, Folded basement-cored tectonic wedges along the northern edge of the Amadeus Basin, Central Australia: evaluation of orogenic shortening: Journal of Structural Geology, v. 21, p. 399-412.
Flottmann, T., M. Hand, D. Close, C. Edgoose, and I. Scrimgeour, 2004, Thrust tectonic styles of the intracratonic Alice Springs and Petermann Orogenies,central Australia: AAPG Bulletin.
Flottmann, T., D. Taylor, and D. Campagna, 2002, Structure, in-situ stress and natural fracture permeability, Scotia field, eastern Queensland (unpublished), Santos Ltd, p. 25.
Forman, D. J., E. N. Milligan, and W. R. McCarthy, 1967, Regional geology and structure of the northeast margin, Amadeus Basin, Bureau Mineral Resources Geology and Geophysics Australia Report 103.
Fossen, H., and J. Hesthammer, 2000, Possible absence of small faults in the Gullfaks Field, northern North Sea: implications for downscaling of faults in some porous sandstones: Journal of Structural Geology, v. 22, p. 851-863.
Fulljames, J. R., L. J. J. Zijerveld, R. C. M. W. Franssen, G. M. Ingram, and P. D. Richard, 1996, Fault seal processes: Hydrocarbon Seals - Importance for Exploration and Production, p. 5.
Gibson, H. J., G. Ambrose, I. R. Duddy, P. R. Tingate, and T. Marshall, 2004, Post-Early Carboniferous thermal history reconstruction from well data in the Amadeus Basin, central Australia: APPEA Journal, v. 44, p. 357-384.
Gil, J. A., and M. J. Jurado, 1998, Geological interpretation and numerical modelling of salt movement in the Barbastro-Balaguer anticline, southern Pyrenees: Tectonophysics, v. 293, p. 141-155.
Golder, 2001, Fracman, http://fracman.golder.com/.
Goleby, B. R., B. J. Drummond, R. J. Korch, B. J. Willcox, G. W. O'Brien, and K. D. Wake-Dyster, 1994, Review of recent results from continental deep seismic profiling in Australia: Tectonophysics, v. 232, p. 1-12.
Goleby, B. R., R. D. Shaw, C. Wright, B. L. N. Kennett, and K. Lambeck, 1989, Geophysical evidence for 'thick-skinned' crustal deformation in central Australia: Nature, v. 337, p. 325-330.
Gray, I., 1987, Reservoir engineering in coal seams: Part 1. the physical process of gas storage and movement in coal seams: SPE Reservoir Engineering, v. 2, p. 28-34.
Griffiths, P. A., S. Jones, N. Salter, F. Schaefer, R. Osfield, and H. Reiser, 2002, A new technique for 3-D flexural-slip restoration: Journal of Structural Geology, v. 24, p. 773-782.
Gronseth, J. M., 1982, Determination of the instantaneous shut-in pressure from hydraulic fracturing data and its reliability as a measure of the minimum principal stress, *in* R. Goodman, E., Heuze, F, E., ed., The 23rd U.S. Symposium on Rock Mechanics, New York, Society of Mining Engineers, p. 183-189.
Gronseth, J. M., and P. R. Kry, 1982, Instantaneous shut in pressure and its

relationship to the minimum in situ stress: Proceedings workshop XVII; workshop on hydraulic fracturing stress measurements, p. 147-166.
Hamilton, P. J., P. J. Eadington, and M. Lisk, 1991, Fluid history analysis of mineralised fractures and host sandstones in Palm Valley-7 core (unpublished), CSIRO Division of Exploration Geoscience, for Magellan Petroleum Australia Limited.
Hammond, R., and C. W. Mallett, 1987, A tectonic framework for coal measure deformation in the southern Bowen Basin: 21st Newcastle symposium on: advances in the study of the Sydney Basin., p. 193-196.
Hand, M., and M. Sandiford, 1999, Intraplate deformation in central Australia, the link between subsidence and fault reactivation: Tectonophysics, v. 305, p. 121-140.
Hardy, S., and M. Ford, 1997, Numerical modeling of trishear fault propagation folding: Tectonics, v. 16, p. 841-854.
Harpalani, S., and G. Chen, 1992, Effect of gas production on porosity and permeability of coal: Symposium on Coalbed Methane.
Harpalani, S., and G. Chen, 1999, Positive impact of gas production induced stress and strain on coal permeability: 9th International Congress on Rock Mechanics, p. 291-294.
Harris, J. F., G. L. Taylor, and J. L. Walper, 1960, Relation of deformational structures in sedimentary rocks to regional and local structure: AAPG Bulletin, v. 44, p. 1853-1873.
Hart, B. S., T. Engler, R. Pearson, and R. L. Robinson, 2002, 3-D seismic horizon-based approaches to fracture-swarm sweet spot (abs), http://aapg.confex.com/aapg/hu2002/techprogram/paper_44683.htm.
Havord, P. J., 1991, Mereenie Oil and Gas Field, Amadeus Basin, Northern Territory, *in* R. J. Korsch, Kennard, J. M., ed., Bureau of Mineral Resources Bulletin 236: Geological and Geophysical Studies in the Amadeus Basin Central Australia, v. 236, p. 493-510.
Henderson, R. A., B. K. Davis, and C. M. Fanning, 1998, Stratigraphy, age relationships and tectonic setting of rift-phase infill in the Drummond Basin, central Queensland: Australian Journal of Earth Sciences, v. 45, p. 579-595.
Hennings, P. H., J. E. Olson, and L. B. Thompson, 2000, Combined outcrop data and three-dimensional structural models to characterize fractured reservoirs: an example from Wyoming.: AAPG Bulletin, v. 84, p. 830-849.
Hillis, R. R., 1998, The influence of fracture stiffness and the in situ stress field on the closure of natural fractures: Petroleum Geoscience, v. 4, p. 57-65.
Hillis, R. R., 2001, Coupled changes in pore pressure and stress in oil fields and sedimentary basins: Petroleum Geoscience, v. 7, p. 419-425.
Hillis, R. R., J. R. Enever, and S. D. Reynolds, 1999a, In situ stress field of eastern Australia: Australian Journal of Earth Sciences, v. 46, p. 813-825.
Hillis, R. R., J. J. Meyer, and S. D. Reynolds, 1998, The Australian stress map: Exploration Geophysics, v. 29, p. 420-427.
Hillis, R. R., and S. D. Mildren, 1995, The contemporary stress regime of the Mereenie Field: implications for the stability of horizontal wells and the orientation of natural and hydraulically-induced fractures (unpublished), University of Adelaide; for Santos Ltd, p. 1-32.
Hillis, R. R., S. D. Mildren, J. J. Meyer, and T. Flottmann, 1999b, In situ stress and natural fracturing in the Mereenie Field: implications for field development (unpublished), National Centre for Petroleum Geology and Geophysics; for Santos Ltd., p. 36.
Hobbs, B. E., W. D. Means, and P. F. Williams, 1976, An Outline of Structural Geology: Brisbane, John Wiley and Sons, 571 p.
Hoek, E., and E. T. Brown, 1980, Underground Excavations in Rock: London, Institute of Mining and Metallurgy, 527 p.
Holcombe, R. J., T. A. Little, R. Sliwa, and C. R. Fielding, 1993, Tectonic elements and evolution of southeast Queensland during the Late Palaeozoic to Early Mesozoic: New England Orogen, Eastern Australia, p. 517-527.
Holcombe, R. J., C. J. Stephens, C. R. Fielding, D. Gust, T. A. Little, R. Sliwa, J. R. Kassan, J. McPhie, and A. Ewart, 1997a, Tectonic evolution of the northern New England Fold Belt: the Permian-Triassic Hunter-Bowen event, *in* P. M. Ashley, and P. G. Flood, eds., Tectonics and metallogenesis of the New England Orogen, Geological Society of Australia. Special Publication 19, p. 52-65.
Holcombe, R. J., C. J. Stephens, C. R. Fielding, D. Gust, T. A. Little, R. Sliwa, J. McPhie, and A. Ewart, 1997b, Tectonic evolution of the northern New England Fold Belt: Carboniferous to Early Permian

transition from active accretion to extension, Tectonics and Metallogenesis of the New England Orogen, Geological Society of Australia. Special Publication 19, p. 66-79.
Houze, O. R., R. N. Horne, and H. J. Ramey Jr, 1988, Pressure transient response of an infinite-conductivity vertical fracture in a reservoir with double-porosity behaviour: SPE 12778.
Hugman, R. H. H., and M. Friedman, 1979, Effects of texture andcomposition on mechanical behaviour of experimentally deformed carbonate rock: AAPG Bulletin, v. 63, p. 1478-1489.
Huiqi, L., K. R. McClay, and C. M. Powell, 1992, Physical models of thrust wedges, *in* K. McClay, R, ed., Thrust Tectonics: New York, Chapman and Hall, p. 71-81.
Hull, J., 1988, Thickness-displacement relationships for deformation zones: Journal of Structural Geology, v. 10, p. 431-435.
Jackson, K. S., D. M. McKirdy, and J. A. Deckelman, 1984, Hydrocarbon generation in the Amadeus Basin, central Australia: APEA Journal, v. 24, p. 42-65.
Jaeger, J. C., and N. G. W. Cook, 1969, Fundamentals of Rock Mechanics: London, Chapman and Hall, 593 p.
Johnson, R. L., T. Flottmann, and D. J. Campagna, 2002, Improving results of coalbed methane development strategies by integrating geomechanics and hydraulic fracture technologies: SPE 77824, p. 1-13.
Jones, B. G., 1991, Fluvial and lacustrine facies in the Middle to Late Devonian Pertnjara Group, Amadeus Basin, Northern Territory, and their relationship to tectonic events and climate, *in* R. J. Korsch, Kennard, J. K., ed., Bureau of Mineral Resources Bulletin 236: Geological and geophysical studies in the Amadeus Basin central Australia, p. 333-348.
Jones, M. A., A. B. Pringle, I. M. Fulton, and S. O'Neill, 1999, Discrete fracture network modelling applied to groundwater resource exploitation in southwest Ireland, *in* K. J. W. McCaffrey, Lonergan, L., Wilkinson, J. J., ed., Fractures, fluid flow and mineralization, Geological Society of London. Special Publication 155, p. 83-103.
Jones, R. M., and R. R. Hillis, 2003, An integrated, quantitative approach to assessing fault-seal risk: AAPG Bulletin, v. 87, p. 507-524.
Jordan, T. E., 1981, Thrust loads and foreland basin evolution, Cretaceous, western United States: AAPG Bulletin, v. 65, p. 2506-2520.
Kattenhorn, S. A., A. Aydin, and D. D. Pollard, 2000, Joints at high angles to normal fault strike: an explanation using 3-D numerical models of fault-perturbed stress fields: Journal of Structural Geology, v. 22, p. 1-23.
Kennard, J. M., and J. F. Lindsay, 1991, Sequence stratigraphy of the latest Proterozoic-Cambrian Pertaoorrta Group, *in* R. J. Korsch, and J. K. Kennard, eds., Bureau of Mineral Resources Bulletin 236: Geological and Geophysical Studies in the Amadeus Basin Central Australia, p. 171-194.
Knipe, R. J., G. Jones, and Q. J. Fisher, 1998, Faulting, fault sealing and fluid flow in hydrocarbon reservoirs: an introduction, *in* G. Jones, Fisher, Q. J., Knipe, R. J., ed., Faulting, fault sealing and fluid flow in hydrocarbon reservoirs, Geological Society of London. Special Publication 147, p. vii-xxi.
Knott, S. D., A. Beach, P. J. Brockbank, L. J. Brown , J. E. McCallum, and A. I. Welbon, 1996, Spatial and mechanical controls on normal fault populations: Journal of Structural Geology, v. 18, p. 359-372.
Korsch, R. J., C. J. Boreham, J. M. Totterdell, R. D. Shaw, and M. G. Nicoll, 1998, Development and petroleum resource evaluation of the Bowen, Gunnedah and Surat basins, eastern Australia: APPEA Journal 1998, v. 38, p. 199-236.
Korsch, R. J., and J. F. Lindsay, 1989, Relationship between deformation and basin evolution in the intracratonic Amadeus Basin, central Australia: Tectonophysics, v. 158, p. 5-22.
Korsch, R. J., and J. M. Totterdell, 1995a, Permian and Mesozoic tectonic and structural events in the Bowen and Surat basins and New England Orogen, southwest Pacific rim: PACRIM 95, p. 305-310.
Korsch, R. J., and J. M. Totterdell, 1995b, Structural events and deformation styles in the Bowen Basin: Bowen Basin Symposium 1995, p. 27-35.
Korsch, R. J., K. D. Wake-Dyster, and D. W. Johnstone, 1992, Seismic imaging of Late Palaeozoic-Early Miocene extensional and contractional structures in the Bowen and Surat basins, eastern Australia: Tectonophysics, v. 215, p. 273-294.
Krystinik, L., J. Lorenz, S. Sturn, and W. Clark, 1999, Exploiting tight gas sand sweet spots, http://www.pttc.org/solutions/109.pdf.
Krystinik, L. F., F. Lim, and J. C. Lorenz, 2000, Hunting fractures three miles down: integrated reservoir geology, drilling and production for the UPR/DOE Rock Island 4-H well, Frontier Formation, southwest Wyoming: 2000 AAPG Annual Meeting.

Labaume, P., S. Sheppard, and I. Moretti, 2000, Structure and hydraulic behavior of cataclastic thrust fault zones in sandstones, Sub-Andean Zone, Bolivia: Journal of Geochemical Exploration, v. 69-70, p. 487-492.
Laubach, S., 2003a, Natural fractures among keys to developing unconventional gas, http://www.pttc.org/columns/aogrcojan03.htm.
Laubach, S. E., 2003b, Practical approaches to identifying sealed and open fractures: AAPG Bulletin, v. 87, p. 561-579.
Laubach, S. E., R. A. Marrett, J. E. Olson, and A. R. Scott, 1998, Characteristics and origins of coal cleat: a review: International Journal of Coal Geology, v. 35, p. 175-207.
Laubach, S. E., J. E. Olson, and J. F. W. Gale, 2004, Are open fractures necessarily aligned with maximum horizontal stress?: Earth and Planetary Science Letters, v. 222, p. 191-195.
Law, B. E., 1993, The relationship between coal rank and cleat spacing: implications for the prediction of permeability in coal: International Coalbed Methane Symposium, p. 435-441.
Lawrence, P., 1998, Seismic attributes in the characterization of small-scale reservoir faults in Abqaiq field: The Leading Edge, v. 17, p. 521-525.
LeBlanc Smith, G., and J. Esterle, 1998, Sedimentary and structural geology assessment for potential underground mining sites: Eureka and Goonyella No2 areas Goonyella Riverside Mine (unpublished), CSIRO Mining and Exploration, p. 150.
Lee, M., M. Hand, and J. Foden, 2002, Contrasting sources of Palaeozoic mafic dykes emplaced during early Palaeozoic rifting in central Australia: Geoscience 2002: Expanding Horizons, p. 124.
Levine, J. R., 1996, Model study of the influence of matrix shrinkage on absolute permeability of coal bed reservoirs, *in* R. Gayer, Harris, I., ed., Coalbed Methane and Coal Geology, v. No 109, Geological Society Special Publication, p. 197-212.
Lie Hui, Z., and F. Yi Yong, 1998, Water breakthrough numerical simulation in fractured gas reservoirs: SPE 39551.
Lindsay, J. F., 1987, Sequence stratigraphy and depositional controls in Late Proterozoic-Early Cambrian sediments of Amadeus Basin, central Australia: AAPG Bulletin, v. 71, p. 1387-1403.
Lindsay, J. F., and R. J. Korsch, 1991, The evolution of the Amadeus Basin, central Australia, *in* R. J. Korsch, and J. K. Kennard, eds., Bureau of Mineral Resources Bulletin 236: Geological and Geophysical Studies in the Amadeus Basin Central Australia, p. 7-32.
Lindsay, N. G., F. C. Murphy, J. J. Walsh, and W. J., 1993, Outcrop studies of shale smear on fault surfaces, Association of Sedimentologists Special Publication 15, p. 113-123.
Lisle, R. J., 1994, Detection of zones of abnormal strains in structures using gaussian curvature analysis: AAPG Bulletin, v. 78, p. 1811-1819.
Lisle, R. J., and C. D. Srivastava, 2004, A test of the frictional reactivation theory for faults and validity of fault-slip analysis: Geology, v. 32, p. 569-572.
Lorenz, J. C., and S. J. Finley, 1991, Regional fractures 2: fracturing of Mesaverde reservoirs in the Piceance Basin, Colorado: AAPG Bulletin, v. 75, p. 1738-1757.
Lorenz, J. C., L. W. Teufel, and N. R. Warpinski, 1991, Regional fractures 1: a mechanism for the formation of regional fractures at depth in flat-lying reservoirs: AAPG Bulletin, v. 75, p. 1714-1737.
Ludwig, W. J., J. E. Nafe, and C. L. Drake, 1970, Seismic refraction, *in* A. E. Maxwell, ed., The Sea: Ideas and Observations on Progress in the Study of the Sea, v. 4: New York, Wiley-Interscience, p. 53-84.
Maboko, M. A. H., I. McDougall, P. K. Zeitler, and I. S. Williams, 1992, Geochronological evidence for ~530-550 Ma juxtaposition of two Proterozoic metamorphic terrains in the Musgrave Ranges, central Australia: Australian Journal of Earth Sciences, v. 39, p. 457-471.
Maerten, L., P. Gillespie, and D. D. Pollard, 2002, Effects of local stress perturbation on secondary fault development: Journal of Structural Geology, v. 24, p. 145-153.
Maltman, A. J., and A. Bolton, 2003, How sediments become mobilized, *in* P. Van Rensbergen, R. R. Hillis, A. J. Maltman, and C. K. Morley, eds., Subsurface sediment mobilization, Geologic Society of London. Special Publication 216, p. 9-21.
Mann, D. M., and A. s. Mackenzie, 1990, Prediction of pore pressures in sedimentary basins: Marine and Petroleum Geology, v. 7, p. 55-65.
Marjoribanks, R. W., 1976, Basement and cover relations on the northern margin of the Amadeus Basin, central Australia: Tectonophysics, v. 33, p. 15-32.
Masaferro, J. L., M. Bulnes, J. Poblet, and N. Casson, 2003, Kinematic evolution and fracture prediction of the Valle Morado structure inferred from 3-D seismic data, Salta province, northwest Argentina: AAPG Bulletin, v. 87, p. 1083-1104.

Mavor, M. J., and H. Cinco, 1979, Transient pressure behaviour of naturally fractured reservoirs: SPE 7977.
McKenzie, D., and D. Fairhead, 1997, Estimates of the effective elastic thickness of the continental lithosphere from Bouger and free air gravity anomalies: Journal of Geophysical Research, v. 102, p. 27,523-27,552.
McNaughton, D. A., and W. A. Huckaba, 1978, Reservoir rock characteristics of Arumbera Sandstone and Late Proterozoic sediments (unpublished), Magellan Petroleum Corporation, technical introduction sheet O.
Meyer, J. J., 2002, The determination and application on in situ stresses in petroleum exploration and production: PhD thesis, The University of Adelaide, Adelaide, 237 p.
Meyer, M., and J. Brooker, 1991, Eliciting and Analysing Expert Judgement: A Practical Guide: London, Academic Press.
Michaelson, P., and R. A. Henderson, 2000, Facies relationships and cyclicity of high-latitude, Late Permian coal measures, Bowen Basin, Australia: Internation Journal of Coal Geology, v. 44, p. 19-48.
Mildren, S. D., R. R. Hillis, T. Fett, and P. H. Robinson, 1994, Contemporary stresses in the Timor Sea: implications for fault-trap integrity: The Sedimentary Basins of Western Australia, PESA Symposium, p. 301-312.
Mildren, S. D., R. R. Hillis, and J. Kaldi, 2002a, APPEA Journal: Calibrating predictions of fault seal reactivation in the Timor Sea, v. 42, p. 187–202.
Mildren, S. D., R. R. Hillis, and J. Kaldi, 2002b, Calibrating predictions of fault seal reactivation in the Timor Sea: APPEA Journal, v. 42, p. 187-202.
Mills, K., 2001, Inbye stress measurements - Goonyella Riverside Mine: report to BHP Australia Coal Ltd (unpublished), SCT Operations Pty Ltd, p. 13.
Milne, N. A., and D. C. Barr, 1990a, Subsurface fracture analysis, Palm Valley gas field: APPEA Journal, v. 1990, p. 321-341.
Milne, N. A., and D. C. Barr, 1990b, Subsurface fracture analysis, Palm Valley gas field: APPEA Journal, v. 30, p. 321-341.
Mitra, S., 2003, A unified kinematic model for the evolution of detachment folds: Journal of Structural Geology, v. 25, p. 1659-1673.
Mogi, K., 1967, Effect of the intermediate principal stress on rock failure: Journal of Geochemical Research, v. 72, p. 5117-5131.
Mollema, P. N., and A. Aydin, 1997, Fracture patterns and fault architecture in the East Kaibab Monocline, Natural fracture systems, Four Corners Geological Society, p. 63-75.
Molnar, P., and H. Lyon-Caen, 1988, Some simple physical aspects of the support, structure, and evolution of mountain belts: Geologic Society of America Special Paper, v. 218, p. 179-207.
Murray, C. G., 1990, Tectonic evolution and metallogenesis of the Bowen Basin: Bowen Basin Symposium 1990.
MVE, 2004, The Fracture Modelling Module for 3DMove, http://www.mve.com/Home/Software/3DMove/FractureModelling.
Narr, W., 1991, Fracture density in the deep subsurface: techniques with application to Point Arguello oil field.: AAPG Bulletin, v. 75, p. 1300-1323.
Naruk, S. J., W. F. Dula, J. P. Busch, B. A. Couzens-Schultz, L. Garmezy, H. Griffiths, A. M. Gunst, C. A. Hedlund, E. McAllister, U. O. Onyeagoro, B. M. Ozumba, and A. Younes, 2003, Common characteristics of proven sealing and leaking faults: AAPG Hedberg Research Conference "Evaluating the Sealing Potential of Faults and Caprocks", p. 71-74.
NASA, 2004, Earth Science Applications Directorate, https://zulu.ssc.nasa.gov/mrsid/.
Nelson, E., R. R. Hillis, S. D. Mildren, and J. J. Meyer, 2004, The in situ stress field of the West Tuna area, Gippsland Basin: implications for natural fracture-enhanced permeability and wellbore stability: Australian Society of Exploration Geophysicists 17th Geophysical Conference and Exhibition.
Nelson, R. A., 2001, Geological Analysis of Naturally Fractured Reservoirs: Boston, Gulf Professional Publishing, 332 p.
Nemcik, J., 2000, In situ stress measurement in coal 19 cut-through A heading Goonyella Riverside underground mine: report to Goonyella Riverside mine (unpublished), SCT Operations, p. 9.
NTGS, 2003, Northern Territory Geological Survey home page, http://www.dme.nt.gov.au/ntgs/.
Odling, N. E., P. Gillespie, B. Bourgine, C. Castaing, J.-P. Chiles, N. P. Christensen, E. Fillion, A. Genter, C. Olsen, L. Thrane, R. Trice, E. Aarseth, J. J. Walsh, and J. Watterson, 1999, Variations in fracture system geometry and their implications for fluid flow in fractured hydrocarbon reservoirs: Petroleum Geoscience, v. 5, p. 373-384.

Osborne, M. J., and R. E. Swarbrick, 1997, Mechanisms for generating overpressure in sedimentary basins: a reevaluation: AAPG Bulletin, v. 81, p. 1023-1041.
Ottesen Ellevset, S., R. J. Knipe, T. Svava Olsen, Q. J. Fisher, and G. Jones, 1998, Fault controlled communication in the Sleipner Vest Field, Norwegian Continental Shelf; detailed , quantitative input for reservoir simulation and well planning, *in* G. Jones, Fisher, Q, J., Knipe, R, J., ed., Faulting, fault sealing and fluid flow in hydrocarbon reservoirs, Geological Society of London. Special Publication 147, p. 283-297.
Ouenes, A., and L. J. Hartley, 2000, Integrated fractured reservoir modeling using both discrete and continuum approaches: SPE 62939, p. 1-10.
Parks, W. L., and M. S. Gale, 1992, Exploring overpressured, naturally fractured reservoirs in the Powder River Basin, Wyoming: a multi-disciplinary effort: AAPG Powder River Basin Symposium, p. 2-11.
Parney, B., E. Jenner, and M. Williams, 2004, Interpreting seismic anisotropy using DFN, geologic and engineering analogs: Characterization of Fractured Reservoirs SEG/EAGE Summer Workshop.
Pashin, J. C., 1998, Stratigraphy and structure of coalbed methane reservoirs in the United States: an overview: International Journal of Coal Geology, v. 35, p. 209-240.
Pattison, C. I., 1990, Igneous Intrusions in the Bowen Basin: MSc thesis, Queensland Institute of Technology, Brisbane.
Pattison, C. I., C. R. Fielding, R. H. McWatters, and L. H. Hamilton, 1995, Nature and origin of fractures in Permian coals from the Bowen Basin and the relationship with in situ reservoir permeability, *in* I. L. Follington, J. W. Beeston, and L. H. Hamilton, eds., Bowen Basin Symposium 1995: Mackay, p. 217-233.
Pattison, C. I., C. R. Fielding, R. H. McWatters, and L. H. Hamilton, 1996, Nature and origin of fractures in Permian coals from the Bowen Basin, Queensland, Australia, *in* R. Gayer, Harris, I., ed., Coalbed methane and coal geology, Geological Society of London. Special Publication 109, p. 133-150.
Payenberg, T. H. D., and S. C. Lang, 2003, Reservoir geometry of fluvial distributary channels-implications for Northwest Shelf, Australia, deltaic successions: APPEA Journal, v. 43, p. 325-338.
Perez, M. A., R. L. Gibson, and M. N. Toksoz, 1999, Detection of fracture orientation using azimuthal variation of P-wave AVO responses: Geophysics, v. 64, p. 1253-1265.
Petit, J.-P., V. Auzias, K. Rawnsley, and T. Rives, 2000, Development of joint sets in the vicinity of faults, *in* L. K. Florian, Janos, U. L., ed., Aspects of Tectonic Faulting: Berlin, Springer, p. 167-183.
Plumb, R. A., 1994, Variations of the least horizontal stress magnitude in sedimentary rocks: 1st North American Rock Mechanics Symposium, p. 71-78.
Poblet, J., and K. McClay, 1996, Geometry and kinematics of single layer detachment folds: American Association of Petroleum Geologists Bulletin, v. 80, p. 1085-1109.
Pontifex, I., R, 2001, Mineralogical Report No. 8120 (unpublished), Adelaide, Pontifex and Associates Pty. Ltd.
Prensky, S., 1992, Borehole breakouts and in-situ rock stress - a review: The Log Analyst, v. 33, p. 304-312.
Price, N. J., and J. W. Cosgrove, 1990, Analysis of Geological Structures: Cambridge, Cambridge University Press, 502 p.
Purcell, W. R., 1949, Capillary pressures - their measurement using mercury and the calculation of permeability therefrom: Petroleum Transactions, American Institue of Mining Engineers, v. 186, p. 39-48.
Ramos, A. C. B., and T. L. Davis, 1997, 3-D AVO analysis and modeling applied to fracture detection in coalbed methane reservoirs: Geophysics, v. 62, p. 1683-1695.
Ranford, L. C., P. J. Cook, A. T. Wells, and A. J. Stewart, 1963, Henbury (1:250,000 geological map): Bureau of Mineral Resources.
Reading, H., G., 1996, Sedimentary environments: processes, facies and stratigraphy, Blackwell Science, 688 p.
Rider, M., 2000, The Geological Interpretation of Well Logs, Second Edition: Caithness, Whittles, 280 p.
Rijken, P., and M. L. Cooke, 2001, Role of shale thickness on vertical connectivity of fractures: application of crack-bridging theory to the Austin Chalk, Texas: Tectonophysics, v. 337, p. 117-133.
Roberts, G., P., 1994, Displacement localization and palaeo-seismicity of the Rencurel Thrust Zone, French Sub-Alpine Chains: Journal of Structural Geology, v. 16, p. 633-646.
Roberts, G. A., and S. T. Chipperfield, 2000, The evolution of a high near-wellbore pressure loss treatment strategy for the Australian Cooper Basin: SPE 63029, p. 1-12.
Rowan, M., G, 1993, Structural geometry of the Wildhorn nappe between the Aar massif and the Brienzer See: Eclogae Geologicae Helvetiae, v. 86, p. 87-119.

Santarelli, F. J., J. T. Tronvoll, M. Svennekjaer, H. Skele, R. Henriksen, and R. K. Bratli, 1998, Reservoir stress path: the depletion and the rebound, p. 203-209.
Scheidegger, A. E., 1983, Interpretation of fracture and physiographic patterns in Alberta, Canada: Journal of Structural Geology, v. 5, p. 53-59.
Schlumberger, 1991, Wireline logging services catalogue, Schlumberger Educational Services.
Schlumberger, 2004, http://www.oilfield.slb.com/media/services/stimulation/fracturing/coilfrac.pdf.
Schowalter, T. T., 1979, Secondary hydrocarbon migration and entrapment: AAPG Bulletin, v. 63, p. 723-760.
Schubarth, S. K., A. C. Byrd, and J. F. Wickham, 2003, U.S. natural gas market: recent dynamics and future concerns: SPE 80949.
Scrimgeour, I., and D. Close, 1999, Regional high pressure metamorphism during intracratonic deformation: the Petermann Orogeny, central Australia: Journal of Metamorphic Geology, v. 17, p. 557-572.
Seedsman, R., 1998, Geotechnical assessment Goonyella exploration adit (unpublished), Seedsman Geotechnics Pty Ltd, p. 20.
Shaw, R., D, and L. Black, P, 1991, The history and tectonic implications of the Redbank Thrust Zone, central Australia, based on structural, metamorphic and Rb-Sr isotopic evidence: Australian Journal of Earth Sciences, v. 38, p. 307-332.
Shaw, R., D, R. Warren, G, and et.al, 1995, Hermannsburg (1:250,000 geological map): Australian Geological Survey Organisation.
Shaw, R. D., M. A. Etheridge, and K. Lambeck, 1991a, Development of the Late Proterozoic to Mid-Paleozoic intracratonic Amadeus Basin in central Australia: a key to understanding tectonic forces in plate interiors: Tectonics, v. 10, p. 688-721.
Shaw, R. D., R. J. Korsch, C. Wright, and B. R. Goleby, 1991b, Seismic interpretation and thrust tectonics of the Amadeus Basin, central Australia, along the BMR regional seismic line, *in* R. J. Korsch, Kennard, J. M., ed., Bureau of Mineral Resources Bulletin 236: Geological and Geophysical Studies in the Amadeus Basin Central Australia, p. 385-408.
Shaw, R. D., A. J. Stewart, and L. P. Black, 1984, The Arunta Inlier: a complex ensialic mobile belt in central Australia. Part 2: tectonic history.: Australian Journal of Earth Sciences, v. 31, p. 457-484.
Shaw, R. D., P. K. Zeitler, I. McDougall, and P. R. Tingate, 1992, The Palaeozoic history of an unusual intracratonic thrust belt in central Australia based on ^{40}AR-^{39}Ar, K-Ar and fission track dating: Journal of the Geological Society, London, v. 149, p. 937-954.
Shipton, Z. K., and P. A. Cowie, 2001, Damage zone and slip-surface evolution over mm to km scales in high porosity Navajo sandstone, Utah: Journal of Structural Geology, v. 23, p. 1825-1844.
Sibson, R. H., 1990, Conditions for fault valve behaviour: Deformation mechanisms, rheology and tectonics, Geological Society of London. Special Publication 54, 15-28 p.
Sibson, R. H., 1996, Structural permeability of fluid-driven fault-fracture meshes: Journal of Structural Geology, v. 18, p. 1031-1042.
Sinka, C., 1998, An investigation into rock and reservoir properties of coal with special reference to stimulated coalbed methane well performance, http://www.huxley.ic.ac.uk/research/envmin/people/csinka_phd.html.
Sleep, N. H., and M. L. Blanpied, 1992, Creep, compaction and the weak rheology of major faults: Nature, v. 359, p. 687-692.
Smith, D. A., 1966, Theoretical considerations of sealing and non-sealing faults: AAPG Bulletin, v. 50, p. 363-374.
Soper, N. J., and A. K. Higgins, 1990, Models for the Ellesmerian mountain front in North Greenland: a basin margin inverted by basement uplift: Journal of Structural Geology, v. 12, p. 83-98.
Southgate, P. N., 1991, A sedimentological model for the Loves Creek Memeber of the Bitter Springs Formation, northern Amadeus Basin, *in* R. J. Korsch, Kennard, J.K., ed., Bureau of Mineral Resources Bulletin 236: Geological and geophysical studies in the Amadeus Basin central Australia, p. 113-126.
Space.com, 2004, Space.com image of the day, http://www.space.com/imageoftheday/image_of_day_040128.html.
Sperrevik, S., P. A. Gillespie, Q. J. Fisher, T. Halvorsen, and R. J. Knipe, 2002, Empirical estimation of fault rock properties, *in* A. G. Koestler, Hunsdale, R., ed., Hydrocarbon Seal Quantification, v. NPF Special Publication 11, Elsevier, p. 109-125.
St George, J. D., and M. A. Barakat, 2001, The change in effective stress associated with shrinkage from gas desorption in coal: International Journal of Coal Geology, v. 45, p. 105-113.

Stearns, D. W., L. Boldt, and S. Muhuri, 1996, Mechanical properties of selected Palm Valley reservoir rocks (unpublished), Magellan Petroleum Australia Limited.
Stearns, D. W., and M. Friedman, 1972, Reservoirs in fractured rocks: AAPG Bulletin, v. 16, p. 82-106.
Storti, F., and K. McClay, 1995, Influence of syntectonic sedimentation on thrust wedges in analogue models: Geology, v. 23, p. 999-1002.
Suppe, J., 1983, Geometry and kinematics of fault-bend folding: American Journal of Science, v. 283, p. 684-721.
Suppe, J., and D. A. Medwedeff, 1990, Geometry and kinematics of fault-propagation folding: Eclogae Geol, v. 83, p. 409-454.
Syarifuddin, N., and I. Busono, 1999, Regional stress alignments in the Kutai Basin, East Kalimantan, Indonesia: a contribution from a borehole breakout study: Journal of Asian Earth Sciences, v. 17, p. 123-135.
Teufel, L. W., 2003, Optimization of infill drilling in naturally-fractured tight-gas reservoirs of the San Juan Basin, http://www.netl.doe.gov/publications/proceedings/02/rockymt/Teufel%20Presentation.pdf.
Teufel, L. W., and J. M. Herrin, 2003, Optimization of infill drilling in naturally-fractured tight-gas reservoirs in the San Juan Basin (abs), http://aapg.confex.com/aapg/sl2003/techprogram/paper_79667.htm.
Teufel, L. W., D. W. Rhett, and H. E. Farrell, 1991, Effect of reservoir depletion and pore pressure drawdown on in situ stress and deformation in the Ekofisk field, North Sea, *in* J. C. Roegiers, ed., Rock Mechanics as a Multidisciplinary Science; proceedings of the 32nd U.S. Symposium on Rock Mechanics, v. 32, A.A. Balkema, p. 63-72.
Teyssier, C., 1985, A crustal thrust system in an intracratonic tectonic environment: Journal of Structural Geology, v. 7, p. 689-700.
Thompson, J. E., C. S. DeVine, J. J. Garner, W. Wood, and G. J. Eller, 2002, Management of completion systems utilizing state-of-the-art technologies: SPE 77707.
Tingate, P. R., 1991, Apatite fission track analysis of the Pacoota and Stairway Sandstones, Amadeus Basin, central Australia, *in* R. J. Korsch, and J. K. Kennard, eds., Bureau of Mineral Resources Bulletin 236: Geological and Geophysical Studies in the Amadeus Basin Central Australia, p. 525-541.
Tingate, P. R., A. J. W. Gleadow, I. R. Duddy, and P. F. Green, 1986, Thermal and tectonic history of the Amadeus Basin: - evidence from fission track analysis: 12th International Sedimentological Congress, p. 304.
Turcotte, D. L., and G. Schubert, 1982, Geodynamics; Applications of Continuum Physics to Geological Problems: New York, John Wiley and Sons, 450 p.
Twiss, R. J., and E. M. Moores, 1992, Structural Geology: New York, W. H. Freeman & Company, 532 p.
Underwood, C. A., M. L. Cooke, J. A. Simo, and M. A. Muldoon, 2003, Stratigraphic controls on vertical fracture patterns in Silurian dolomite, northeastern Wisconsin: AAPG Bulletin, v. 87, p. 121-142.
Vavra, C. L., J. G. Kaldi, and R. M. Sneider, 1992, Geological applications of capillary-pressure - a review: AAPG Bulletin, v. 76, p. 840-850.
Velseis, 2002, Seismic data interpretative 3D processing Goonyella Riverside Mine combined Goonyella 2001 3D seismic survey (unpublished), Velseis Processing Pty Ltd, p. 1-34.
Voight, B., and B. H. P. St. Pierre, 1974, Stress history and rock stress: Proceedings of the International Society of Rock Mechanics, the 3rd Rock Mechanics Congress, p. 580-582.
Walker, D., and M. D. Berry, 1993, Palm Valley No. 9 Well completion report, Magellan Petroleum Australia Limited (unpublished).
Walter, M. R., J. J. Veevers, C. R. Calver, and K. Grey, 1995, Neoproterozoic stratigraphy of the Centralian Superbasin, Australia: Precambrian Research, v. 73, p. 173-195.
Washburn, E. W., 1921, A note on the method of determining the distribution of pore sizes in a porous material: Proceedings of the National Academy, v. 7, p. 115-116.
Watts, A., B, 2001, Isostacy and Flexure of the Lithosphere: Cambridge, Cambridge University Press, 458 p.
Wellman, P., 1991, Amadeus Basin, Northern Territory: structure from gravity and magnetic anomalies, *in* R. J. Korsch, Kennard, J, K, ed., Bureau of Mineral Resources Bulletin 236: Geological and geophysical studies in the Amadeus Basin central Australia, p. 33-40.
Wells, A. T., D. J. Forman, and L. C. Ranford, 1961, Mount Liebig (1:250,000 geological map): Bureau of Mineral Resources.
Wells, A. T., D. J. Forman, L. C. Ranford, and P. J. Cook, 1970, Geology of the Amadeus Basin, Bureau of Mineral Resources Bulletin, 100, p. 222.

Wells, A. T., and F. J. Moss, 1983, The Ngalia Basin, Northern Territory: stratigraphy and structure, v. Geology and Geophysics Australia Bulletin 212, Bureau of Mineral Resources.
Wells, A. T., L. C. Ranford, P. J. Cook, A. J. Stewart, and D. J. Forman, 1962, Lake Amadeus (1:250,000 geological map): Bureau of Mineral Resources.
Whale, R., 2004, Seismic attribute studies for fracture identification: Pinedale Field, Wyoming: Characterization of Fractured Reservoirs SEG/EAGE Summer Workshop.
Wiebols, G., and N. Cook, 1968, An energy criterion for the strength of rock in polyaxial compression: International Journal of Rock Mechanics and Mining Sciences, v. 5, p. 529-549.
Williams, G. K., R. M. J. Hopkins, and D. A. McNaughton, 1965, Pacoota reservoir rocks, Amadeus Basin: APEA journal, v. 5, p. 159-167.
Winslow, M. A., 1983, Clastic dike swarms and the structural evolution of the foreland fold and thrust belt of the southern Andes: Geologic Society of America Bulletin, v. 94, p. 1073-1080.
Wiprut, D., and M. D. Zoback, 2002, Fault reactivation, leakage potential, and hydrocarbon column heights in northern North Sea, *in* A. G. Koestler, and R. Hunsdale, eds., Hydrocarbon seal quantification, v. NPF Special Publication 11: Amsterdam, Elsevier Science, p. 109-125.
Worotnicki, G., 1993, CSIRO triaxial stress measurement cell, *in* J. Hudson, A., ed., Comprehensive Rock Engineering, v. 3: Oxford, Pergamon Press, p. 329-394.
Wright, C., B. R. Goleby, R. D. Shaw, C. D. N. Collins, R. J. Korsch, T. Barton, S. A. Greenhalgh, and S. Sugiharto, 1991, Seismic reflection and refraction profiling in central Australia: implications for understanding the evolution of the Amadeus Basin.: Bureau of Mineral Resources Geology and Geophysics Bulletin, v. 236, p. 41-59.
Wu, H., and D. D. Pollard, 1995, An experimental study of the relationship between joint spacing and layer thickness: Journal of Structural Geology, v. 17, p. 887-905.
Wynn, T. J., and S. A. Stewart, 2003, The role of spectral curvature mapping in characterizing subsurface strain distributions, *in* M. Ameen, ed., Fracture and in-situ stress characterization of hydrocarbon reservoirs, Geological Society of London. Special Publication 209, p. 127-143.
Yale, D. P., 2003, Fault and stress magnitude controls on variations in the orientation of in situ stress, *in* M. Ameen, ed., Fracture and in-situ stress characterization of hydrocarbon reservoirs, Geological Society of London. Special Publication 209, p. 55-64.
Yielding, G., 2002, Shale gouge ratio - calibrating by geohistory, *in* A. G. Koestler, and R. Hunsdale, eds., Hydrocarbon seal quantification, v. NPF Special Publication 11: Amsterdam, Elsevier Science, p. 109-125.
Yielding, G., B. Freeman, and D. T. Needham, 1997, Quantitative fault seal prediction: AAPG Bulletin, v. 81, p. 897-917.
Yielding, G., T. Needham, and H. Jones, 1996, Sampling of fault populations using sub-surface data: a review: Journal of Structural Geology, v. 18, p. 135-146.
Zoback, M. D., and J. H. Healy, 1984, Friction, faulting and in situ stress: Annales Geophysicae, v. 2, p. 689-698.
Zoback, M. L., 1992, First- and second-order patterns of stress in the lithosphere: the world stress map project: Journal of Geophysical Research, v. 97, p. 11703-11728.
Zuber, M. D., and C. M. Boyer, 2002, Coalbed-methane evaluation techniques-the current state of the art: Journal of Petroleum Technology, v. 54, p. 66-69.
Zuber, M. T., T. D. Bechtel, and D. W. Forsyth, 1989, Effective elastic thickness of the lithosphere and mechanisms of isostatic compensation in Australia: Journal of Geophysical Research, v. 94, p. 9353-9367.